

# THÈSE

Pour obtenir le grade de  
**Docteur**

Délivré par l'**Université Montpellier II**

Préparée au sein de l'école doctorale **I2S\***  
Et de l'unité de recherche **UMR AGAP**

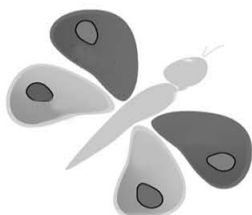
Spécialité: **Informatique**

Présentée par **Mathilde Balduzzi**

*mathilde.balduzzi@gmail.com*

*Version mise à jour le 5 mai 2015*

## Plant canopy modeling from Terrestrial LiDAR System (TLS) distance and intensity data



Labex NUMEV



Soutenue le 24 Novembre 2014 devant le jury composé de :

W. PUECH	Professeur	Univ. Montpellier II	Président
P.-E. LAURI	HDR	INRA	Membre invité
F. BARET	HDR	INRA	Examineur
F. TARDIEU	HDR	INRA	Examineur
J.-D. DUROU	Professeur	IRIT	Rapporteur
R. FOURNIER	Professeur	Univ. Sherbrooke	Rapporteur
C. GODIN	HDR	INRIA	Directeur de thèse

*[Shape-From-Shading method adapted to TLS data for outlier  
points correction]*





## Résumé

La mesure de la géométrie des feuilles d'une plante est une étape importante lorsqu'il est nécessaire d'étudier la physiologie de la plante ou encore son interaction l'environnement. Les scanners 3D de type "Scanner LiDAR (Light Detection And Ranging) Terrestre" (ou TLS) sont des outils de mesures qui ont permis d'extraire des variables géométriques pour la modélisation des plantes. Ces variables peuvent être globales (e.g., canopée) ou locales (e.g., feuille). De nombreuses méthodes d'extraction de variables globales ont déjà été proposées dans la littérature. Par contre, l'extraction de variables locales dans des conditions in situ n'ont pas été encore bien mises au point. Le TLS est un appareil de mesure de distance qui émet une lumière laser et qui enregistre le temps de vol de cette lumière après avoir été réfléchi par une surface. Il utilise ce temps de vol pour en déduire sa distance à cette surface. Généralement, les TLSs sont équipés d'un système mécanique et optique permettant le scan complet d'une scène et ainsi, la génération d'un nuage de points de cette scène. L'analyse des données TLS nous permet de dire que la qualité des nuages de points des TLSs est variable en fonction de la configuration de la mesure : lorsque le TLS mesure le bord d'une surface ou une surface fortement inclinée, il intègre dans sa mesure la partie de l'arrière plan. Ces configurations de mesures produisent des points aberrants, ou "outliers". On retrouve souvent ce type de configuration pour la mesure de feuillages puisque ces derniers ont des géométries fragmentées et variables. Ainsi, la qualité des scans ne permettent pas, en général, d'extraire correctement les feuilles d'arbres car la suppression des points aberrants devient rapidement fastidieuse. L'objectif de cette thèse est de développer une méthodologie permettant d'intégrer les données d'intensité TLS aux distances pour corriger automatiquement ces points aberrants et ainsi fournir une représentation réaliste des feuilles de canopée à partir de scan TLS. Le principe du Shape-From-Shading (SFS) est de retrouver les valeurs de distance à partir des intensités d'un objet pris en photo. Les points aberrants étant au bord du nuage de points représentant les feuilles, nous choisissons de développer une méthode de SFS par propagation initialisée par les régions du nuage de points qui sont de bonne qualité. Les valeurs d'intensité d'une image sont fonction de l'angle d'incidence entre le rayon lumineux et la surface. Nous donnons une preuve mathématique que les surfaces qui ont une intensité (i.e., un angle d'incidence) constante sur une image sont nécessairement des surfaces dites d'égales pentes, ou dites de "tas de sable". Ces surfaces ont des propriétés géométriques intéressantes ce qui nous a amené à choisir de développer une méthode de SFS par propagation le long de ces régions iso-intenses. Notre méthode de SFS a d'abord été testée sur des surfaces synthétiques. Elle est ensuite appliquée à des données TLS de poirier Conférence pour la reconstruction de feuilles manuellement sélectionnée. En amont de ces reconstructions, les données d'intensité TLS sont calibrés (correction radiométrique de l'effet distance, transformation des intensités en valeur d'angles d'incidence).

**Mots-clefs :** TLS, point aberrants, shape-from-shading, surface foliaire et inclinaison



## Abstract

Plant geometry measurement is an important step to study plant's physiology and interaction with its environment. 3D "Terrestrial LiDAR (Light Detection and Ranging)Scanners" are measuring tools that allowed scientists to extract geometrical variable of plants for their modeling. Those variables can be global (e.g., canopy shape), or local (e.g., leaf shape). Despite they have been showed efficient for global variables extraction, local variables extraction within in situ condition has not been well set up yet. TLS device is a distance measuring tool that emits a laser light and records time-of-flight of reflected laser light. It uses this time-of-flight to determine distance between its aperture and the surface. Generally, TLS are equipped with mechanical/optical system to make it possible to scan a scene, and consequently the generation of a 3D point cloud. TLS data analysis shows that the point cloud quality is variable. This quality depends upon the measurement set up. When the TLS laser beam reaches the edge of a surface (or a steeply inclined surface), it also integrates background measurement. Those set up produce outliers. This kind of set up is common for foliage measurements as foliages have in general fragmented and complex shapes. TLS data quality is severally biased and the quantity of leaves in a scan makes the correction of outliers fastidious. This thesis goal is to develop a methodology to integrate TLS intensity data with TLS distance to make an automatic correction of those outliers and to provide a realistic representation of canopy leaves from TLS scan. Shape-from-shading (SFS) principle is to reconstruct an object from the intensities of its photography. Outliers being along the edge of surface point cloud, we chose to develop a propagation SFS method with an initialization yield with portions of the TLS 3D point cloud that are of good quality. Intensity values of a photograph depend on incidence angle between light beam and surface. In this thesis, we prove that surface with constant intensity (i.e., incidence angle) are necessarily surfaces of constant slope, or "sand-pile" surfaces. Those surfaces have interesting geometrical property that made our decision to develop a propagation method along iso-intensity regions. Our SFS method has been tested on synthetic surfaces. Then it has been applied on Conference pear tree leaves that have been manually extracted from TLS point cloud. Upstream those reconstructions, TLS intensity data are calibrated (radiometric correction of the distance effect, intensity to incidence angle transformation).

**Keywords:** TLS, outlier points, shape-from-shading, leaf area and inclination



# Contents

<b>Contents</b>	<b>v</b>
<b>Résumé en Français</b>	<b>2</b>
<b>Introduction</b>	<b>20</b>
<b>I Introduction: Terrestrial LiDAR Scanner (TLS) for canopy geometry assessment?</b>	<b>23</b>
<b>1 Terrestrial LiDAR Scanner (TLS)</b>	<b>25</b>
1 LiDAR principle . . . . .	26
1.1 Distance measurement . . . . .	26
1.2 Intensity measurement . . . . .	27
1.3 Laser beam footprint . . . . .	28
1.4 Optical and mechanical design . . . . .	28
2 Data quality . . . . .	29
2.1 Distance value . . . . .	30
2.2 Intensity value . . . . .	33
2.3 Outlier points . . . . .	34
2.4 Point density . . . . .	36
2.5 Ratio outliers/number of points (ROP) . . . . .	36
2.6 Quality factors . . . . .	37
3 Conclusion . . . . .	37
<b>2 Toward a geometric reconstruction of leaves from orchard trees</b>	<b>39</b>
1 Plant morphology . . . . .	40
1.1 Plant structure and fruit production . . . . .	40
1.2 Plant diseases . . . . .	42
2 Measurements and representations of vegetation structure . . . . .	44
2.1 The plant as a single entity . . . . .	45
2.2 Leaves geometry distribution . . . . .	49
2.3 Virtual plants . . . . .	54

3	TLS quality factors for pear tree leaves measurements . . . . .	61
3.1	Material and methods . . . . .	62
3.2	Results and discussion . . . . .	64
4	Conclusion . . . . .	66

## **II Algorithm: Shape-From-Shading propagation along isophote region for TLS data 69**

<b>3</b>	<b>Shape-From-Shading: state-of-art</b>	<b>71</b>
1	Image intensities modeling . . . . .	72
1.1	Scene geometry . . . . .	72
1.2	Modeling light radiance and irradiance . . . . .	73
1.3	Reflectance map and irradiance equation . . . . .	75
1.4	General intuition of the SFS problem . . . . .	78
2	SFS proof of existence and uniqueness . . . . .	80
3	GLOB-SFS method . . . . .	80
3.1	Minimization method . . . . .	81
3.2	Linear resolution . . . . .	82
3.3	Viscosity solution . . . . .	82
4	PROP-SFS methods . . . . .	83
4.1	Along level height curve . . . . .	84
4.2	Propagation along isophote regions . . . . .	85
5	Comparison of the methods . . . . .	86
6	Conclusion . . . . .	87
<b>4</b>	<b>Parametric properties of isophote surfaces</b>	<b>89</b>
1	Scene modeling . . . . .	90
2	Greatest slope and level height curves . . . . .	91
3	Squared domain . . . . .	92
4	Remarkable geometric properties of curves . . . . .	95
5	Fundamental theorem on iso- $\alpha$ domains . . . . .	98
6	General nature of surfaces corresponding to iso- $\alpha$ region . . . . .	101
7	Conclusion . . . . .	103
<b>5</b>	<b>PROP-SFS propagation of sand-pile surfaces along iso-<math>\alpha</math> regions</b>	<b>105</b>
1	Pipeline principle . . . . .	105
2	Pipeline description . . . . .	106
2.1	Input data . . . . .	106
2.2	Iso- $\alpha$ domain chains extraction . . . . .	107
2.3	Seed-based initialization . . . . .	108

2.4	SPS propagation . . . . .	109
2.5	Algorithmic set up . . . . .	113
3	Pipeline analysis . . . . .	117
3.1	Propagation algorithms comparison . . . . .	117
3.2	Segmentation . . . . .	120
3.3	Sensitivity analysis . . . . .	120
3.4	Complexity . . . . .	126
4	Conclusion . . . . .	128

### **III Application: Conference pear tree leaf area and inclination estimation from TLS FARO LS880 data 131**

<b>6</b>	<b>Intensity properties of a TLS FARO LS880 to measure Conference pear tree leaves geometry</b>	<b>133</b>
1	Material and methods . . . . .	133
1.1	TLS FARO LS880 . . . . .	133
1.2	Measurement setup . . . . .	135
1.3	TLS data pre-processing and analysis . . . . .	138
2	Results . . . . .	140
2.1	Correction of the distance effect on TLS intensity . . . . .	140
2.2	Validation of the incidence angle provided by a LSR . . . . .	141
2.3	Relationship between intensity and incidence angle for Conference pear tree leaves . . . . .	143
3	Discussion . . . . .	150
4	Conclusion . . . . .	151
<b>7</b>	<b>PROP-SFS method for Conference pear tree leaf area and inclination estimation from TLS FARO LS880 data</b>	<b>153</b>
1	Material and Method . . . . .	153
1.1	Orchard . . . . .	153
1.2	TLS FARO LS880 data . . . . .	154
1.3	Leaf measurement . . . . .	154
1.4	PROP-SFS pipeline description . . . . .	156
1.5	PROP-SFS extension . . . . .	157
1.6	Analysis . . . . .	159
2	Results and discussion . . . . .	160
2.1	Primary results . . . . .	160
2.2	Geometrical variable extraction from PROP-SFS mesh . . . . .	160
2.3	Mesh reconstruction from PROP-SFS point cloud . . . . .	161
2.4	PROP-SFS algorithm analysis . . . . .	163

2.5	Extreme cases . . . . .	167
2.6	rppp <sub>1</sub> distribution . . . . .	167
3	Discussion . . . . .	168
4	Conclusion . . . . .	169

## **IV Conclusion** **171**

## **V Appendices** **179**

### **I Traditional point cloud process** **181**

1	Generation of the virtual surface . . . . .	181
2	Pre- and post-processing . . . . .	183
2.1	Scan registration . . . . .	183
2.2	Objects segmentation, recognition and classification . . . . .	183
2.3	Noise reduction . . . . .	185
2.4	Outliers correction . . . . .	186
2.5	Simplification . . . . .	186
2.6	Surface completion . . . . .	186
3	Discussion . . . . .	187

### **II Geometry** **191**

1	Curve . . . . .	191
1.1	Frenet trihedron . . . . .	191
1.2	Inflexion point of a curve . . . . .	192
1.3	Involute and evolute . . . . .	192
1.4	Helix . . . . .	192
1.5	Chapter 4: Lemma 15 on curves. . . . .	193
2	Surface . . . . .	195
2.1	Greatest slope, level curve and gradient property . . . . .	195
2.2	Chapter 5: Equation 2.7 . . . . .	197
2.3	Chapter 5: Equation 2.12 . . . . .	199
2.4	Ruled and developed surfaces . . . . .	199
2.5	Sand-pile surface . . . . .	201

### **III Tangent-driven reconstruction of discrete contour** **203**

1	Prerequisite . . . . .	204
1.1	Freeman code . . . . .	204
1.2	Euclidean path . . . . .	205
1.3	Remarks . . . . .	205
1.4	Discrete line . . . . .	205



1.5	8-connected discrete line segment recognition algorithm . . . . .	206
2	Algorithm . . . . .	208
2.1	Path extraction . . . . .	208
2.2	Discrete tangent and Euclidean point calculation . . . . .	209
3	Time complexity . . . . .	210
<b>List of publications</b>		<b>211</b>
<b>Bibliography</b>		<b>213</b>



# Acknowledgment

Je tiens à remercier le Labex NUMEV qui m'aura attribué une bourse d'un an pour commencer ma thèse à l'Université de Montpellier II au sein de l'équipe Virtual Plants. Je remercie aussi l'Agropolis Fondation, l'INRIA pour les financements qu'ils m'ont accordés pour la seconde année de thèse. Enfin, un grand merci à l'UMT CAPTE de l'INRA sans qui je n'aurais pu venir à bout de ma troisième année de thèse. Je remercie les doctorants, post-doctorants, ingénieurs et permanents de l'équipe Virtual Plants pour m'avoir si gentilleement accueillie. Merci à mes amis et ma famille qui m'auront soutenues pendant ces années. Et enfin, un grand merci au Prof. Christophe Godin pour sa bienveillance, ses bons conseils et son excellent encadrement.



# **Résumé en Français : Modélisation géométrique des feuilles d'arbres fruitiers à partir des données d'intensité et de distance fournies par un Système LiDAR Terrestre (ou TLS)**

L'arboriculture fruitière est une spécialité agricole qui consiste à gérer un verger et sa production, tant pour la conduite d'arbres que pour la livraison des fruits aux industries agro-alimentaires, aux distributeurs et/ou aux ménages. Par rapport à d'autres types d'agriculture, le choix d'une exploitation en arboriculture fruitière expose l'agriculteur à certaines difficultés, caractéristiques remarquables de cette activité<sup>1</sup> :

- l'investissement initial est non négligeable ( $\sim 10$  k€/ha) ;
- le temps de mise en production du verger est long ; celui-ci varie de 3 à 5 ans selon les variétés et les porte-greffes ;
- il est difficile de faire marche arrière lorsque le verger est mis en place ;
- il est impossible de mettre en place des rotations de culture sur la production des arbres ;
- l'entretien des arbres est complexe (ex. : conduite, contrôle de la vigueur) ;
- l'amplitude de la marge directe peut varier de -10k€/ha/an à 10k€/ha/an selon les conditions météorologiques et l'entretien du verger.

A cause de ces difficultés, l'arboriculture fruitière est une agriculture risquée et les vergers peuvent rapidement se retrouver dans le rouge. Ainsi, il est souhaitable de réduire le risque au maximum. Cette réduction peut se faire via les coûts (intrants, charges) ou encore par la garantie d'une qualité et d'une régularité de production en contrôlant, par exemple : l'impact des facteurs biotiques (ex. : maladies), abiotiques (ex. : irrigation), ou encore humain (ex. : élagage).

---

<sup>1</sup>Observatoire des exploitations fruitières, données 2012. FranceAgriMer, CER France, Ctil, FNPF.

Ces facteurs – biotiques, abiotiques et humains – sont interdépendants, et donc, leur modélisation est complexe. Toujours est-il, la mise en place de ces modèles permettent aujourd’hui aux scientifiques de comprendre la dynamique de cette interdépendance et ils pourront, in fine, s’inscrire dans un processus décisionnel pour la gestion optimale des vergers. Par exemple, la simulation de la configuration d’un verger (ex. : densité de plantation, système de conduite – voir Figure 1) permettrait d’étudier sa rentabilité et ce, de manière beaucoup plus rapide et systématique que ce qui est fait habituellement. En effet, pour mener à bien ce genre d’étude, il a été jusqu’à présent nécessaire de planter et d’entretenir des vergers-tests pendant plusieurs années afin d’obtenir une statistique satisfaisante sur leur production et leur gestion<sup>2</sup> (ex. : nombre d’unités horaires, charges d’intrant, etc.). La simulation de la dynamique d’un verger permettrait de prendre en compte plusieurs scénarii (climat, sols, topographie) à partir d’un système de conduite donnée et de rendre compte rapidement de son efficacité et de son adéquation au lieu. Un second exemple que l’on peut donner concerne la détection et l’étude de la propagation des stress biotiques et abiotiques. Comme on peut l’imaginer, modéliser leur dynamique permettrait de mieux anticiper leur apparition et leur propagation, ce qui pourrait permettre une meilleure irrigation et une application plus adéquate des produits phytosanitaires. En conclusion, la modélisation des stress biotiques et abiotiques amènerait à une meilleure gestion des vergers, c’est-à-dire, à une réduction du coût des intrants et à une augmentation de la qualité de la production. Il est remarquable que ces stress induisent bien souvent une déformation observable des organes de la plante. La mesure de ces déformations serait une étape importante pour mener à bien l’étude et la modélisation de la dynamique de ces stress.

Avec ces deux exemples, nous avons montré que pour estimer l’efficacité d’un système de conduite appliqué à une variété plantée dans un environnement spécifique, l’utilisation de modèles informatiques pourrait s’avérer intéressante mais qu’il est nécessaire de mener des études approfondies de la dynamique de la physiologie de la plante pour mettre en place ces modèles. Dans nos deux exemples, nous avons vu que la description géométrique telle que celle du couvert ou de l’architecture mais aussi de la forme précise des feuilles étaient nécessaires. Ces descriptions nécessitent des outils permettant de fournir rapidement et de manière exhaustive des mesures de géométrie, et à toutes les échelles de la plante, c’est-à-dire, du couvert aux organes.

Traditionnellement, la géométrie du couvert peut être estimée grâce aux photos hémisphériques desquelles sont déduits le Leaf Area Index<sup>3</sup> (ou LAI, voir Figure 2-1). Ce LAI représente la densité globale du couvert. Les mesures de la position des organes ainsi que de l’architecture de l’arbre

---

<sup>2</sup>La station de recherche PCFruit (Belgique) a mené pendant 7 ans (2003-2010) une étude portée sur une seule variété (poirier Conference) et avec 7 systèmes de conduites différents. Cette étude a consisté à comparer la gestion et la production de ces systèmes de conduite par rapport à un système de conduite de référence, le «Slender Spindle» (valeur = 100%). PCFruit a montré que les systèmes de conduite en « V-system » et « Super Spindle » avaient, respectivement, un coût de main d’œuvre de 394% et 272%, un investissement initial de 180% et 234%, et une production de 137% et de 120%.

<sup>3</sup>Louarn et al., “A three-dimensional statistical reconstruction model of grapevine (*Vitis vinifera*) simulating canopy structure variability within and between cultivar/training system pairs”, 2008.

peuvent, elles, se faire de manière laborieuse avec un digitaliseur 3D<sup>4,5</sup> (voir Figure 2-2). Comme nous l'avons vu, des mesures de plantes à une échelle fine, c'est-à-dire au niveau des organes, sont nécessaires et ces mesures devraient être faites rapidement, c'est-à-dire au débit de plusieurs ares de cultures par jour. Il y a quelques années, des scanners 3D abordables et portatifs, sont apparus sur le marché. Ces scanners 3D permettent de mesurer rapidement la 3D d'un objet, c'est-à-dire, de produire un nuage de point 3D représentant cet objet en vue de générer son modèle 3D<sup>6</sup>. De ces modèles 3D peuvent être extraits des informations géométriques (ex. : volume, surface). Les scanners 3D de type « Terrestrial LiDAR System (TLS) » ont la particularité de fournir des données de qualité tant à de courtes qu'à de longues distances. Pour ma thèse, je me suis intéressée à ce type de scanner 3D car ses caractéristiques sont adaptés aux mesures de la géométrie des organes des arbres fruitiers pour des conditions de mesures en champs.



**FIGURE 1:** *Différents systèmes de conduite : (1) V-system, (2) Super Spindle, et (3) Slender Spindle. A chacun de ces systèmes de conduite correspond un type de gestion (taille, irrigation) ainsi qu'un type de rendement.*

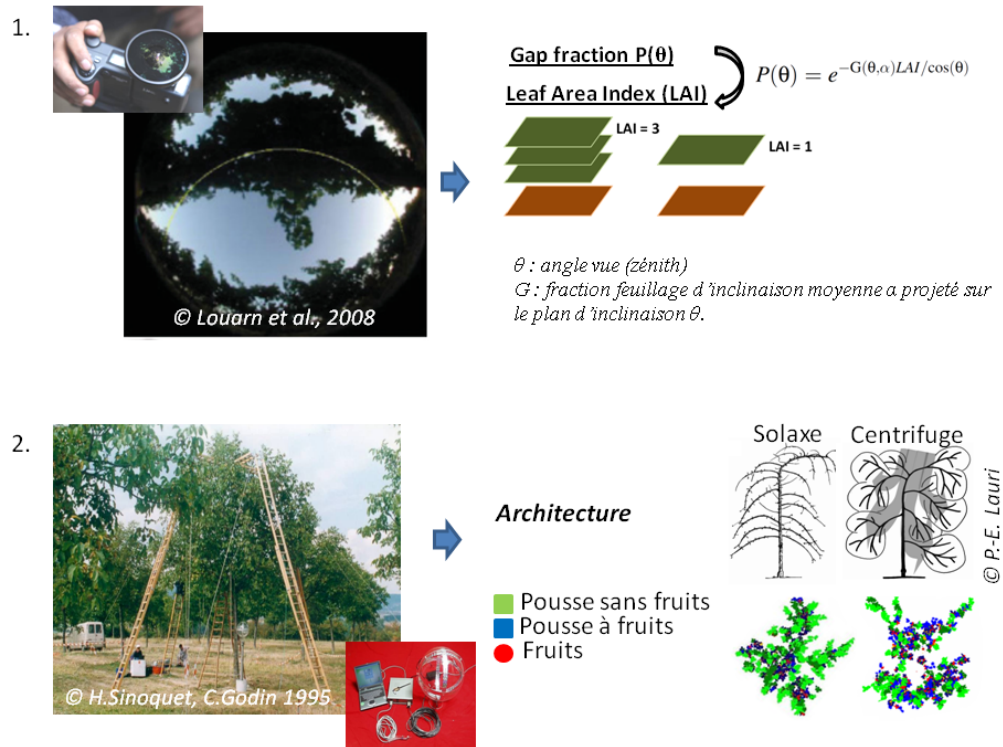
## Principes du TLS

Un TLS est un outil de mesure qui émet un rayon laser et qui enregistre soit le temps de vol de ce signal lumineux (Time-of-Flight, ou ToF), soit son décalage de phase (Amplitude Modulated Continuous Wave, ou AMCW). Avec cet enregistrement, le TLS déduit une distance, et depuis peu, l'intensité retour de ce laser. Grâce à la double rotation (azimutale et zénithale) de son couple émetteur/capteur, le TLS peut scanner la totalité d'une scène pour produire l'image de distance et d'intensité de son environnement (voir Figure 3). Les TLS à technologie AMCW sont mieux adaptés aux mesures de verger en champs. En effet, contrairement au TLS équipé d'une technologie ToF, les TLS-AMCW permettent de faire des mesures de courtes distances (<1 mètre) ; leur préci-

<sup>4</sup>Un digitaliseur 3D est un appareil de mesure qui émet un champ magnétique et qui enregistre une position et une orientation 3D à partir de la déformation de ce champ magnétique induite par une sonde en carbone. Chaque point de mesure est enregistré, un par un, par une personne, ce qui, pour des mesures exhaustives, rend cette méthode de mesure difficilement applicable pour un haut débit de mesure.

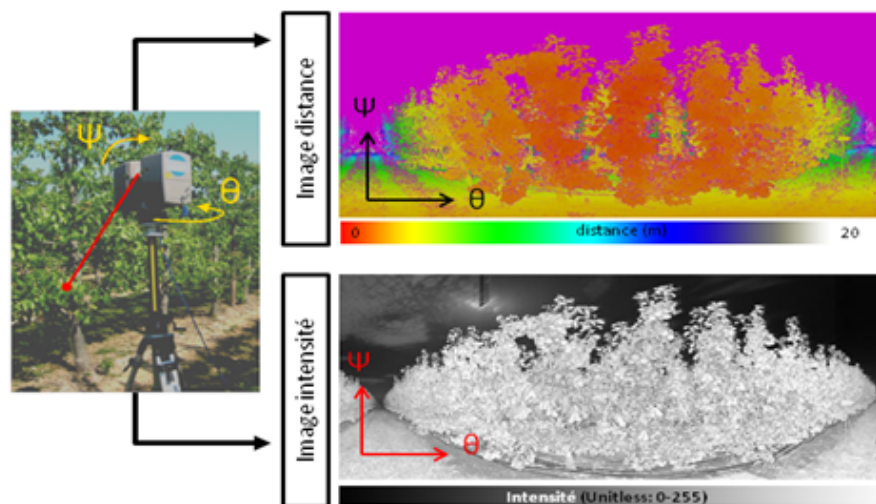
<sup>5</sup>Voir par exemple le site de l'INRA-PIA.F. (<http://www6.clermont.inra.fr/piaf/Methodes/Architecture-3D>)

<sup>6</sup>Ces modèles virtuels 3D sont en général représentés sous forme de maillage 3D produit à partir du nuage de point (ex. : Marching Cube). Les images de synthèse utilisent ces types de modèles d'objets pour être générées.



**FIGURE 2:** Mesure de la géométrie de la plante : (1) Le LAI est déduit du Gap Fraction calculé à partir d'une photo hémisphérique de la canopée vue d'en dessous, (2) Le digitaliseur 3D peut être utilisé pour mesurer l'architecture des plantes et la position des organes.

sion, de quelques millimètres, est plutôt constante selon la distance mesurée, celle-ci est en outre suffisante pour la mesure d'organes ; et ils peuvent acquérir plus d'un million de points de mesure par scan par rapport au TLS-ToF qui ne peut en acquérir que quelques centaines de milliers<sup>7</sup>.



**FIGURE 3:** Le TLS fournit une image de distance (haut) et d'intensité (bas) de son environnement. Ici, une ligne de verger de poiriers.

<sup>7</sup>[www.lidarnews.com](http://www.lidarnews.com) : "The Reality : ToF vs Phased based scanners"



## Vers une reconstruction géométrique des feuilles d'arbres fruitiers ?

Les données TLS ont déjà été exploitées pour l'extraction de la géométrie des plantes et de leur utilisation en agriculture. Par exemple (Figure 4) :

- Des méthodes similaires pour l'extraction de LAI à partir de photos hémisphériques ont été utilisées avec des données TLS<sup>8</sup>. Ces mesures de LAI peuvent être utilisées pour étudier la pénétration de la lumière dans la plante par exemple.
- Les volumes de lignes d'arbres fruitier ont pu être estimés à partir des données fournies par un TLS placé sur un tracteur<sup>9</sup>. Cette méthode de mesure a été développée notamment pour l'application de produits phytosanitaires en fonction du volume des plantes.
- L'architecture des arbres<sup>10</sup> a pu être reconstruite via des méthodes de simulation de croissance d'arbre, où la densité du nuage de point 3D fourni par le TLS est utilisée pour indiquer les directions de croissance de l'arbre simulé<sup>11</sup>. Ce genre de méthode a été mis en place dans le contexte d'études menées sur les systèmes de conduite.
- Enfin, les densités de surface foliaire (LAD) par voxel (ou volume-pixel) ont pu être extraites des données TLS. Ce type de modèle de plantes a pu être utilisé pour des estimations locales de l'interception lumineuse, ou encore pour des estimations locales de l'échange gazeux entre une plante et son environnement (ex. : H<sub>2</sub>O, CO<sub>2</sub>). Ce genre de représentation donne une description plus fine de la plante que le LAI.

Comme nous pouvons le remarquer, les TLS ont pu être utilisés pour extraire les informations géométriques des plantes, et ce, de l'échelle du couvert à l'échelle des organes : son utilisation recouvre toutes les échelles, de la plus grossière à la plus fine. Seulement, nous remarquons aussi qu'aux échelles les plus fines, le développement des méthodes d'extraction n'a pu aboutir à l'extraction des organes à proprement parler.

Pour comprendre ce manque, il nous faut regarder le nuage de points de plus près pour nous rendre compte qu'une grande quantité de points aberrants (ou outliers) sont enregistrés pendant le scan de feuillage (Figure 5-1). Ceux-ci sont présents le long du bord des feuilles (Figure 5-2 et 3) et ils interfèrent avec les méthodes de maillage traditionnelles (Figure 5-4).

Il s'avère que ces outliers sont propres à la technologie AMCW puisque ce type de TLS enregistre la moyenne des distances présentes dans l'empreinte laser (Figure 6-A-i et ii). Ainsi, lorsque le

---

<sup>8</sup>Danson et al., "Forest canopy gap fraction from terrestrial laser scanning", 2007.

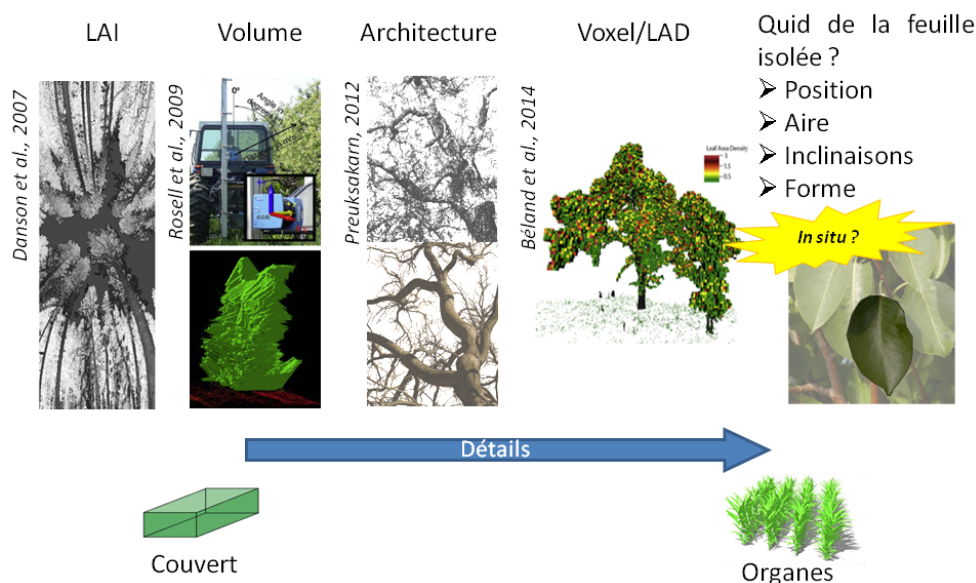
<sup>9</sup>Rosell et al., "A tractor-mounted scanning LiDAR for the non-destructive measurement of vegetative volume and surface area of tree-row plantations : A comparison with conventional destructive measurements", 2009.

<sup>10</sup>L'architecture d'un arbre représente la géométrie et la topologie (description de la connexion entre branches consécutives) de son branchage.

<sup>11</sup>Preuksakarn, "Reconstructing plant architecture from 3D laser scanner data", 2012.

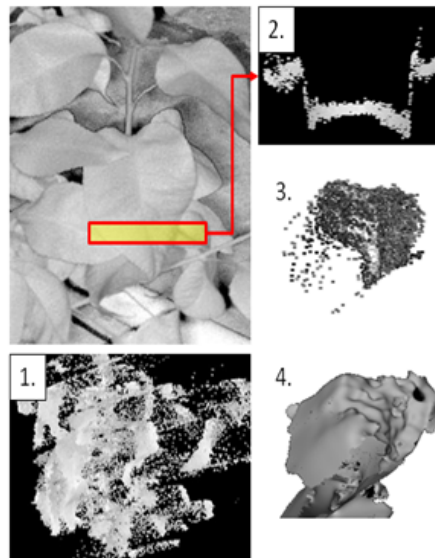
laser du TLS atteint le bord d'une surface (ex. : une feuille), le laser se coupe en deux et enregistre une distance intermédiaire, c'est-à-dire : un outlier (Figure 6-B-i et ii). Toujours est-il : pour extraire correctement les informations géométriques des organes d'une plante, il est nécessaire de traiter ces outliers.

Une première solution, intuitive, consiste à les sélectionner<sup>12</sup> puis à les supprimer. Seulement, ces outliers peuvent recouvrir une grande partie du nuage de points représentant les organes de la plante. Par exemple, à 1.5 mètres, ils peuvent représenter jusqu'à 10% de la surface d'une feuille de 9 cm de diamètre placée perpendiculairement au laser du TLS. Si cette feuille est placée à 5 mètres, ils peuvent représenter jusqu'à 30% de sa surface. En général, le feuillage des arbres fruitiers sont composés d'une grande variété de type de feuilles, tant pour leur forme, leur inclinaison, mais aussi leur taille qui, dans le cas des poiriers, peut varier de 3 à 10 cm de diamètre. On peut facilement imaginer que la suppression de ces outliers n'est pas la solution optimale lorsqu'on veut récupérer la géométrie des organes. Une autre solution serait de corriger ces outliers, mais cette solution reste vaine lorsqu'on considère uniquement l'information 3D puisque la correction du nuage de points nécessiterait une connaissance à priori de la forme de l'objet scanné et que, comme il vient d'être mentionné, les forme de feuilles d'arbre fruitier sont très variables. Pendant ma thèse, je me suis tournée vers l'information d'intensité fournie par le TLS pour corriger ces outliers.

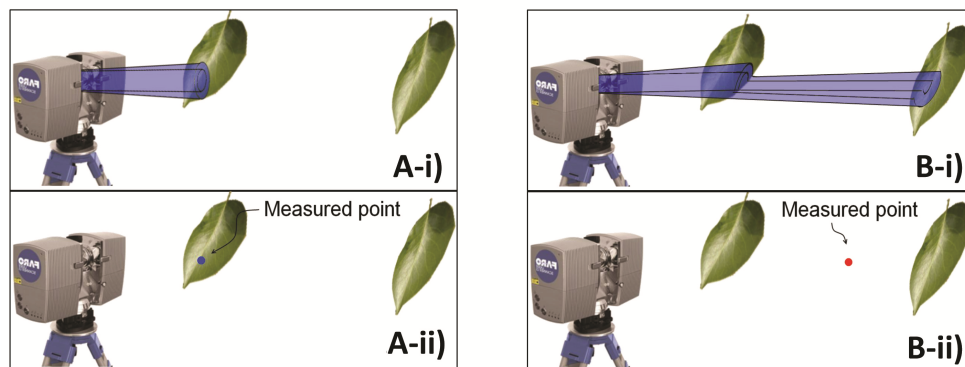


**FIGURE 4:** Les données TLS ont été utilisées pour extraire la géométrie des plantes de l'échelle du couvert à celle des organes. Mais quid des feuilles isolées pour des mesures TLS en champs ?

<sup>12</sup>Deux catégories de méthodes de sélection d'outliers dans les nuages de points existent. Ce sont les méthodes basées sur la distance ou encore basées sur la densité. Voir Sotoodeh. "Outlier detection in laser scanner point clouds", 2006



**FIGURE 5:** Image d'intensité du scan d'un groupe de feuille : (1) Nuage de points. (2) Vue de profil de la sélection (jaune). (3) Sélection d'une feuille dans le nuage de point 3D : les outliers sont visibles. (4) Maillage : les outliers dégradent le résultat final.



**FIGURE 6:** (A-i) L'empreinte laser est dans la surface. (A-ii) Un point vraisemblable est enregistré. (B-i) L'empreinte laser est au bord de la surface. (B-ii) Un point aberrant (ou outlier) est enregistré.

## Une méthode de « Shape-from-Shading » (SFS) par propagation pour la reconstruction des organes de la plante à partir de l'image d'intensité du TLS

L'intensité est la donnée représentant la quantité de lumière enregistrée par un capteur (ex. : un appareil photo, le capteur TLS) une fois réfléchi par un objet placé dans une scène. Une image d'intensité (ou photographie) est l'ensemble des intensités renvoyées par tous les points d'un objet sur le capteur. Cette intensité dépend de la position de la source d'éclairage par rapport au capteur, de la distance de l'objet illuminé, de son matériau, et, de sa géométrie. Lorsque la configuration de la scène (position source lumineuse/capteur, distance objet) est connue pour un objet avec un matériau donné, on peut dire que l'intensité dépend seulement de la géométrie de l'objet. En d'autres

termes, elle dépend de l'inclinaison locale - c'est-à-dire, du plan tangent - de la surface par rapport aux directions d'éclairage et de capture. Observant cette relation entre intensité et inclinaison, nous pouvons imaginer que, pour une intensité donnée, nous avons une inclinaison locale de la surface. C'est en partant de ce principe que depuis les années 50, des méthodes dites de Shape-From-Shading (SFS) ont été développées : elles consistent à reconstruire les surfaces par l'analyse de l'intensité.

Les méthodes de SFS peuvent être catégorisées en deux types : les méthodes globales et les méthodes par propagation (voir Figure 7). Ces méthodes sont en général basées sur des hypothèses qui peuvent être traduites de la manière suivante : (i) le capteur est dans le «hot spot» de l'émetteur, c'est-à-dire, ils sont alignés, et par convention, on les suppose être à la verticale, (ii) les objets sont positionnés à l'infinie du capteur/émetteur, et (iii) les objets sont sans texture. Ces hypothèses correspondent tout à fait avec les conditions de scan d'arbre fruitier avec un TLS : (i) le capteur TLS est dans le hot-spot de l'émetteur laser du TLS, (ii) les organes sont petits par rapport à leur distance au TLS et peuvent être considéré « à l'infinie », et (iii) les organes (dans le cas de poirier) peuvent être considérés sans texture. Ainsi, une méthode de SFS pour la reconstruction de la surface des organes d'arbres fruitiers pourrait être développée pour corriger les outliers.

Mon choix s'est plutôt porté sur une méthode de SFS par propagation. En effet, les résultats des méthodes SFS globales sont sensibles au choix d'une surface initiale. Or, les surfaces représentées dans les nuages de points TLS sont biaisés à cause des outliers et donc ces dernières ne peuvent être utilisées comme surfaces initiales. Les méthodes de propagation, au contraire, sont, par principe, plus souples quant à la sélection de données initiales. Les bonnes données du nuage de points (ex. : celles où l'intensité correspond à la 3D du nuage de points) peuvent être utilisée comme données de départ et la propagation se faire vers les données de mauvaise qualité pour ainsi reconstruire ces dernières. Ainsi les méthodes de SFS par propagation m'ont semblées être mieux adaptées. Aussi, j'ai choisi de propager la reconstruction long de domaines iso-intenses, c'est-à-dire les domaines d'intensité constante, puisque cette stratégie m'aura permis d'utiliser l'information 2D (i.e., la forme du domaine) fourni par l'image. En outre, j'ai utilisé l'intuition de Peternell & Steiner<sup>13</sup> qui fut d'utiliser des surfaces dites en « tas de sable », ou STS (Figure 8) pour reconstruire les domaines iso-intenses de l'image.

Cette intuition peut être rapportée à un résultat de Monge<sup>14</sup> qui stipule que si on prend une photo d'une STS avec les hypothèses de SFS mentionnée ci-dessus, alors nous obtenons une image iso-intense. Ces types de surfaces sont pratiques car : (i) ce sont des surfaces développables (c'est-à-dire, qu'elles sont soit des plans, soit des cônes, ou soit générées par l'ensemble des tangentes à une courbe 3D, par exemple, la développée de l'hélice) et que (ii) leurs courbes de plus grande pente sont rectilignes. Ces deux propriétés peuvent être utilisées pour mettre en place un algorithme de SFS par propagation le long des domaines iso-intenses de l'image.

---

<sup>13</sup>Peternell & Steiner. "A geometric idea to solve the eikonal equation", 2005.

<sup>14</sup>Monge, "Application de l'analyse à la géométrie", 1850.

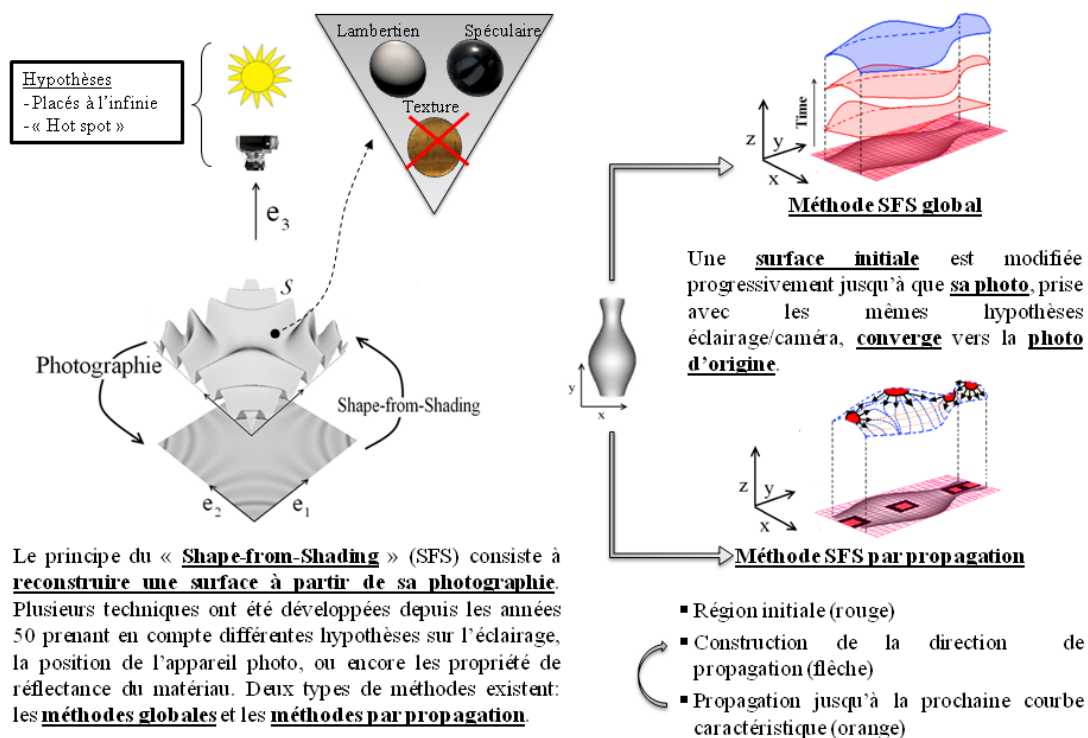


FIGURE 7: Différentes méthodes de Shape-From-Shading.

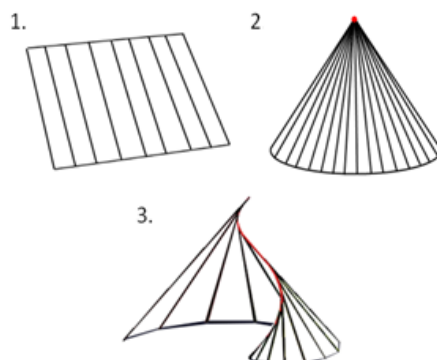


FIGURE 8: Exemple de surfaces en tas de sable (STS) : (1) un plan, (2) un cône, (3) la développée d'une hélice.

## Propriété paramétrique des surfaces correspondants aux domaines iso-intenses de la photo

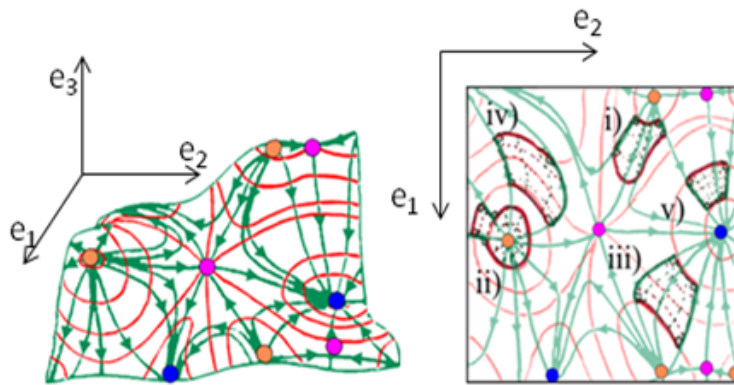
Avant de mettre en place l'algorithme, il a été nécessaire de prouver la réciproque du résultat de Monge, c'est-à-dire, de prouver rigoureusement qu'un domaine iso-intense correspond nécessairement à une STS. Pour ce faire, j'ai considéré l'intensité comme étant directement lié à l'angle d'incidence (noté  $\alpha$ ) entre la direction émetteur/capteur du TLS et la normale à la surface<sup>15</sup>. La

<sup>15</sup>Théoriquement, cette considération est raisonnable avec les hypothèses de SFS mentionnées précédemment. En ce qui concerne le TLS, on doit procéder à des phases de calibration (ex : correction de l'effet de distance) avant de récupérer directement l'angle  $\alpha$ .

réci-proque du résultat de Monge peut s'exprimer alors ainsi : si une image  $\alpha^{16}$ , a un domaine iso- $\alpha$  alors ce domaine iso- $\alpha$  correspond nécessairement à une STS.

Pour faire cette démonstration, j'ai dû démontrer des propriétés spécifiques aux courbes de niveau et de plus grande pente d'une surface lisse (Figure 9 - courbes rouges et vertes) ; ainsi qu'aux domaines quadrillés d'une surface lisses (Figure 9 - i à v).

Grâce à ces propriétés, j'ai pu montrer (voir Figure 10) que si nous considérons un domaine iso- $\alpha$ , nous pouvions trouver, pour n'importe lequel de ses sous-domaines, un domaine quadrillé contenant une courbe de plus grande pente avec un point d'inflexion. Comme ceci est vrai pour n'importe quel sous-domaine, alors l'ensemble des points d'inflexion est dit « dense » dans le domaine iso- $\alpha$ . Par continuité, j'ai pu prouver ainsi que les courbes de plus grande pente ont des points d'inflexion partout. En d'autre terme, qu'elles sont rectilignes. En outre, comme ces courbes de plus grande pente sont d'inclinaison constante  $\alpha$ , elles forment des STS ce qui aura conclu la démonstration de la réci-proque de Monge.

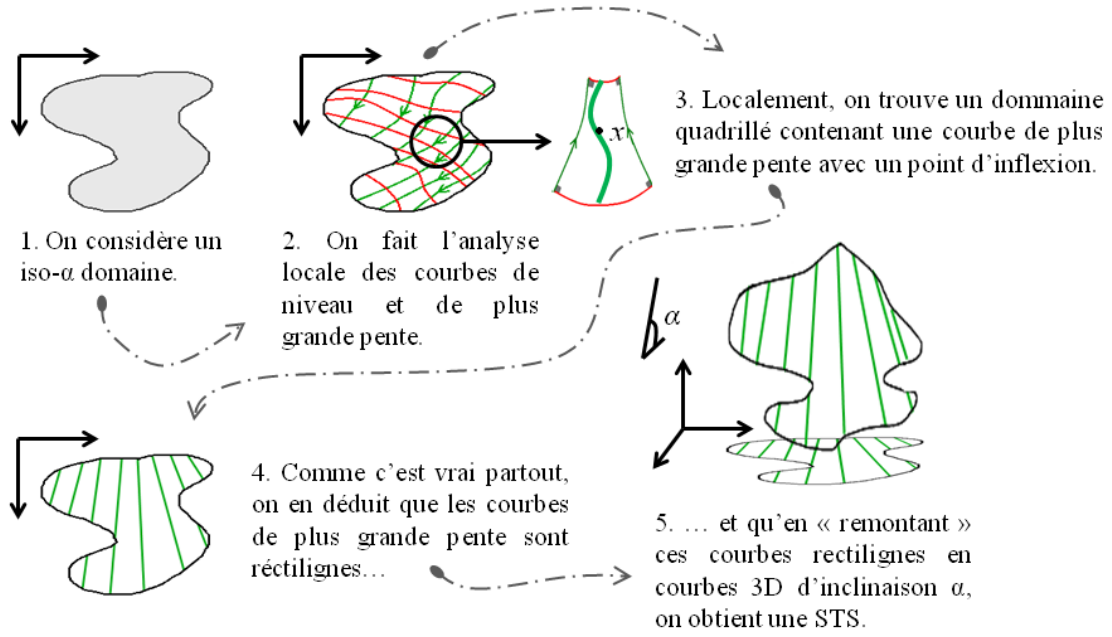


**FIGURE 9:** Une surface 3D est composée de courbes de niveau (hauteur constante – en rouge) et des courbes de plus grande pente (orthogonales aux courbes de niveau – en vert). Les points singuliers de la surface sont les points où plusieurs courbes de même type se croisent : ce sont, dans le cas de surfaces lisses, les sommets, puits et cols de la surface. Les domaines quadrillés sont formés par deux courbes de niveaux et deux courbes de plus grande pente. Il en existe cinq types, dont quatre qui dépendent de leur courbure : (i) quelconque, (ii) singulier, (iii) simple, (iv) conforme et (v) droit.

## SFS par propagation le long des domaines iso-intenses de l'image d'intensité

Une fois que j'eus prouvé que les domaines iso- $\alpha$  correspondent à des STS, l'algorithme SFS par propagation le long de ces domaines a pu être développé. Cet algorithme est composé de trois compartiments (Figure 11) :

<sup>16</sup>Une image  $\alpha$  est une image obtenue par la transformation des intensités d'une image en valeur  $\alpha$  avec une relation prédéfinie.



**FIGURE 10:** *Propriétés d'un domaine iso- $\alpha$ .*

1. L'extraction des domaines iso- $\alpha$  : d'abord, l'image d'intensité est transformée en image d'angle d'incidence  $\alpha$  ; cette image est segmentée en plusieurs sous parties contenant une et une seule région initiale (ou graine) qui sont les régions où  $\alpha$  est minimal<sup>17</sup> (ou nul) ; les domaines iso- $\alpha$  sont extraits. La propagation se fait à partir des valeurs  $\alpha$  minimal (ou nul) jusqu'aux valeurs  $\alpha$  maximales, par voisinage, aussi : les domaines iso- $\alpha$  sont ordonnés le long des valeurs  $\alpha$ , croissantes.
2. Le contour 3D de la graine est initialisé avec les données 3D de l'image de distance. En outre, les directions de propagation (pour résoudre l'ambiguïté concave/convexe<sup>18</sup>) sont initialisées.
3. Les iso- $\alpha$  domaines avec la première courbe 3D sont données en entrée de l'algorithme de SFS par propagation à proprement parlé. Cet algorithme se déroule comme suit (Figure 12) :

- a) **Calcul des directions de plus grande pente** : on calcul à partir du contour 3D de la dernière région iso- $\alpha$  de la surface, les directions de plus grande pente  $G_X$ , modulo l'identité suivante :

$$\varphi = \text{acos} \left( \frac{\tan(\gamma)}{\tan(\alpha)} \right),$$

avec :  $\alpha$  l'angle d'incidence,  $\gamma$  l'élévation de la tangente du dernier contour reconstruit (ou de la graine), et,  $\varphi$  l'azimut de la direction de plus grande pente  $G_X$  par rapport à la tangente de ce contour au point  $X$ .

<sup>17</sup>Ces régions peuvent être considérées contenues dans un plan orthogonal à la direction émetteur/capteur (verticale). Cette observation fait d'elles des régions de premier choix pour une propagation.

<sup>18</sup>Les processus de création d'images – et réciproquement, la reconstruction d'objet à partir de celles-ci – sont faites modulo une orientation (vers le haut ou vers le bas pour un éclairage vertical). Dans le cas d'une reconstruction par méthode de SFS, ce phénomène est connu sous le nom d' « ambiguïté concave/convexe ».



- b) **Propagation rectilinéaire** : comme on propage la reconstruction des régions iso- $\alpha$  de la surface, on utilise la propriété des courbes de plus grande pente d'une STS, c'est-à-dire, leur linéarité :

$$X' = X + \frac{\Delta d}{\cos(\alpha)} \cdot G_X,$$

avec :  $X$  le point sur le dernier contour 3D reconstruit et duquel part la courbe de plus grande pente courante,  $X'$  le point d'arrivée de cette courbe de plus grande pente,  $\Delta d$  la distance entre  $x$  et  $x'$ , les projections respectives de  $X$  et  $X'$ .

- c) **Complétion avec les STS** : les régions iso- $\alpha$  sont complétées avec des STS : on utilise les lignes de propagation pour paramétrer localement ces surfaces.

- d) **Retour à l'étape 1.**

Finalement, en sortie de cet algorithme sont générés : (i) un maillage de la surface, (ii) une nouvelle image de distance et (iii) un nuage de point 3D.

Cet algorithme fut testé sur plusieurs types de surfaces synthétiques (Figure 13) allant de surfaces simples (sphère, ellipsoïde, surface en forme de selle) à des surfaces plus complexes (combinaison de sommets/selles asymétriques). Malgré des discontinuités dans les reconstructions ainsi que des redondances dans les points reconstruits, les reconstructions étaient réalistes et satisfaisantes.

La sensibilité aux paramètres d'entrées a aussi été testée. Ces paramètres sont : (i) le nombre de domaines iso- $\alpha$  et (ii) la valeur de lissage du bruit présent sur le contour 3D de la graine. Pour le premier paramètre, nous avons observé que le choix du nombre de domaine iso- $\alpha$  dépendait de la résolution de l'image. Plus grande était cette résolution, plus grand était le nombre de domaines iso- $\alpha$  qui pouvaient être sélectionnés pour améliorer la qualité de la reconstruction. Dans le cas d'images de basse résolution, la génération d'artéfacts sont produits à cause de la pixellisation des contours. Nous en avons déduit que la sélection d'un nombre limité de domaines iso- $\alpha$  était une meilleure stratégie dans ce cas. Le second paramètre est un paramètre de filtre passe-bas. Sa bonne sélection est un facteur déterminant pour la vraisemblance de la forme reconstruite. Pour choisir ce paramètre, nous avons mis en place un compartiment algorithmique prenant en entrée une information sur la forme générale de la surface (ex : forme de selle). Grâce à ce compartiment, nous avons pu obtenir des résultats satisfaisants.

## Reconstruction de feuille de poirier Conference et validation

En Août 2010, je suis allée dans un verger à Bierbeek (Figure 14), en Belgique, pour scanner une ligne de poirier avec un TLS de type FARO LS880. L'effet causée par la distance sur les données d'intensité du TLS furent corrigés et la relation entre intensité et angle d'incidence entre le rayon laser du TLS et les surfaces foliaire, calculée<sup>19</sup>. 58 feuilles entièrement visibles dans le scan furent sélectionnées manuellement pour être reconstruite avec ma méthode de SFS par propagation.

<sup>19</sup>Balduzzi et al. "The Properties of Terrestrial Laser System Intensity for Measuring Leaf Geometries : A Case Study with Conference Pear Trees (*Pyrus Communis*)", 2011



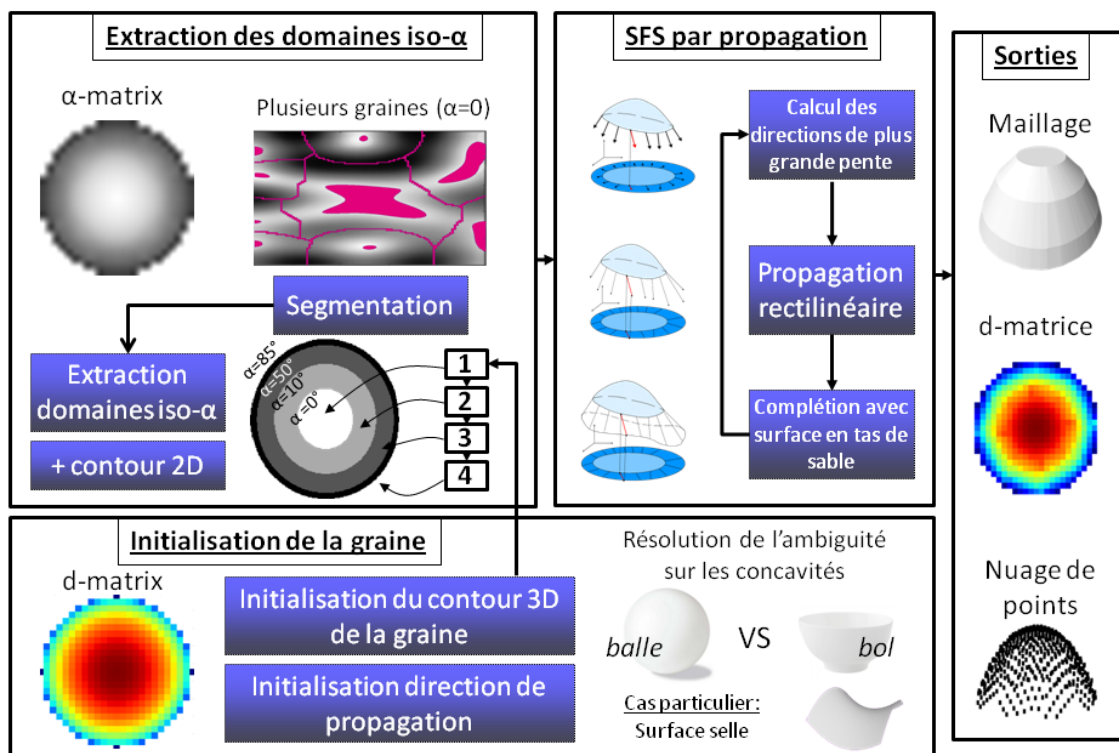


FIGURE 11: Vue d'ensemble de l'algorithme de propagation.

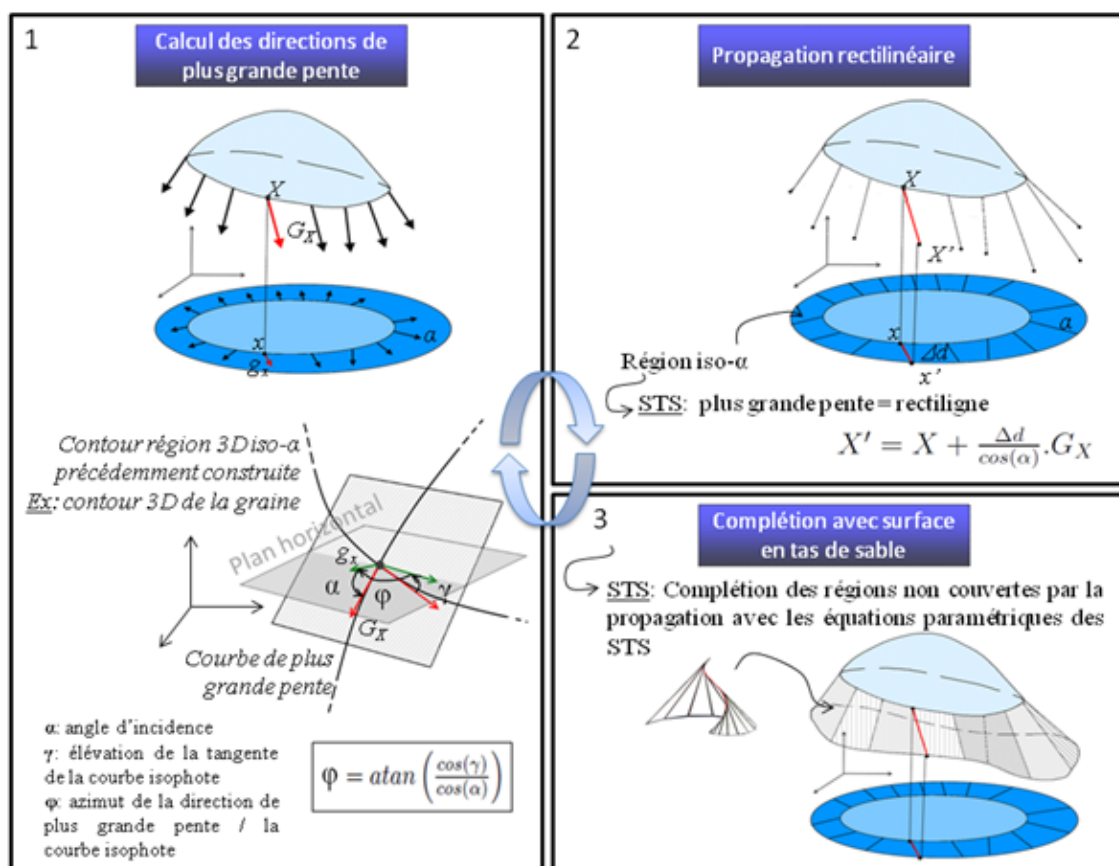
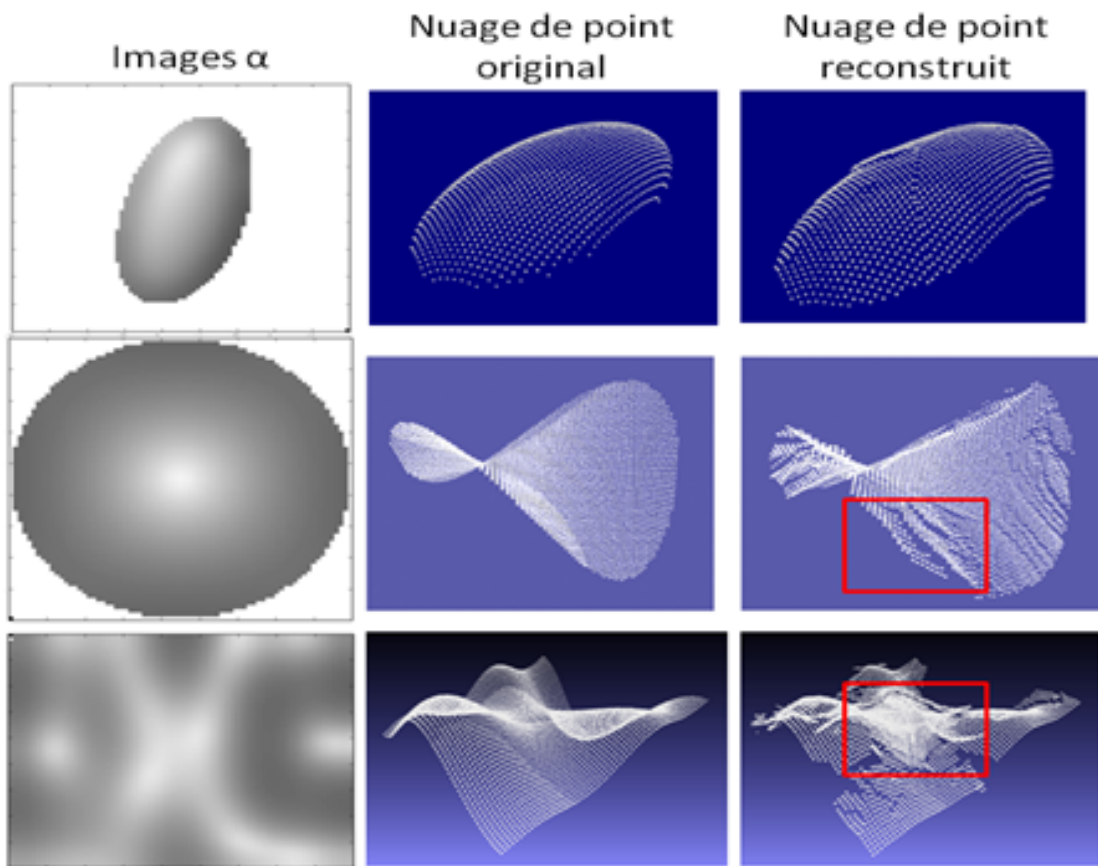


FIGURE 12: Détail sur l'algorithme de propagation utilisant les propriétés des STS.



**FIGURE 13:** *De haut en bas : Reconstruction d'un ellipsoïde, d'une surface en forme de selle et d'une surface complexe. En rouge : cas de discontinuités et de redondances dans le nuage de point.*

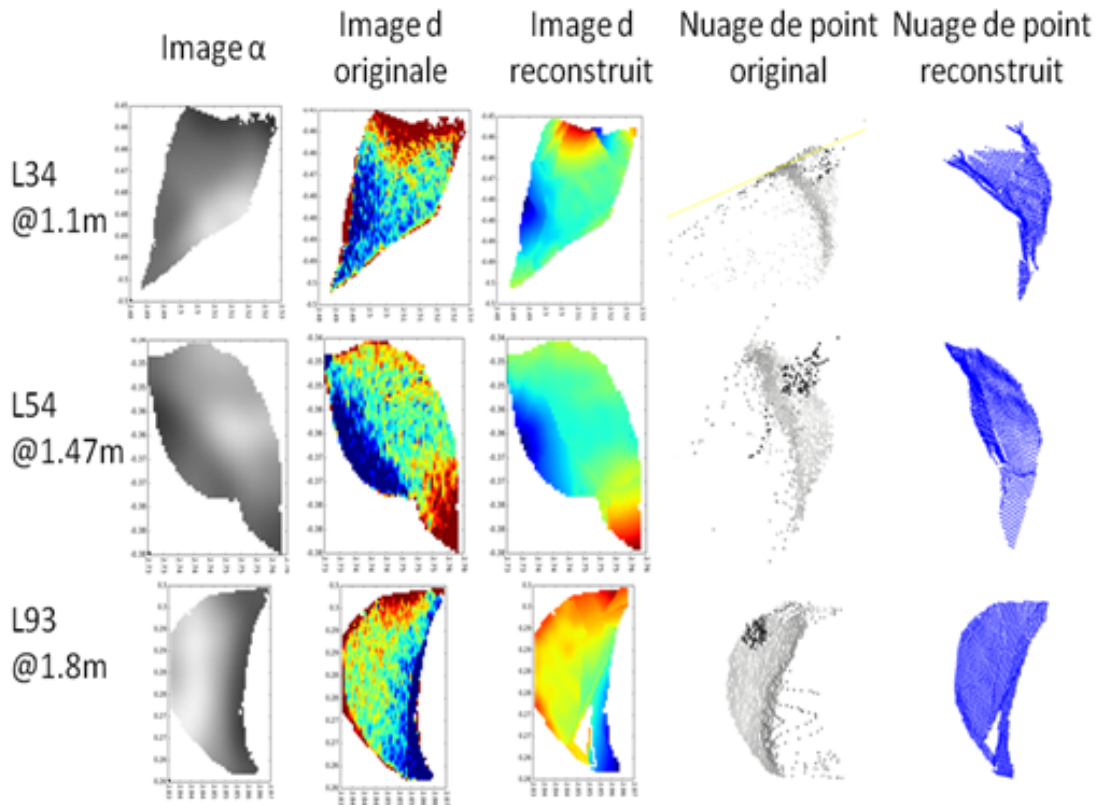
Les feuilles reconstruites sont visuellement réalistes, et lorsque leur aire et inclinaisons calculées à partir des maillages reconstruits (Figure 16) sont comparés avec les mesures manuelles, de bons résultats sont obtenus, notamment pour l'estimation des aires ( $R^2=0.95$ ). En général, le problème des outliers a été éliminé avec ma méthode puisque toutes les distances ont pu être ré-estimées, même là où il y avait des outliers (voir Figure 15). En conclusion, l'estimation de la géométrie des feuilles a pu se faire avec tous les points de mesure.



**FIGURE 14:** *Verger scanné à Bierbeek.*

Mesure TLS		Mesure manuelle	
Marque & série	FARO LS880	58 feuilles	0.8-2 m
Technologie	AMCW	Aire	Scanner plat
Champs de vision	320° × 360°	Résolution	0.01 cm <sup>2</sup>
Longueur d'onde	785 nm (NIR)	Min-max	12-65 cm <sup>2</sup>
Diamètre laser	3 mm	Azimuth	Boussole
Divergence laser	0.014°	Résolution	10°
Champs de vision capteur	3 mrad	Min-max	0-120°NE
Résolution angulaire	0.018°	Elévation	Rapporteur
Portée	0.6 m-78 m	Résolution	5°
Précision	±3 mm @ 25 m	Min-max	0-120°

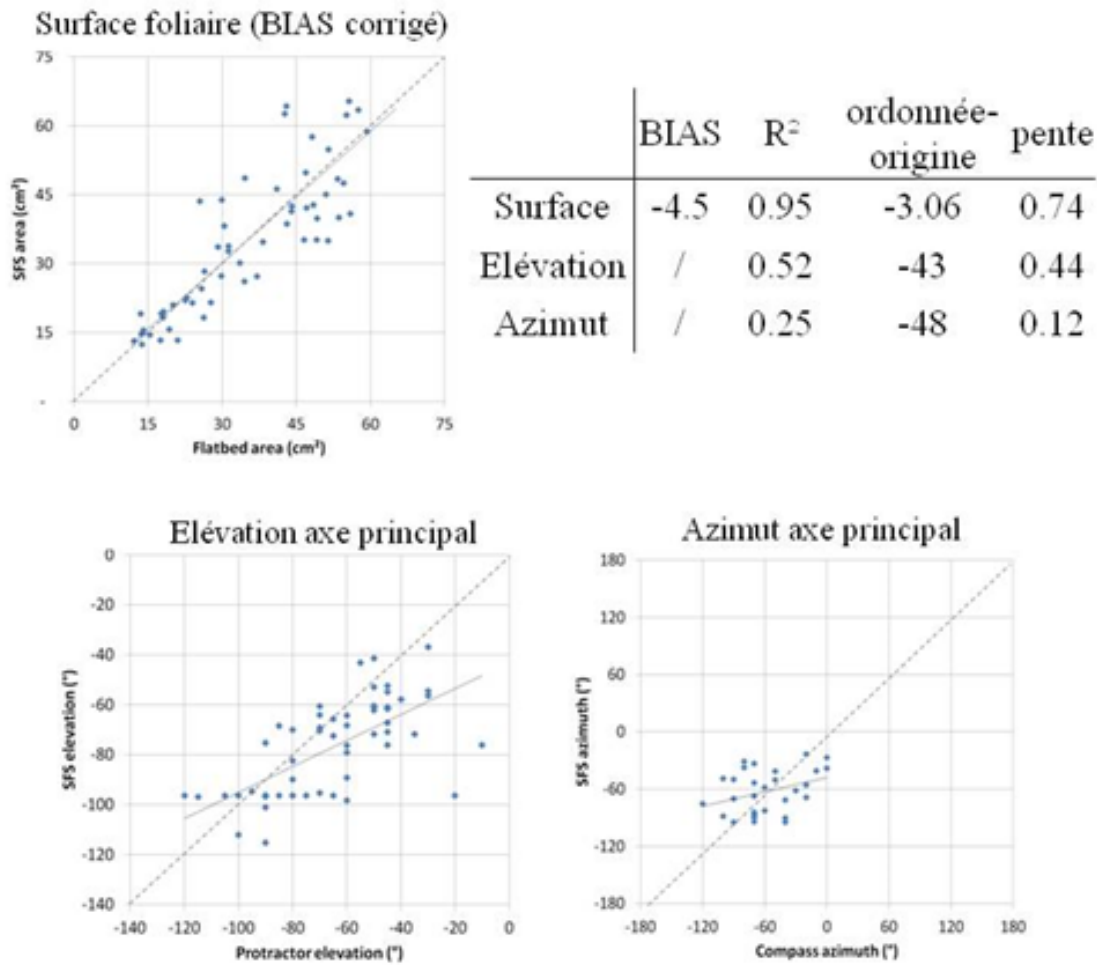
**TABLE 1:** *Gauche : récapitulatif des caractéristiques du TLS FARO LS880. Droite : Description des mesures manuelles*



**FIGURE 15:** *Exemple de feuilles reconstruites.*

## Conclusions et perspectives

Dans ma thèse, j'ai pu mettre en place un algorithme de SFS par propagation le long de domaines iso-intense pour reconstruire les surfaces foliaires à partir de données TLS à technologie de décalage de phase pour pouvoir corriger les outliers présent le long du bord de ces surfaces. Pour



**FIGURE 16:** Validation de l'extraction des surfaces et inclinaison des feuilles.

ce faire, j'ai prouvé la réciproque du résultat de Monge, c'est-à-dire, j'ai établi que les domaines iso-intenses d'une image correspondent nécessairement à des STS. Grâce à ce résultat, j'ai pu développer un algorithme de SFS en utilisant les propriétés de ces STS, c'est-à-dire : (i) leurs courbes de plus grande pente sont rectilignes, et (ii) leurs équations paramétriques définies localement par ces courbes. Ces propriétés m'auront permis de : (i) propager de manière rectilinéaire, et (ii) reconstruire localement les morceaux de surfaces représentant les régions iso-intenses entre deux courbes de propagation. Malgré des cas de redondances et de discontinuités, cet algorithme fonctionne tant sur des surfaces simples que sur des surfaces complexes ainsi que sur des surfaces réelles, scannées avec un TLS. L'utilisation de cet algorithme m'a permis d'extraire formes, aires et inclinaisons de feuilles de poiriers scannés en champs par un TLS et ce, en dépit de la présence d'outliers. Malgré le fait que mon algorithme n'ait été validé que sur des feuilles, celui-ci est le premier qui a pu extraire des géométries vraisemblables d'organes de plantes à partir de mesure TLS en champs. En général, mon algorithme peut être encore amélioré, notamment pour le traitement de la redondance. Dans un premier temps, cette redondance pourrait être utilisée comme un indicateur de qualité de la reconstruction : si une trop grande redondance de point est détectée, alors les paramètres pourraient être re-estimé (ex : changer le nombre de domaines iso- $\alpha$ ).

Dans le cadre d'une utilisation de TLS en arboriculture fruitière, plusieurs problèmes n'auront pas été traités dans ma thèse :

- Tout d'abord, l'utilisation des données 3D du TLS : nous avons vu que seules les données de distance associées aux graines de propagation ont été utilisées, c'est-à-dire, une petite portion sur la totalité des données fournies. Ceci remet en cause la fonction première du TLS qui est de mesurer des distances de manière exhaustive. Pour utiliser de manière optimale les deux informations de distance et d'intensité, l'utilisation d'une méthode de fusion de données (ex. : filtre de Kalman<sup>20</sup>) pourrait être intégrée au fur et à mesure de la propagation.
- La segmentation des organes de la plante : cette segmentation pourrait être faite sur un principe similaire que celui que j'ai développé dans ma thèse : la correction d'outliers indiquant le bord d'un objet et cette correction pourrait être utilisée pour sélectionner les bords, et donc pour segmenter des objets présents dans le scan.
- L'effet d'occlusion : toutes les feuilles ne sont pas visibles dans le scan du TLS et une réflexion plus poussée menant à un protocole de mesure devra être faite.
- La combinaison avec la mesure de l'architecture et la détection/labellisation des différents organes (feuilles, fruits, etc.).

Une fois ces problèmes résolus, alors une application optimale des TLS en arboriculture fruitière pourra être envisagée. Puisque la croissance et la production des arbres fruitiers sont dépendantes du lieu (sol et météo), le suivi phénotypique des plantes pourra être mené aux quatre coins du globe et les données, ainsi acquises, partagées pour avoir une meilleure compréhension de la physiologie des plantes.

---

<sup>20</sup>Kalman "A new approach to linear filtering and prediction problems", 1960



# Introduction

Agro-forestry aims to manage orchards and fruit yield from early stage of trees to the delivery to agro-industry and consumers of the crop production. As fruit production is driven by plant physiology, agro-foresters seek to control biological processes of trees. For instance, they manipulate tree architecture (e.g., tree training, pruning, girdling) to control fruit quality (size, color, sugar) [1, 2] and to understand plant occupation in space to limit pesticide application [3, 4].

Studying plant organ geometry and growth dynamic makes it possible to simulate physiological processes occurring within the plant, and thus, to optimize their manipulation. Since the 90's, computer simulation of plant functioning have been developed [5]. Those models are becoming increasingly sophisticated. For instance, functional-structural-plant-models (FSPMs) are computer models used to simulate biological processes, such as nutriment transports [6], cellular growth and morphogenesis [7], plant morphology [8] and plant interaction with its environment such as gravitational forces [9] or sun [10]. FSPMs are usually associated with 3D plant models and deal with the spatial distribution of both environmental and biological processes [11]. Once processes simulated by FSPMs are well established, we can imagine that horticulturists use those computer models to optimize pest management, plant water uptake, nutriment application and architecture manipulation [5]. To reach this goal, robust tool of 3D acquisition of plant geometry at organ scale are necessary.

3D scanners are metrology tools that deliver 3D point cloud representation of a scene. For instance, stereo photography is a dual-view and passive system requiring proper calibration and geometrical interpretation to provide 3D point cloud representing a scene. Laser triangulator is a 3D active scanner that emits laser lines to film them with a camera placed in a slight inclined direction. Object's 3D shape are estimated with the laser line deformation. LiDAR (Light Detection And Ranging) is an active measurement tool that: (i) emits either continuously a laser signal or a laser pulse in a range of direction, (ii) records with a sensor placed in the hot-spot, time of flight of the emitted light to (iii) computes its distance to objects that have reflected the emitted light and eventually the associated reflectivity, i.e., the light intensity data. Terrestrial LiDAR System (TLS) is a portable LiDAR system equipped with rotating mirrors or terrestrial carrier system to provide a 3D point cloud of its surrounding scene. 3D scanners have been used in several fields such as topography [12], architecture [13] and mechanical engineering [14]. In agro-forestry, they have been used to estimate plant Leaf Area Index (LAI) [15], volume [16] and foliage density [17], but also for individual organ geometry extraction under controlled condition, e.g., picked organ [18] or

in greenhouse [18, 19, 20]. Compared to stereo photography and laser triangulator, TLS scanners have an interesting range of measurement (few decimeters to several meters with a large angular range) and they are flexible (e.g., simple system geometry, robustness, size). Generally, they are considered well adapted for intensive study of plant geometry with *in situ* condition. Yet there is very little TLS studies dealing with fine level plant architecture (leaves and fruit scale) and dealing with complex *in situ* measurements (e.g., [21, 22, 23]) and none aims to extract automatically complete geometry of tree organs.

TLS measurement quality depends on several factors such as object's distance, inclination and reflective properties [24], but also on the good calibration of its mechanical system [25]. In addition, distance measurement can be severely biased when LiDAR laser beam reaches object edge: in this case, the beam is split and a mixed distance value is recorded, i.e., an outlier point. The size of the LIDAR laser spot is thus a very important aspect. The current affordable TLS have footprints on the order of few millimeters that makes the amount of outliers point per scanned tree organs non-negligible. Deleting them reduce severely organ sampling and their correction seems to be more appropriate.

Intensity is an additional value provided by most of actual TLS. Intensity data has been used for object segmentation [17] and classification [26], yet it has not been used for outliers detection and correction. Shape-from-Shading (SFS) is a computer technique to reconstruct object shape from their photography. In this thesis manuscript, we will propose a SFS method adapted to TLS data that corrects outlier points. To do so, complex shape will be reconstructed from an initial set of 3D points supposedly correct and will correct outliers by an interpretation of the intensity data. This manuscript is organized as follows:

1. In a first part, we will talk about TLS technology and its application in agro-forestry. Chapter 1 will describe TLS technical features. Chapter 2 will make the state of art on plant geometry measurement with TLS and in the framework of tree architecture manipulation and pest detection. We will illustrate TLS limitations for plant organ reconstruction.
2. In a second part, we will develop a SFS technique adapted to organ extraction from TLS data. In Chapter 3, we will split SFS techniques in two main categories: (i) global SFS, and (ii) SFS by propagation. From our discussion, we will set up guideline to develop a SFS method adapted to TLS data. The proposed solution will be the object of a topological and geometrical analysis that will be made in Chapter 4 in order to gather mathematical properties for our SFS algorithm. This latest will be set up and tested on synthetic images in Chapter 5.
3. In a last part, we will give first results on our SFS algorithm application on TLS scans of pear tree canopy. Pre-processing (e.g., TLS radiometric calibration) required for the application of our SFS method will be set up in Chapter 6. Finally, our SFS method will be validated with manual measurement of Conference pear tree leaves shape, area and inclinations in Chapter 7.



## **Part I**

### **Introduction: Terrestrial LiDAR Scanner (TLS) for canopy geometry assessment?**



# Chapter 1

## Terrestrial LiDAR Scanner (TLS)

The measurement of distances and geometric shapes has always been important in human history, especially for technical fields such as architecture or mechanics. To support the development of those fields, research in metrology led to specialized tools that can be split into two main categories of technologies: measurements with or without contact [27]. Measurements with contact (e.g., with a ruler, a 3D touch probe) are usually time-consuming. Therefore they apply primarily for small objects and they usually lack precision. In contrast, measurements without contact (e.g., RADAR, distance measurement with triangulation) can apply to distant and/or large objects and usually involve high accuracy.

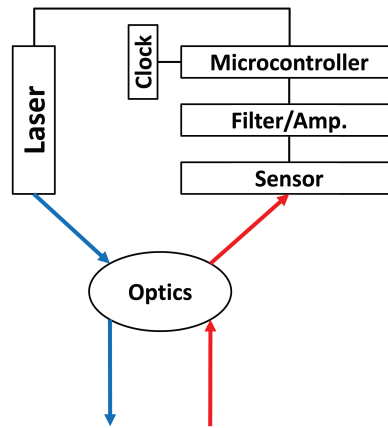
A Light Detection and Ranging (LiDAR) device is a tool designed for measurement without contact using a laser beam to measure the distance to an object surface. It is widely used in topography [12], architecture [13], mechanical engineering [14], forestry [28] and agriculture [16]. When scanning a scene, a LiDAR device collects two measurements from each laser beam emitted: (1) the distance between the laser source and the scene objects and (2) the return intensity of the laser beam. The set of measured distances can be subsequently converted into a 3D point cloud corresponding to the surface of the scanned objects (see Appendix I). This 3D point cloud can then be approximated by a virtual surface [29], e.g. a mesh composed of a set of triangles from which local geometric properties of the objects can be estimated. The quality of these estimations depends on LiDAR data quality and in the complexity of the scanned scene.

In complex environments, many factors affect LiDAR data quality. For canopy scenes, for example, the heterogeneous distribution of leaves in space, their varying shapes, sizes and inclinations, induce a large variability in the LiDAR data quality which in turn makes it difficult to extract exact vegetation geometry of some elements [30]. Yet with the possibility of very high spatial density sampling rate (e.g., the FARO LS880 can sample surface points at 1 m with a resolution of 0.1 mm [31]), LiDAR is becoming a practical tool to measure plants canopy architecture [32, 33, 34, 20, 23].

In this first chapter we will describe LiDAR's features, namely the different types of measurements approaches for distance measurement and their error sources. We will also describe how return intensity is estimated.

# 1 LiDAR principle

A LiDAR scanner is a device which is primarily used to measure distances to a source by using a laser beam that is mechanically distributed in space for spatial sampling. It is composed of a laser emitter, a laser sensor, optics and electronic components (computer, clock, etc.) (Figure 1). The laser beam is emitted through optics and deviated outside the device. It is back-scattered by an object surface and a part of the reflected light reaches the LiDAR aperture. With alignment of optics within the device, the sensor records the portion of back-scattered light in the direction of the emitted beam, i.e., the sensor is in the hotspot direction. The analysis of this reflected light is used to derive the LiDAR distance and intensity, at a pace synchronized with the emission clock of the laser beams.



**Figure 1:** *LiDAR principle: the laser is emitted through optics (blue). A part of the back-scattered energy (red) is sensed and the produced signal is processed by electronic filters and amplifiers before it is sent through a micro-controller.*

## 1.1 Distance measurement

The main technologies to record distance with a laser beam are [35]: (i) the time-of-flight; and (ii) the phase-shift technologies.

The time-of-flight system records the travel time of a pulsed beam light (Figure 2-1). The distance is deduced from the time of flight of light:

$$d = \frac{\Delta t \cdot c}{2}, \quad (1.1)$$

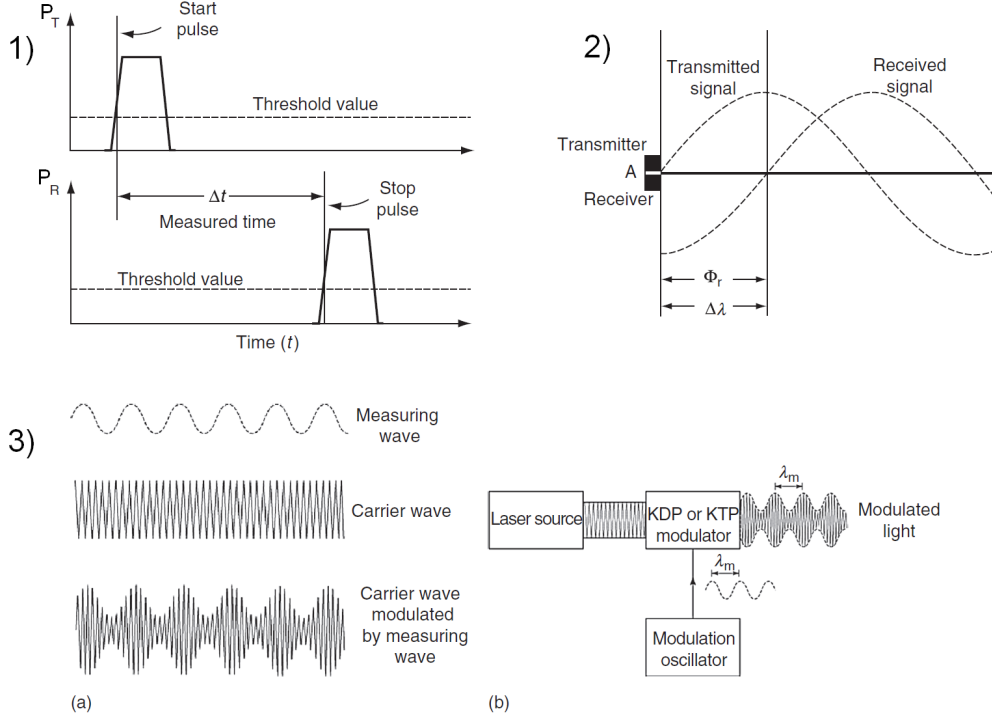
with  $\Delta t$  the recorded time between the light emission and reception and  $c$  the light speed.

A phase-shift system modulates the amplitude of a continuous wave laser beam with a measuring wave (Figure 2-3-a) and compares the phase shift between the emitted and the returned signal (Figure 2-2). Travel time is deduced from the phase shift  $\phi$  and the period  $\lambda$  of the measuring wave:

$$\Delta t = \frac{\phi}{2 \cdot \pi} \cdot \lambda. \quad (1.2)$$

The distance is then deduced with equation 1.1.

Time-of-flight and phase-shift systems are based on different techniques of distance measurement and have consequently different characteristics. For instance, a time-of-flight LiDAR returns distances based on first or multiple return pulses whereas phase-shift LiDAR probe continuously surfaces. That makes their measurement rate different [36]: time of flight LiDAR makes 50-150 kilo points per scan whereas phase-shift technology can provide until one millions points per scan.



**Figure 2:** Distance measurement principle (from [35]): (1) Time-of-flight: the distance is deduced from the measured time  $\Delta t$  between the emitted light pulse  $P_T$  and the received light pulse  $P_R$ . (2) Phase shift: the phase comparison between the two signal provides the time travel  $\Delta t$ . (3) Continuous wave laser beam principle: (a) the amplitude of the laser beam (carrier wave) is modulated (measuring wave); and (b) the wave modulator is directly placed after the laser source.

## 1.2 Intensity measurement

A LiDAR device measures distance by computing travel time of a pulsed or continuous laser beam. Since a few years, most of the LiDAR devices provide returned light intensity of the laser beam.

If we suppose that the laser beam is collimated, i.e. the beam rays are parallel, the light power received by the LiDAR sensor depends mainly on: (i) the object's material reflectance  $\rho$ , which depends on the incidence angle  $\alpha$ ; and (ii) the distance  $d$  between the device and the measured object. In other words, the relationship between the received light power  $P_R$  and the transmitted light power  $P_T$  is [37]:

$$P_R = \eta \cdot \frac{A_R \cdot P_T \cdot \rho(\alpha) \cdot \cos(\alpha)}{\pi \cdot d^2}, \quad (1.3)$$

with  $A_R$  the receiver aperture area and  $\eta$  the receiver's efficiency. Received light power follows an inverse square law with respect to distance, also known as the light extinction effect [38]. This power can be very large for close distances, whereas it can be low for a large distance and to avoid sensor saturation, physical filter are used to decrease the returned light power for short distances [39]. The intensity data, denoted  $I$ , often represents the received power of the back-scattered light energy [40].

The availability of LiDAR intensity makes it possible to extract either the material's reflectance or the incidence angle between the scanned surface and the laser beam. To do so, a correction of the distance effect should be carried out [40] before a radiometric calibration [41] or the settlement of an incidence angle/intensity relationship [42]. Radiometric calibration makes use of the fact that the intensity is highly dependent on the LiDAR wavelength. For instance, a green laser beam (520-570 nm) will have a larger light energy return for a green material than for a red material [43]. Similarly, near-infrared laser beam (750-1400 nm) could be sensitive to material moisture [44].

Even if intensity values are generally far less used than distance values [45], they were found to hold great potential for object classification such as land cover classification for airborne LiDAR [26], distinction between stem and leaves [23], or trunk detection and diameter estimation [46]. With the appropriate wavelength, LiDAR has also been used to measure chlorophyll content in broad-leaves [47].

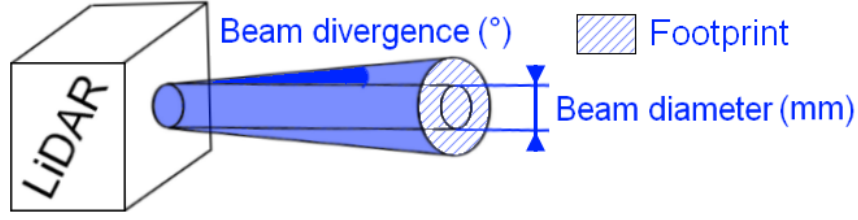
### 1.3 Laser beam footprint

The laser beam is neither dimensionless nor perfectly collimated. It has an initial diameter the size of the LiDAR aperture, and a divergence which is a function of the laser wavelength [48, 49] (Figure 3-1). For instance, the FARO LS880 has a beam diameter of 3 mm and a beam divergence of  $0.014^\circ$ . The laser beam creates a spot on the scanned surface called the footprint (Figure 3-3 and 5), and this footprint has the shape of an ellipse with two axis of different dimensions, i.e., the minor axis  $\Delta d_{min}$  and the major axis  $\Delta d_{max}$  [50]. The distance  $d$  and intensity  $I$  are respectively the average distance and average intensity recorded within this footprint and those values are recorded with the laser beam position (established with the distance value) with which they are associated [51].

Finally, the cross-section of the laser beam from the LiDAR that is perpendicular to the propagation (also called the footprint) increases with distance between the object and the sensor. The footprint can be approximately of the same size if an object is small, when it is strongly inclined or when it is placed at a large distance. Object identification is strongly compromised in such cases.

### 1.4 Optical and mechanical design

Since the first LiDAR developments where airborne LiDAR system (ALS) were used as profiler [52], the mechanical design of the device has been developed to increase the range of application of the technology. Nowadays ALS have a scanning device that allows users to sample around



**Figure 3:** *The laser beam has a diameter and a divergence and LiDAR records distance and intensity within the footprint.*

+/- 20 degrees across the flight line. In contrast, hemispherical terrestrial LiDAR systems (TLS), such as the FARO LS880 (Figure 4-left), use a 45° rotating mirror for a circular scan in zenith ( $\psi$ ) combined with a rotating or a moving platform for the azimuthal ( $\theta$ ) rotation. The mechanical displacement in these two directions allows a full hemispherical view (with the exception of the masked area by the instrument's base forming an occluded region of about 20 degrees underneath). A clock sets the pace of the motors rotation and the laser beam return recording while distributed in space, and the resolution of this pace determines the angular resolution of the scan as well as the density of the point cloud. In other words, hemispherical TLS collects the distance and intensity values together with their spherical direction, i.e., it produces the distance and intensity map of the surrounding scene (Figure 5). If required, the spherical coordinates of measured points can easily be transformed in Cartesian coordinates with the center point (0,0,0) at the optical center of the LiDAR system [53].

Mobile LiDAR system (MLS) are polar LiDAR system (one angular dimension, e.g., the azimuth angle) placed on a mobile carrier (car, tractor, robot, etc.). For instance, Rosell et al. designed a MLS [16] with a SICK LMS200 placed on a tractor (Figure 4-right). Natural coordinates system of the MLS distance map is cylindrical. Here again these data points can be easily transformed into the Cartesian coordinates system [54]. Compared to static TLS, MLS optical center of the LiDAR system moves along the path followed by the LiDAR carrier.

In general, mechanical design of LiDAR devices make the data expressed in a natural coordinates system (spherical, cylindrical or polar in the case of the SICK LMS400) and to get distance and intensity maps, LiDAR systems return either a measurement of the laser beam direction in the case of hemispherical TLS (e.g., the angles ( $\theta, \psi$ )) or the position of the optical center of the LiDAR system together with the angular position of the laser beam in the case of MLS.

## 2 Data quality

LiDAR systems measure distance with the time of return of an emitted signal in addition to the return intensity of its laser beam. Since the first development of LiDAR technology, their range of application have been increased. Hemispherical TLS became common in research field such



**Figure 4:** *Left: Hemispherical TLS. The beam direction is rotated with a 45° mirror ( $\psi$ ) and the device is placed on a motor with azimuthal rotation ( $\theta$ ). Right (From [16]): MLS. A polar LiDAR system is mounted on a tractor.*

as agronomy, horticulture and forestry. In the following we will mainly discuss about this type of LiDAR scanner.

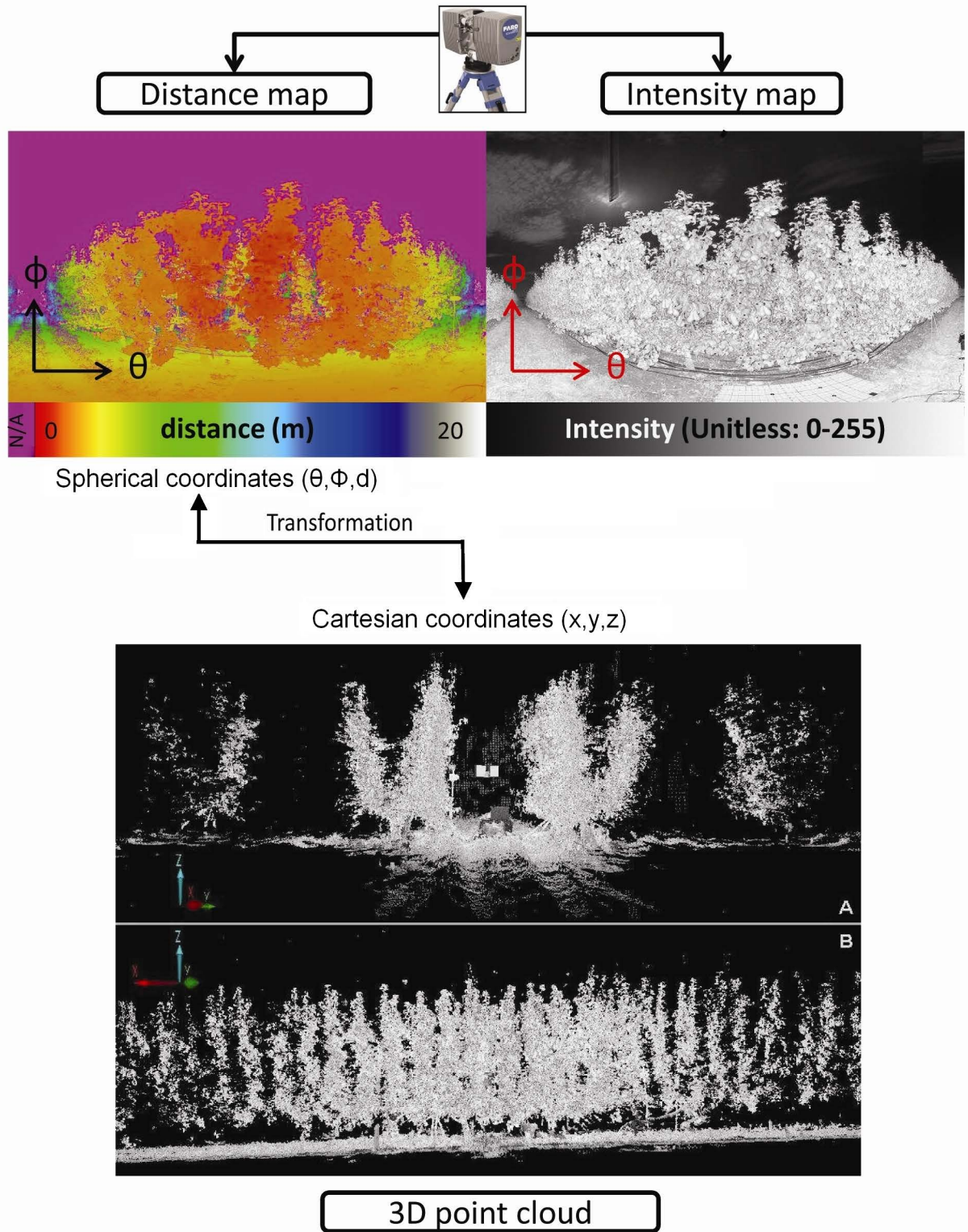
The output of the TLS measurement is a 3D point cloud representing the laser beam returns of the scanned object according to the selected sampling point density. However, the presence of noise led researchers to investigate how to improve the data quality. Quality is generally expressed in term of precision and accuracy (Figure 6) which correspond, respectively, to error and bias. In this section, we will talk about LiDAR technical features such as point cloud quality and density, as well as intensity quality and ratio outliers/number of points (ROP).

## 2.1 Distance value

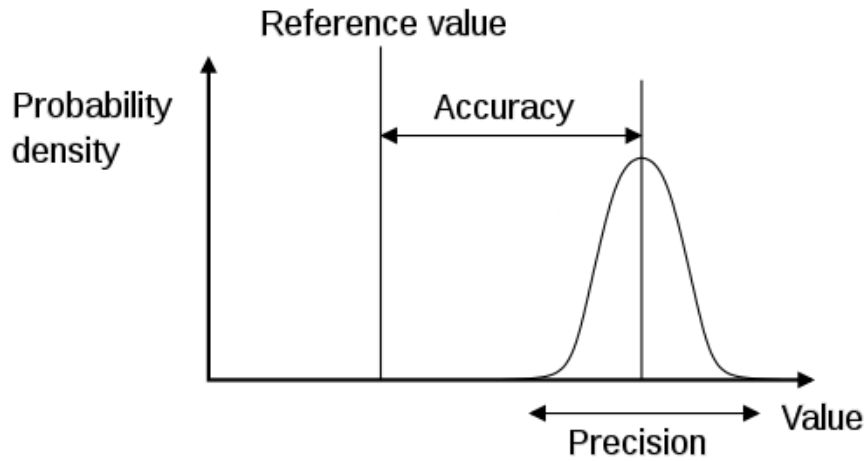
The precision of TLS distances depends on many aspects dominated by three: (1) the distance of the TLS laser aperture to an object, (2) the light beam incident angle, and (3) the material reflectance and the ambient light [24]. Because of light extinction [38], the farther is an object, the lesser is the light energy that is coming back. This implies a decrease in distance measurement precision. Similarly, when less energy is returned, TLS are more prone to make errors on distance measurements. This is actually the case for low reflectance materials and, in general, for inclined surfaces. For instance, with a surface target of 90% reflectance, the phase-shift TLS FARO LS880 has a root mean square error of 2.6 mm at 10 m and of 4.2 mm at 25 m. With a surface target of 10% reflectance, those precisions are brought down to 5.2 mm and 10 mm respectively [31].

Distance measurement is computed with the integration of the distance within the laser beam footprint. Depending on the surface inclination, the distance can be overestimated, i.e. it can have a bias: (i) in the case the laser beam hits the middle of a slightly inclined surface, the average distance is representative to the distances present within the laser beam footprint and an accurate distance is measured (Figure 7-1); (ii) in the case of a surface that is strongly inclined, the footprint has an ellipsoid shape (Figure 7-2) and the average distance corresponds to the distance at the middle





**Figure 5:** TLS FARO LS880 (pear tree orchard scan): hemispherical images (spherical coordinates) of the depth (up left) and intensity map (up right). The 3D point cloud is obtained with proper transformation.



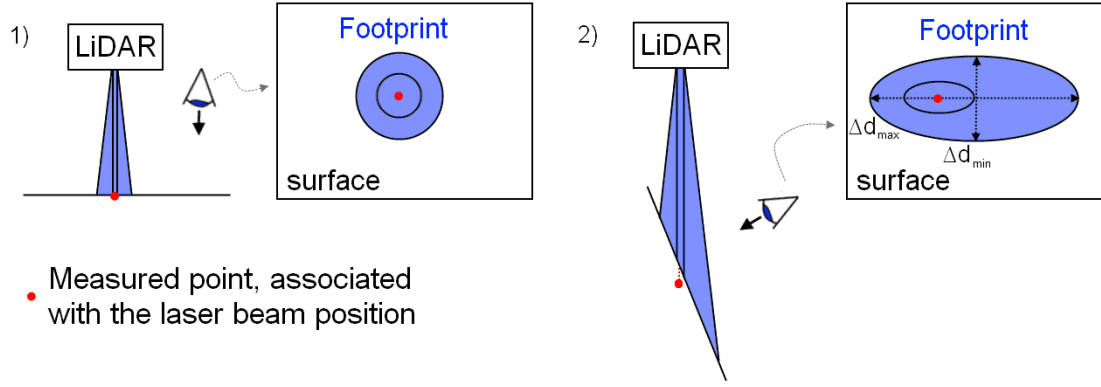
**Figure 6:** *Precision of the distance measurement is the degree to which repeated measurements show the same results. Accuracy is the degree of closeness to the correct distance value.*

point of the footprint. However, this middle point does not correspond to the laser beam position and there is a bias in the interpretation of distance which is over-estimated. This overestimation is generally negligible because the laser beam has in general a Gaussian irradiance density [55] and the beam diameter of most TLS is usually small. It can be important for strongly inclined surfaces though.

Measurement technology also affects the quality of the measurement [36]. Phase-shift TLS are more suitable for short distance ( $< 2$  m) than time-of-flight TLS, which provides incoherent point cloud at such ranges. However, the measurement of a time-of-flight TLS takes into account the first pulse return of the TLS laser beam that makes its measurement more accurate in the case of large range. Ambient light affects differently those two light recording systems. In [43], Voegtle et al. recommended to proceed measurements with the time-of-flight TLS TRIMBLE GX during night-time, whereas the manufacturer of the LiDAR FARO LS880 (phase shift technology) declares that the effect of light environment on the point cloud precision is negligible.

In the case of hemispherical TLS devices, incorrect motors alignment and device vibration create respectively bias and errors in the measurement of the laser beam angular direction [56]. Still, it is possible to correct bias with proper calibration [25], and in the case of static and high precision TLS, the errors created by vibration are negligible compared to the distance measurement error [24]. However, in the case of MLS, vibrations can cause severe errors and bias in the measurement of the laser beam direction, and correction methods should be applied to merge every 3D point into a coherent point cloud [57].

Proceeding to TLS scan requires an a priori reflection on the scan configuration (object position and geometry) and on the device choice (LiDAR of technology and design). In general, proper calibration of the LiDAR mechanical system and the post-process of its point cloud are necessary.



**Figure 7:** (1) If the surface is perpendicular to the laser beam, the footprint is circular and the measured distance is accurate (red dot). (2) If the surface is inclined, the measured point distance is overestimated (red dot) and the footprint has an ellipsoid shape.

## 2.2 Intensity value

As previously mentioned in Section 1.2, the intensity depends mainly on three factors: (1) the incidence angle between the laser beam and the object surface, (2) the optical property of the scanned material, and (3) the distance between the object reflecting the beam and the sensor. Similarly to the distance measurement, those three factors also influence the quality of the intensity values.

Intensity is a function of the returned light power within the TLS beam footprint. Even if equation 1.3 holds for smooth and opaque material and at varying incidence angle, the intensity is almost constant with varying incidence angle in the case of irregular surfaces [58] (e.g., gravel with roughness larger than the laser beam footprint). In general, intensity measurement can be biased due to the complexity of the surface geometry and the size of the laser beam footprint.

Pfeifer et al. [59] showed that for the time-of-flight scanner Riegl LMS-Z420i, an increase on material reflectance produces an increase on the measured intensity error which is always below 3% of recorded intensity. In the case of a time-of-flight TLS TRIMBLE GX, Voegtle et al. [43] also showed a correlation between the increase of this error and the increase of the material reflectance. However, with the time-of-flight TLS Optech ILRIS 3D, Höfle et al. [60] found an error constantly equal to 10% which exemplifies how the quality of the intensity values is also related to LiDAR's technical specifications. In addition, they showed that both incidence angle and reflectance have an influence on the intensity precision: if the incidence angle produces a lower intensity value, then the error becomes lower with the increase of this angle.

Most of the studies showed that there is no clear impact of the distance on the error of measured intensity: none were recorded for large range (up to 50m and with time-of-flight TLS Riegl LMS-Z420i [59]), middle range (up to 25m and with phase-shift TLS Leica HDS 6000 [61]), nor close range (up to 2.6 m and with time-of-flight TLS Leica ScanStation 2 [47]).

The increase of light power return due to material reflectance and incidence angle increase induces an increase of the LiDAR intensities measurement error. Still, the precision of those measurements stays stable when the distance between the scanned surface and the TLS aperture gets larger. In

other words, distance effect on intensity recording (see Equation 1.3) can be corrected and intensity calibrated to the material reflectance [40]. This calibration depends on the design of the TLS recording system: for instance, physical filter used to avoid sensor saturation at close range, makes the intensity measurements less accurate for close range in the case of phase-shift TLS FARO LS800 less accurate [42].

## 2.3 Outlier points

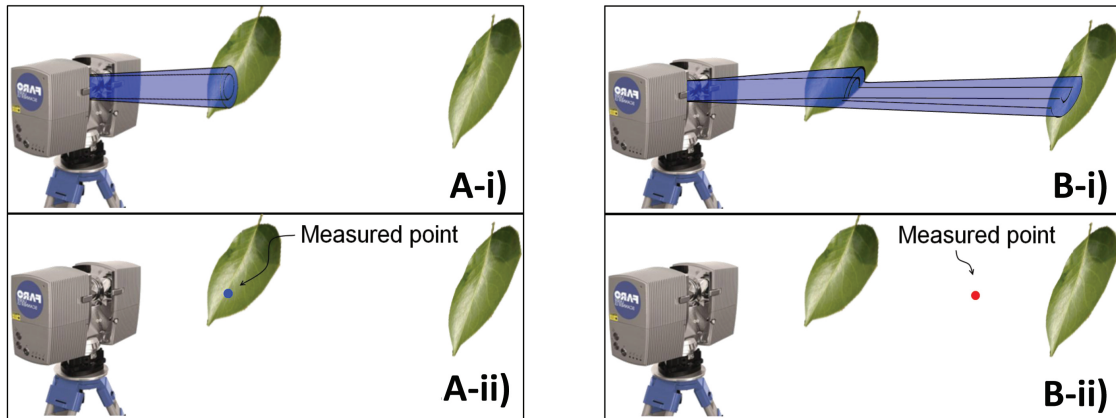
The distance and intensity values recorded by the TLS are values within the laser beam footprint. During the scanning process, the laser beam can either completely or partially intercept a surface [50]. When the footprint is contained within an object surface (Figure 8-A-i), the recorded distance and intensity are relatively accurate (Figure 8-A-ii): the measured point is an inlier. Still, the recorded distance can be overestimated due to the surface inclination (see discussion in subsection 1.3) (Figure 9-1). When the laser beam has reached an edge, it is split between a foreground object and a background object (Figure 8-B-i). In the case of time-of-flight measurements, the use of first returned pulse guarantees that the foreground object is measured, but in the case of phase-shift technology, the estimated distance and intensity become equal to intermediate values. Consequently the recorded values are not representative (Figure 8-B-ii) and are called outlier points, or outliers. Depending on the object's geometry and the edges position, several outliers could be recorded during the scanning process.

Determining whether a point is an outlier or an inlier is a difficult task. The point clouds represented by Figure 9-1 and 9-2 are similar but do not represent the same object configuration. In the first drawing, the measured surface is continuous and the points are inliers (in red), whereas in the second drawing, the surface is discontinuous and a portion of the points are outliers. In the case of outliers, the configuration of the surface inclination can also lead to ambiguities. For instance, when the upper surface has no strong inclination relatively to the TLS laser beam, the points at the object's edge are clearly outliers (Figure 9-2). However when the upper surface does have a strong slope, the difference between outliers and inliers is more subtle (Figure 9-3).

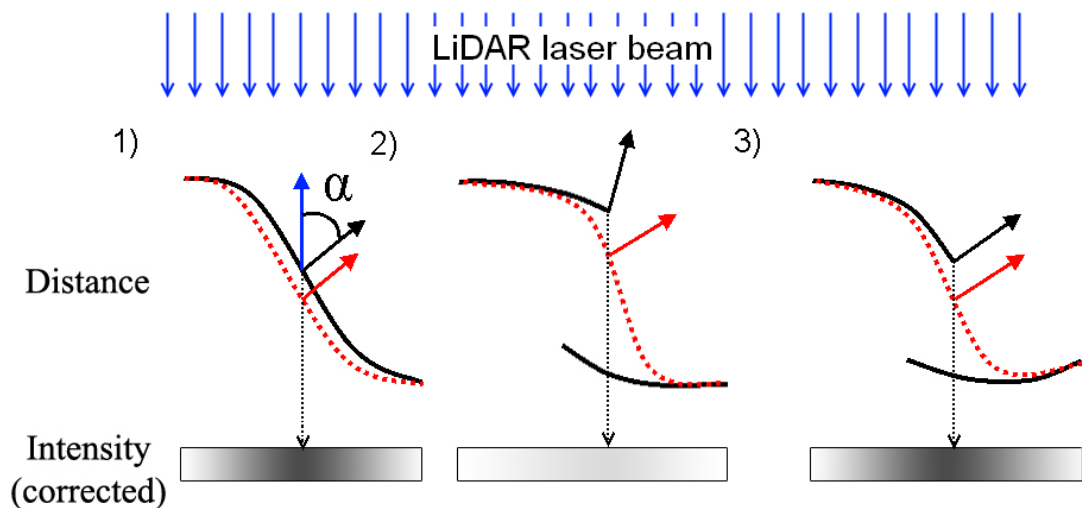
Two types of outliers detection algorithm based on distance exist (see Appendix I) [50]. In the first type of algorithm, a point is considered as an outlier if a defined portion of the scanned surface is at least at a minimal distance to this point. In the second type of algorithm, a point is considered as an outlier if it has not enough neighbors in its surrounding. This latest algorithm requires the knowledge of local density, which is not always easy to estimate. Those two algorithms of outliers detection based on distance works properly when the surface distance are large, with simple shape, and not too strongly inclined (e.g., house's wall). They can be misleading in the case of complex and fragmented shapes such as tree canopy. In addition, they only detect outliers and do not correct them.

In some cases the intensity values can be used as much to detect outliers as to correct them. Intensity values are related to the local inclination of the surface with respect to the LiDAR laser

beam. For example, Figure 9-1 and Figure 9-3 show two cases where intensity and point cloud information are consistent. In contrast, Figure 9-2 shows a case of inconsistency where locally the normal associated with intensity does not match the normal derived from the point cloud. In this later case, this mismatch reflects the existence of outliers and can be used in order to detect them. Moreover, the consistency between intensity and surface inclination can lead to a correction of the outliers.



**Figure 8:** (A-i) The laser beam footprint is in the middle of the surface. (A-ii) Accurate estimation of the point distance. (B-i) The footprint is split between the measured surface and a background surface. (B-ii) An outlier point of intermediate distance is recorded.



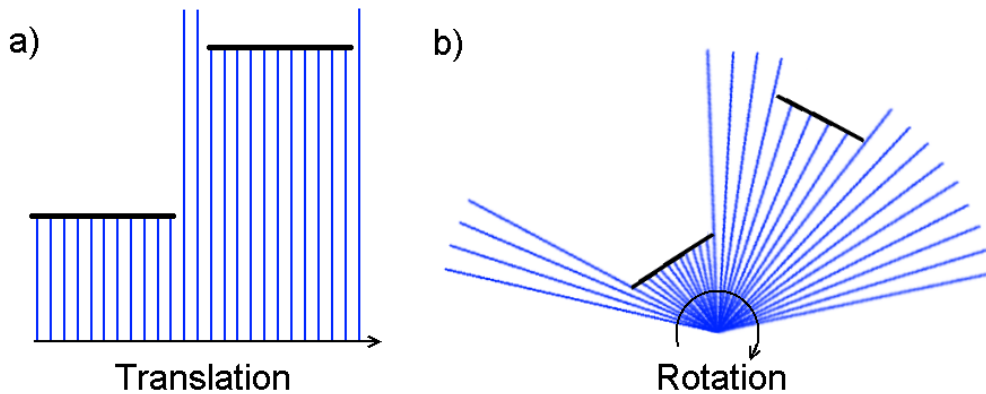
**Figure 9:** Side view of a point cloud (red dots) and their corresponding surface (black curves). (1) Smooth surface forming a large incidence angle with the LiDAR laser beam. Intensity is correlated to incidence angle (black arrow) and to the point cloud local inclination (red arrow). (2) Laser beam at a slightly inclined surface's edge: there are clear outliers. Intensity is correlated to the incidence angle but not to the recorded point cloud. (3) Laser beam at a strongly inclined surface's edge: difference between inliers and outliers is more subtle. Intensity is correlated to a mixture of the local incidence angle.

## 2.4 Point density

The point density describes the number of scan points within a given surface area. It is often referred to as the resolution of the TLS recording. On most TLS systems point density depends first on setting the clock associated with the emission/reception of the laser beams [56]. Distance is an important factor which affects the point cloud density when LiDAR has a rotary system (Figure 10-b). Yet it has no impact in the density measurement along the carrier path of MLS (such as an ALS or vehicle-mounted LiDAR) (Figure 10-a).

For both system of mobile and rotary, the incidence angle is a factor which is impacting on point density: the larger this angle, the lower the point density becomes. On all TLS, several point density are preprogrammed so these critical selected acquisition parameters are easily retrieved from the data collected.

Another factor, external to the selected TLS parameters, which affects the point density is the scanned scene composition. An object can be partially occluded and the number of laser hits on its surface is lesser than expected. This phenomenon is called occlusion [62]. Similarly, an object cannot be entirely scanned with one scan, mainly because of the occlusion of the element most distanced or on the opposite side from the TLS. It is therefore frequently needed to scan an object or a scene from several points of view.



**Figure 10:** *The point density depends on the travel resolution of the LiDAR laser beam. If the laser beam is in rotation, the point density also depend on the object's distance. (a) A laser beam in translation; (b) A laser beam in rotation.*

## 2.5 Ratio outliers/number of points (ROP)

In the case of phase-shift TLS, the laser beam footprint can be large enough to cover a large proportion of an object's surface and, during the scan, this footprint can reach the object's edge and create several outliers. To quantify the proportion of outliers, we define the notion of ratio outliers/number of points (ROP) as the number of outliers divided by the total number of points representing a surface. For a given surface area, the density of points decreases with distance, in contrast to the



footprint diameter which increases. Thus the ROP increases with distance. Similarly, the ROP increases with incidence angle, occlusion, footprint diameter, and angular resolution.

## 2.6 Quality factors

The table 1 recaps the main factors that have an impact on TLS data quality. All these factors have been discussed in this section except for the wind speed. We see that the TLS data quality highly depends on the TLS technical design, the scanned scene (object material, position and geometry) but also on the environment (light and wind). Consequently it is predictable that scanning vegetation (trees orchards, forest, etc.) produce a very complex point cloud to analyze with a wide gradient of data quality, even within the same scene.

Factor	Distance Precision	Intensity Precision	ROP(*)	Point density	Literature
↗ Distance	↘	=	↗	↘	[30]
↗ Incidence angle	↘	↗	↗	↘	[63]
↗ Object size	↗	↗	↗	=	[51]
↗ Object reflectance	↗	↘	=	↗ (**)	[61, 64]
↗ Occlusion	=	=	↗	↗	[62]
↗ Footprint diameter	↘	↘	↗	=	[51, 47]
↗ Angular resolution	=	=	↗	↗	[56]
↗ Ambient light	=	↘	=	↘ (**)	[61]
↗ Wind speed (***)	↘	↘	↗	↘	[65]

**Table 1:** Main factors on the LiDAR quality. If those factors increase (↗), the distance precision, intensity precision, ROP and point density could increase (↗), decrease (↘) or be insensitive (=). (\*) For phase-shift technology. (\*\*) For low reflectance. (\*\*\*) For vegetation material.

## 3 Conclusion

LiDAR technology consists of emitting a pulsed or a continuous and modulated light signal, and recording the time of travel of this light signal in order to measure distance. Hemispherical TLS is a LiDAR system with double rotations and it can quickly produce a dense 3D point cloud of a scene. Three main factors affect the precision of TLS measurements: the distance between TLS aperture and scanned surfaces, those surfaces geometry and the material reflectance. When the scan configuration is adapted to the scene (e.g., object are close enough, slightly inclined, etc.), TLS devices provide data with satisfactory quality to extract geometry information. Yet in the case of phase-shift TLS, footprint size makes distance measurement overestimated, and when the laser beam reaches an edge, the consequent outliers make the TLS point cloud severely biased. In addition, when the surface is inclined, it is not always possible to see the difference between outliers and inliers and the surface representation can be incorrect. Plant canopies are fragmented surfaces. As a result, leaf shape extraction from TLS scan is a difficult task.

Intensity is function of the return light power recorded by the TLS sensor. This data is available in most TLS and has been used mainly for scan segmentation. As recorded intensity depend on surface inclination, it provides geometrical information on the scanned surface. In Section 2.3, we showed that, on critical surface points which are the edges, the recording of intensity has a behavior different from the distance recording. In some cases, intensity measurement has more likelihood than the distance measurement and the use of this intensity could lead to the detection and the correction of outliers.

The combination of the high throughput of data and their quality makes TLS devices common in most fields where geometric measurements are needed. In agronomy it is used to extract global descriptor of plant canopy such as the density of leaves. Yet TLS devices have not been used for the leaf shapes extraction with *in situ* scans. In the next chapter, we will make an overview of the main biological facts that make plant description at organs scale necessary, and we will discuss the reason why the state of the art of TLS measurements of plants did not reach this scale yet. In the following of the thesis, we will investigate the geometrical properties of intensity in order to develop an outlier correction algorithm that we will apply on complex plant scene and illustrate our approach on pear tree orchard scans.



## Chapter 2

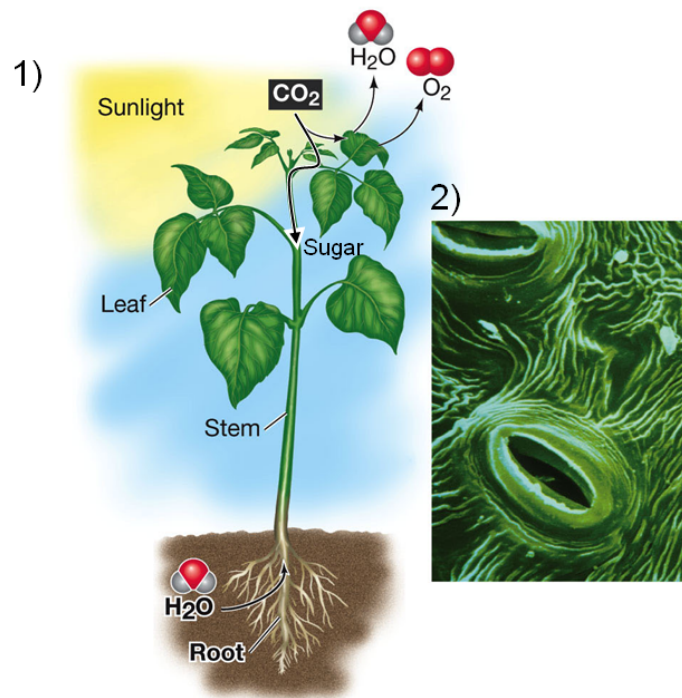
# Toward a geometric reconstruction of leaves from orchard trees

Bio-engineers and horticulturist are seeking to improve the management of their orchard. For instance, they wish to optimize the quantity and quality of their crop production (e.g. fruit size, taste and density) [1], the quantity of pesticide to apply to decrease expenses and bio-impact [3], and the management of their irrigation system in order to control the fruit growth [66]. From a biological prospective, understanding plant physiology help improving orchards' management. Sugar production is driven by water uptake, CO<sub>2</sub> availability and sunlight [67] and the plant morphology determines the efficiency of the sugar spread in the plant and fruits (see Figure 1-1). In other words, understanding plant growth mechanisms and their interaction with the plant's environment can help improving orchards management. Developing this understanding requires to acquire specific information on plant geometry.

TLS produces a dense 3D point cloud that can be used to extract geometrical characteristics of scanned object. TLS measurements proved to be more adapted than traditional measurements for the estimation of geometrical descriptors on plant morphology. Most studies investigating plant architecture used TLS only to extract global indicators (e.g. [68, 22, 21, 32, 33, 65, 69, 15, 70]), and a very few of them proposed measurements of canopy elements at organ scale [18, 47, 71, 72]. Moreover, the fine level work on plant architecture generally proposed an analysis under controlled conditions. Therefore there is very little TLS studies dealing with fine level plant architecture (leaves and fruit scale) and dealing with complex *in situ* measurements (e.g.,[21, 22, 23]).

In the first section of this chapter, we will investigate the biological aspect of plant morphology in order to assess which geometrical characteristics are needed by agronomists and horticulturist. Then, we will give a short description of the traditional measurements available to describe plant geometry at different scales. This is followed by the description of measurement of the spectral properties with spectrometers and the measurement of geometrical information with TLS. These descriptions will help appreciate the different scales of measurements using TLS and traditional measurements. In a last section, we propose a preliminary study to investigate TLS point cloud quality of complex canopy to allow an entry level discussion on the use of TLS intensity to assess

leaf geometry.



**Figure 1:** (1) Schematic illustration of the plant interaction with sunlight, atmosphere and ground. (2) Zoom on the leaves stomata. (taken from [73])

## 1 Plant morphology

Orchard tree morphology is a main factor that drives fruit production. The position of photosynthetic material and fruits in addition to their connectedness, determine the efficiency of sugars production and storage [74]. Morphology also affects the spread of pest and drought [75]. In the following, we will see which factors in plant structure play an important role for fruit yield and quality. In addition, we will give a short overview of pest and stress impacts on trees geometry.

### 1.1 Plant structure and fruit production

The management of orchards fruit production by the control of the tree morphology is one of the main issues for the agronomists. Tree growth is a complex process and it is not easy to assess which branching configurations will occur, i.e, how many new shoots will occur, their type and their location. For instance on a pear tree, short shoots (< 5cm length) and long shoots (> 5 cm length) appear every year. They can be lateral (on the side of a parent branch), or apical (continuing the growth of a branch). In addition to the buds, they can bear a flower cluster (and consequently fruits) or only leaves. Spur leaves are on shoot that bears the flower cluster, fruit and lateral bourse shoot, and shoot leaves are on the shoots that do not produce fruit. Sugar produced by spur leaves is more bio-available to the fruit than the sugar produced by shoot leaves [74].

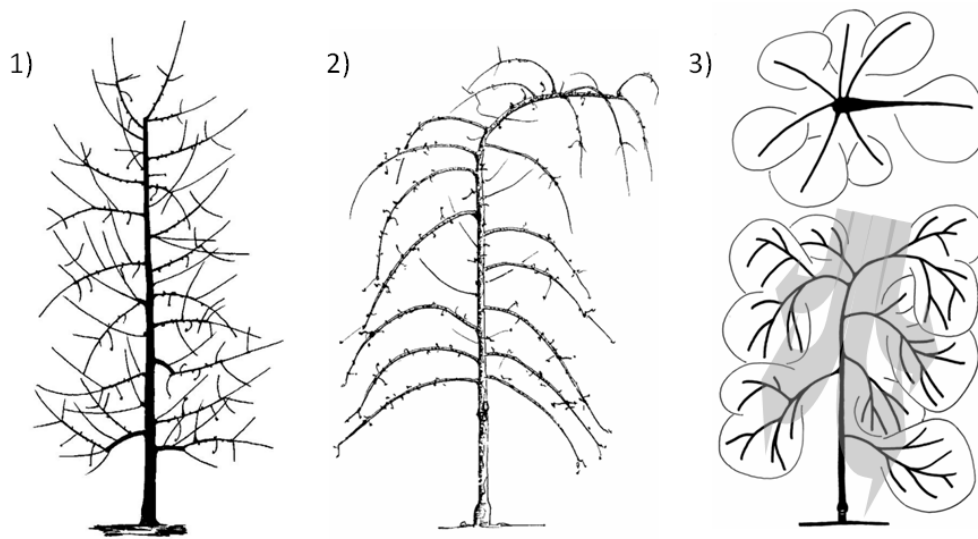
The imperatives on improving productivity impose the implementation of pruning rules to guide the growing process of orchard trees, that is, to impose a training system to the tree. Since the XVIIIth century when king's garden were horticultural research places [76], two different types of training system have been developed: one seeks to limit the growth to a few principal branches that are generally held by a structure, and the other one trends to let the tree getting a free shape. For instance, the V-shape training is a training system using an artificial structure. V-shape tree is composed by its trunk and four branches. Couples made of two branches forming a V with an aperture of  $40^\circ$  allow a better sun penetration. Iron cables hold the tree structure and new long shoots are pruned on the top and the bottom of the canopy every year. Fruiting shoots are better exposed to sun in this way. The vertical axis training, the Solaxe training system (ST), and the centrifugal training system (CT) are free shape training system. The ST (Figure 2-2) is a derivative of the vertical axis training [77] (Figure 2-1), where tree is made up of a vertical trunk, and along which fruiting branches are regularly distributed. However instead of the vertical axis training, the ST involves combining the bending of the central axis and the fruiting branches, developing free growing lateral fruiting branches and removing the competing vegetative branches. The CT (Figure 2-3) is also a derivative of the vertical axis training. It involves pruning the shoot within the canopy in order to create a shaft of light.

The comparison of fruits yield between different trainings is a common method to assess the efficiency of a training system. For instance, in [78], six training system (four with artificial structure and two with free structure) are evaluated on the behavior of four nectarine trees (Maria-Laura, Katia, Red Diamond and Stark Red Gold). Authors compared the fruit yield, size, weight, and tree flowering, vigor and branching for each of those training system. They showed that the training system Palmette Arbor (with artificial structure) is the best training system for fruit yield for the Maria-Laura and Katia varieties. Training system Palmette Arbor and Gobelet (free system) is the best training system for the Red Diamond variety. Training system Palmette (with artificial structure) is the best training system for the Stark Red Gold variety. In addition, they showed that the training system Gobelet (free system) was more adapted to stimulate new branching shoot.

Another type of research lead in horticulture is the understanding of the relationship between sunlight, plants and fruit yield [79, 1, 80]. Light interception is a key factor to photosynthesis rate. However, increasing the orchard productivity by increasing light interception by higher planting density does not necessarily lead to the highest fruit yield and quality [74]. Plant structure and fruiting versus leaves shoots position can have more impact. Willaume et al. [2], compared the ST and CT systems on six Gala apple trees to compare the sunlight interception by spur leaves. To do so, they measured leaves position and geometry of 20 to 30 shoots of different types (fruiting versus vegetative shoots). They showed that CT enhances significantly spur leaves area when compared with ST (Figure 3-1). With the vertical distribution of spur leaves in the canopy (represented by the silhouette to area ratio (STAR) index, see Figure 3-3), they showed that light is more available to spur leaves and consequently, that more sugars are bio-available to fruits. In addition, they observed that CT induces a change in the color of the fruit positioned within the canopy (Figure

3-2). In other words, their work shows that it is necessary to let sunlight reach spur leaves in order to improve fruits quality. Yet their study was conducted on a single apple tree variety, and as each tree species has an optimal training type that depends on its branching and fruiting configuration [81, 82], it is necessary to extend this kind of research to other species.

Orchards management are expensive and the study of the relationship between light interception and fruit tree structure is interesting as it allows a better understanding of the plant and thus to better anticipate the plant needs and production. Yet, this type of study requires the measurements of tree architecture and leaves position in addition to their labeling (spur versus shoot). Manual measurements make this type of research tedious and time consuming, and researchers seek to have rapid and reliable measurements tools.

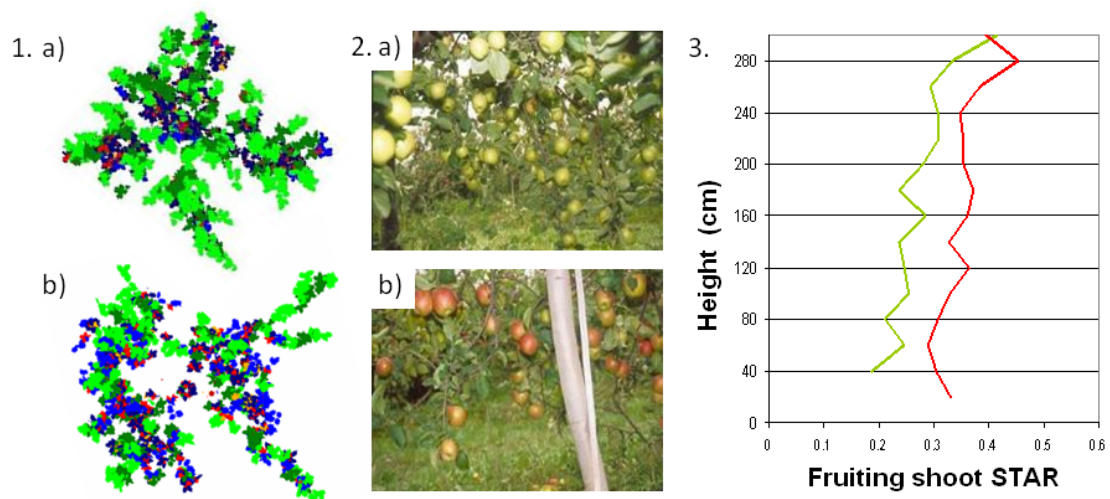


**Figure 2:** (1) Vertical training system (from [82]). (2) ST system (from [77]). (3) CT system (from [2]).

## 1.2 Plant diseases

Another key issue in agronomy and horticulture is the limitation of fruit tree biotic and abiotic damages, and the optimization of phytosanitary applications. The cause of tree damages can either be due from animal, bacterial, environmental, fungal or insects. The main damages caused on apple and pear trees and that have a visual impact on the foliage are (from [83, 84]):

- (1) Aphids (insect, Figure 4-1) that are small sap-sucking insect. On infested trees, terminal leaves are curled downward and sticky with honeydew secreted by the aphids. This honeydew may drip onto the fruit causing russet spots and promote growth of black sooty mold and the highly infested shoots of young trees are stunted or malformed.
- (2) The fire blight pathogen (bacterial, Figure 4-2), where major symptoms are blossom blight, fruit blight, shoot blight, and canker. First symptoms usually start with the



**Figure 3:** (1) Top view of the canopies: (a) ST tree, and (b) CT tree (green: shoot leaves, blue: spur leaves, red: fruits). (2) Fruits: (a) ST tree, and (b) CT tree. (3) Vertical distribution of the silhouette to area ratio (STAR) per fruiting shoot (green: ST, red: CT). (©Pierre-Eric Lauri)

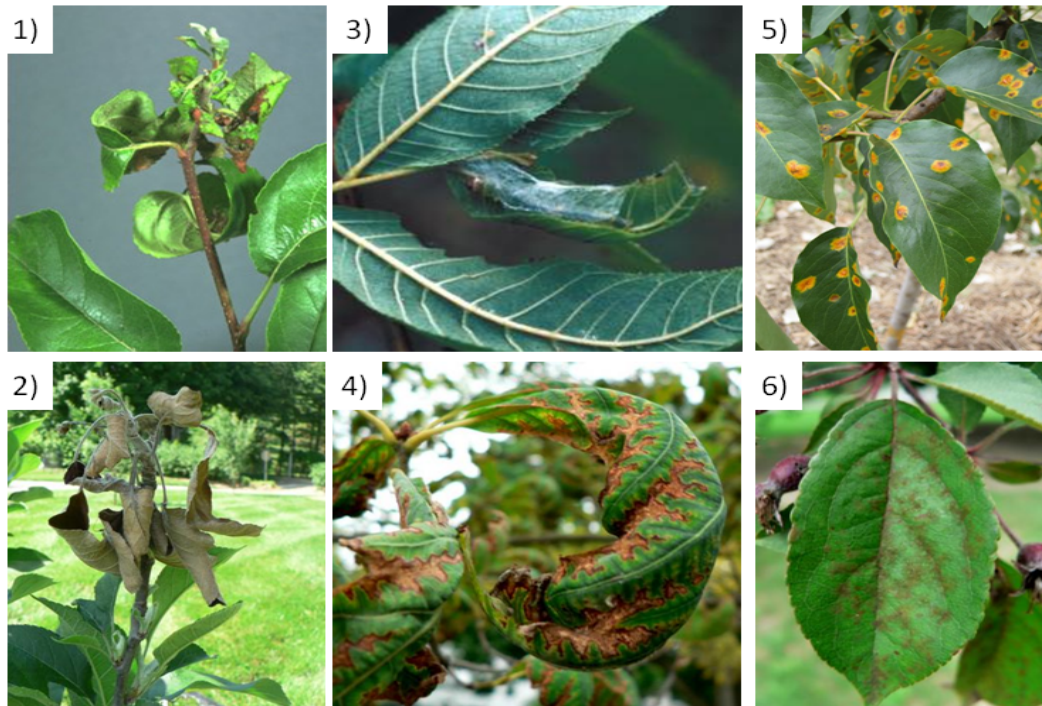
blossom appearing water soaked then drooping and browning. The disease continues growing down through the shoot, killing as it moves systemically.

- (3) Leaf-rollers (insect, Figure 4-3) that are in general solitary and web a leaf so that the leaf appears rolled or folded. Once the leaf is rolled, the insect feeds inside. In severe cases, individual leaves will turn brown or lace-like due to the feeding of the caterpillar.
- (4) Drought (abiotic, Figure 4-4) where the foliage become limp, curl, wilt and go off color. Plant cells furthest from the veins can turn brown and die. The entire leaf may eventually die.
- (5) Pear rust mites (insect, Figure 4-5) are small sap-sucking insects. Their damages consist of bronzing or darkening of pear leaves and fruit. This discoloration, called russetting, begins on the underside near the vein that runs down the center of the leaf and gradually spreads outward. The tops of the leaves may remain green and look healthy.
- (6) Apple scab (fungal, Figure 4-6). Leaf spots appear in spring as small olive-green lesions on the upper and lower leaf surfaces. As spores form, lesions develop a velvety brown appearance. Later, lesions are more elongate and often follow veins, but the same velvety brown look is present. As leaves age, they turn yellow (except for the scab lesions) and fall from the tree.

The commonality of those damages factors are that the leaves aspect changes: color and/or geometry are progressively changing during the propagation of the infestation. It is clear that each of

those factors can destroy the plant either partially or entirely, and a great challenge for agronomist would be to better understand their apparition and propagation.

At the orchard scale, there is a trend in pest management research to understand the spatial distribution and propagation of the plant aggressors [85, 86]. At the organ scale, only a few research studies have taken place to determine the relationship between the leaves geometry and drought [87]. Research on *in situ* plants to quantify their local geometrical change due to insect, fungal and bacterial invasion, are missing in the literature.

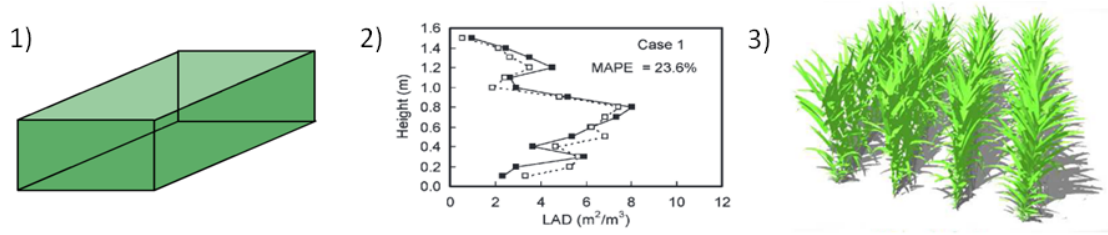


**Figure 4:** Common fruit tree damages (from [83, 84]): (1) aphids (insect), (2) fire blight (bacterial), (3) leaf-roller (insect), (4) drought (abiotic), (5) pear rust (insect), and (6) apple scab (fungal)

## 2 Measurements and representations of vegetation structure

Exact geometrical representation of plants at the scale of the organs is useful for many subjects studied in agronomy and in plant biology. Various methods of plant measurements have been set up, either at the scale of the canopy or organ, to understand physiological response of plants to management and stress. In the following, we established the state of the art of different types of plant descriptors and measurements, enumerating the methods in decreasing scale: starting by methods considering the plant as a single entity (Figure 5-1), then dealing with distributions of leaves geometries (Figure 5-2), and ending on methods at organ scale and on virtual plant models (Figure 5-3).





**Figure 5:** *Canopy descriptor at different scale. (1) The plant as a single entity: simple turbid medium. (2) Distribution of leaves geometry: vertical profile of leaf area density (from [69]). (3) Virtual plants: ADEL-Maïze (from [88]).*

## 2.1 The plant as a single entity

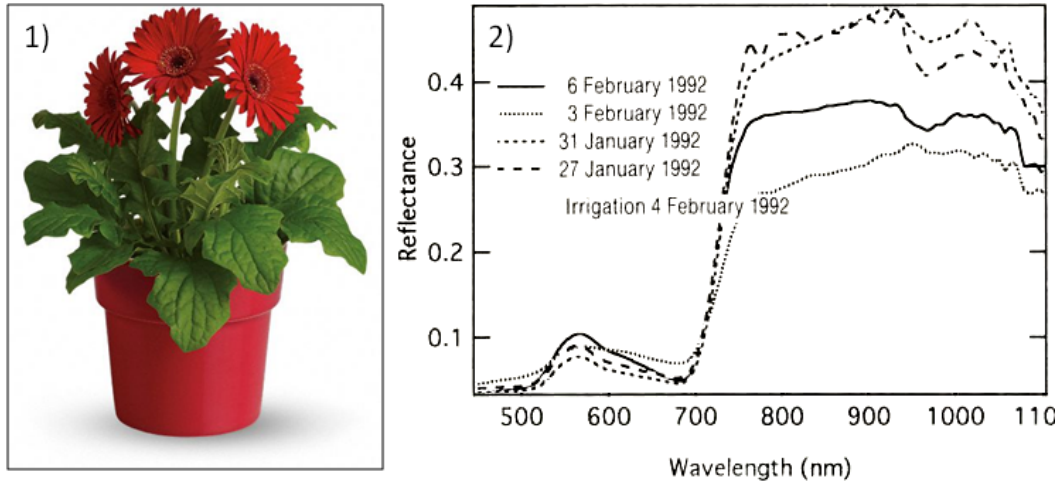
Biotic and abiotic stresses induce physiological responses of plants at various scales. For instance, the closure of the stomata cells due to water stress affects  $\text{CO}_2$  assimilation, transpiration, temperature and leaf water potential [67] (see Figure 1-2). In other words, water stress induces change in the cellular structure and in the biochemical processes of the plant, which consequently has an impact on the plant morphology, on its physiology and on its spectral response to sun light. This spectral response can be recorded with remote sensing devices such as satellite multispectral sensors in order to monitor plant water content [89]. To do so, it is possible to consider the plant or a set of plants canopy as a simple entity. With such perspective it is possible to interpret spectral response as plant stress indicator but also to estimate canopy efficiency to intercept light. In the first case, the radiometric signal can be viewed as a single pixel representing the plant. In the second case, structural measurement such as Leaf Area Index (LAI), can be extracted from a radiative transfer equation. In the following, we will investigate those two types of plant models.

### 2.1.1 Spectral measurement

The recording of spectral response of plant can be carried out with a spectrometer. Spectrometers are tools for the precise measurement of the incoming radiometric intensity on several spectral bands ranging from UV to infrared. Among a large spectrum of uses, it is useful to measure the spectral response of different plants in various contextual/environmental conditions. The spectrometers can take one measure for the whole field of view or imaging spectrometers provide an image where each pixel contains the viewed intensity of a scanned object. The intensity measured represent the contribution of every returned light ray once interacted with the canopy in the viewing direction. Spectral information of plants varies with plant physiology. For example Peñuelas et al. [90] used a spectrometer SE590 (©Spectron Engineering with 252 bands covering 390-1100 nm) placed at an azimuthal angle of  $50^\circ$  towards the canopy of a Gerbera (ornamental flowering plant, see Figure 6-1) to assess canopy response to water stress (Figure 6-2), with focus on the 950-970 nm wavelength bands.

The spectral response of plants depends in large part on how vegetation material occupies the space. For instance, clumped canopy has different interaction with light than canopy with homogeneous distribution of leaves. It is necessary to understand the space dependency or plant archi-

texture to interpret correctly spectral measurements. For instance, the ratio of light intercepted by the canopy, i.e. its radiative transfer, can be investigated to determine plant occupation in space.



**Figure 6:** (1) A *Gerbera* plant. (2) Spectral response of a *Gerbera* canopy under various water condition (from [90])

### 2.1.2 Leaf area index

When penetrating plant canopy, light energy is reduced due to its repeated interaction with the plant material. Studies showed that the relationship between the quantity of leaf material and radiative transfer follows the form of the Beer-Lambert equation of light extinction [91]. Beer-Lambert law states that there is a logarithmic dependence between the transmission  $T$ , of light through a turbid medium [92] (Figure 5-1):

$$T = \frac{I}{I_0} = e^{-\sigma \cdot \ell \cdot N}, \quad (2.1)$$

where  $I_0$  and  $I$  are the intensity (power per unit area) of the incident light radiation and the transmitted light radiation, respectively;  $\sigma$  is attenuation cross section;  $N$  is the concentration of attenuating medium (e.g., number of leaves per unit volume); and  $\ell$  is the distance the light travels through the material (i.e., the light path length). Monsi and Saeki [91] showed that equation 2.1 can be transformed into:

$$P_\theta = e^{-K_\theta \cdot \text{LAI}}, \quad (2.2)$$

where  $P_\theta$  is the probability of beam radiation penetrating a canopy without being captured at an incident light direction  $\theta$ ,  $K_\theta$  is the so-called extinction coefficient representing the ratio of light intercepted for a given light energy and at incident light direction  $\theta$ , and LAI is the Leaf Area Index [93] which is defined as the one-sided area of synthetic tissue per unit ground surface area ( $\text{m}^2$ ).

LAI is the principal variable of radiative transfer model representing the energy transfer in a canopy. Several direct and indirect measurement protocols have been set up to measure LAI [94, 95, 96, 93, 97]. The mains techniques to estimate LAI include (i) the direct methods with a planimeter and indirect methods with (ii) the hemispherical photography and (iii) TLS data,



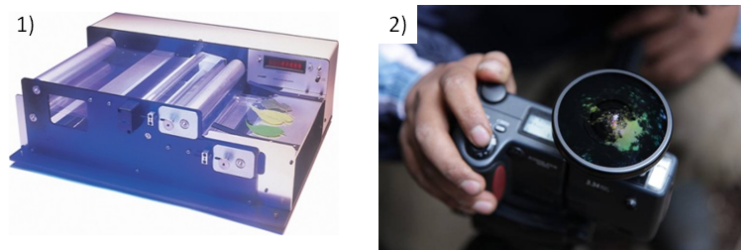
LAI measurements with a planimeter is the most direct method of LAI measurement for deciduous stands requiring intensive field work [93] (Figure 7-1). This type of measurement consists on gathering a partial amount of the vegetation leaves (either by destructive sampling or by non-harvesting litter traps during leaf-fall period) and to insert them into a planimeter device. Each leaf is placed on a conveyor and are lit in a chamber. Their shadow area is measured to give an estimation of the leaves area. The total area is correlated to the dry weight of the sampled leaves. Since the sampled area can be a fraction of the forest floor, the total stand LAI is estimated with the extrapolation of that fraction of the sampled stand towards the entire stand assuming a uniform distribution (or sufficient sampling). This method usually gives a sufficiently good estimation of the LAI to be considered as a reference value. However, this method could be time consuming, it shows underestimation in the case of curled leaves and it applies primarily for deciduous stands.

Hemispherical photograph is an indirect measurement method of LAI [95] (Figure 7-2). A photograph of the canopy is taken from below looking upward with a fish-eye lens. Separating the sky portion and the vegetation portion of the photograph is used to assess the gap fraction which is used to estimate the Plant Area Index (PAI). Method to segment woody element are used to estimate LAI from PAI [98]. LAI is often under-estimated when calculated from hemispherical photography because of the effects of vegetation clumping, structural complexity involving object occlusion and the difficulty to separate wood from foliage. Still, a clumping factor can be integrated in the computation to improve LAI estimation [94]. The use of hemispherical photograph to estimate LAI may be approximate but it has several advantages over the direct method: it is simple and fast and this type of measurement is broadly used.

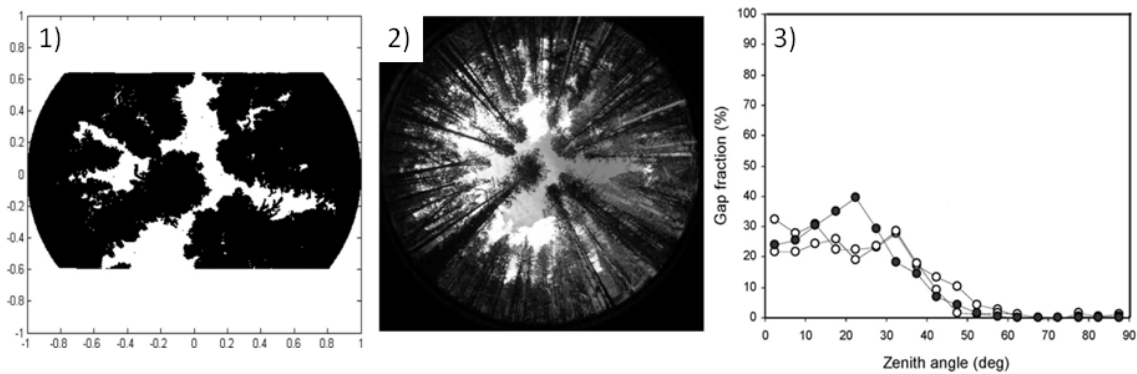
TLS is also used for indirect measurement of canopy gap fraction and LAI. Danson et al. [99] measured the gap fraction of a Pine forest canopy with a TLS Riegl LMZ210i (Figure 8-1) and a Nikon Coolpix 4500 hemispherical camera (Figure 8-2). They computed gap fraction within zenithal band of  $5^\circ$  from the two types of data and showed that results obtained with spherical photograph and TLS were similar (Figure 8-3). Moorthy et al. [15] used a TLS ILRIS-3D to compute gap fraction and LAI of an artificial Ficus tree that was progressively defoliated. They compared their results to: (1) manual measurement of the LAI, and (2) to the gap fraction deduced from a high resolution photograph (Nikon D50). They found good correlations between the traditional measurement method and the TLS measurements for LAI and gap fraction extraction. TLS measurements of LAI and gap fraction are close to measurement made with hemispherical photograph. Similarly to the hemispherical photograph measurement, TLS tends to provide underestimated values of LAI when compared to planimeter measurements. Yet hemispherical camera and TLS are way less tedious and time-consuming methods than the planimeter method.

Radiative transfer studies using LAI have been broadly used to study plant spectral response to stresses (e.g., [100]). Yet scientists are interested to get a more precise description of the plant canopy. This interest comes from a need for better accuracy of the LAI and the light interception process. LAI is dimensionless and it does not directly represent leaf distribution [94] (e.g. canopy clumping) and shape in the canopy [96]. Chen & Black [96] noticed that leaf inclination and shape

were parameters that were neglected in indirect estimation of LAI; Biswas [101] showed that it was necessary to include leaves inclination distribution in the light interception models; and Wang et al. [102] used several type of leaf angle distribution model to prove that leaf inclination has an impact for light interception when zenith angle increases. Still, it is possible to integrate leaf angle distribution in LAI computation [94]: in Equation 2.2, the extinction coefficient  $K_0$  can be replaced by  $G(\theta, \alpha)/\cos(\theta)$ , where  $G$  is the so-called G-function that corresponds to the fraction of foliage projected on the plane normal to the zenith direction.  $G(\theta, \alpha)$  depends on leaf-angle distribution  $\alpha$ . Yet LAI is not sufficient to describe plant geometry at a fine-scale (at the level of the leaves) for a good representation of plant architecture, and consequently, LAI is not adapted for extensive plant physiology study.



**Figure 7:** (1) Planimeter. (2) Hemispherical camera



**Figure 8:** (1) Hemispherical picture of the TLS; (2) Hemispherical photograph; and (3) Comparison of the gap fraction computed from the TLS data (solid circles) and the hemispherical camera (open circles) for each class of 5° zenithal angle (from [99]).

### 2.1.3 Concluding remarks

Many methods proved the effectiveness of considering the canopy as an entity to obtain information on its physiological state. For example spectrometric methods can detect stresses from the plant spectral response. Also, direct and indirect measurement methods allow operational estimate of the LAI, an important structural attribute used in most radiative transfer models of plant canopy interaction with incoming radiation.

Yet considering the canopy as a single entity under-represents important plant geometry attributes of importance, especially in the case of complex canopy. Oversimplification of canopy geometry undermine methods based on spectral response or radiative transfer models, greatly removing their

ability to assess fine-scale plant physiology if needed. For instance, water stress induces geometrical deformations of leaves that induce a variation of the global spectral response of the plant. This variation can compensate or amplify the initial spectral response of leaves and geometrical deformation of the canopy should be taken into account to obtain the signal variation associated to biochemical processes at leaf scale. In addition, the under-representation of the plant geometry in LAI makes the radiative transfer models almost useless when it is necessary to have a full understanding of the plant functioning and growth at finer scale in order to prune the tree. Descriptors at fine scale have been set up to allow better understanding of the plant mechanisms.

## **2.2 Leaves geometry distribution**

Fine scale plant geometry can be tackled by describing the geometry of its main components (branches and leaves) such as their position, density, angle shape, etc. Intuitively, we can expect that a fine scale representation of plant can lead to a better understanding of its physiology. In the following sections, we describe three types of distribution of plant geometry: (i) the Vertical Leaf Area Distribution (VLAD) and the Vertical Plant Area Distribution (VPAD), (ii) the Leaf Angle Distribution (LAnD), and (iii) the 3D voxelized space filled with Leaf Area Density (LAD).

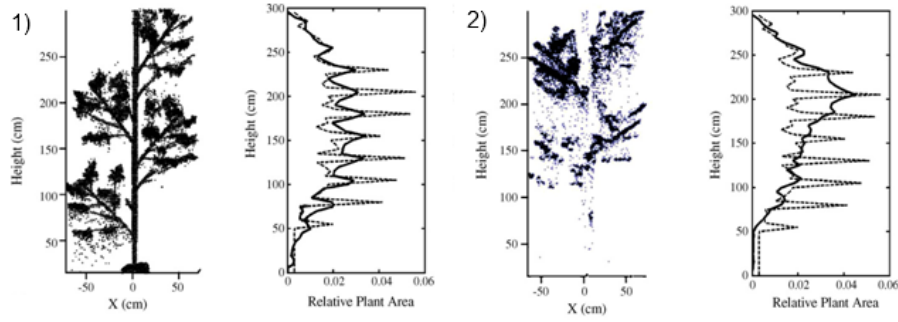
### **2.2.1 Vertical plant profile**

Another way to see plant interaction with sun light is to consider the following geometry: vertical distribution of photosynthetic elements in canopy induces subsequent variation in light transmittance along the plant profile [91]. The characterization of this profile is required for many radiative transfer models. Therefore the LAI per height bin, i.e. the VLAD, is a common structural canopy descriptor [103]. The planimeter method can be used to measure this vertical distribution: the canopy is split into height layer and litter-trap are placed at adequate place to gather leaves. Yet those measurements are tedious and time-consuming to collect.

VPAD is an extension of the VLAD descriptor to all the plant components (branches, fruits, etc.) that can be estimated with TLS measurements (Figure 9-1). Van der Zande et al. [30] acquired several scans on an artificial tree with a TLS placed at different position and with different viewing direction. They counted the number of points for every bin of chosen height to obtain a vertical plant profile. Because the geometry of their artificial tree, some portions of the leaves were occluded. They extended their VPAD with local LAI computed with a gap probability model to tackle this occlusion effects. In addition, they showed that the local density of points, which depends on the TLS position and direction, impacts on the VPAD: from a top-down view, VPAD is under-estimated in the bottom part of their artificial canopy, and conversely, it is under-estimated on the top with a bottom-up TLS viewing direction. Finally, they drew attention on impact of the outliers on VPAD computation and proposed a preliminary method for their correction.

Vertical distribution of plants elements have been shown suitable to study light penetration, especially to compare the shaded versus sunlit portion of the crown [1, 91]. Such as the LAI, VLAD

alone does not represent leaf shape and inclination. Yet it is possible to integrate in their computation leaf angle distribution.



**Figure 9:** *VPAD of an artificial tree (from [30]). Left column: side view of point cloud representing an artificial tree scan. Right column: VPAD derived from the point cloud (solid line) versus the reference measurements (dash lines). (1) scan from side view, (2) scan from top-bottom view.*

### 2.2.2 Leaf angle distribution (LAnD)

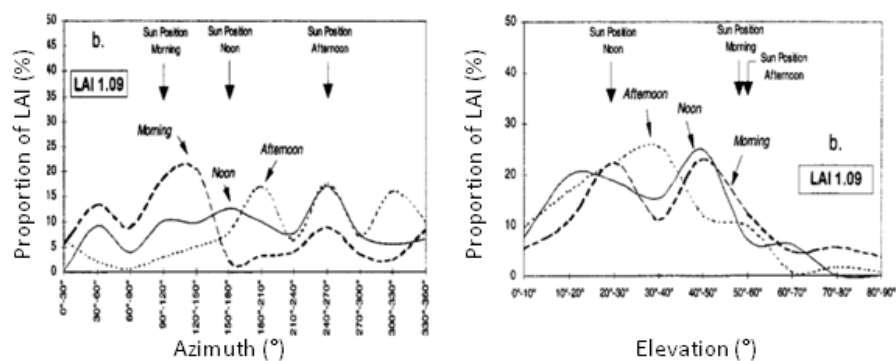
LAnD is a canopy descriptor that gives assumptions on leaves orientation using simple functions. A priori assumption on leaves inclination, such as planophile, erectophile or spherical distribution of leaves, is generally sufficient to carry out a light interception study [102]. However complex canopy require a detailed description of the LAnD. To do so, it is possible to measure the LAnD on a sub-sample of leaves canopy and extrapolate the results to the entire canopy.

LAnD can be measured manually with protractors [104] or with electromagnetic 3D digitizer [49, 105]. A 3D digitizer consists of [105]: an electronic system unit, one to four receivers to measure points, and a single transmitter. The transmitter generates a low-frequency magnetic field which induces current in coil included in the receiver. The intensity of the induced current depends on the location and orientation of the receiver in the active volume around the magnetic source. The Cartesian coordinates, i.e.  $x$ ,  $y$  and  $z$ , and the Euler orientation angles, i.e. azimuth, elevation and twist angles, of the receiver are determined and recorded. Those data correspond to the leaf position and inclination. Detailed measurements of LAnD with 3D digitizer made it possible to enhance leaf movement with sun with a precision of  $\pm 15^\circ$  for azimuth and  $\pm 5^\circ$  for elevation angle [105] (Figure 10). This device is well designed to obtain the LAnD for a small amount of leaves; carrying out a measurement campaign on an entire fruit tree canopy, such as a pear or an apple tree, becomes tedious and time-consuming though.

TLS can be used to estimate LAnD. For instance, Hosoi et al. [106], used a TLS based on trigonometry technology (Pulsec TDS-130L) to extract leaves inclination in order to get the LAnD of a Japanese Zelkova tree. Trigonometric TLS are tools designed to provide precise range values. They emit a scan line on a surface. A camera placed in a slightly different position records the line deformation to estimate range data. Those scanners have a very good precision at short range. Yet they are generally light sensitive and cannot measure surfaces at large distance. Hosoi et al. se-

lected 200 leaves manually within their TLS point cloud and made a least square regression plane fitting in order to get the leaf surface normal orientation relatively to the vertical. Because the high precision tools they used, they got realistic LAnD. Béland et al. [23] used the same method than Hosoi et al. with a time-of-flight TLS ILRIS-3D.

Even if a priori assumption on leaves inclination LAnD are sufficient for light interception study [102], it is necessary to carry measurements at leaf scale in order to assess more detailed distribution though, especially when more physiological process are studied, e.g., leaf movement [105]. Despite 3D digitizer is an adequate tool for inclination estimation of small canopy leaves, it cannot be used for large and dense canopies. Even if TLS were used to extract detailed LAnD [23], it is important to notice that those LAnD estimation with phase-shift and time-of-flight TLS has not been validated.



**Figure 10:** LAnD distribution (azimuth and elevation) at varying time in day (morning, noon, afternoon) (from [105]).

### 2.2.3 Voxelized space of leaf area density

Light interception by canopy can also be studied using ray tracing simulation which simulate the sun light rays and their reflection on objects [107]. Ray tracing models have been used for radiative transfer studies to understand, for instance, the light exchange between the leaves due to multiple-scattering [108], or the radiative transfer model sensitivity to geometrical variation of the canopy (e.g. leaf inclination [109]).

Ray tracing models need 3D representation of plants to simulate realistic light penetration in plants. The use of voxels, i.e. unit cube of the 3D space, is an interesting compromise between excessive 3D rendering and a very general 3D representation. Each voxel is associated with a value representing the plant geometric values in space. For instance, the LAD can be attributed to each voxels of a voxelized space [23]. LAD is a vegetation descriptor which provides the quantity of leaf area per volume [109], i.e. it is a spatial distribution of LAI. it is a spatial distribution of LAI. Point-quadrat measurements can also be used to build a 3D representation with voxelized LAD. This method consists on passing a long and thin needle with an orientation  $\theta$  through the vegetation (Figure 11-2) ) to count the number of plant material touched by the needle tip, i.e. it provides a contact frequency  $F_\theta$ . The measurement of this contact frequency is repeated along a specific grid,

i.e. the voxel grid. The output of this measurement is a 3D grid of voxels together with a contact frequency with vegetative materials from which the LAD per voxel  $v$  can be estimated with a direct radiation model [110]:

$$LAD(v) = \frac{K_\theta}{F_\theta(v)}, \quad (2.3)$$

with  $F_\theta$  the contact frequency measured at inclination  $\theta$  and  $K_\theta$  the light extinction coefficient. Because it is a manual measurement, point-quadrat method become rapidly tedious and time consuming.

As for LAI estimation, this LAD estimation does not necessarily take leaf inclination into account. Yet LAnD can be integrated in the LAD calculation if known [23]:

$$LAD(v) = \frac{F_\theta}{G(\theta, \theta_L)}, \quad (2.4)$$

where  $G$  is the so-called G-function derived from LAnD and that provides the mean projection of a unit foliage area of mean inclination  $\theta_L$  in a particular direction of interest  $\theta$ .

TLS data can be used to estimate LAD with equation 2.4. For instance, Béland et al. [23] scanned six Shea trees with a TLS ILRIS-3D to build a voxelized space with LAD. They estimated LAnD with Hosoi et al.'s method [106] and used this LAnD to compute LAD on voxels of 10, 30 and 50 cm from Equation 2.4 (see figure 11-3). In addition, they used distance-corrected intensity to segment the point cloud scan into woody and foliage parts to avoid woody sections in their LAD computation. Finally, they carried out several scans around the trees to limit occlusion effects due to foliage.

Signal occlusion while using TLS remains the main limiting factor for the construction of 3D voxelized space filled with LAD. Several studies [65, 111, 112] showed that occlusion leads to LAD under-estimated which is related to foliage clumping. They proposed two strategies to account for this occlusion for the estimation of LAD. As a first strategy, Béland et al. [23] used Côté et al.'s [22] method to measure the light availability within the canopy and to use a light transmission model to indirectly simulate the local LAD. The analysis of a VLAD estimation from the two techniques, i.e., with and without the completion of LAD with light model, showed that the use of light recording within the canopy complete properly their LAD extraction from TLS: TLS position relatively to the trees make the upper and inner part of the canopy less sampled and they were able to complete the missing data with local LAD estimation from light transmission. This completion is especially efficient for large canopy with lots of clumping. As a second strategy, Béland et al. [17] defined an optimal voxel size that should: (1) be small enough to take into account foliage clumping, (2) be large enough such that associated LAD is coherent with light extinction effect, and (3) such that occluded voxels are detectable. In this second study, they made TLS measurements on two different tree species (Oak and Shea) that have leaves with similar shape but of different size and found an optimal voxel size of 10 times the leaf size.

TLS scan segmentation of foliage versus woody parts is required to correctly build 3D voxelized space filled with only LAD. Béland et al. [17, 23] made the intensity segmentation approach

effective. Yet the intensity correction is a critical step and they suggested that this segmentation most likely always involve a level of misclassification between wood and leaves components [23].

Béland et al. chose to integrate LAnD derived from time-of-flight TLS measurement [23]. Yet their TLS is of lower resolution than TLS based on trigonometric used in [106] and their estimation of LAnD is consequently of lower precision. They did not proceed to their LAnD validation but suggested that the error induced by the point cloud quality is not large enough to affect their result. Still LAnD stays an important information allowing a link between plant structural attributes and their physiology.



**Figure 11:** (1) *Point-quadrat method for LAD measurements.* (2) *Voxel (color: LAD) extracted from TLS measurement (from [113]).*

## 2.2.4 Concluding remarks

Manual measurements of those distributions can be done on small canopy but they are tedious and time-consuming for large and complex canopies. Instead TLS devices are suitable for accurate and extended estimate of plant VLAD, LAnD and voxels representation of leaves density. Yet three main issues need to be taken into account for exact estimate of VLAD and LAD with TLS devices: (i) signal occlusion, (ii) segmentation of wood and foliage from the point cloud, and (iii) outliers.

- (i) Occlusion of the laser beam is the main factor reducing the accuracy of VLAD and LAD estimation from TLS devices. Even when several scans from different position are done to reduce occlusion from a more comprehensive sampling of the plant [23, 62], large portions of the canopy can be missing in the point cloud. Signal occlusion therefore leads to under-estimation. Fortunately some strategies exist to compensate this problem. For example, Côté et al. [22] used a light penetration model to complete the point cloud data where foliage clumping was too intense. Béland et al. [17] also suggested to use an optimal voxel size that accounts for leaf size and the clumping effect.
- (ii) Leaf material extraction is possible only if woody part are removed. TLS intensity showed great potential in woody material detection in the case of 3D voxelized space of LAD [17]. Still, the analysis of the TLS data should be improved in order to separate the foliage entirely from the woody section.

- (iii) Outlier points showed to affect the quality of the VPAD estimation [30]. Optimal scan configuration can be chosen to reduce their impact on the estimation. Still, outliers stays a side factors in VPAD and LAD estimation.

LAnD stays a difficult distribution to assess exhaustively. Even if it is a second factor for LAD computation, it is a great descriptor in order to study plant reaction to environment, such as leaves movement due to sun position [105] (Figure 11-4). Other TLS technologies have been used to extract correctly shapes and leaves orientation [20], yet time-of-flight and phase-shift TLS have not been validated for *in situ* measurement of LAnD.

Light interception studies with VLAD, LAD and LAnD are more detailed (e.g. [108, 102, 91]) and consequently more convenient than LAI to assess biotic and abiotic stresses with radiative transfer studies. Compared to models that consider plant canopies as a single entity, distributions of the various leaves geometries extend radiative transfer study to a way more accurate description of the plant relation with sunlight. In addition, researchers were able to study the influence of leaves orientation in the LAD computation [102], the nested radiosity within canopies[108], the up-scaling of tree transpiration [33], and the leaves orientation changes with sun position with exhaustive measurement of LAnD [105]. Other leaf geometry distribution such as the silhouette to area ratio (STAR) mentioned in Section 1.1, provided understandable indicator for light penetration to improve tree training and pruning techniques [2]. However, those leaf geometry distributions lack of details when it is necessary to understand the plant functioning, e.g., nutriments transport and their bio-availability to fruits. The knowledge of the plant structure, such as the connectivity of its organs and their position, is necessary.

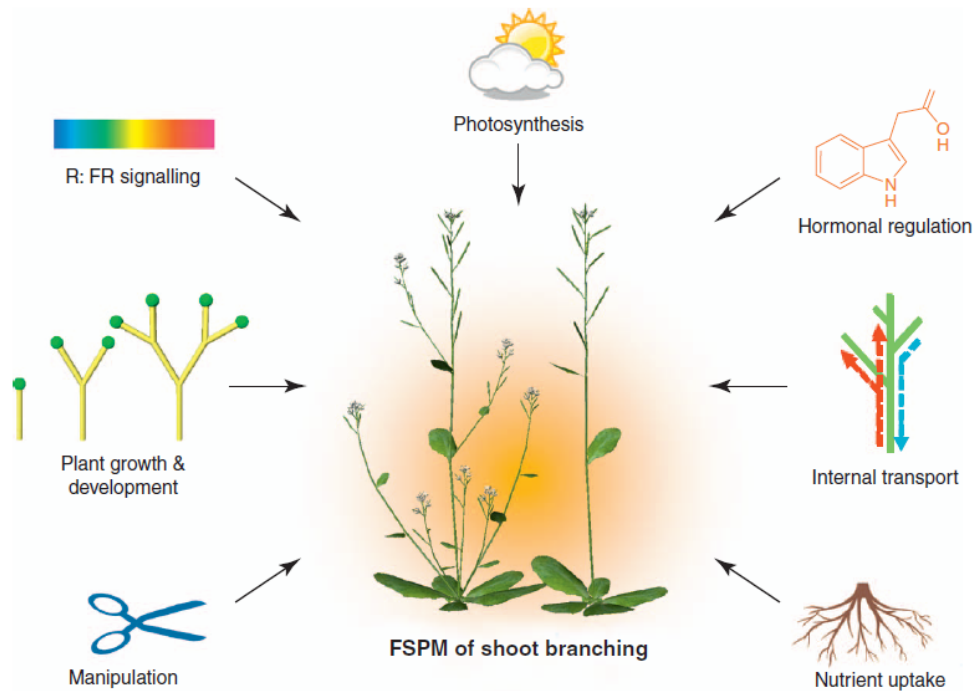
## 2.3 Virtual plants

Virtual plants are computer models of plants that recreate plants structure and which simulate their growth, functioning and interaction with its environment (Figure 12). The representation of plant architecture is one of the main aspects of a virtual plant. Plant architecture is defined by any individual description based on decomposition of the plant into components, specifying their biological type and/or their geometries (shape, location, orientation) and/or the way these components are physically related one with other, i.e., their topology [114].

Virtual plants are an essential component of virtual laboratories [115], which are computational platforms that allow the management of several models such as the virtual plants itself, its physiological mechanisms, weather simulation, etc. For instance, those models can be used to simulate nutriments and water transport in the plant [6], or the plant response to gravitational forces [9]. In addition, their visual representation makes the virtual plants usable for ray tracing simulation [10]. Generally, virtual plants representation uses the notions discussed in the two previous sections. Yet the framework of virtual plants use is different: they are used for studies on growth dynamic and plant physiology whereas descriptors such as the LAI and LAD rather enhance the plant occupation in space and the light penetration in its canopy. In the following sections, we will give a short



overview on the procedures required to produce virtual plants and providing a realistic estimate of plant architecture.



**Figure 12:** *Virtual plants in its virtual laboratory (FSPM: Functionnal Structural Plant Modeling). From [116]*

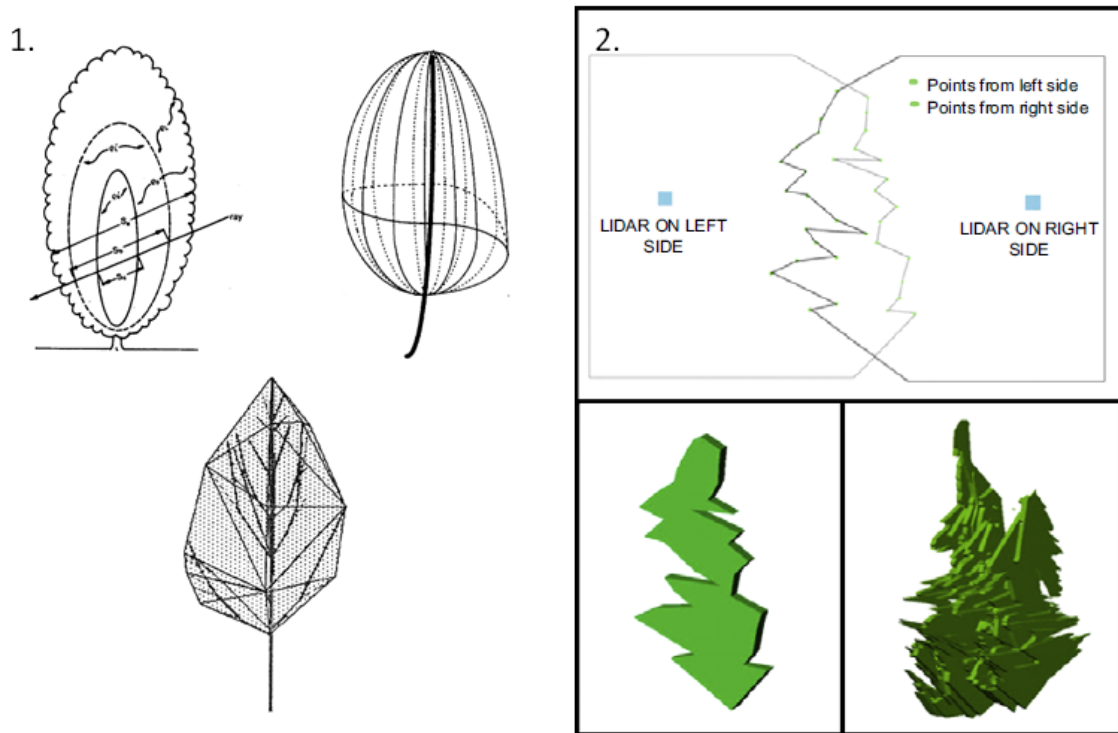
### 2.3.1 Canopy volume

Canopy volume is a global representation of plant [114] that considers the plant as a single entity, i.e., its crown shape. For instance, crown can be modeled with parametric shapes [117, 107] or with the convex hull of the tree branching system [118] (Figure 13-1).

Crown geometric representation has been used for radiative transfer [117] but also to define allometric relationship with the diameter at breast height [118]. An interesting application of canopy volume measurement is the optimization of pesticide application. Palacín et al. [4] proposed to use a MLS (polar LiDAR SICK LMS200 on a tractor) to estimate local canopy volume of orchard trees in order to adapt in real-time phytosanitary application. Their polar LiDAR provides canopy profile at a given tractor position. They estimated a volume section of the canopy with the traveling of their MLS and along the two sides of the canopy [32, 16] (Figure 13-2). Their results led to a correlation coefficient of 0.97 between the TLS estimated and the manually measured crown volume of Conference pear trees. In the same framework, Palleja et al. [119] showed that volume measurement with MLS are: (1) linearly dependent on speed error of the MLS, (2) little dependent on the LiDAR height, (3) highly sensitive to MLS distance to canopy error and to (4) LiDAR beam alignment with travel path. Real-time adaptation of phytosanitary application requires fast measurement tools. Manual measurements are not applicable to this purpose. Conversely, re-

mote measurement tools such as MLS can be considered as a potential tool to adapt phytosanitary application in function of the canopy volume and shape.

Volume shape measurement of canopy is linked to the 3D distribution variables described in the two last sections. Similarly, this descriptor is limited to a rough description of the plant and cannot help understanding fine level plant physiology. Still, it is possible to investigate how the crown is composed through the size and number of its components instead of representing it as a single component. Virtual plants need that fine scale description with the distribution of components at organ scale and with their topology and geometry.



**Figure 13:** (1) *Parametric and hull-based canopy model (from [114]).* (2) *Measurement of canopy volume with MLS (from [16]).*

### 2.3.2 Plant architecture and topology

Plant architecture topology refers to the representation of the connectedness of the branching system. The measurement of plant architecture requires rigorous methods to avoid missed objects and repetition of branches measurement [120]. In general, those measurements start from the tree root, and goes from nodes to nodes to reach each of the branching point and with the following protocol:

1. The inter-nodes between the root and the first branch is measured.
2. Then the inter-nodes between the branching point of this first branch and a first child branch is measured.
3. Similarly, this second branch is measured along consecutive inter-nodes and branching points.

4. Once every child branches of the first branch are measured, the second inter-nodes set of the trunk, i.e., defined by its first and second branch, is measured.
5. Finally, the measurement process is continued on the second branch of the trunk.

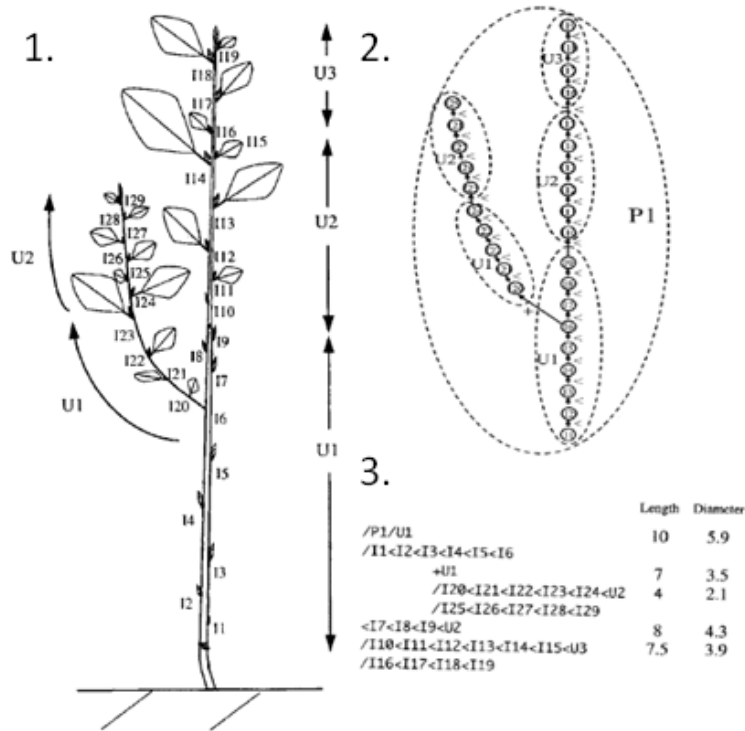
Several type of branching system encoding can be defined with this type of measurement protocol [114]. For instance, each node can be represented by a character and the entire tree by a word that is the concatenation of the characters. The connectedness of two nodes on the same branch is represented by the concatenation of the two corresponding characters. The childhood of a branch is represented with an opening and closing bracket containing the word representing the branch and its children. Most of those encoding lead to a graph representations where tree branching points are represented by the graph nodes and their direct connection by the graph edges (Figure 14).

Geometrical information can be attached to the encoding of a plant architecture. For instance, inter-node length and branches inclination can be measured manually with a ruler and a protractor [121]. Yet those measurements are tedious and time-consuming because the complexity of the object. TLS have been showed to be more adequate for those architecture measurements [122, 123, 124, 125, 22]. For instance, Preuksarkarn [122] used two data set produced by a TLS Leica Geosystems HDS series on a Cherry and Lime tree in order to extract their architectures topology and geometry. They used a skeleton model to define the tree architecture. As for manual measurement, the construction was propagated from the root and along the branching system of the plant. Point clouds cluster were used as attractor: new skeleton section was built from the local point cloud and progress towards the point cloud cluster with the largest density. In the case of multiple branching, the point cloud has several clusters and each branch can be detected with fine tuning of the model parameters and several skeleton sections are produced to represent the corresponding branches junction. Finally, skeleton representing the scanned tree was encoded and interpreted as a graph. Branches dimensions were computed from the point cloud and associated with the skeleton sections. Preuksarkarn managed to produce realistic plant architecture with this method. Yet those type of architecture computations from TLS data should be augmented to take into account occlusion [122, 125], branches junction geometry [122, 123], and uncertainties of the skeleton construction inherent of the complexity of the object [122].

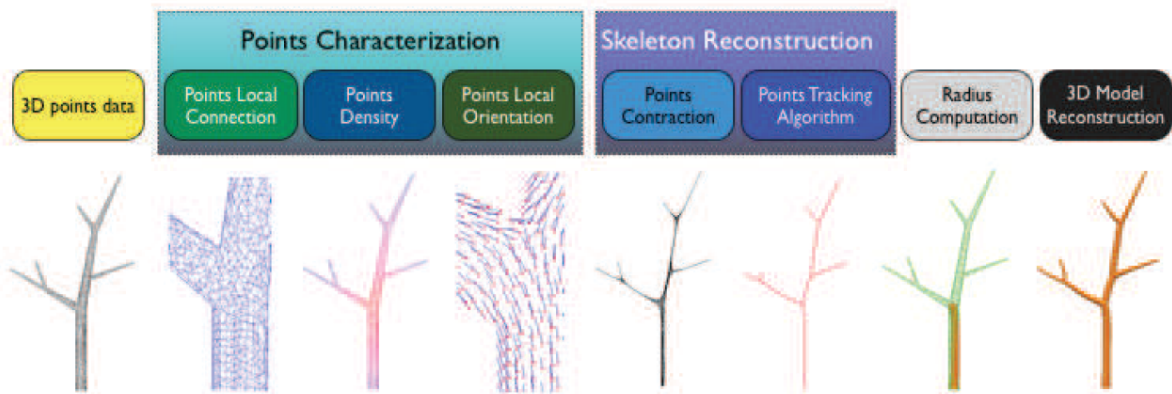
Pattern repetitions in the plant architecture are observable with the analysis of its encoding. This self-similarity of plants have been the basis of L-system [126]. L-system are formal grammar, i.e., a set of transforming rule that are applied on a characters chain. As for the representation of virtual architecture, L-system characters represent the components of a virtual plants. An initial character chain, called axiom, represent the initial state of the plant. The grammar rule is applied on this chain and to make the L-system simulating the plants growth [8]. Plants are not necessarily an automatic repetition of a pattern though. L-system are adequate to represent plants growth in optimal condition, but it lacks of representing external events (diseases, pruning, competition). Still plants keep local similarity and patterns can be observed and be factorized [127]. Moreover, the differences between measured architecture and a modeled architecture, e.g., a L-system, can

be studied with proper graph theory [128, 122]. Multi-scale tree graph (or MTG) are composite graph that provides plants architecture description at different scales [114].

Plant architecture topology is an important information in biological studies. It has been used to study nutriment transport [6] and gravity effect on the plant shape [9]. Moreover this architecture representation can be augmented with organ positions on the branches: those positions can be either measured [18], or taken into account in a L-system development with proper encoding [129], or with the integration of statistics on those organs apparition [130].



**Figure 14:** (1) Plant architecture measurement. (2) Multi-scale tree graphic. (3) Encoding of the plant architecture.



**Figure 15:** Tree architecture reconstruction from TLS data (from [122])

### 2.3.3 Leaf measurements

3D shape measurements of organs are becoming more common since the spread of 3D measurement tools such as stereo camera and LiDAR devices. Fruits, flowers, branches and leaves can be rapidly measured, but with a quality depending on the measurement configuration. In the following, we will investigate those measurements configuration, results and issues, in the case of leaves measurements.

Leaves can be measured either when picked [71, 131, 132], or included in a canopy that can be simple, i.e., made up of a single stem [133, 134, 135, 136], or complex [137, 138, 20]. In parallel, several types of measurements tools can be used: flatbed scanner [139, 140], digitizer [131, 132], stereoscopic photography [136, 134, 133, 137, 138], TLS based on trigonometry technology [71, 20] or phase-shift and time-of-flight TLS [18, 47].

The measurement set up (scene complexity and measurement devices) affects the type of analysis and issues. In general, once the 3D information of the leaves are available, e.g. when they are segmented from a point cloud, either virtual leaf surfaces is fitted [131, 132], or a mesh is generated [136, 20].

Picked leaf measurements are generally done with a flatbed scanner [139, 140, 141] (Figure 16-1). Developed methods to extract leaves geometry depends on the shape type of the leaves (e.g., number of lobes, simple shape versus with compounds) and the produced leaf measurements are used to defined statistical distribution of leaf area and dimension (width, length). In most cases, validation of those outputs is good: for instance, Bylesjö et al. [140] obtained a correlation coefficient larger than 0.99 with the measurement of 500 *Populus tremula* leaves. Yet flatbed scanner measurement is not adapted to reconstruct 3D shape of leaves, especially if those latest have complex shape. Some studies used TLS to investigate their potential of 3D shape reconstruction of picked leaves [47, 131, 71, 42] (Figure 16-2) and proved that leaves inclination and dimensions can be well recovered. For instance, Chambelland et al. [18] used TLS based on trigonometry (Konica Minolta VIVID 910 NCLSD) to measure picked young beech flat leaves. Their picked leaves were placed perpendicularly to the TLS laser beam and at a short distance from its aperture. Their reconstruction allowed them to prove leaf shape variation as a function of light availability.

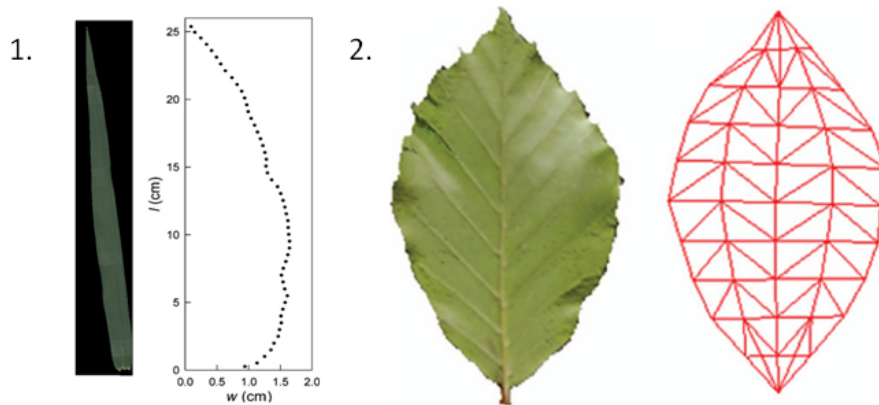
Because their portability, TLS can be used for non-picked leaf geometry extraction. Yet leaves segmentation is a main pre-process for measurements of leaves when lying within a canopy. Leaves segmentation can either require an a priori number of leaves [136, 142] or carried out with user interaction [138, 20]. Occlusion is an additional issue as there is no control on the leaf position and inclination [19]: it leads to an incomplete point cloud that affects the quality of the estimation of leaves geometry. In other words, canopy complexity plays an important role in the leaves measurement.

If the leaves are in a simple canopy, e.g. plant composed of a single stem and of about ten leaves, it is possible to place the plant in a pot that is on a rotating platform and to use stereoscopic photography [133, 134, 135, 136] (Figure 17). In this case, sampling is exhaustive, occlusion is

reduced and leaf segmentation can be handled because of the small amount of leaves. Validation of the leaves dimensions is generally good. For instance, Paproki et al. [136] obtained a correlation coefficient larger than 0.88 for the length and width extraction of a young *Gossypium hirsutum*, Santos et al. [133] get a mean absolute percent error of 4.3% on mint leaves.

In the case of complex and large canopy, it is generally difficult to put the plant on a rotating platform and thus to control the amount of point acquisition. Leaf contact, distance or occlusion can lead to under-estimation of foliage components [19, 134]. In general, correct leaf segmentation requires user intervention [20, 138]. In the case of single stem, leaf area, dimension and inclination estimation are good if well segmented [20]. Estimations can hardly be validated on the entire canopy though. To get correct leaves representations (e.g. low noise, no outliers), leaves geometry extraction from complex canopy are either computed from stereoscopic photography [138] or from TLS based on trigonometry [20]. Phase-shift and time-of-flight measurement of leaves geometry in complex canopy are missing in the literature.

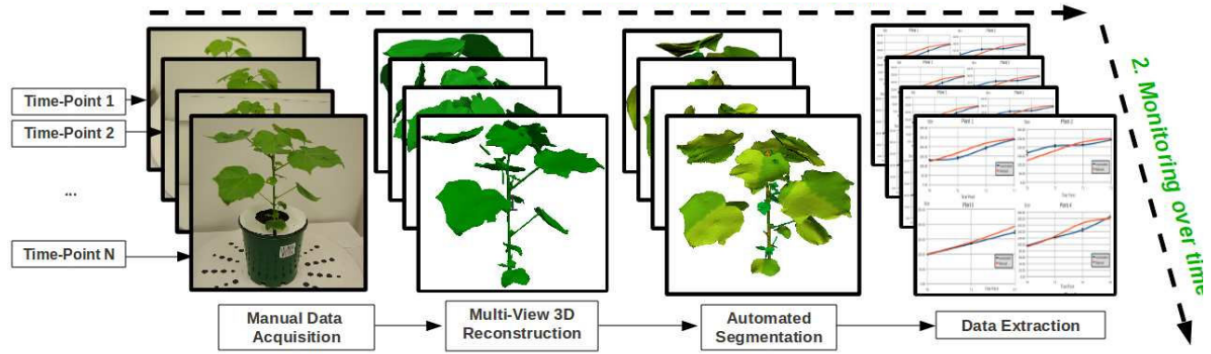
Stereoscopic photography and TLS have been showed to be efficient in order to extract either picked or non-picked leaves geometry. However segmentation and occlusion are major issues in the case of non-picked leaves. Generally, leaf segmentation needs a priori knowledge (number of leaves, user directive). Still, those remote measurement tools are adapted to measure leaves geometry, especially for high throughput measurement of simple canopies [135]. Because their conveniences, phase-shift and time-of-flight TLS are more suitable for outdoor measurements compared to stereographic photography and TLS based on trigonometry. Yet they have not been used to extract leaf geometry in complex and *in situ* canopy.



**Figure 16:** (1) Flatbed scan of a leaves and the leaves shape extraction (from [139]). (2) TLS scan and reconstructed shape of a picked leaf (from [18]).

### 2.3.4 Concluding remarks

Virtual plants are models that represent plant system at a given scale and that aim to study plant physiology. Virtual plants extend the descriptor mentioned in Sections 2.1 and 2.2 to finer level geometry descriptors of plants. In addition to their application to radiative transfer study [117], virtual plants allow study on plant functioning and interaction with its environment, such as the



**Figure 17:** Segmentation pipeline of leaves from stereoscopic photography of a plant placed on a rotating platform (from [136]). Application to phenotyping.

study of nutriment transport in plant [6] or the gravity impact on the architecture [9]. Another interesting and potential application of virtual plants is the real-time adaption of phytosanitary application with MLS measurements. Still we have sought to look for plant description at organ scale in order to make an extensive study of its physiology.

Organ geometry and the plant architecture acquisition can lead to a good description of plants. They allow horticulturists to study their plant with the type of method proposed by Willaume et al. [2] in order to improve orchards yields. In addition, they have the potential to make scientists understanding plant diseases and stresses propagation and effect on organs geometry.

TLS showed great potential for architecture extraction despite issues caused by occlusion and complexity of branching. TLS have also been showed to be adapted for picked leaves geometry extraction. In the case of unpicked leaves, geometry extraction from other type of 3D scan (e.g., stereoscopic photography, trigonometry-based TLS) provides good results but the developed segmentation methods, which are a main step for leaves extraction from point cloud, need a priori knowledge or user intervention. Phase-shift and time-of-flight TLS have not been used to extract geometry of leaves in the case of complex canopy yet. In the next section we will investigate the reason why those TLS have not been used yet.

### 3 TLS quality factors for pear tree leaves measurements

Plant geometry is important information useful for biological and agronomic studies. We saw that depending on the scale of the study, either a global structural variable such as the LAI, or complementary canopy descriptors such as LAnD and LAD are necessary. Analysis of TLS point cloud allow estimating 3D variables at global and fine scale more accurately and extensively as they provide similar or better results than traditional measurements. Signal occlusion however is the stronger limitations for improving results accuracy. Yet the possibility to estimate structural variables at a fine resolution brings new opportunities in the understanding of the plants physiology and consequently for their management (tree training, disease detection). Estimation of precise geometrical plant descriptors are necessary but not always easily measurable for complex canopy.



Fruit tree orchards are composed of several rows of tree spaced of few meters when their training uses an artificial structures. TLS are generally placed between two consecutive rows (i.e., at few decimeters from the canopy) in order to scan them. Closest parts of the canopy ( $< 1.50$  meter) are magnified in the TLS photograph (Figure 18-a), and the farther parts of the canopy ( $> 1.50$  meter) are scanned in a tighter perspective. This tighter view favors situations of canopy self-occlusion (Figure 18-f) and decreases point cloud density due to distance (Figure 18-b). In comparison, a scan set up with a TLS placed at a few meters from the vegetation will produce a more homogeneous density scan of the tree. In general, the configuration of tree orchards makes it difficult to obtain homogeneous scan density.

Pear tree leaves have complex shape and their reflectance depend on their maturing stage. Leaves are generally small (few centimeters) and numerous (few hundreds). The number of leaf edge in the scan increases the occurrence of outliers (Figure 18-d). Reflectance and TLS beam incidence angle have a substantial impact on the point cloud quality. In Figure 18-c and -e, those impact are illustrated with simple objects, i.e., with a sphere and radiometric targets, respectively.

In conclusion, the scans of orchard trees are of heterogeneous density and quality that leads to the presence of outlier points. As we will see, those outlier points mislead surface reconstruction. Outlier deletion methods have been proposed to process TLS point cloud (see Appendix I), but because the size of canopy leaves, we can expect that outlier deletion will not be adequate for plant geometry extraction at organ scale. In this third section, we will make a short investigation on the TLS outliers and leaves scan ROP (see Chapter 1, Section 2.5) for pear trees scanned at range between one to five meters. That will illustrate impact of outlier points on plant organ geometry extraction in addition of the impact of their deletion.

## **3.1 Material and methods**

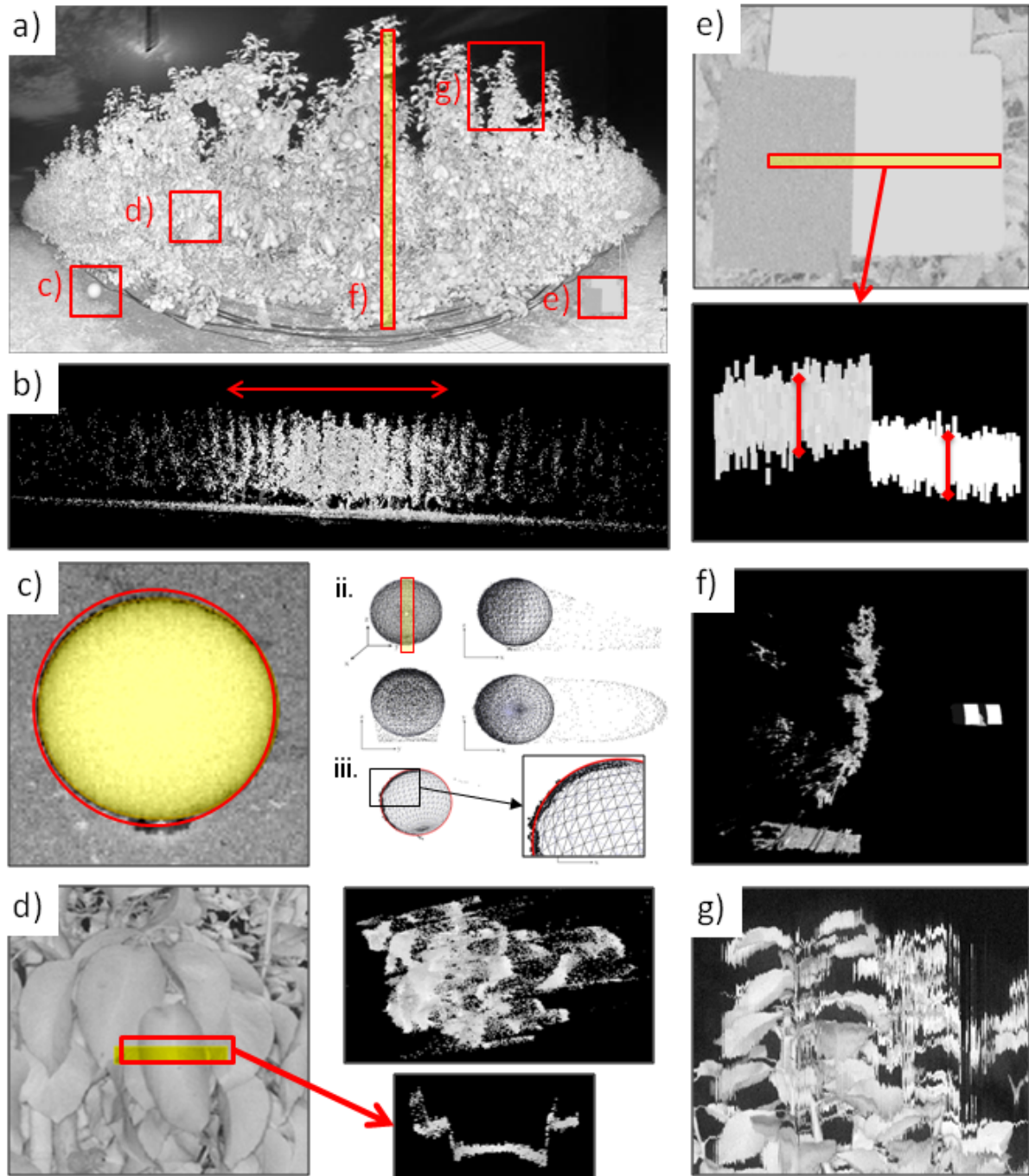
### **3.1.1 Pear tree orchards and leaves**

A row of Conference pear tree orchards have been scanned in August 20th 2010, in Bierbeek, Belgium. This orchard is composed of row of trees of 2.50-3 m high and with a distance of 3.4 m from each other. The trees were trained in a V-shaped system (see Section 1.1). Because summer time, several long branching shoot were presents at the bottom and the top of the canopy in addition to the principal branches, leaves were mature and the fruits were at half of their growth.

### **3.1.2 TLS**

We scanned the trees with a hemispherical TLS (FARO LS880) that uses phase-shift technology. It has a field of view of  $320^\circ \times 360^\circ$ , a beam aperture of 3 mm and a beam divergence of 0.24 mrad (0.014°). The sensor field of view is of 3 mrad (0.17°) and the zenithal and azimuthal resolutions are both of 0.31 mrad (0.018°). This device has a measurement range of 0.6 to 76 m with a distance error of  $\pm 3$  mm at 25 m and an accuracy of 2.6 mm (resp. 5.2 mm) for material with 90% reflectance (resp. 10%) at 10 m. This TLS provided both distance and intensity measurement. The





**Figure 18:** (a) Scan view of a pear tree orchard row. (b) Side view of the row point cloud. (c) Registration sphere: i. Sphere selection; ii. Side, front, and top views of the point cloud and the sphere model (mesh); iii. Section. (d) Canopy point cloud and outliers. Zoom on a leaf edge. (e) Radiometric target (22% and 99% reflectance) and point cloud section. (f) Canopy section. (g) Wind effect.

scanner was placed in the middle of the orchard inter-row. The closest leaves were at a distance of approximately 1m and it was possible to visually recognize them up to a distance of approximately 10m. The measurements were carried out during a windless day to avoid fuzzy point cloud (Figure 18-g).

### 3.1.3 Leaves

Leaves had an average length of 6 cm along the principal vein axis and an half-width of 2.5 cm (Figure 19-1). As we can see on Figure 19-2, the footprint diameter covered almost entirely the half leaves portions and thus TLS has a higher chance to record outlier points (see Chapter 1, Section 2.3).

Nine leaves of the TLS point cloud were selected manually with the software FARO Scene® (Figure 19-3). Those leaves were at an approximate distance of 1.5, 3 and 5 meters from the TLS aperture and had a length of approximately 9 cm. In Figure 19-4, the point cloud representing one of the nine leaves is represented. Outliers were present along its edge (in red).

The point cloud was stored in a .xyz file for each of the nine leaves selected. Each of those point clouds had outliers, and the number of outliers increased with the distance to the scanner. We used the software MeshLab to erase manually the outliers and produce a second .xyz file containing a point cloud free of outliers. We generated a rough and a fine reconstruction of those leaf surfaces with a Marching Cube algorithm [143] and for both of the point cloud, i.e. with and without outliers. In addition, the number of points for the original point cloud and for the one without outliers, were computed to generate the ROP:

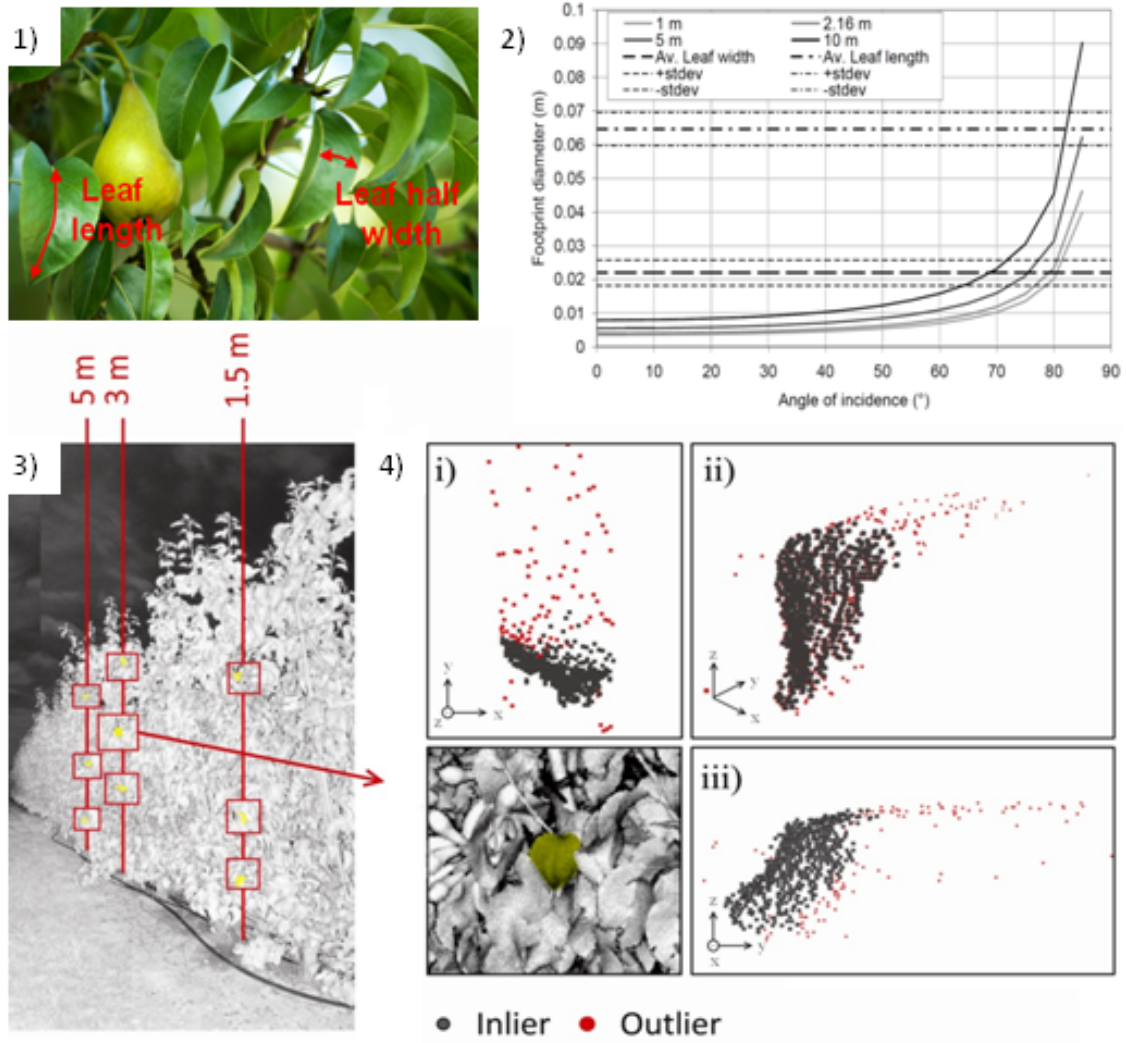
$$ROP = \frac{\#outliers}{\#points}. \quad (3.1)$$

Finally, a small sample of the point cloud is extracted from each leaves point cloud to compute the distance precision and the noise/signal ratio (denoted RNS), defined as the ratio between the computed precision and the size of the leaves, i.e.:

$$RNS = \frac{precision}{leaf\ size}. \quad (3.2)$$

## 3.2 Results and discussion

Table 1 shows the quality factor of the leaves point cloud at 1.5, 3 and 9 m (precision, RNS, number of points, number of outliers and ROP). Precision varies between 5.5 and 6.7 mm, with corresponding RNS value of 5% and 8%, respectively. The number of points per leaves decreases with distance. Consequently, ROP increases with distance from 8% at 1.5 m to 33% at 5 m. Those figures show that precision is not the main issue for leaves of this size (~ 9 cm length). Yet in the case of smaller leaves, RNS can rapidly increase. ROP is shown to be more problematic though, especially for the furthest leaves. Similarly than RNS, ROP increase when leaf size decreases. The nine leaves selected were larger than the average (~ 6 cm length) thus we can expect more



**Figure 19:** (1) Leaf length and half width. (2) Beam footprint maximal diameter  $\Delta d_{max}$  in function of the incidence angle for different distance (1, 2.16, 5 and 10 m). Dotted lines: average with standard deviation of mature pear tree leaf length and half width. (3) Selection of nine leaves at distance of approximately 1.5, 3 and 5 meters from the TLS aperture. (4) Leaf point cloud with inliers (gray) and outliers (red): (i) top view; (ii) side view; and (iii) lateral view.

problematic cases for the quality factors of the point cloud representing the other pear tree leaves. In other words, outlier points process should rather make their correction than their deletion in order to keep a maximum information on leaves geometry.

Figure 20 shows three leaves point cloud (at 1.5, 3 and 5 m), in addition to their rough and fine mesh reconstruction. In Figure 20-1, the outliers have not been removed. In this figure, we see that there are points along leaves edge which have no real impact on the leaf point cloud shape (boxed in blue) whereas other ones have a great impact on the shape of their mesh reconstruction (boxed in red). We call the first ones the subtle outliers and the second ones the true outliers. In Figure 20-2, the true outliers have been manually deleted. The constructed meshes were more realistic especially with fine parameters. As it has been discussed in Chapter 1, Section 2.3, the detection of outliers is difficult when the incidence angle between the TLS beam and the surface is large.

The selection of true versus subtle outlier points in Figure 20 illustrates this case.

We have proved that ROP is the main issue for leaves reconstruction especially for small and/or far leaves. It might also bring issues for their segmentation. Subtle and true outliers deletion for close leaves can decrease a little the shape reconstruction quality for close and large leaves. It would make their reconstruction significantly wrong for small and/or far leaves though. In addition, the selection of subtle versus true can be hardly implemented without any other knowledge or user intervention. In other words, the safer strategy to take outliers into account would be rather to correct them.

Leaves length: $\sim 9$ cm	1.5 m	3 m	5 m
Precision (mm)	5.5	6.7	5.7
RNS	5%	8%	5%
Number of points	5560	1260	350
Number of outliers	760	300	110
ROP	8%	18%	33%

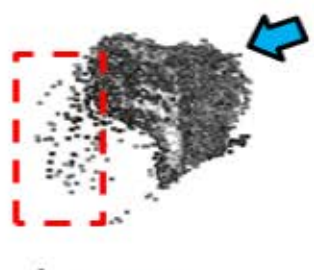
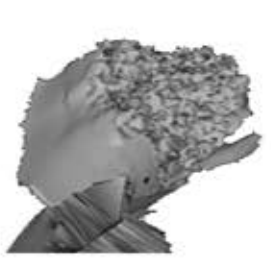
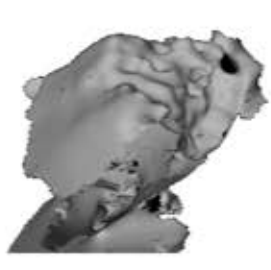
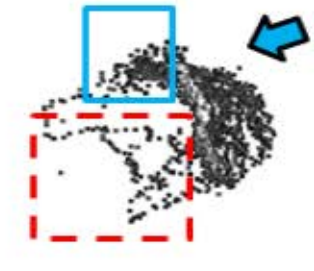
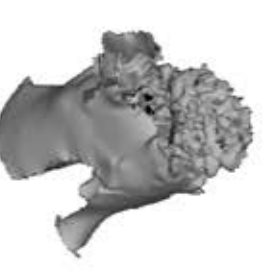
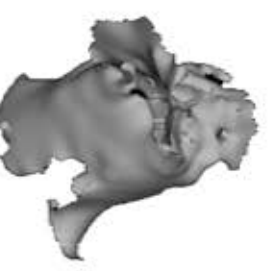
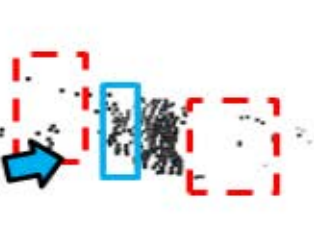
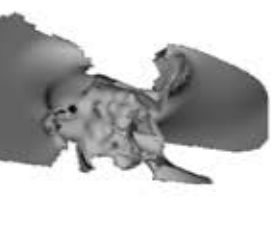

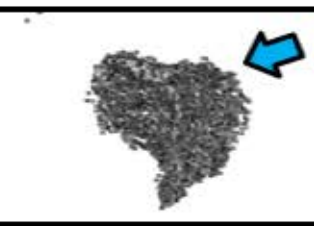
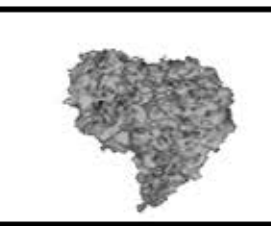
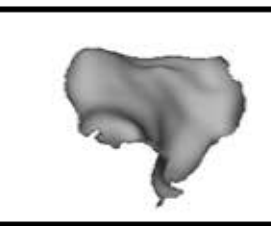


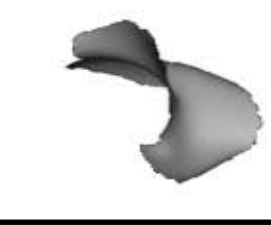



**Table 1:** *Quality factors of nine leaves point cloud. Each value represents the average value for three leaves at 1.5, 3 and 5 meters.*

## 4 Conclusion

Physiological study of plant requires geometric models of plant. Those models should provide organ and architecture description in order to study the plant physiology in details, such as the training and pruning impact on fruit production, or the biotic and abiotic stresses effects and spread on organs. Until today, several descriptors of plant canopy have been proposed. Those models can be expressed either at the scale of a single plant, with distributive function or at a fine scale compatible with the leaves compatible to create virtual plants. We have seen that single plant and distributive models are generally not adequate for such detailed study even if they fit to more global study such as a radiative transfer study [91].

TLS have been showed to be adequate for most of those descriptors extraction. Occlusion is the main issue in most cases. Yet scientists proposed smart strategies to complete TLS scans, such as the integration of radiometric measurement within canopy clusters [23]. Leaves geometry extraction has been done with 3D scanner and stereoscopic photography on picked leaves (e.g., [18]) but also on unpicked leaves within simple canopy (e.g., [134]). In the case of complex canopy, phase-shift and time-of-flight TLS require more work to improve method development.

In Section 3, we have investigated the quality factors of the point cloud representing nine large leaves. ROP has been shown to be the main issue for their reconstruction and segmentation. ROP increased with both increasing distance and decreasing leaf size. It is not possible to delete outliers in order to reconstruct leaves and their selection is complicated. Correction of outlier points is a more adapted strategy. Yet the procedures found in the literature to deal with outliers from a point

1)	Point cloud	Rough reconstruction	Fine reconstruction
@1.5m			
@3m			
@5m			
2)	Point cloud	Rough reconstruction	Fine reconstruction
@1.5m			
@3m			
@5m			

**Figure 20:** Point cloud, rough reconstruction, and fine reconstruction of three leaves at 1.5 m, 3 m, and 5 m: (1) with outliers, and (2) without true outliers. Blue box: subtle outliers. Red dashed box: true outliers. Blue arrow: TLS beam direction.

cloud involve primarily point suppression. In Chapter 1, we have seen that intensity can be used in order to detect outlier points. This thesis investigated in the next chapters how intensity values from TLS returns can be used to develop a correction method for outlier points.

## **Part II**

### **Algorithm: Shape-From-Shading propagation along isophote region for TLS data**





# Chapter 3

## Shape-From-Shading: state-of-art

In photographic processes, light interacts with objects placed in a scene before it is captured by a light-sensitive surface (a sensor, a photographic film, etc.). The various interactions between light and objects create a gradient of intensities within the photograph based on the object's material, orientations and shapes. Those intensities are represented by an intensity gradient on the photograph which gives us the perception of a shape [144]. As a result, to each 3D shape in the scene will correspond an intensity pattern in the photograph. Conversely, one can ask whether it is possible to reconstruct the 3D shape corresponding to a given 2D intensity picture and how. This issue is known as the Shape-From-Shading (SFS) problem and, beginning in the 50's, several mathematical techniques have been developed to address this question.

The first attempts of SFS reconstruction have been done within the framework of planetary topography. In 1951, the Dutch astronomer Van Diggelen tried to retrieve the height of the Moon's hills near the terminator (i.e. the limit between shadowed and lit area) from photographs [145]. His method integrated height variation with recorded intensity, taking into account the spherical shape of the Moon. Van Diggelen's method was formalized and generalized to the complete photo of the Moon by Rindfleisch in 1965 [146]. Rindfleisch gave a differential expression of the height variation as a function of the intensity variation and along a given path on the picture.

In 1970, Horn gave a general method for SFS reconstruction [147]. He considered a scene with a given light source direction, a camera position, and he supposed that the object's optical properties were known at every point. He remarked that singular points (i.e. with maximal intensity) corresponded to surface normal aligned with light source direction. Solving a system of five equations, he was able to reconstruct the surface shape by propagating the reconstruction from the normal of those singular points along characteristic curves.

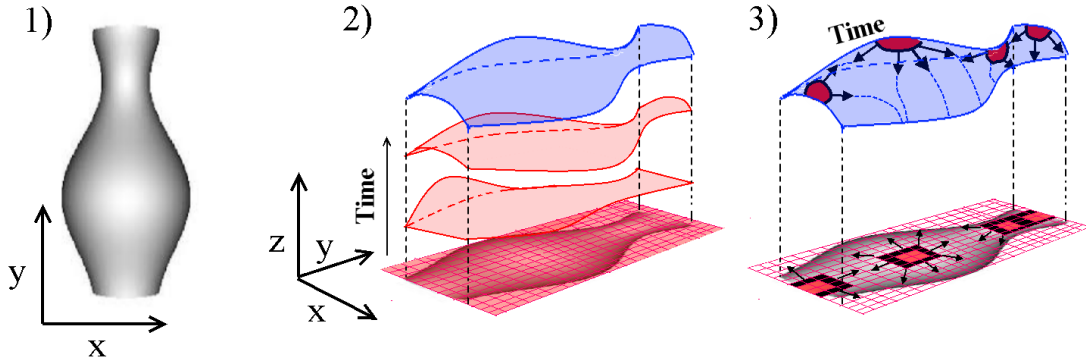
Since Horn's publication, the SFS theory became part of computer vision field and started to be applied: (i) in imagery (scanning electron microscope imagery [148], endoscopic and intraoral imagery [149, 150, 151, 152]); (ii) for 3D reconstruction improvement (differential light absorption technique improvement [153] and stereoscopy [154]); and (iii) to photometric stereo [155], augmented reality [156] and radar clinometry [157]. At the same time, scientists became interested by the proof of existence and uniqueness of the SFS issue [158, 159, 160, 161, 162]. Since the

reference book of Horn and Brook has been published in 1989 [163], two kinds of techniques have clearly appeared: (i) the global (GLOB-SFS) and (ii) the propagation methods (PROP-SFS).

GLOB-SFS methods use the surface photograph as a matrix of intensity values (the pixels) and aims to recover by a global analysis the height corresponding to those pixels. Some initial 3D values of the matrix are provided (boundary conditions, initial surface) in addition to assumptions on the height function (continuity, parametric). Pixels height is recovered through an iterative optimization, i.e. a global criterion is minimized (Figure 1-2).

As a generalization of Van Diggelen's method, the PROP-SFS methods propagate the surface reconstruction from an initial 3D region (points, curves) and along specific propagation curves. Intensity variation is integrated along those curves to compute neighboring regions (Figure 1-3).

In this chapter we will review the physical concepts that are used in the SFS framework to model material appearance and object picturing when the camera is aligned with the direction of the light source (i.e. when the camera is in the hotspot direction). We will see that the intensity is directly related to the incident light angle. We will introduce the reader with the basic conclusions provided by the proofs of existence and uniqueness of SFS reconstruction and give him a short introduction to traditional GLOB-SFS and PROP-SFS methods. Finally, we will focus on the type of SFS method that we will develop for the 3D reconstruction of surfaces from LiDAR intensity and point cloud.



**Figure 1:** *GLOB-SFS vs PROP-SFS. (1) We want to reconstruct the vase from its picture. (2) GLOB-SFS: each pixel is processed at the same time in a matrix. The reconstructed surface (blue) is the result of a converging process (red). (3) PROP-SFS: some areas, i.e. the propagation seeds, are initiated with 3D data (in red). The reconstruction is propagated (black arrows) along specific curves (blue dashed lines).*

## 1 Image intensities modeling

### 1.1 Scene geometry

Even if SFS methods have been developed for surfaces containing sharp edges [164], such as cubes or pyramids, common SFS methods consider a single object with a smooth surface  $\mathcal{S}$  of  $\mathbb{R}^3$ , and

$(e_1, e_2, e_3)$  the Cartesian coordinate system of  $\mathbb{R}^3$  (figure 2). Let us introduce the basic notation used in this chapter and in the rest of this thesis.

Let  $\Omega$  be an open and connected subset of  $\mathbb{R}^2$  and the surface  $\mathcal{S}$  be defined by its height function on  $\Omega$ :

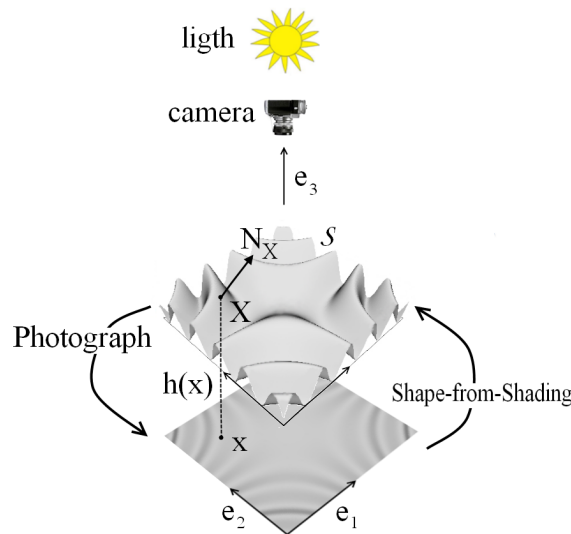
$$\begin{aligned} h : \Omega &\rightarrow \mathbb{R} \\ x &\mapsto h(x). \end{aligned} \quad (1.1)$$

Let  $x := (x_1, x_2)$  be a point of  $\Omega$ . We denote by  $X$  the point on  $\mathcal{S}$  which corresponds to  $x$  and parametrically defined by:

$$X = x_1 \cdot e_1 + x_2 \cdot e_2 + h(x_1, x_2) \cdot e_3. \quad (1.2)$$

We suppose that: (i)  $h$  induces a bijection between  $\Omega$  and  $\mathcal{S}$ ; (ii)  $\mathcal{S}$  is bounded, connected, and  $C^m$ -continuous (with  $m \geq 3$ ); and (iii) its boundary  $\partial\mathcal{S}$  is of dimension 1,  $C^{m'}$  continuous ( $m' \geq 2$ ) and defined such that  $\partial h : \partial\Omega \rightarrow \partial\mathcal{S}$  is the extension by continuity of  $h$  on the boundary of  $\Omega$ . We define  $p := \frac{\partial h}{\partial x_1}$ ,  $q := \frac{\partial h}{\partial x_2}$  and recall that  $\nabla h = (p, q)$ . With these notations, for any  $x \in \Omega$  the upward-oriented surface normal  $N_X$  at  $X$  is defined as:

$$N_X := \frac{1}{\sqrt{1 + |\nabla h(x)|^2}} \cdot \begin{pmatrix} -p \\ -q \\ 1 \end{pmatrix}. \quad (1.3)$$



**Figure 2:** We consider a scene with an object surface  $\mathcal{S}$ , a light source, and a camera in the hotspot direction. They are placed at infinity relatively to the object. The camera creates the intensity picture. Shape-from-Shading problem is to recover the object shape from this picture, i.e. for every  $x$  of the surface projection, to recover  $h(x)$ .

## 1.2 Modeling light radiance and irradiance

The photograph of an object surface can be decomposed into two consecutive processes. The light is first emitted by a source and reaches the object surface; then, the light is reflected (and thus

re-emitted) and reaches the camera sensor. Those two steps can be seen as two sides of a radiative process: a source (the light source or the light back-scattered by the surface) is radiating energy on a surface (the object surface or the camera sensor). This latest surface is irradiated. Let us first consider how the process of radiance and irradiance is usually formalized [165].

A scene is composed of objects, one or several light sources, and a camera. Let us consider a point  $X$  on the object surface and its normal  $N$  to the surface, which is oriented upward.  $N$ , together with two perpendicular directions in the surface tangent plane at  $X$ , define a normal-oriented coordinate system. The incident radiance  $L_i$  is the flux of light energy falling at this point within a given solid angle relatively to  $N$  (Figure 3-1); it is expressed in watts per steradian per square meter ( $W.sr^{-1}.m^{-2}$ ). Incident radiance is a function of spherical directions  $\theta_i$  and  $\phi_i$ , respectively, the azimuth and zenith of the incident light source direction relatively to the surface normal. The incident irradiance  $E_i$  is the density of energy received on  $X$  and it is expressed in watts per square meter ( $W.m^{-2}$ ) and we denote by  $dE_i := L_i.cos\phi_i.d\omega_i$  the incident irradiance contributed by the portion of the source found within the solid angle  $d\omega_i$  in the direction  $(\theta_i, \phi_i)$  (Figure 3-2), i.e. represented by  $L_i$ , and  $E_i$  is the integration of the light energy contributed by every sources found within each solid angles of the hemisphere (Figure 3-3):

$$E_i = \int_{hemisphere} L_i.cos\phi_i.d\omega_i. \quad (1.4)$$

The outgoing radiance  $L_o$  represents the flux of light energy after reflection and within a given solid angle (Figure 3-1). It is a function of azimuthal and zenithal directions, respectively,  $\theta_o$  and  $\phi_o$ . We denote by  $dL_o(\theta_i, \phi_i; \theta_o, \phi_o)$  the outgoing radiance for a given source placed in the direction  $(\theta_i, \phi_i)$ .

To study the optical properties of a given material, we can measure its bidirectional reflectance distribution function (*BRDF*). For a given viewing direction  $(\theta_o, \phi_o)$ , it is the ratio between the outgoing radiance  $dL_o$  of the surface if lit by a single light source placed in the direction  $(\theta_i, \phi_i)$ , and the irradiance produced by this light source, i.e.  $dE_i$  [165, 166, 167]:

$$BRDF(\theta_i, \phi_i; \theta_o, \phi_o) := \frac{dL_o(\theta_i, \phi_i; \theta_o, \phi_o)}{dE_i(\theta_i, \phi_i)}, \quad (1.5)$$

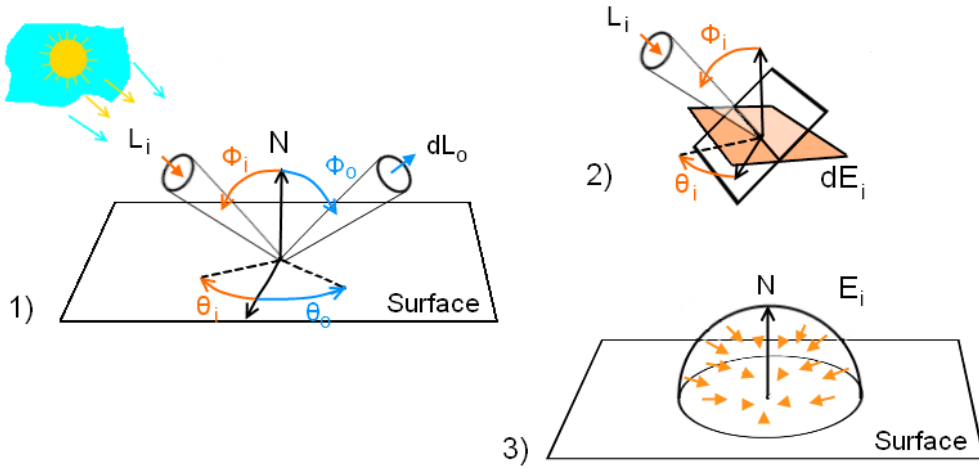
The *BRDF* can be interpreted as the proportion of light coming from direction  $(\theta_i, \phi_i)$  that will be re-emitted in a direction  $(\theta_o, \phi_o)$ . It is a feature of the object's material: (i) it has a value between 0 and 1; (ii) its values are independent from the light sources and the camera distance; and (iii) it is used as a coefficient function that one applies on all the incident radiance to know the quantity of energy re-emitted by the material within a specific direction.

When a surface is photographed, the camera direction is not necessarily aligned with every surface normal direction and it makes it difficult to understand the photogrammetric process if expressed in a coordinate system which is normal-oriented. To make the expression of scene radiance coherent

with the camera point of view, we consider the coordinate system viewer-oriented (i.e. with a vertical viewing direction). We can express the outgoing radiance  $L_o$  as a function of the surface normal orientation  $(\theta_N, \phi_N)$  relatively to the viewer: it is the integration of the incident radiance  $L_i$  over all possible source directions  $(\theta_s, \phi_s)$  times the  $BRDF(\theta_i, \phi_i; \theta_o, \phi_o)$  and we use a proper coordinate change, we have (see [163] chapter 8.13):

$$L_o(\theta_N, \phi_N) := \int_{-\pi}^{\pi} \int_0^{\pi/2} BRDF(\theta_i, \phi_i; \theta_o, \phi_o) \cdot L_i(\theta_s, \phi_s) \cdot \max(0, \cos(\phi_i)) \cdot \sin(\phi_s) \cdot d\phi_s d\theta_s. \quad (1.6)$$

with  $(\theta_N, \phi_N)$  the spherical coordinates of  $N$  relatively to the vertical direction, i.e.  $\theta_N$  and  $\phi_N$  are, respectively, the azimuth and zenith of  $N$ .



**Figure 3:** (1) The incident radiance  $L_i$  is the emission of energy falling on a surface point within a given solid angle and at a certain azimuth  $\theta_i$  and zenith  $\phi_i$ . The outgoing radiance  $dL_o$  is the light reflection within a given solid angle and at a certain azimuth  $\theta_o$  and zenith  $\phi_o$  and for a given incident radiance  $L_i$ . (2) The incident irradiance  $dE_i$  is the energy contributed by the portion of the source found within the solid angle in the direction  $(\theta_i, \phi_i)$ , i.e.  $L_i$ . (3) The incident irradiance  $E_i$  is the spherical integration of all the energy falling on the point

### 1.3 Reflectance map and irradiance equation

The reflectance map  $R$  gives the scene radiance as a function of the surface orientation in a viewer-centered coordinate system, i.e. it is either as a function of the surface gradient  $(p, q)$  [167] or as a function of  $N$ . For a sake of simplicity, we consider this reflectance map as a function of the normal, i.e. we consider  $R(N)$  instead of  $R(p, q)$ , even if it is commonly expressed as a function of  $(p, q)$ .

The reflectance map depends both on the nature of the object material which is modeled by the  $BRDF$ , and on the distribution of light sources. In a viewer-oriented coordinate system,  $R$  can be set equal to the outgoing radiance:

$$R(N) = L_o(\theta_N, \phi_N). \quad (1.7)$$

Let us now introduce the main assumptions made in this thesis.

### 1.3.1 Assumption on camera and light source position

We assume that a single light is illuminating the scene and a camera is placed between the light source and the object, i.e. the camera is in the hot-spot direction. We also assume that the object is at a distance  $d$  from the light source and the camera, and that this object has a small size compared to  $d$ . In other words, we can consider both of the camera and light source placed at infinity and we can assume that the perspective effect is negligible. In addition, we assume that camera lens effect is negligible. Then the photograph of the scene is orthographic, i.e., it is an orthographic photograph, and we can assume a coordinate system which is viewer-oriented. For every point  $X \in \mathcal{S}$  and their corresponding normal  $N_X$  and gradient  $(p_X, q_X)$ , the equation 1.7 holds, i.e.:

$$R(N_X) = L_o(\theta_{N_X}, \phi_{N_X}). \quad (1.8)$$

Light extinction is the consequence of the spherical spread of light energy depending on  $d$  which can be modeled by the inverse squared law [38], i.e.  $L_i = \frac{L_{light}}{d^2}$  with  $L_{light}$  outgoing source radiance. As we can consider that the camera and light source are placed at infinity, the object lies in a range between  $d$  and  $d + \Delta d$  for  $\Delta d \ll d$ . Then  $\frac{L_{light}}{d^2} \sim \frac{L_{light}}{(d + \Delta d)^2}$ . In other words, the light extinction is negligible in the neighborhood of the object. In addition, the light rays can be considered parallel. We can thus make the assumption of constant surface radiance.

Once the light rays reach the surface, they are re-emitted as the scene radiance. Those reflected light rays reach the camera sensor. The produced gray levels, i.e intensities, are quantized measurement of image irradiance. With proper intensity normalization on the picture, the reflectance value can be set equal to the pixel intensity [168], i.e we have the irradiance equation:

$$R(N_X) = I(x), \quad (1.9)$$

with  $I(x) \in [0, 1]$  the intensity value on  $x$ .

The assumptions made in this section are the most common in SFS theory [169] even if other methods have also been developed to deal with several light sources [170], pinhole camera (i.e. perspective projection) [171], and light extinction [172].

### 1.3.2 Object material

Because of heterogeneous micro-scale structures, textured materials (such as fabrics (velvet), wood barks (pine) or minerals (tiger's eye)) have an appearance that is not isotropic to azimuthal rotation around the light source direction. Yet, in [168, 163], the authors recall that most materials have no texture and are composed of two mains components depending on the surface roughness: (1) the diffuse and (2) the specular reflection (figure 4).

Diffuse reflection gives material a mat appearance. We call Lambertian a material which has a perfect diffuse reflection. This kind of material appearance only depends on the light source

direction and not on the viewing direction. For a single light source, the  $BRDF$  only depends on  $dE_i$  and if this source is fixed, it is constant. We have:

$$R(N) = N \cdot e_3 = \cos(\phi_i) \quad . \quad (1.10)$$

For the case of diffuse reflection and of light-aligned camera, we obtain from equations 1.9 and 1.10:

$$I(x) = \frac{1}{\sqrt{1 + |\nabla h(x)|^2}}, \quad (1.11)$$

which is equivalent to:

$$|\nabla h(x)| = \sqrt{\frac{1}{I(x)^2} - 1}. \quad (1.12)$$

This equation is reminiscent of the Eikonal equation  $|\nabla h(x)| = f(x)$  [173] and several authors have proposed a SFS solution by solving it [174, 164, 175, 176]. Similar equations for non light-aligned camera have also been studied [177, 178].

The specular reflection gives the material its glossy appearance. Specular components are present on surface points for which the surface normal bisects the angle between the light source and the camera direction. For perfectly specular reflectance material, such as mirror, we have [165, 179]:

$$L_o(\theta_o, \phi_o) = L_i(\theta_o + \pi, \phi_o). \quad (1.13)$$

Most of the SFS authors assumed Lambertian materials even if it is possible to consider specular ones [180]. Besides, Shape-from-Specularities [181] and Shape-from-Texture [182] are methods which have been developed in parallel to SFS.

When the camera is in the hotspot direction, the specular components of the surface correspond to the regions with maximal intensity and from equation 1.13, they correspond to points with a normal also aligned with the light direction. As we are considering this case of light-aligned camera, the reflectance is diffuse for other incident angle and it is isotropic to object rotation around the light axis. In other words, the irradiance equation can be written:

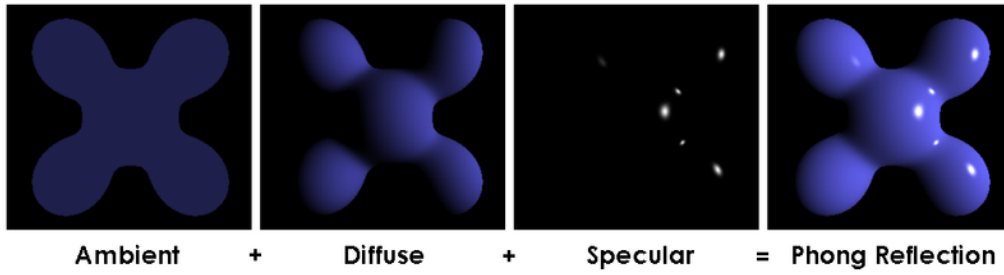
$$R(\alpha_X) = I(x), \quad (1.14)$$

with  $\alpha := \phi_s$ , the angle between the surface normal and the incidence light at  $X$  and  $I(x)$  the intensity value at  $x$ .

### 1.3.3 Surface normal orientation

Let us suppose that we know the reflectance map  $R$  for every  $\alpha$  [184, 42], i.e. for every surface orientation configuration. Then, from the equation 1.14, we can determine  $\alpha$  from  $I$ , i.e. for a given point  $x$  of the picture, we have:

$$\alpha_X = R^{-1}(I(x)). \quad (1.15)$$



**Figure 4:** *Illustration of diffuse and specular reflection: the Phong reflection model [183]. An extra ambient component (multiple scattered light due to the scene environment) is added to the diffuse and specular reflection of the direct light.*

For a given surface normal orientation, we have a single  $\alpha$  (figure 5 - a and b). Reciprocally, to each given  $\alpha \neq 0$  corresponds an infinity of potential normal orientation lying in an uncertainty cone of angle  $\alpha$  (figure 5 - c). We say that  $x$  is a singular point when  $I(x) = 1$ , i.e., a singular point corresponds to a surface point  $X \in \mathcal{S}$  with  $\alpha = 0$  (Figure 5-d) and this latest could be either a surface summit, sink or saddle point [161] (Figure 7-a, b and g) or points of an horizontal plane.

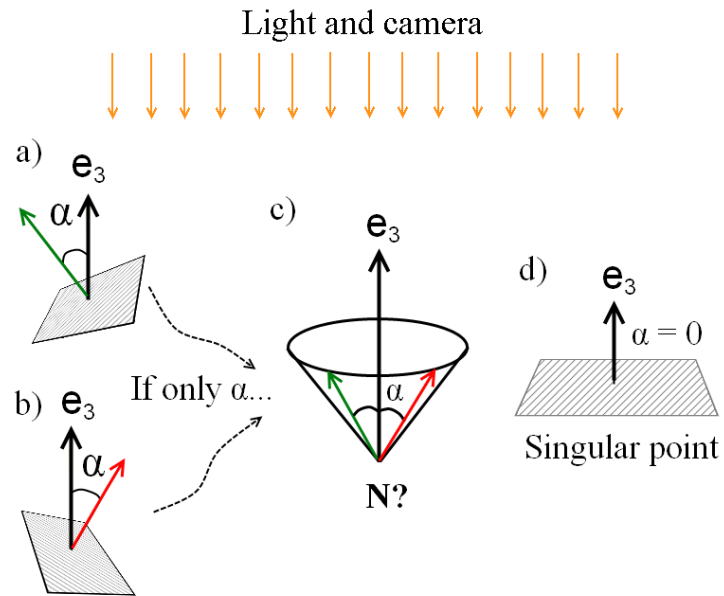
Picture regions with constant intensity are called iso-intensity regions. In some literature, they are also called the isophote regions [185]. Isophotes is a terminology used in astrophysics to define the constant intensity curves found on galaxies pictures [186]. It is also used in surface interrogation research field where they are the surface curves or regions, along which the surface normals are forming a constant angle with the vertical direction [187, 188]. In this thesis, we are considering this latest definition, i.e. the isophote regions are the regions  $\mathcal{R} \in \mathcal{S}$  such that for every  $x \in \mathcal{R}$ ,  $\alpha_x$  is constant. We notice that isophote regions correspond to iso-intensity curves if and only if: (i) the material is Lambertian; or (ii) the camera is aligned with the hotspot direction and the reflectance map is isotropic to azimuthal rotation which will be considered to be the case in the framework of this thesis.

## 1.4 General intuition of the SFS problem

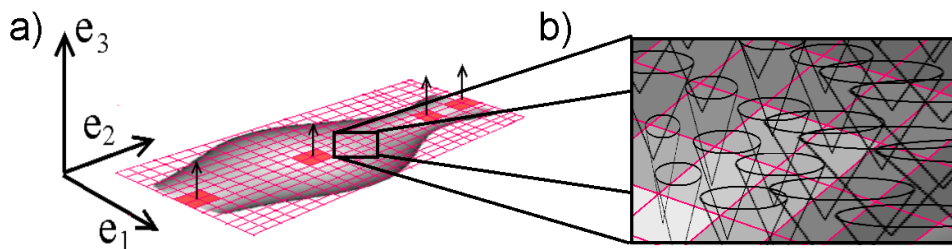
With the assumptions made in section 1.3.1 on light and camera position, the intensity corresponds to the angle  $\alpha$  between the incident light and the surface normal. In other words, this intensity provides a partial information on the local normal orientation: the normal at each point  $X$  is lying on an uncertainty cone of angle  $\alpha_x = R^{-1}(I(x))$ . The picture of a surface can be viewed as the map of cones that correspond to the normals to this surface at every point (Figure 6). Solving the SFS problem can thus be thought of choosing consistently throughout the whole image a particular position for the normal on the cone at each pixel. The purpose of the SFS methods can be seen as the problem of removing the normal orientation ambiguity at each pixel.

In the next sections, we will investigate the proof of existence and uniqueness of the SFS solution and will have a brief look at the GLOB-SFS and PROP-SFS methods.





**Figure 5:** (a) and (b) The incident light forms an angle  $\alpha$  with the surface normal  $N$ . (c) We know the incident angle  $\alpha$  between the incident light and the surface normal at a point. How can we deduce the normal  $N$ ? This normal lies on an uncertainty cone of angle  $\alpha$ . (d) When  $\alpha = 0$ , the point is said to be singular. The surface orientation at this point is determined.



**Figure 6:** (a) For singular points (red pixels), the surface normal is defined (arrow). (b) If we know the relationship between  $R$  and  $\alpha$ , the intensity can be replaced by an uncertainty cone for each pixel of the picture.

## 2 SFS proof of existence and uniqueness

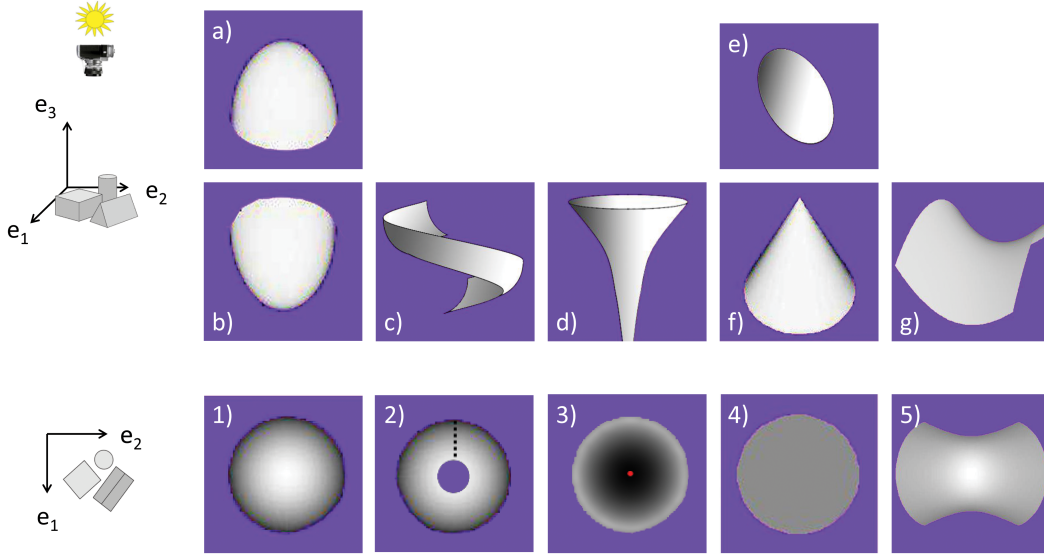
Several works have addressed the question of the existence and uniqueness of the SFS solution. Even if several authors noticed the concave/convex ambiguity issue [172, 174] (figure 7-a and b), only a few have given the theoretical limits of the SFS methods. In [159], Bruss studied the existence of a solution for the Eikonal equation 1.12. She proved that in some neighborhood of a point that is either a sink or a summit, it exists a unique convex solution. In the case when the surface projection is bounded by its silhouette and has no other singular point, the SFS solution exists everywhere. She generalized this proof to surfaces bounded by a closed isophote curve and with a unique singular point. In [161], Oliensis proved the uniqueness of surface reconstruction from intensity picture with several singular points and for object silhouette having an intensity value of 0, i.e. with  $\alpha = \frac{\pi}{2}$ .

Brooks [158], nuanced later by Kozera [160], gave two examples of the SFS resolution for which ambiguity is not only about the concave-convex shape of the surface (Figure 7-1, a and b). In his first example, he talked about an inclined plane (Figure 7-e) which forms a constant incidence angle with a vertical ray light and which produces picture pixels of constant intensity (Figure 7-4). In general, a vertical cone trunk of such angle provides the same intensity map (Figure 7-f). In his second example, he tried to reconstruct part of the hemisphere from its picture and without taking the singular point into account (Figure 7-2). He showed that an helical surface can also fit the selected zone picture (Figure 7-c). These new type of ambiguities requires that one uses other specific features of the image and the surface to allow a correct SFS reconstruction.

In [189], Horn et al. defined the impossible shaded images in the framework of continuous surface reconstruction and for camera in the hotspot direction. Those images were composed of nested and closed iso-intensity curves which were of decreasing intensity (Figure 7-3). There could not be any continuous surface that corresponds to such intensity picture configuration. Those image were not necessarily impossible for camera which were not light-aligned: in this case, the dark point can be hidden by the surface itself. Similar impossible images were also illustrated in [161] where Oliensis explained that intensity perturbation in the intensity picture could raise impossible continuous surface reconstruction.

## 3 GLOB-SFS method

A GLOB-SFS method consists of recovering the photographed surface taking advantage of the convergence of consecutive surface reconstructions. This kind of method is the most common and it has already been the subject of surveys and comparisons since the late 90's [174, 178, 169]. The global method can be split into three main subtypes: (i) the minimization; (ii) the linear approximation; and (iii) the partial differential equation (PDE) resolution with viscosity solution methods. We are going to illustrate each subtype of GLO-SFS method. Note that other types of method do exist : e.g. neural network [154]. Those alternative methods have in general similar



**Figure 7:** (1) Picture of a hemisphere corresponding to: (a) to the concave or (b) to the convex hemisphere. (2) hemisphere picture without the singular point: (c) an helical surface can correspond to this picture. (3) Picture of concentric and decreasing intensity region that tends to 0: (d) the corresponding surface has a singularity on the central point. (4) A constant iso-intensity can correspond to: (e) a piece of plane, or (f) a cone. (5) and (g): Saddle surface.

features to one of those three subtypes of GLOB-SFS methods.

### 3.1 Minimization method

In [190, 176], the authors applied a minimization method in the framework of the Eikonal equation resolution. Their method consisted of: (i) discretizing the Eikonal equation, (ii) defining an error function, and (iii) applying an optimization algorithm (e.g. gradient descent) until the error became smaller than a certain threshold. For instance, they considered the first partial derivative as the difference between two adjacent pixels height of the picture, i.e.:

$$\begin{cases} p_{i,j} = h_{i+1,j} - h_{i,j}, \\ q_{i,j} = h_{i,j+1} - h_{i,j}, \end{cases} \quad (3.1)$$

which lead them to the new irradiance equation derived from 1.11:

$$I_{i,j} = \frac{1}{\sqrt{1 + (h_{i+1,j} - h_{i,j})^2 + (h_{i,j+1} - h_{i,j})^2}}. \quad (3.2)$$

The authors defined the error function related to this equation:

$$\varepsilon = \sum_{(i,j)} \left( \frac{1}{\sqrt{1 + (h_{i+1,j} - h_{i,j})^2 + (h_{i,j+1} - h_{i,j})^2}} - I_{i,j} \right)^2. \quad (3.3)$$

Finally, they considered other assumptions which add extra term to the error function. For instance, they used the Schwartz's theorem which states that:

$$\frac{\partial^2 h}{\partial x_1 \partial x_2} - \frac{\partial^2 h}{\partial x_2 \partial x_1} = 0 \quad (3.4)$$

when the surface is  $C^2$ -continuous and they applied to this identity an expression similar to 3.1.

The strength of their method was that it can deal with noisy image and the error function was a control on the quality of the solution. However, it had the risk of providing a wrong solution. It was the reason why they proposed to give an initial surface which had common features with the solution (concavities, singular points, etc.).

### 3.2 Linear resolution

In [177], Tsai and Shah proposed a linear resolution of the SFS with camera which is not necessarily in the hotspot direction. As for the minimization method, they approximated  $p$  and  $q$  on each pixel by equation 3.1 and injected it into the irradiance equation 1.9 to obtain an equation with the unknown height function  $h$ , i.e.:

$$\underbrace{I(x_{i,j}) - R(h(x_{i,j}) - h(x_{i-1,j}), h(x_{i,j}) - h(x_{i,j-1}))}_f = 0. \quad (3.5)$$

The authors propose an iterative method to solve this equation. Let  $h^n$  be the height map at stage  $n$ . Then, the authors derived a recurrence formula from the Taylor expansion of equation 3.5:

$$h^n(x_{i,j}) = h^{n-1}(x_{i,j}) + \frac{-f(h^{n-1}(x_{i,j}))}{\frac{df}{dh}(h^{n-1}(x_{i,j}))} \quad (3.6)$$

with:

$$\frac{df}{dh}(h^{n-1}(x_{i,j})) = \frac{(p+q)(1+pp_s+qq_s)}{\sqrt{(1+p^2+q^2)^3} \cdot \sqrt{1+p_s^2+q_s^2}} - \frac{(p_s+q_s)}{\sqrt{1+p^2+q^2} \cdot \sqrt{1+p_s^2+q_s^2}} \quad (3.7)$$

and  $(p_s, q_s)$  the direction corresponding to the azimuth and the elevation of the light source direction. Assuming an initial estimate  $h^0(x_{i,j}) = 0$ , the depth map can be refined using equation 3.6 and with an iterative process [177].

This method is not able to deal with edged surfaces. In addition, there is no guarantee on the likelihood of this reconstruction as there is no optimization process and extra iterations in the calculation do not necessarily improve the result. As for the previous method, Tsai and Shah proposed giving initial height values to guarantee the convergence.

### 3.3 Viscosity solution

Viscosity solution is a weak solution of a PDE, i.e.: (i) it is defined everywhere, but (ii) it is not differentiable everywhere; and (iii) it is equal to the solution of the equation almost everywhere, i.e.

the equality does not hold on a set of measure zero. In 1997, Falcone and Sagona used this concept of viscosity solution to solve Eikonal equation in the framework of SFS theory [175]. It has been developed later by Prados and Faugeras as a PDE resolution technique [164, 162, 191, 172, 171]. To do so, they gave an explicit solution of the Eikonal equation 1.12. First, they defined it as an Hamiltonian  $H$ , i.e. they expressed the equation in the form of a ordinary differential equation (ODE)

$$H(x, \nabla h(x)) = |\nabla h(x)| - \sqrt{\frac{1}{I(x)} - 1} = 0. \quad (3.8)$$

They considered Dirichlet boundary conditions, i.e.,  $h = \varphi$  on  $\partial\Omega$  with  $\varphi$  a scalar function. Finally, they performed a Legendre transform of  $H$  to change the ODE 3.8 into a PDE, i.e. they built the new function:

$$H^*(x, q) := \sup_{p \in \mathbb{R}^2} \{p \cdot q - H(x, p)\}. \quad (3.9)$$

To solve equation 3.9, they considered the functions:

$$L(x, y) := \inf_{\xi \in C_{x,y}, T_0 > 0} \left\{ \int_0^{T_0} H^*(\xi(s), -\xi'(s)) . ds \right\}, \quad (3.10)$$

and:

$$\tilde{h}(x) := \inf_{y \in \partial\Omega} \{\varphi(y) + L(x, y)\}, \quad (3.11)$$

where  $C_{x,y}$  is the set of the paths  $\xi$  lying within  $\Omega$  such that  $\xi(0) = x$ ,  $\xi(T_0) = y$  and with  $\varphi$ ,  $L$ ,  $\xi$  and  $H$  under some topological assumptions (continuity, convexity, etc.). They proved that  $\tilde{h}$  is a viscosity solution of equation 3.8.

In practice, they used the dynamic programming principle to propagate the construction of  $\tilde{h}$  from a starting point on  $\partial\Omega$  and they locally expressed the integral term of  $L(x, y)$  from a linear approximation. This method can be considered as a mixed GLOB-SFS and PROP-SFS method. The particular features of this method is that it needs boundary height information and that it is not able to deal with singular point. Its strength is that it can deal with noisy image and edged surfaces but it is more time-consuming than the two previous methods [169].

## 4 PROP-SFS methods

PROP-SFS methods propagate surface reconstruction along specific curves from a group of seed points where the solution is locally defined. PROP-SFS methods are the least represented methods despite the fact that they were the first ones to be developed [145, 146, 147]. In general, the propagation is carried out along the greatest slope curves. Those curves tangent projection are collinear to the gradient of the height function which defines the surface, i.e.  $\nabla h = (p, q)$  (see Appendix II). We will describe two main PROP-SFS propagation methods found in the literature: (1) the propagation along the level height curves, and (2) the propagation along the isophotes regions.

## 4.1 Along level height curve

A level height curve is a surface curve of constant height. PROP-SFS along level height curve method has been introduced by Bruckstein in 1988 [192]. He proposed to propagate the reconstruction along the curves of greatest slope by integrating the intensity to build consecutive level height curves. To do so, Bruckstein considered an initial level height curve  $h_0$  of parametric representation  $(x_1(\theta), x_2(\theta)) \in \mathbb{R}^2$ , with  $\theta \in [0, 1]$  and of height  $H_0$ . As  $h$  is constant for any  $\theta \in [0, 1]$ , then:

$$\frac{d}{d\theta}h(x_1(\theta), x_2(\theta)) = 0 \implies dh = p \cdot dx_1 + q \cdot dx_2 = 0, \quad (4.1)$$

meaning that  $\nabla h$  is collinear to  $n_\theta$ , the principal normal of  $h_0$ . He noticed that  $n_\theta$  is equal to:

$$n_\theta = \frac{1}{(x'_1(\theta) + x'_2(\theta))^2} \cdot \begin{pmatrix} -x'_2(\theta) \\ x'_1(\theta) \end{pmatrix}. \quad (4.2)$$

From the Eikonal equation 1.12, he got:

$$\begin{cases} p = \pm \frac{x'_2(\theta)}{(x'_1(\theta) + x'_2(\theta))^2} \cdot \frac{(1-I(\theta))^{1/2}}{I(\theta)}, \\ q = \mp \frac{x'_1(\theta)}{(x'_1(\theta) + x'_2(\theta))^2} \cdot \frac{(1-I(\theta))^{1/2}}{I(\theta)}. \end{cases} \quad (4.3)$$

To move to a vertical offset  $\Delta H$  along the greatest slope curve, a distance of  $d_\theta$  in the horizontal plane should be traveled (Figure 8). Bruckstein suggested that in the Lambertian case,  $I$  is the cosine of the angle between the normal to the surface and the vertical direction. Therefore, he directly deduced that:

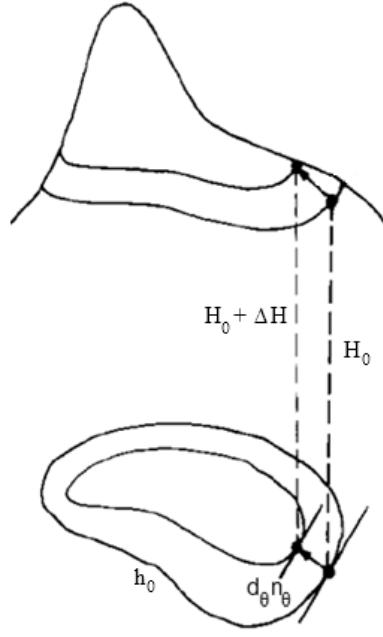
$$d_\theta = \Delta H \cdot \frac{I(\theta)}{(1 - I(\theta))^{1/2}}. \quad (4.4)$$

As a consequence, the next level curve is of parametric representation:

$$\begin{pmatrix} x_1(\theta, \Delta H) \\ x_2(\theta, \Delta H) \end{pmatrix} = \begin{pmatrix} x_1(\theta) \\ x_2(\theta) \end{pmatrix} + d_\theta \cdot n_\theta \quad (4.5)$$

$$\begin{aligned} &= \begin{pmatrix} x_1(\theta) \\ x_2(\theta) \end{pmatrix} + \frac{1}{(x'_1(\theta) + x'_2(\theta))^2} \\ &\quad \times \Delta H \cdot \frac{I(\theta)}{(1 - I(\theta))^{1/2}} \cdot \begin{pmatrix} -x'_2(\theta) \\ x'_1(\theta) \end{pmatrix} \end{aligned} \quad (4.6)$$

This PROP-SFS method has been set up for unimodal surfaces (sink or summit) but in [193], authors extended the approach to multimodal surfaces by using Morse classification of singular points. In addition, they integrated a weighted distance map to control the reconstruction propagation and the blending between two connected reconstructions (i.e. starting from two neighboring singularities). This PROP-SFS method has been reused by Braquelaire & Kerautret for synthetic and real image reconstruction [194] on which a contour tangent estimation of the propagation seeds with Euclidean path [195] has been integrated. The strength of this method is its fast computational rate. However, an error is spread along the propagation: the greater the distance to the initial curve, the worse is the accuracy of the reconstruction.



**Figure 8:** *To reconstruct an unimodal surface, Bruckstein proposed to use the level height curves. (taken from [192]).*

## 4.2 Propagation along isophote regions

The PROP-SFS along isophote regions method has been introduced simultaneously by Peternell [196] and Dragnea and Angelopoulou [185] in 2005.

Peternell proposed a geometrical construction to interpolate a single iso-intensity regions of the picture with sand-pile surfaces [196]. Sand-pile surfaces are developed surface (see Appendix II). Their greatest slope curves are their generatrices, i.e. they are lines and are of constant inclination. Because this constant inclination, the pixels of sand-pile surface picture are of constant intensity. Peternell proposed to build those sand-pile surfaces from a level height curve: as for the Bruckstein's method, he used the fact that the direction of the greatest slope curves projection are orthogonal to the level height curve and he used this level height curve as the directrix of the sand-pile surface construction. He also proposed a strategy to solve the self-intersections of those sand-pile surfaces. However, no algorithmic strategy has been implemented so far to deal with surfaces with several isophote regions, singular points or with surface curves which are not level height curves.

Dragnea and Angelopoulou proposed to estimate the surface normal along consecutive isophote regions boundaries and propagating this normal along lines transecting the isophote region [185]. Their algorithm consisted of: (i) initiating a random normal orientation for the propagation seed; (ii) propagating linearly the normal orientation; and (iii) estimating geometrically the normal associated with a next isophote region using the next isophote curve principal normal and the current estimated surface normal. They processed recursively point (ii) and (iii) to propagate the reconstruction.

The strength of this method is that it can deal with saddle point case. However, it is sensitive to

the normal estimation and the algorithm was tested only on symmetric and simple surfaces with single singularity.

## 5 Comparison of the methods

In section 2, several different SFS reconstruction ambiguities have been introduced and it has been shown that several surfaces can give the same picture [158]. Generally, we can consider that SFS problem has at most two solutions (concave/convex ambiguity) for pictures that (i) contains singular points and (ii) is contained either in the surface silhouette or within an isophote curve of the surface [161, 159]. Most of the methods introduced in this chapter are reconstructing the surfaces that fulfill those assumptions.

GLOB-SFS methods are proposing robust the reconstruction of surface, yet there is no guarantee that the solution is correct. Intensity picture of the produced surface is close to the original picture, but original and reconstructed surface can be very different. For instance GLOB-SFS using viscosity solution provides only unimodal surfaces solution [164]. Still, it is possible to provide initial height value to improve results [176, 177]. In the case of GLOB-SFS using viscosity solution, boundary values are required.

Authors who studied the SFS proof of existence proved that SFS solution is sensitive to intensity noise: in the case of small perturbations, the reconstruction can be wrong [161]. Yet authors who have proposed GLOB-SFS methods managed to carry out valid reconstructions with noisy pictures as those type of methods use convergence and minimal error principle. Nonetheless, Daniel and Durou noticed that noise can be wrongly interpreted by their minimization GLOB-SFS [176]. In the case of PROP-SFS, we can easily imagine the issues brought by noises. For the level height method, the noise can bring ambiguity in the identification of the singular points. For the isophote method, the noise can disturb the selection of isophote regions.

Minimization and linear approximation GLOB-SFS methods can handle surfaces with summit, sink and saddle points [176, 177] whereas the GLOB-SFS method using viscosity solution can only handle unimodal method [164]. The PROP-SFS are defined for unimodal surface [192, 185], but strategies have been defined to handle more complex surfaces [193].

In PROP-SFS, greatest slope curves propagation are done from a propagation seed, which is a close curve. This curve is chosen to be a level height curve in [192] and [196], and it is an isophote curve containing a singular point in [185]. Greatest slope curves are either directly computed from level height curves [192, 196] or deduced from an arbitrary normal initialization scheme [185]. Those greatest slope curves are assumed to be linear within the isophote regions [196, 185]. Interestingly, this assumption is supported by an ancient result obtained by Monge in 1850 [197], stating that sand-pile surfaces verify the equation  $|\nabla h| = c$ , where  $c$  is a constant, i.e. a sand-pile surface is an isophote surface.



According to Durou et al. [174], GLOB-SFS methods are slower than PROP-SFS method. In their survey, they show that the PDE is the slowest, whereas the linear method is the fastest and the minimization method has an intermediate speed. Tested on a SUN Enterprise E420, the global methods could take either a few second (linear resolution), about 20 seconds (minimization), or several minutes (viscosity solution) to reconstruct a surface from a picture of  $250 \times 250$  pixels.

Generally, it is difficult to compare PROP-SFS with GLOB-SFS methods [169] as PROP-SFS methods may need extra pre-processing (contour extraction, initialization). Propagation is in general of linear time complexity as the computing of the surface along the propagation curves are made using explicit equations. However, a reconstruction error is propagated for the PROP-SFS while GLOB-SFS guarantees an homogeneously bounded error.

## 6 Conclusion

As it has been discussed in Section 1.4, we intend to use SFS techniques to reconstruct TLS scanned surface from their intensities and in the scope of outlier points correction. In this chapter, we have investigated the SFS techniques whose assumption correspond to the situation of LiDAR scanner systems.

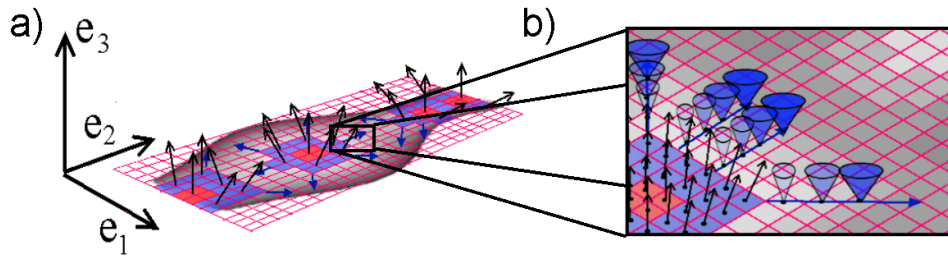
As we have seen in the previous chapter, 3D point cloud outlier are situated along scanned object edge and silhouette. Those outliers, together with the inliers point, form a point cloud that may contain large errors. To be optimal, GLOB-SFS needs initial height values [176, 177] or boundary conditions [164]. We can neither use boundary conditions nor initial TLS point cloud for this type of SFS reconstruction. Still, we can use distance information provided by the LiDAR scanner in the case they are corresponding to correct measurement points.

Singular points can be easily determined as they correspond to maximal intensity value. Because they represent surface region that are orthogonal to TLS beam, they are easily differentiated from outlier points. GLOB-SFS method do not use this type of point of maximal intensity whereas PROP-SFS method does (Figure 9-a). That lead us to chose to develop PROP-SFS method adapted to TLS data.

Geometrical information related to intensity are represented by the uncertainty cones. PROP-SFS uses the greatest slope curves for propagation. We expect that those curves can be determined from the solution propagation in the uncertainty cone space (Figure 9-b). Reducing this space to constant uncertainty cone space could make this determination easier. Constant uncertainty cone space are associated to isophote region. To find the relationship between uncertainty cone space and greatest slope, isophote regions should be investigated.

To conclude, I was led to develop a PROP-SFS method to reconstruct surface from LiDAR distance and intensity map in the spirit of Peternell, and Dragnea and Angelopoulou [196, 185]. Compared to Dragnea and Angelopoulou's article [185], we will need to set up a direct greatest slope computation from isophote curves. Compared to Peternell [196], we will deal with arbitrary

isophote regions, and thus we will have to generalize the correspondence between isophote region and sand-pile surfaces established by Monge in 1850 [197].



**Figure 9:** (a) We use normal orientation known on a given region to propagate the reconstruction.  
(b) What is the relationship between uncertainty cone space and propagation curves?

# Chapter 4

## Parametric properties of isophote surfaces

As it has been mentioned in Chapter 1, TLS distance data is used to reconstruct objects surface. Yet the presence of outliers along the scanned object edge can interfere with its surface reconstruction. It is especially true for small surfaces such as canopy leaves. Intensity return of the TLS laser beam is in general provided and we noticed in Chapter 3, that TLS optical setup corresponds to particular assumptions of the Shape-From-Shading (SFS) theory. The intensity is assumed to be related to the incidence angle  $\alpha$  between the incident light and the surface normal  $N$ . For every point  $x$  of the TLS intensity picture, the cone of angle  $\alpha$  (or the uncertainty cone of angle  $\alpha$ ) on which the normal  $N$  lies is taken into account. In the case of smooth surfaces, we guessed that if the normal orientation is known on a portion of the surface, then the uncertainty cone can vanish continuously along the neighboring of this portion, i.e.,  $N$  can be determined by continuity. In other words, the TLS intensity is directly related to the surface geometry and it is possible to reconstruct the surface shape from a known region and from the intensity values attributed to the surrounding points.

The general aim of this thesis is to use this intensity information to extract object's shape. In turn this impose to correct the TLS point cloud outliers and we chose to use a SFS-based method to help in their correction. Because the quality of the TLS point cloud is variable and the boundaries of the object representation are of poor quality, we selected a PROP-SFS method as it is expected to be better adapted to solve the outliers issues. Because isophote regions are corresponding to iso-intensity domains on the photograph of a surface if some optical properties of the material are met, we chose to develop a PROP-SFS method along isophote regions.

In 1850, Monge [197] stated that the sand-pile surfaces (SPS), or constant slope surfaces, are isophote surfaces, i.e., they are projected on an iso-intensity region. SPS surfaces are developed surfaces (see Appendix II, Section 2.5) that makes them convenient to use. In order to use them to reconstruct surfaces with a PROP-SFS method along isophote curves, we will give in this chapter a topological and geometrical proof of the reciprocal of Monge's statement, that is: if the photograph of a surface is an iso-intensity domain, then this surface is necessarily covered by a finite set of SPS.

# 1 Scene modeling

As introduced in Chapter 3, we denote by  $S$  a single  $C^3$ -continuous, bounded and connected surface of  $\mathbb{R}^3$ , defined by its height function  $h$  on an open and connected domain  $s \subset \mathbb{R}^2$ :

$$\begin{aligned} h : s &\rightarrow \mathbb{R} \\ x &\mapsto h(x), \end{aligned} \tag{1.1}$$

i.e., if  $x \in s$ , then its corresponding point on the surface  $S$  is  $X := \begin{pmatrix} x \\ h(x) \end{pmatrix}$  (Figure 1-right).

We assume that the scene is composed of this surface, a single and vertical light source and an orthographic camera which is in the hotspot direction, i.e., along  $-e_3$ . Both of the light source and the camera are placed at infinity. The effect of distance on intensity is thus negligible and the light ray can be considered parallel. The camera takes a picture of the lit surface and the resulting photograph is the orthographic projection of the surface with each of the intensities of shade on each of the visible surface points (Figure 1-left). We suppose that the effect of the sensor features on the photograph is negligible on the intensity recording.

We saw in Chapter 3 that if:

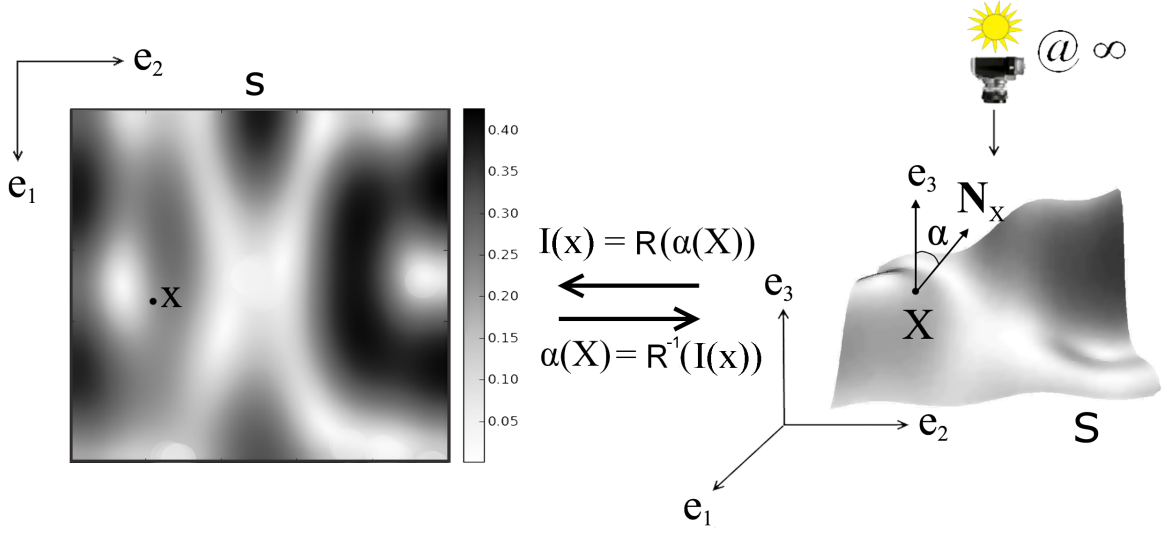
- (i) the light source and camera direction are aligned; and
- (ii) the material is without texture and its BRDF is isotropic to rotation around the light source direction (e.g. Lambertian material),

then the intensity only depends upon the reflectance map  $R$  and the incidence angle  $\alpha(X) := \angle(e_3, N_X) \in [0, \frac{\pi}{2}]$ . In other words, it is expressed by the image irradiance equation of the form  $I(x) = R(\alpha(X))$  and we can express the incidence angle as:

$$\alpha(X) = R^{-1}(I(x)). \tag{1.2}$$

If  $\alpha(X)$  is constant for every  $X \in S' \subset S$ , then we say that the  $S'$  is an isophote region of  $S$ , or iso- $\alpha$  region. An iso- $\alpha$  region is projected on an iso-intensity domain  $s' \subset s$ , or iso- $\alpha$  domains.

For a given iso- $\alpha$  domain  $s$ , is it possible to reconstruct the associated isophote region ? We know that for each point of an iso- $\alpha$  domain, there is an uncertainty cone of angle  $\alpha$ . Yet several surfaces can be projected on this iso- $\alpha$  domain, such as a plane of inclination  $\pi/2 - \alpha$  or a cone portion. Nevertheless, is it possible to give a general characterization of geometry of the iso- $\alpha$  domains and corresponding isophote regions? To answer this question, we are going to prove the reciprocal of Monge's statement, that is, the iso- $\alpha$  domains with a non-empty interior are corresponding to SPS projections.



**Figure 1:** Right:  $S$  is a surface lit by a single light source placed at infinity. It is pictured by a camera placed in the hotspot. Left: The produced photograph.

## 2 Greatest slope and level height curves

To characterize the iso- $\alpha$  domains, we need first to introduce basic concepts and notations of differential geometry.

The surface greatest slope curves (GS) and their projections (GSP) are denoted respectively by  $G$  and  $g$ . They are both parametrized by  $u$  and we recall that  $G := (g, h \circ g)$ . The surface level height curves (LC) and their projections (LCP) are denoted respectively by  $L$  and  $l$ . They are both parametrized by  $v$  and are different only by a translation of a vector collinear to  $e_3$ .  $G_X$  and  $L_X$  denote respectively the tangents of the GS and LC at a point  $X \in S$  and  $g_x$  and  $l_x$  denote respectively the tangents of the GSP and the LCP at point  $x \in s$ . We recall that the GS and LC have the following properties on parametric surfaces (a proof is given in Appendix II, Section 2.1):

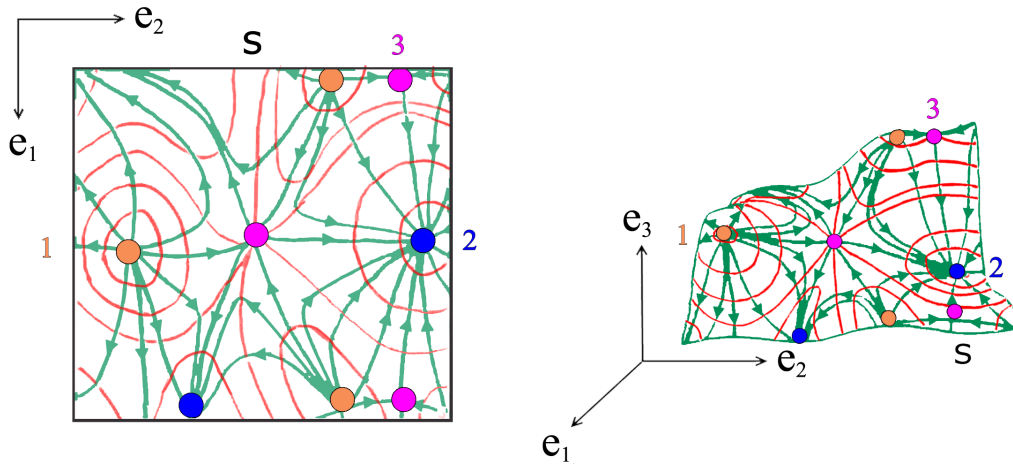
**Property 1.** If  $|\nabla h(x)| \neq 0$  for every  $x \in s$ , then:

1.  $g_x$  is collinear to the gradient of the height function on  $x$ , i.e.,  $g_x \propto \nabla h(x)$ ;
2. For any point  $x \in s$  and  $X := (x, h(x)) \in S$ ,  $G_X$  and  $g_x$  are, respectively, orthogonal to  $L_X$  and  $l_x$ ;
3. The angle formed by  $G_X$  and  $g_x$  is equal to  $\alpha(X)$ , i.e.,  $\angle(G_X, g_x) = \alpha(X)$ .

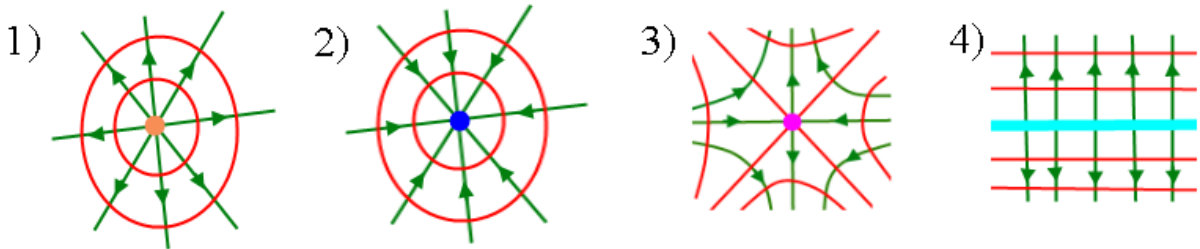
For every point  $X \in S$  such that  $|\nabla h(x)| \neq 0$ , i.e.,  $\alpha(X) \neq 0$ , there exist a unique GS and a unique LC passing by  $X$ , i.e., the surface  $S$  is covered by GS and LC. We denote them by  $G^X$  and  $L^X$ , respectively. Similarly, there exist a unique GSP and a unique LCP passing by  $x$ , i.e., the domain  $s$  is covered by GSP and LCP. We denote them by  $g^x$  and  $l^x$ , respectively (Figure 2-1). All of those functions, e.g.,  $X \mapsto G^X$ , are continuous.

In the case  $\alpha(X) = 0$ , then the points  $x$  and  $X$  are called singular. For  $C^3$ -continuous surfaces, those points are the only locus where several GS can cross (Figure 2). There are three kinds of singular points depending on the local curvatures sign [198], i.e., on the local surface orientation (Figure 3): (i) the elliptic (e.g. a summit); (ii) the hyperbolic (e.g. a saddle); and (iii) the parabolic point (e.g. a horizontal cylinder). Flat points, i.e., point contained in a flat region of the surface, are of degenerate parabolic kind [199], and if  $\alpha(X) = 0$  for every  $X \in S$ , then  $S$  is necessarily a plane portion which is orthogonal to  $e_3$ . To summarize, points with  $\alpha = 0$  have a normal orientation which is determined (vertical) and they can be classified depending on the local orientation of the surface.

In this chapter, we will consider isophote regions with  $\alpha \neq 0$ . To characterize the iso- $\alpha$  domains on which they are projected, we will have a closer look to the geometry of GSP and LCP.



**Figure 2:** If  $|\nabla h| \neq 0$ , the surface  $S$  is covered by GS (green) and LC (red). For every point  $X \in S$ , there exists a unique GS and LC, except on the singular points: (1) orange: the summits; (2) blue: the sinks; and (3) pink: the saddles. The GS are projected onto the GSP whereas the LC are projected on the LCP.



**Figure 3:** Example of singular points: (1) summit; (2) sink; (3) saddle; (4) horizontal cylinder.

### 3 Squared domain

Let us consider a  $C^3$ -continuous surface  $S$  and  $s$  its domain as it is defined in Section 1. To characterize the GSP and LCP geometry, we will first cut  $s$  into sub-domain delineated by two

GSP and two LCP (Figure 4).

**Definition 2** (Sub-arc of extremities and length). Let  $c$  be a parametric curve of  $\mathbb{R}^2$ . We denote by  $c[x, y] := \{c(u) \mid c(0) = x, c(1) = y \text{ and } u \in [0, 1]\}$  the sub-arc of  $c$  of extremities  $x$  and  $y$ . We denote by  $|c[x, y]|$  the length of this sub-arc between  $x$  and  $y$ , i.e:

$$|c[x, y]| = \int_0^1 |c'(u)| du. \quad (3.1)$$

**Definition 3** (Squared domain). A squared domain  $sd$  is a sub-domain of  $s$ , which does not contain singular point, which is bounded by two LCP (denoted by  $l^0$  and  $l^1$ ) and two GSP (denoted by  $g^0$  and  $g^1$ ), and which is of genus 0 (i.e., it has no hole). We denote by  $(a, b, c, d)$  the points corresponding respectively to the intersection  $g^0 \cap l^0$ ,  $g^0 \cap l^1$ ,  $g^1 \cap l^0$  and  $g^1 \cap l^1$ , and call them the summits of  $sd$ .  $g^0, g^1, l^0$  and  $l^1$  are called the boundaries of  $sd$ . In other words:

$$sd := \{(g^0[a, b], g^1[c, d], l^0[a, c], l^1[b, d]) \mid g^0, g^1, l^0, l^1 \text{ and } a, b, c, d \in s\}. \quad (3.2)$$

A squared domain has the following properties:

- neither  $l^0$  and  $l^1$  nor  $g^0$  and  $g^1$  are intersecting within the square domain or on its boundary;
- more generally, two LCP or two GSP contained in a squared domain cannot intersect since there is no singular point in a squared domain;
- a GSP and a LCP can intersect once and only once in  $sd$ ;
- from Property 1, for any point  $x \in s$ ,  $g^x$  and  $l^x$  cross orthogonally. This is particularly true for the summits of the squared domain.

Notice that those four properties imply that the angle at the squared domain summits are equal to  $\pi/2$  (Figure 4-i) and not to  $3\pi/2$  (Figure 4-ii). Indeed, if one of the summit angle is equal to  $3\pi/2$  then the corresponding GSP and LCP must necessarily cut respectively another GSP and LCP to exit the squared domain. This is only possible if the squared domain contains a singular point. Finally, we can consider the squared domains homeomorphic to a square.

Let us define a natural parametrization of a squared domain  $sd$  by the GSP and LCP (Figure 4-i):

$$\begin{aligned} [0, 1] \times [0, 1] &\rightarrow sd \\ (u, v) &\mapsto x(u, v). \end{aligned} \quad (3.3)$$

We recall that  $g^x$  and  $l^x$  are respectively the unique GSP and LCP that pass through  $x := x(u, v)$ . These curves make it possible to define at each point  $x$  a pair of curvatures  $\kappa^g(x)$  and  $\kappa^l(x)$  and the continuous function:

$$\kappa(u, v) := (\kappa^g(x(u, v)), \kappa^l(x(u, v))), \quad (3.4)$$

for every  $(u, v) \in [0, 1]^2$ .

If we consider the surface domain  $s$  with its GSP and LCP and without its singular points, then  $s$  is covered by squared domains (Figure 4). Several cases for the squared domain boundaries configuration, i.e., the convexity of their boundaries relatively to each others, can occur and we need to introduce the following definitions:

**Definition 4** (Convexity relatively to a curve). Let  $c^0$ ,  $c^1$  and  $c^2$  be three curves with their corresponding Frenet trihedron  $(t_0, k_0, b_0)$ ,  $(t_1, k_1, b_1)$  and  $(t_2, k_2, b_2)$ , respectively. We suppose that  $c^0$  and  $c^1$  intersect  $c^2$  once and only once, i.e., there exist two unique point  $a$  and  $b$  such that  $a = c^0 \cap c^2$  and  $b = c^1 \cap c^2$ . We suppose that  $c^2$  has neither inflexion point nor straight curve arc between  $a$  and  $b$ . We say that  $c^0$  and  $c^1$  are of same convexity relatively to  $c^2$  if  $\angle(k_2, k_0)$  at  $a$  and  $\angle(k_2, k_1)$  at  $b$  have same sign (Figure 5-a). Similarly, we say that  $c^0$  and  $c^1$  are of opposite convexity to  $c^2$  if  $\angle(k_2, k_0)$  at  $a$  and  $\angle(k_2, k_1)$  at  $b$  have opposite sign (Figure 5-b).

We are now going to define different types of squared domains:

**Definition 5** (Simple squared domain). A squared domain is said to be simple if each of its boundary curves (i.e.,  $l^0$ ,  $l^1$ ,  $g^0$  and  $g^1$ ) have a non-null curvature, i.e., there is no inflection point (Figure 4-iii).

**Definition 6** (Conform squared domain). A squared domain is said to be conform if it is simple and if  $g^0$  and  $g^1$  are of same convexity relatively to  $l^0$  and to  $l^1$  and conversely, if  $l^0$  and  $l^1$  are of same convexity relatively to  $g^0$  and to  $g^1$  (Figure 4-iv).

**Definition 7** (Right squared domain). The squared domain  $sd$  is said to be right for GSP if for every  $x \in sd$ , the curvature  $\kappa^g(x)$  is null (Figure 4-v). It is right for LCP if for every  $x \in sd$ ,  $\kappa^l(x)$  is null. It is right if it is both right for GSP and right for LCP, i.e., if for every  $x \in sd$ ,  $\kappa(x) = (0, 0)$ .

Consequently, a squared domain  $sd$  is said to be non-right for GSP if there exists a  $x \in sd$  such that the curvature  $\kappa^g(x)$  is non-null. It is non-right for LCP if there exists a  $x' \in sd$  such that  $\kappa^l(x')$  is non-null. We say it is non-right if it is both non-right for GSP and non-right for LCP, i.e., there exists  $x$  and  $x' \in sd$  such that  $\kappa^g(x)$  is non-null and  $\kappa^l(x')$  is non-null.

We notice that both the simple and conform squared domains are defined with assumptions on their boundary curves whereas a right squared domain is defined with its inner GSP and LCP. The different kinds of squared domain have properties relating to each other. By definition, a conform squared domain is necessarily simple whereas a right squared domain is neither simple nor conform. In addition, the two following propositions hold:

**Proposition 8.** *Let  $sd$  be a simple squared domain of  $s$ . If  $g^0$  and  $g^1$  are of reverse convexity relatively to  $l^0$ , then there exists  $x \in sd$  such that  $\kappa^{g^x}(x) = 0$ .*

*Proof.* Let  $sd$  be a simple squared domain such that  $g^0$  and  $g^1$  are of reverse convexity relatively to  $l^0$  (see Figure 6-1). Let  $u, v \in ]0, 1[$ . We have  $\kappa^{g^0}(x(u, 0)) < 0$  and  $\kappa^{g^1}(x(u, 1)) > 0$ , thus there exists  $v' \in ]0, 1[$  such that if  $g^x$  is the GSP that passes through  $x = x(u, v')$ , then  $\kappa^{g^x}(x(u, v')) = 0$ .  $\square$



**Proposition 9.** *If  $sd$  is non-right for GSP, one can always find a sub-squared domain  $sd' \subset sd$  which is either right for LCP and non-right for GSP, or conform.*

*Proof.* Let us suppose that  $sd$  is non-right for GSP (see for instance Figure 6-2). Then there exists  $x := x(u, v) \in sd$  such that  $\kappa^{g^x}(x) \neq 0$ . As  $\kappa$  is continuous, then there exists  $\varepsilon > 0$  such that for every  $u' \in ]u, u + \varepsilon[$  and  $x' := x(u', v)$ ,  $\kappa^{g^x}(x')$  has the same sign than  $\kappa^{g^x}(x)$ . Similarly, there exist  $\varepsilon' \neq 0$  such that for every  $v' \in ]v, v + \varepsilon'[$  and  $y := x(u, v')$ ,  $\kappa^{g^y}(y)$  has the same sign than  $\kappa^{g^x}(x)$ . We notice that, in fact, we can choose  $\varepsilon$  and  $\varepsilon'$  such that for every  $u', v' \in ]u, u + \varepsilon[ \times ]v, v + \varepsilon'[$  and  $z := x(u', v')$ ,  $\kappa^{g^z}(z)$  has the same sign than  $\kappa^{g^x}(x)$ .

We build the sub-squared domain of summit  $x, x', y$  and  $y' := x(u + \varepsilon, v + \varepsilon')$ , i.e.:

$$sd' := \{(g^x[x, x'], g^y[y, y'], l^x[x, y], l^{x'}[x', y']) \mid g^x, g^y, l^x, l^{x'} \text{ and } x, x', y, y' \in sd\}. \quad (3.5)$$

This squared domain is obviously non-right for GSP and it has been constructed such that every of its inner GSP are of same convexity than  $g^x$  relatively to  $l^x$ .

$sd'$  is either right for LCP or non-right for LCP. In the first case, we found a candidate which matches the proposition. In the second case, we can build a sub-squared domain  $sd'' \subset sd'$  with the same previous reasoning, i.e.:

$$sd'' := \{(g^x[x, x''], g^y[y, y''], l^x[x, y], l^{x''}[x'', y'']) \mid g^x, g^y, l^x, l^{x''} \text{ and } x, x'', y, y'' \in sd'\}. \quad (3.6)$$

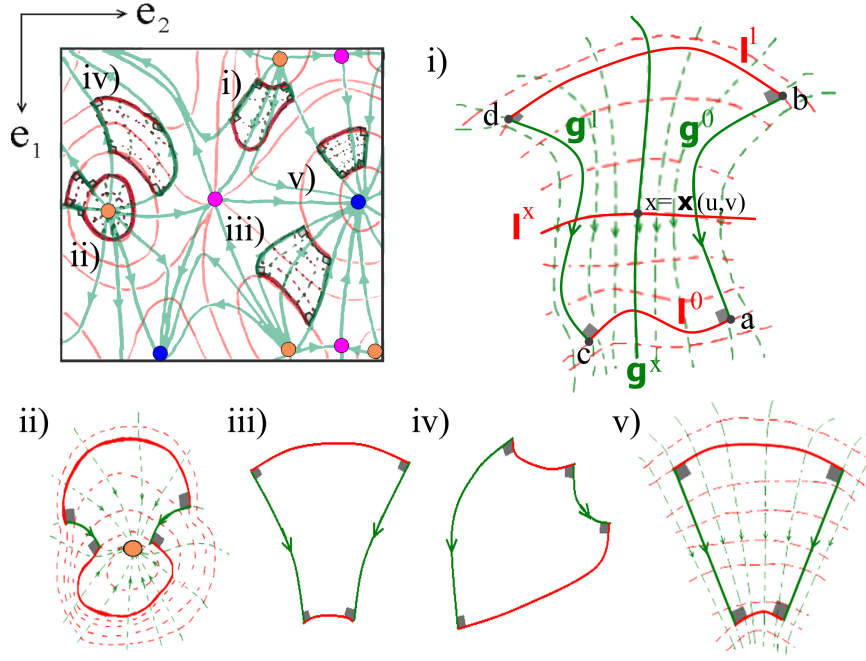
with the two LCP boundaries of  $sd''$  which are of same convexity relatively to one of the GSP boundary of  $sd''$ . Finally, we built a squared domain  $sd''$  that is conform which complete the proof.  $\square$

We defined several types of squared domain: the simple, the conform and the right; and we discussed their properties. We will use them to cover  $s$  and prove that if  $\alpha$  is constant on a squared domain, then it is necessarily right. This proof will be based on an analysis of the locus and shape of the LCP relatively to the GSP and thus on the two previous properties. Then, we will extend the analysis to the entire domain, i.e., we will prove that the GSP are necessarily a straight line segment in  $s$ .

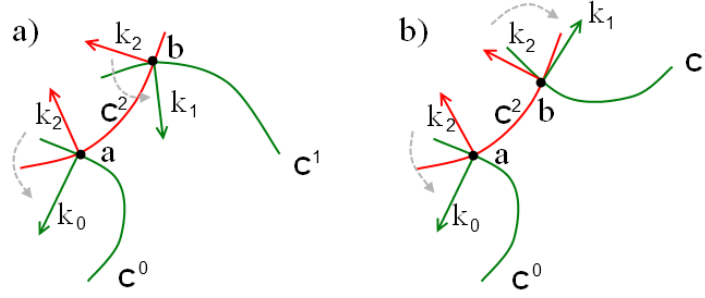
First and foremost, we need to introduce some extra geometric properties which will be specific to the type of curves manipulated hereafter.

## 4 Remarkable geometric properties of curves

Let us consider  $I := [0, s_{max}] \subset \mathbb{R}$ ,  $C$  a 3D curve defined on  $I$  and  $c$  its projection on  $\mathbb{R}^2$ . We assume that  $c$  has no inflexion point, i.e., for every  $s \in I$ ,  $\kappa^c(s) \neq 0$ . Let  $T_s$  and  $t_s$  be, respectively, the tangent vector of  $C$  and  $c$  at the points  $C(s)$  and  $c(s)$ . We recall the definition and basic properties of a generalized helix [200]:



**Figure 4:** Upper left: The surface domain, deprived of its singular points, is covered by squared domain. (i) Ordinary squared domain and notations; (ii) Domain containing a singular point; (iii) Simple squared domain; (iv) Conform squared domain and (v) Right squared domain. In red: LCP. In green: GSP.



**Figure 5:** (a)  $c^0$  and  $c^1$  are of same convexity relatively to  $c^2$ . (b)  $c^0$  and  $c^1$  are of opposite convexity.

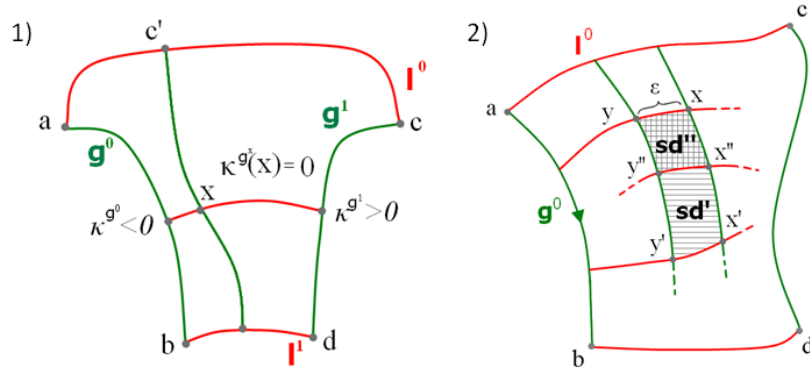
**Definition 10** (Generalized helix). If for every  $s \in I$ ,  $\alpha(s) := \angle(t_s, T_s)$  is constant, then  $C$  is said to be a generalized helix of angle  $\alpha$  (Figure 7-1).

**Property 11.**  $C$  is a generalized helix of angle  $\alpha$  if and only if, for every  $s \in I$ :

$$C(s) = \begin{pmatrix} c(s) \\ \tan(\alpha) \cdot \int_0^s \left| \frac{dc(s')}{ds'} \right| ds' \end{pmatrix}, \quad (4.1)$$

and for every  $s^0, s^1 \in I$ , we have:

$$\int_{s^0}^{s^1} \left| \frac{dC(s')}{ds'} \right| ds' = \frac{1}{\cos(\alpha)} \cdot \int_{s^0}^{s^1} \left| \frac{dc(s')}{ds'} \right| ds'. \quad (4.2)$$



**Figure 6:** (1) Proof of the proposition 8: if we consider a simple squared domain, then we necessarily find a GSP with an inflexion point  $x$ . (2) Proof of the proposition 9: if we consider an ordinary squared domain, we can find two GSP and two LCP that form a conform square domain.

**Property 12.** Let  $C^0$  and  $C^1$  be two generalized helices of angle  $\alpha$  such that there exist four points  $A, B \in C^0$  and  $C, D \in C^1$  with their corresponding projection  $a, b \in c^0$  and  $c, d \in c^1$ , respectively. We suppose that  $A$  and  $B$  have the same height, respectively, than  $C$  and  $D$ . Then:

$$|c^0[a, b]| = |c^1[c, d]|. \quad (4.3)$$

Now let us recall the definition and property of an involute [198]:

**Definition 13** (Involute). Let  $c$  and  $c_0$  be two planar curves and, respectively,  $(t, k, b)$  and  $(t_0, k_0, b_0)$  their associated Frenet trihedron.  $c_0$  is said to be the involute of  $c$  if its equation is of the form:

$$c_0(u) = c(u) + (u^0 - u) \cdot t(u). \quad (4.4)$$

**Property 14.** For every  $u \in ]-\infty, u^0]$ , we have:

1.  $t(u)$  and  $t_0(u)$  are orthogonal;
2. and (Figure 7-2):

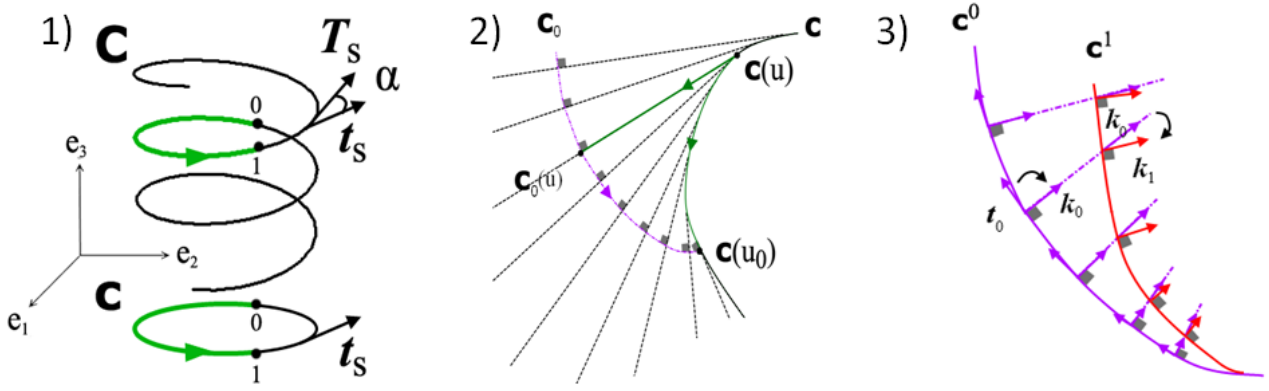
$$|c_0(u) - c(u)| = \int_u^{u^0} \left| \frac{dc(s)}{ds} \right| ds. \quad (4.5)$$

Finally, we introduce a lemma about the convexity of a curve relatively to another one for which a proof is given in Appendix II, Section 1.5.

**Lemma 15.** Let  $C^0$  and  $C^1$  be two planar curves with their parametric representation  $c^0$  and  $c^1$  and their Frenet trihedron  $(t_1, k_1, b_1)$  and  $(t_0, k_0, b_0)$ . Let us suppose that both  $c^0$  and  $c^1$  has no inflexion point and  $c^0$  is a natural representation of  $C^0$ . If there exists  $f : \mathbb{R}^+ \rightarrow \mathbb{R}$  strictly increasing and such that:

$$\begin{cases} (1) \ c^1(s) = c^0(s) + f(s) \cdot k_0(s), \\ (2) \ c^1(0) = c^0(0), \\ (3) \ t_1(0) = t_0(0), \end{cases} \quad (4.6)$$

then  $\angle(k_0(s), k_1(s))$  and  $\angle(t_0(s), k_0(s))$  are of same sign (see Figure 7-3).



**Figure 7:** (1) A generalized helix  $C$ , its projection  $c$  and their tangents. The length between 0 and 1 is conserved to a factor  $1/\cos(\alpha)$ . (2) Involute properties: for every  $u \in ]-\infty, u_0]$ ,  $|c_0(u) - c(u)| = \int_u^{u_0} |\frac{dc(s)}{ds}| ds$ . (3) Lemma 15:  $\angle(k_0, k_1)$  and  $\angle(t_0, k_0)$  are of same sign.

## 5 Fundamental theorem on iso- $\alpha$ domains

Let us consider a  $C^3$ -continuous surface  $S$  and  $s$  its domain as it has been defined in section 1 and such that for every  $X \in S$ ,  $\alpha$  is constant and non-null. To prove that the GSP of  $s$  are line segments, we will show that the inner squared domains of  $s$  are necessarily right. We first need to prove that for a given squared domain  $sd \subset s$ , there should be an inflection point on one of the GSP contained in its interior, i.e., in  $\overset{\circ}{sd}$ .

**Lemma 16.** *Let  $sd$  be an ordinary squared domain. If  $\alpha(X)$  is constant and non-null for every  $x \in sd$ , then there exists  $x' \in \overset{\circ}{sd}$  such that  $\kappa^{g^{x'}}(x') = 0$ .*

*Proof.* Let  $sd$  be an ordinary squared domain such that  $\alpha(X)$  is constant and non-null for every  $x \in sd$ . We shall reason ad absurdum and suppose that for every  $x \in \overset{\circ}{sd}$  we have  $\kappa^{g^{x'}}(x') \neq 0$ , i.e.  $sd$  is not right for GSP. From the Proposition 9, if  $sd$  is not right for GSP, then there exists a sub-squared domain  $sd' \subset sd$ , i.e.:

$$sd' := \{(g^0[a, b], g^1[c, d], l^0[a, c], l^1[b, d]) \mid g^0, g^1, l^0, l^1 \text{ and } a, b, c, d \in sd\}. \quad (5.1)$$

which is either right for LCP or conform, i.e.,  $l^0$  and  $l^1$  are either segments of straight line, or of same convexity.

For a given  $c' \in l^0$ , we will build  $g^{c'}$ , and more specifically, we will find  $d' = g^{c'} \cap l^1$ , i.e., we will construct the sub-squared domain of  $sd'$ :

$$sd'' := \{(g^0[a, b], g^{c'}[c', d'], l^0[a, c'], l^1[b, d']) \mid g^0, g^{c'}, l^0, l^1 \text{ and } a, b, c', d' \in sd\}. \quad (5.2)$$

As  $\alpha$  is constant in  $sd$ , then every GSP in  $sd$  are corresponding to an helix (see definition 10). This is especially true for the GSP of  $sd'$  and  $sd''$ . Thus, if we consider the couple of point  $c'$  and  $d'$  which are respectively on  $l^0$  and  $l^1$ , then their corresponding height, i.e.,  $C'$  and  $D'$ , have, respectively, the same height than  $A$  and  $B$  and, and from property 11, we should have:

$$|g^{c'}[c', d']| = |g^0[a, b]|. \quad (5.3)$$

Let us now consider the two half lines  $d^0$  and  $d^1$  of respective equations  $d^0(s) = a + s.k(0)$  and  $d^1 = b + s.k(1)$  (with  $k(u)$  the normal of  $g^0$  at  $u$ ). If  $sd'$  is right, then  $l^0 = d^0$  and  $l^1 = d^1$ . If it is conform, then  $l^0$  and  $l^1$  are of same convexity relatively to  $g^0$  and they are both lying on the same side of  $d^0$  and  $d^1$  (Figure 8-1). Let  $c^a$  be the involute of  $g^0$  that passes through  $a$  and of equation  $c^a(u) = g^0(u) + (u - u_b).g^0(u)$ . We are now going to build  $d'$ .

The three following cases can happen:

1.  $l^0$  is equal to  $d^0$  or it is between  $d^0$  and  $c^a$  (Figure 8-1). Let us consider the circle  $C$  of center  $c'$  and of radius  $|b - c'|$ . Firstly, the segment  $[c', b]$  cuts  $c^a$  in  $c''$  and:

$$|b - c'| > |b - c''| = \int_0^1 \left| \frac{dg^0(u)}{du} \right| . du. \quad (5.4)$$

with  $\int_0^1 \left| \frac{dg^0(u)}{du} \right| . du$  the length of the helix projection portion, i.e.:

$$\int_0^1 \left| \frac{dg^0(u)}{du} \right| . du = |g^0[a, b]|. \quad (5.5)$$

Secondly,  $d^1$  is tangent to  $C$  and  $l^1$  is on the same side of  $d^1$  than  $l^0$  is of  $d^0$ . Then, there cannot be a point  $d'$  such that  $|g^{c'}[c', d']|$  is equal to  $|g^0[a, b]|$ . Thus,  $l^0$  cannot be neither equal to  $d^0$  nor be placed between  $d^0$  and  $c^a$ .

2. For every  $u \in [0, 1]$  and  $v = u - u_b$ ,  $l^0(v)$  is equal to  $c^a(u)$  (Figure 8-2). For similar reason than the previous point, the only curve arc  $g^{c'}[c', d']$  which would be equal to  $\int_0^1 \left| \frac{dg^0(u)}{du} \right| . du$  is the segment  $d[b, c']$  of length  $|g^0(1) - c^a(1)|$  (property 14). This would mean that  $g^{c'}$  intersects  $g^0$  at  $b = d'$  which is not possible as there exists only one GSP that passes through  $b$ . In conclusion,  $l^0(v)$  cannot be equal to the involute  $c^a$ .
3.  $l^0$  is between  $d^1$  and  $c^a$  (Figure 8-3). In this case, we are considering the function  $f : \mathbb{R}^+ \rightarrow \mathbb{R}$  which defines  $l^0$  relatively to  $c$ , i.e.,  $l^0(v) = c(v) + f(v).k^0(v)$ . Necessarily, there exists  $v' \in [0, 1]$  such that  $f$  is increasing on  $[0, v']$  and we are using the Lemma 15 and show that  $g^{c'}$  and  $g^0$  are of opposite convexity relatively to  $l^0$ .

From the last point, we obtained two boundary curves  $g^{c'}$  and  $g^0$  which are of opposite convexity relatively to  $l^0$ . From the Proposition 8, we can find a point  $x(u, v) \in sd''$  such that  $\kappa^g(u, v) = 0$ . That concludes the proof.  $\square$

We can now prove the following theorems:

**Theorem 17.** *Let  $sd$  be an ordinary squared domain. If  $\alpha(X)$  is constant and non-null for every  $x \in sd$ , then  $sd$  is right for GSP.*

*Proof.* It is obvious that every open set  $o \subset sd$  contains a sub-squared domain  $sd'$  of  $sd$ . From the previous Lemma, there exists at least one point  $x \in sd' \subset o$  such that  $\kappa^{g^x}(x) = 0$ . In other word, if we consider the subset of  $sd$ :

$$Infl := \{x(u, v) \in sd \mid \kappa^{g^x}(u, v) = 0\} \quad (5.6)$$

and any open  $o \subset sd$ , then  $o \cap Infl \neq \emptyset$ . Thus  $Infl$  is dense in  $sd$  and as  $\kappa^{g^x}$  is continuous for every  $x \in sd$ , then  $\kappa^{g^x} = 0$ , i.e.,  $g^x$  is a straight line inside  $sd$ . This property can be extended to  $sd$  by closure of  $sd$ . In conclusion,  $sd$  is right for GSP.  $\square$

**Corollary 18.** *Let  $S$  a  $C^3$ -continuous surface which is projected on the open domain  $s$  of  $\mathbb{R}^2$  as it has been defined in Section 1 and such that for every  $X \in S$ ,  $\alpha(X)$  is constant. For every  $x \in s$ ,  $g^x$  is a straight line segment in  $s$ .*

*Proof.* Let  $s$  be a domain of  $\mathbb{R}^2$  such that for every  $x \in s$ ,  $\alpha(X)$  is constant and non-null. Let us consider:  $x$  a point of  $s$ ,  $g^x$  the GSP that passes through it, and  $x' \neq x$  another point of  $g^x$ . For every  $y \in g^x[x, x']$ , there exists a squared domain  $sd_y$  that strictly contains  $y$ , i.e.,  $y$  does not lie on the boundaries of  $sd_y$ , and which is necessarily right for GSP as it is stated by Theorem 17. Thus,  $\kappa^{g^x}(y) = 0$ . As this latest statement is true for every point  $y \in g^x$ , then  $g^x$  is necessarily a straight line segment.  $\square$

**Definition 19** (Coherence of a squared domains set). A set of squared domain  $Set_{sd}$  is said to be coherent if:

1.  $\bigcup_{sd \in Set_{sd}} sd$  is a connected domain;
2. For every  $sd, sd' \in Set_{sd}$ ,  $x \in sd$  and  $x' \in sd'$ , there is at most one GSP which connects  $x$  to  $x'$  and if this GSP exists, it is  $C^2$ -continuous.

**Theorem 20.** *Let  $S$  a  $C^3$ -continuous surface which is projected on the open domain  $s$  of  $\mathbb{R}^2$  as it has been defined in Section 1 and such that for every  $X \in S$ ,  $\alpha(X)$  is constant and non-null. Then, we can cover  $s$  with a finite and coherent set of squared domains that are right for GSP.*

*Proof.* Lets  $x$  a point of  $s$ . As  $\alpha(X)$  is constant, then there exists a squared domain  $sd_x \subset s$  that is right for GSP and which strictly includes  $x$ , i.e.,  $x$  does not lie on the boundaries of  $sd_x$ . Thus, the interior of  $sd_x$ , i.e.,  $\overset{\circ}{sd}_x$ , contains  $x$  and:

$$Set_{int} := \{\overset{\circ}{sd}_x \text{ with } x \in s\} \quad (5.7)$$

is a cover of  $s$ . As  $s$  is a subset of  $\mathbb{R}^2$ , which is compact, there exists a finite sub-set:

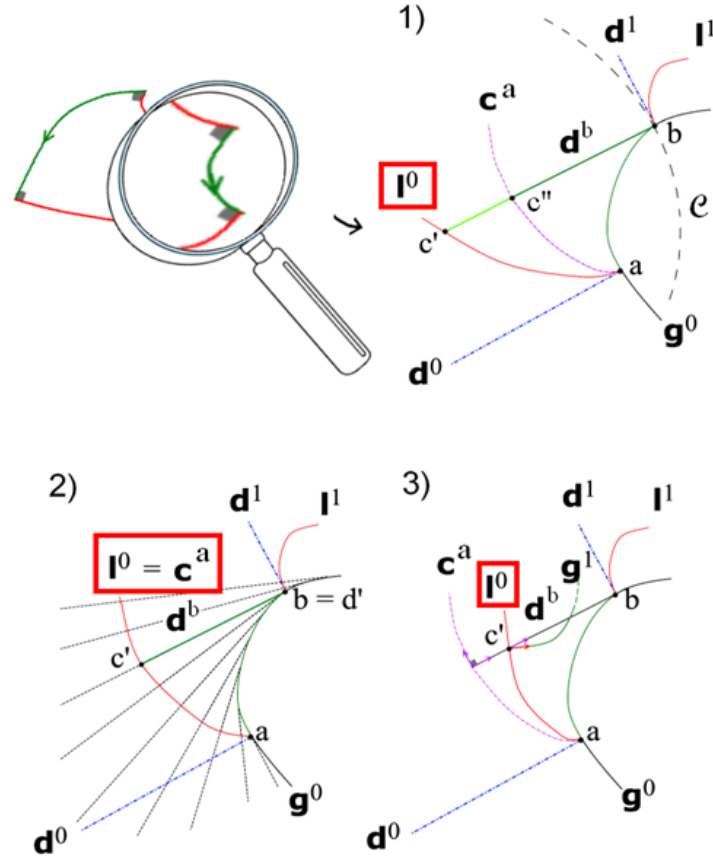
$$Set'_{int} := \{\overset{\circ}{sd}_x \text{ with } x \in I_s \subset s\} \subset Set_{int} \quad (5.8)$$

that covers  $s$ . Finally:

$$Set_{sd} := \{sd_x \text{ with } x \in I_s\} \quad (5.9)$$

is a finite set of right squared domains that cover  $s$ . The coherence of  $Set_{sd}$  is a direct application of the Corollary 18.  $\square$

We notice that, as for every  $x \in s$ , the elevation of  $G$  is constant, i.e., equals to  $\frac{\pi}{2} - \alpha$ , then  $G^X$  is also a straight line. Let us now show that the surface  $S$  is covered by a finite and coherent set of sand-pile surfaces portions. To do so, we will consider the finite and coherent set of squared domain that cover  $s$  and use the fact that both the GS and GSP are straight line segment. It is clear that the definition of coherence of a covering set is a valid definition for the subregions of  $S$ .



**Figure 8:** Zoom on sd. (1) Considering the circle  $C$  of center  $c'$  and of radius  $|b - c'|$ , we cannot find a point on  $l^1$  such that a GSP links  $l^0$  and  $l^1$  and such that its length equals  $|g^0[a, b]|$ . (2) If  $l^0 = c^a$ , then  $b$  is the only point that can be built such that the previous condition is hold. (3) In the case  $l^0$  is between  $c$  and  $g^0$ , then  $g^1$  has not the same convexity than  $g^0$  relatively to  $l^0$ .

## 6 General nature of surfaces corresponding to iso- $\alpha$ region

In Appendix II, Section 2.4, we gave the basic definition of ruled and developed surfaces. Those objects will allow us to characterize the surface that is projected on an iso- $\alpha$  domain with  $\alpha$  non-

null. We recall the definition of those surfaces [201]:

**Definition 21** (Ruled surface). A  $C^k$ -continuous ruled surface  $S$  is a surface defined by the parametrization:

$$\begin{aligned}\mathbb{R}^2 &\rightarrow \mathbb{R}^3 \\ (u, v) &\mapsto X(u, v) = F^0(u) + v.F^1(u),\end{aligned}\tag{6.1}$$

where  $F^0 : \mathbb{R} \rightarrow \mathbb{R}^3$  is a  $C^k$ -continuous function and  $F^1 : \mathbb{R} \rightarrow \mathbb{R}^3$  a  $C^k$ -continuous function that maps a real to a vector and such that  $F^1(u) \neq 0$ .

**Definition 22** (Developed surface).  $S$  is said to be a developed surface if for every  $u \in \mathbb{R}$ :  $\frac{dF^0}{du}, \frac{dF^1}{du}$  and  $F^1$  are coplanar.

In this latest case, three kinds of developed surface can be identified depending on the relationship between  $\frac{dF^0}{du}, \frac{dF^1}{du}$  and  $F^1$  [201]: the conical, the cylindrical and the development of the tangent of a curve. In this latest case, the curve is called the regression edge of the developed surface and the parametrization of the surface can be written as:

$$\begin{aligned}\mathbb{R}^2 &\rightarrow \mathbb{R}^3 \\ (u, v) &\mapsto X(u, v) = F(u) + v.\frac{dF}{du}(u),\end{aligned}\tag{6.2}$$

with  $F : \mathbb{R} \rightarrow \mathbb{R}^3$  a  $C^k$ -continuous function.

**Definition 23** (Sand-pile surface). The surface  $S$  is a sand-pile surface (or constant slope surface, denoted SPS) of angle  $\alpha$  if it is either a plane of inclination angle  $\alpha$ , a circular cone of angle  $\alpha$  or a developed surface with a generalized helix of angle  $\alpha$  as regression edge.

**Theorem 24.** *Let  $S$  a  $C^3$ -continuous surface which is projected on the open domain  $s$  of  $\mathbb{R}^2$  as it has been defined in Section 1 and such that for every  $X \in S$ ,  $\alpha(X)$  is constant and non-null, then  $S$  is covered by a finite and coherent set of SPS.*

*Proof.* As it has been stated in the Theorem 20,  $s$  is covered by a finite and coherent set of squared domain (denoted  $Set_{sd}$ ) that are right for GSP. Let us consider  $sd \in Set_{sd}$  with  $l^0$  one of its LCP boundary,  $v \in ]0, 1[$  and  $g^v$  the GSP that passes by  $l^0(v)$ . From Theorem 17,  $g^v$  is a straight line and its corresponding GS, denoted  $G^v$ , is also a straight line and, by assumption, its slope equals  $\frac{\pi}{2} - \alpha$ . We can define a parametrization of the surface patch which is projected on  $sd$  (denoted  $S_{sd}$ ) by:

$$X(u, v) = L^0(v) + u.G(v).\tag{6.3}$$

with  $L^0$  the LC associated to the LCP  $l^0$  and  $G(v)$  the tangent vector of  $G^v$ .  $S_{sd}$  is a ruled surface.

Let us consider  $(T, K, B)$  the Frenet trihedron associated with  $L^0$ . From Property 1, we know that  $G$  and  $T$  are orthogonal. In addition, we notice that  $B \propto e_3$ . We have:

$$G = \sin(\alpha).K + \cos(\alpha).B,\tag{6.4}$$



and:

$$\frac{dG}{dv} = \sin(\alpha) \cdot \frac{dK}{dv} + \cos(\alpha) \cdot \frac{dB}{dv}. \quad (6.5)$$

From the Frenet-Serret formula [198], we have:

$$\frac{dK}{dv} = -\kappa^{L^0} \cdot T + \tau^{L^0} \cdot B, \quad (6.6)$$

and:

$$\frac{dB}{dv} = -\tau^{L^0} \cdot K, \quad (6.7)$$

with  $\tau^{L^0}$  the torsion of  $L^0$ . As  $L^0$  is planar, then  $\tau^{L^0} = 0$  and  $\frac{dB}{dv} = 0$ . From equation 6.5, we obtain:

$$\frac{dG}{dv} = -\sin(\alpha) \cdot \kappa^{L^0} \cdot T \quad (6.8)$$

Thus  $\frac{dG}{dv}$  and  $\frac{dL^0}{dv} \propto T$  are coplanar which implies that  $S_{sd}$  is a developed surface and as  $\angle(G(v), e_3) = \alpha$  for every  $v \in [0, 1]$ ,  $S_{sd}$  is a SPS. Because this is true for every squared domain of  $Set_{sd}$ , we obtain a finite set of SPS which cover  $S$  and which is coherent.  $\square$

In the case we have a sub-domain of  $s$  such that  $\alpha(X) = 0$ , we know that it corresponds to a piece of plane which is a degenerate case of SPS. Finally, we proved that to an iso- $\alpha$  region of a surface is necessarily corresponding a finite and coherent set of SPS which are developed surfaces (see Appendix II, Section 2.5).

## 7 Conclusion

In Chapter 3, we saw that under specific assumptions on the camera direction, light source position and material optical properties, the SFS problem can be thought of choosing throughout the whole image a particular position for the normal on an uncertainty cone of angle  $\alpha$ . In this chapter, we investigated the properties of iso- $\alpha$  regions of  $S$ , a  $C^3$ -continuous and bounded surface defined by its height function  $h$ , with a constant and non-null angle  $\alpha = \angle(e_3, N)$ . This surface is projected on an open and connected domain  $s$  of  $\mathbb{R}^2$  and its iso- $\alpha$  regions are projected on the iso-intensity domains of the photograph, i.e., the domain on which the uncertainty cones are constant. We proved that those iso- $\alpha$  regions are covered by a finite and coherent set of SPS.

To prove this, we analyzed the geometrical properties of the GSP for a given iso- $\alpha$  domain  $s_\alpha$ . We defined the squared domains which are sub-domains of  $s$  defined by two GSP and LCP and proved that squared domains were necessarily right if  $\alpha$  is constant and non-null (Theorem 17). Iso- $\alpha$  domains can be covered by a finite and coherent set of right squared domains (Theorem 20) and we proved that to each of those squared domains corresponds a surface which is necessarily a SPS. Finally, we concluded that the iso- $\alpha$  region  $S_\alpha$  which is projected on  $s_\alpha$  can be covered by a finite and coherent set of SPS (Theorem 24) even if  $\alpha = 0$ . In other words, we generalized the correspondence between isophote region and SPS introduced by Monge [197].

As it is mentioned in Appendix II, Section 2.5, SPS are a geometrical generalization of the cone. This recall the initial intuition of solving the SFS problem by vanishing the uncertainty cone and this characterization of the iso- $\alpha$  regions of  $S$  will help us to propose a rigorous SFS method which will generalize the idea of Peternell [196], and Dragnea and Angelopoulou [185]. We know that an iso- $\alpha$  region of the surface is necessarily covered by SPS and we will use their properties to propagate a SFS reconstruction along iso- $\alpha$  curves.

# Chapter 5

## PROP-SFS propagation of sand-pile surfaces along iso- $\alpha$ regions

TLS scanner has been shown adequate to extract information of vegetation geometry such as LAI, vertical profile, voxelized LAD or tree architecture. Yet researchers encountered limits to extract geometries at organs scale with TLS distance data, especially with phase-shift LiDAR technology. This is due to the complexity of plant canopy and the consequent large quantity of outliers points present along the edge of the organs. Intensity data is an extra data provided by most of TLS today. The intensity information has been used for 3D scans segmentation [26] or scan registration [202]. Here, we investigate the potential of intensity information in order to alleviate the difficulties brought by outliers.

SFS consists of using the intensity of a surface photograph to estimate the third coordinate, i.e. the height, of every point of this surface. In Chapter 3, several techniques of SFS techniques have been introduced. Those methods can be classified in two main categories: the global methods (GLOB-SFS) and the propagation methods (PROP-SFS). We sought to use SFS method for TLS outliers correction to retrieve object surface. Because the configuration and the availability of the data, we chose to develop a PROP-SFS method. Inspired by the works of Peternell and Steiner [196], and of Dragnea and Angelopoulou [185], we investigated the properties of iso- $\alpha$  surfaces and prove that smooth iso- $\alpha$  surfaces are necessarily sand-pile surface. In this chapter we will use those surface properties and propose a PROP-SFS algorithm to reconstruct surfaces along iso- $\alpha$  domains of  $\alpha$ -photograph of surfaces.

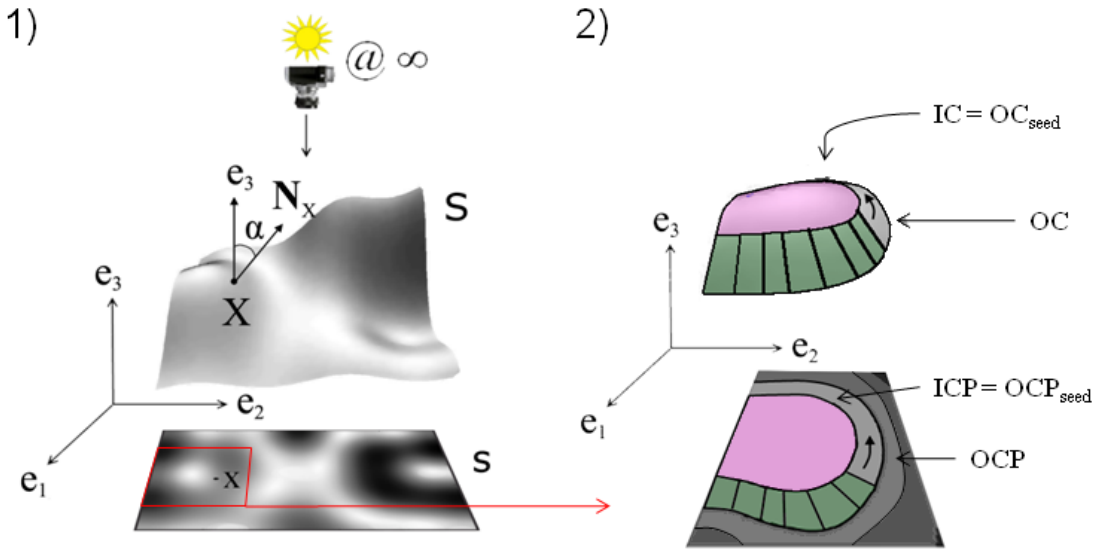
### 1 Pipeline principle

Let  $S$  be a surface and  $I$  its intensity photographed as specified in Chapter 4. We call  $\alpha = R^{-1}(I)$  the  $\alpha$ -photograph of the surface (Figure 1-1). The  $\alpha$ -photograph is first simplified as a set of quantized iso- $\alpha$  domains (Figure 1-2). Each domain with constant  $\alpha$  is bounded by either one, two or more close curves: seeds are bounded by one iso- $\alpha$  curve and iso- $\alpha$  regions encircling a seed are bounded by two curves [159], an inner (IC) and the outer curve (OC). Their projection are

respectively called the inner (ICP) and the outer curve projection (OCP). Our idea is to propagate the geometrical 3D reconstruction of the surface, starting from the seed regions whose OC are known (Figure 1-2, in pink), and iterate SPS construction outwards on adjacent iso- $\alpha$  regions (Figure 1-2, in green).

In the following, we will propose a PROP-SFS algorithm pipeline to reconstruct surfaces along iso- $\alpha$  regions and that will have the following components:

1. Iso- $\alpha$  domain chains extraction: each seed can be associated with a set of encircling iso- $\alpha$  domains that are used to define the propagation.
2. Seed-based initialization: the propagation starts from the 3D values associated with the seed OC.
3. SPS propagation: the consecutive 3D values recovered by the reconstruction are used to define new SPS sets.



**Figure 1:** 1) The surface  $S$  and its  $\alpha$ -photograph  $s$ . 2) The  $\alpha$ -photograph is simplified. Zoom on an area: the seed (in pink) encircled by an iso- $\alpha$  domain with its ICP and OCP. SPS surfaces reconstructions (in green) is used to estimate regions of  $S$ .

## 2 Pipeline description

### 2.1 Input data

Two types of matrices are output by the LiDAR device: (i) an  $\alpha$ -matrix  $M^\alpha$  of size  $N \times M$  composed of pixels representing the  $\alpha$  values of the imaged surface, and (ii) a  $h$ -matrix  $M^h$  with identical dimensions representing the distance values recorded by the LiDAR. Points in the considered image domains will be referred as either a pair of integers  $(i, j)$ , or as a pair of real numbers  $x = (x_1, x_2)$

depending on whether discrete or continuous quantities are considered. The map  $sc$  to pass from one description to the other one is defined as:

$$\begin{aligned} sc : [0, N] \times [0, M] &\rightarrow \mathbb{R}^2 \\ (i, j) &\mapsto (x_1 = a_1 \cdot i + b_1, x_2 = a_2 \cdot j + b_2), \end{aligned} \quad (2.1)$$

where  $a_1, b_1, a_2$  and  $b_2$  are parameters associated with the LiDAR. The two matrices  $M^\alpha$ ,  $M^h$  and the map  $sc$  are the three inputs of our algorithm. Note that  $M^\alpha$  and  $M^h$  are actually pre-processed versions of the corresponding LiDAR raw matrices (to correct distance effect and noise on raw intensity data, and to perform  $\alpha$  value calibration as detailed in Chapter 6).

## 2.2 Iso- $\alpha$ domain chains extraction

A first component of our pipeline is applied to the matrix  $M^\alpha$  to output ordered iso- $\alpha$  domains encircling the seeds. This component is composed by three modules:

1. Quantization
2. Segmentation and chain extraction
3. Boundary curve extraction

**Quantization.** The first step is to construct iso- $\alpha$  domains. For this, a set  $V_\alpha = \{\alpha_0, \dots, \alpha_i, \dots, \alpha_n\}$  of  $n + 1$  increasing values  $\alpha_i \in [0, \pi/2]$  is defined, with  $\alpha_n = \pi/2$ . An iso- $\alpha$  domain  $s^i$  of value  $\alpha_i$  (with  $i \in 0, \dots, n$ ) is the sub-domain of  $M^\alpha$  such that for every  $x \in s^i$ :

$$\alpha_{i-1} < \alpha(x) \leq \alpha_i \quad \text{if } 0 < i \leq n, \quad (2.2)$$

$$0 < \alpha(x) \leq \alpha_0 \quad \text{if } i = 0. \quad (2.3)$$

Let us also define the max- $\alpha$  domains  $\bar{s}^i$  with:

$$\bar{s}^i = \bigcup_{0 \leq m \leq i} s^m. \quad (2.4)$$

**Segmentation and chain extraction.** In a second step, the  $\alpha$ -matrix is split into sub-domains such that each of the produced domains contains at most one iso- $\alpha$  domain of value  $\alpha_i$  (Figure 2-2).

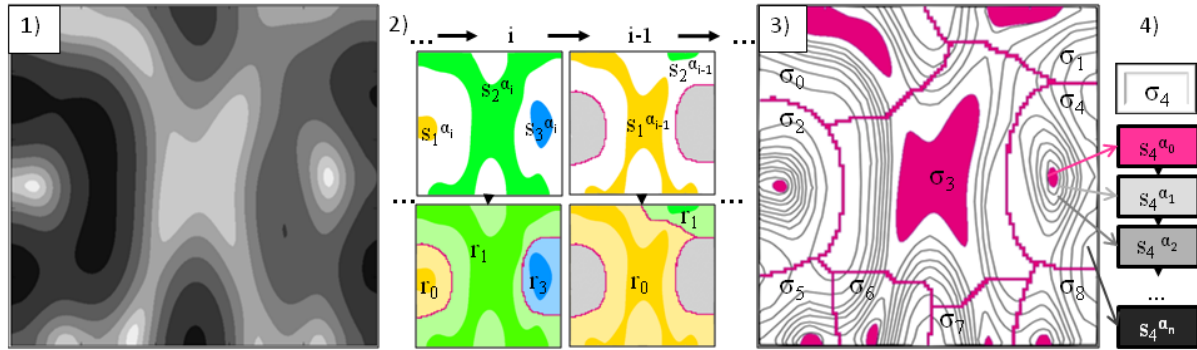
Let us assume that a domain  $s$  contains a set of  $K$  disjoint sub-domains that we want to segment into  $K$  parts so that each sub-domain is in its own part. For this, we use a watershed algorithm [203] where seed regions are defined by those  $K$  sub-domains. As an output, the watershed algorithm produces a partition of the original domain  $s$  in  $K$  parts  $\{r_1, \dots, r_K\}$  as illustrated in Figure 2-2.

Using this core procedure, our segmentation algorithm consists of segmenting recursively the original  $\alpha$ -matrix in disjoint parts based on the watershed seeds  $\bar{s}^i$  corresponding to decreasing values of  $\alpha_i$ . At each iteration step  $i$ , starting from  $i = n$ , the segmentation algorithm is applied to each

part  $r$  produced at the previous step. Initially,  $r$  is the greatest domain represented in  $M^\alpha$ . To this aim, only the portion of the watershed seeds contained in  $r$ , i.e.,  $\bar{s}^{i-1} \cap r$ , are used. The output of this segmentation is a partition of  $r$  into  $K$  parts,  $\{r_1, \dots, r_K\}$ , on which the segmentation algorithm can be iterated. The algorithm terminates when  $i = 0$  (Figure 2-3). The final partition resulting from the overall execution of this algorithm is denoted  $\Sigma = \{\sigma_1, \dots, \sigma_K\}$  such that each part  $\sigma_k \in \Sigma$  contains only one propagation seed. If  $s_k^i$  denotes the iso- $\alpha$  domain of value  $\alpha_i$  presents in  $\sigma_k$ , i.e.,  $s_k^i = s^i \cap \sigma_k$ , then  $\{s_k^i\}_i$  form a chain [204] of iso- $\alpha$  domains at an increasing large distance from the propagation seed. This ordered chain is used in the sequel to propagate the reconstruction from the seeds outwards.

**Boundary curve extraction.** The OC of an iso- $\alpha$  region (i.e., on the surface) is built from the propagation of GS that are reconstructed with the iso- $\alpha$  region IC. Yet it is necessary to extract the corresponding 2D curves (i.e., ICP and OCP) from  $M^\alpha$ . This is done in several steps: (i) Binary morphological operations make it possible to extract the pixels representing those curves [205] (see Appendix III). (ii) From these pixellated curves, a 4-connected path is constructed and a Freeman code is extracted [206]. (iii) An Euclidean path algorithm is then applied to approximate the curve and to provide estimation of curve tangents [195] (Figure 2-3). (iv) Finally, the value of the curve points and tangents are placed in the correct reference frame using  $sc$  (Equation 2.1).

The iso- $\alpha$  domain chains extraction component thus computes an ordered chain of iso- $\alpha$  domains and the related ICP and OCP curves.



**Figure 2:** 1) Quantified  $M^\alpha$ . 2)  $M^\alpha$  segmentation process at step  $i$  and  $i - 1$ . 3)  $M^\alpha$  segmented, seeds (in pink) and iso- $\alpha$  domains contour. 4) Ordered chain of  $\sigma_2$ .

## 2.3 Seed-based initialization

To start the reconstruction, it is necessary to initialize the seeds and their OC. To do so, a second component with two modules is applied to the seeds extracted from  $M^\alpha$  and the  $h$ -matrix  $M^h$ :

1. Seeds 3D initialization
2. GS sign function initialization

**Seeds 3D initialization.** Each point height of the seeds are initialized with the height matrix  $M^h$ , i.e. for every point  $x \in s^0$ ,  $h(x) = M^h(x)$ . Similarly, 3D values are associated to each point of the seeds OCP. If noise, a low-pass filter is applied to estimate the OC shape [207]. The tangents  $T$  of the 3D curves as well as their elevations  $\gamma$  and sign function  $sg(\gamma)$ , defined as:

$$sg(\gamma_X) := \begin{cases} 1 & \text{if } \gamma_X \geq 0, \\ 0 & \text{else.} \end{cases} \quad (2.5)$$

are also initialized with  $M^h$ .

**GS sign function initialization.** In order to compute the GS direction from the iso- $\alpha$  region IC, it is necessary to know their orientation (upward versus downward). A local least square regression is computed on  $M^h$  along the seed OC to determine the local surface normal and associated GS. From this computation, we can extract  $\phi_x \in ]-\pi, \pi]$  the azimuth of the GS and:

$$sg(\phi_x) := \begin{cases} +1 & \text{if } \phi_x > 0, \\ 0 & \text{if } \phi_x = 0, \\ -1 & \text{if } \phi_x < 0. \end{cases} \quad (2.6)$$

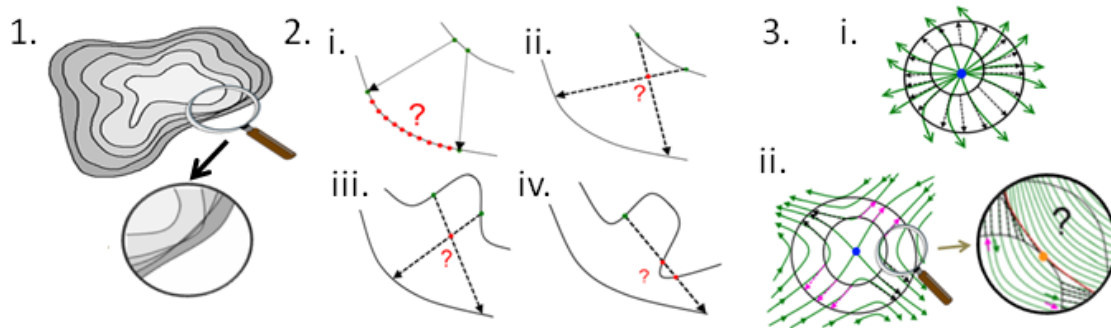
the GS sign function of the seed OC. When  $sg(\phi_x)$  is null, then we say that  $x$  is a toggle point. This sign function is used to determine the propagation orientation of the GS estimated from the iso- $\alpha$  domains.

## 2.4 SPS propagation

The two previous components of the PROP-SFS pipeline provide a chain of iso- $\alpha$  domains with their boundary curves and the 3D seeds OC. In the following, we will establish the core component of our PROP-SFS pipeline: the iso- $\alpha$  domains of the chain will be browsed and consecutive 3D iso- $\alpha$  regions of the surface will be reconstructed with the linear propagation of SPS GS. Yet the surface  $\alpha$ -photograph pixelization and simplification for the iso- $\alpha$  domains extraction, raises a number of issues that might be encountered during the surface reconstruction:

- **ICP and OCP crossing:** Consecutive ICP and OCP can be very close and touch each other due to discretizing (Figure 3-1). In this case, the curve estimation may interpret that the curves are crossing each other. On such point, the GS is neither constructed nor propagated.
- **GS and GSP divergence:** the reconstructed GS are propagated from a given iso- $\alpha$  domain IC in order to reconstruct the 3D values of the iso- $\alpha$  domain OC. Yet two consecutive GS and associated GSP can diverge and a portion of the OC (Figure 3-2.i) and the area defined by the two GS and this portion are not reconstructed. We use the SPS equation parameterized by the two consecutive GS to interpolate the surface between those points.

- **GSP crossing:** two consecutive GSP can converge and cross each other (Figure 3-2.ii). A buffer value should be used to replace the computed point of OC by the last well computed point.
- **ICP concavity:** concavity shape of ICP makes higher the chance that a GSP crosses either another GSP (Figure 3-2.iii) or itself (Figure 3-2.iv) before the targeted OCP. Similarly to the last point, a buffer value is used.
- **Singular and toggle points:** Singular points are factors driving the local surface shape and consequently, the orientation of the SPS propagation:
  - If the 3D boundary curve of a surface iso- $\alpha$  region is encircling a summit or a sink point, GS have a constant orientation along this curve, i.e., downward and upward, respectively (e.g. Figure 3-3.i). Those GS are propagated linearly.
  - If it is encircling a saddle point, the GS has an orientation that goes alternatively upward and downward (Figure 3-3.ii) and that makes the curve containing toggle points. When SPS are propagated outwards from this iso- $\alpha$  region, SPS regression edges touch the curve on those toggle points, and define an area not covered by the propagation (see zoom in Figure 3-3.ii). In this case, we cannot use SPS surface. We rather use level curves, i.e., LC, direction for the propagation. We make the assumption that they can be propagated linearly.



**Figure 3:** 1. Curves of the iso- $\alpha$  domains that are close: the extracted curves can cross. 2. i) GSP divergence; ii) GSP crossing; iii) two GSP built in an ICP concavity can cross; iv) a GSP built in an ICP concavity can cross this ICP. 3: i) Iso- $\alpha$  domain encircling a summit point. Propagation goes downward (black); ii) Saddle case: the propagation is either downward (black dashed arrow) or upward (pink dashed arrow). Orange point: toggle point. In green: real GS curves.

Those scenariis should be taken into account in the different SPS propagation components. This SFS propagation is decomposed in seven main components:

#### 1. Curves crossing inspection



2. GS and LC vector construction
3. GS and LC vector propagation
4. Propagation line crossing
5. Surface construction
6. OC tangent updating
7. Propagation orientation updating

We denote by  $A_\alpha$  and  $A_{\alpha'}$ , the IC and the OC of  $S^\alpha$ , and by  $a_\alpha$  and  $a_{\alpha'}$ , the ICP and the OCP of  $s^\alpha$ , respectively. The ICP  $a_\alpha$  will be traveled counter-clockwise. Each consecutive points  $x$  of  $a_\alpha$  and corresponding 3D point  $X$  of  $A_\alpha$  (called the current points) will be considered to build, respectively, the GSP and GS direction. We want to reconstruct the point  $X'$  and  $x'$  of  $A_{\alpha'}$  and  $a_{\alpha'}$  with the reconstructed GS and GSP direction, respectively.

**Curve crossing inspection.** We test if the current point is a crossing point, i.e., if  $x$  of  $a_\alpha$  is either in  $a_{\alpha'}$  or outside the iso- $\alpha$  domain defined by its IC and OC. In this case, no propagation of the GS is carried out. Yet the previous reconstructed point does not necessarily correspond to a curve crossing point and there is still an empty OC portion and an empty iso- $\alpha$  region area defined before  $x$ . The SPS construction in those zones should be processed.

**GS and LC vector construction** If  $x$  is not a crossing point, a vector is constructed from  $X$ . If this point is not a toggle point, we can use the property given in Appendix II, Section 2.2, to construct a SPS GS vector, denoted  $G^X$  (Figure 4-1). To do so, we first construct the GSP, denoted  $g_x$  with the following formulas:

$$\phi_X = sg(\phi_X) \cdot \left( |sg(\gamma_X) \cdot \pi - \arccos\left(\frac{\tan(|\gamma_X|)}{\tan(|\alpha|)}\right)| \right), \quad (2.7)$$

$$g_x = \begin{pmatrix} \cos(\phi_X) & -\sin(\phi_X) \\ \sin(\phi_X) & \cos(\phi_X) \end{pmatrix} \cdot t_x, \quad (2.8)$$

where  $t_x$  is the tangent of  $a_\alpha$  at  $x$ ,  $\gamma_X$  the elevation of this tangent,  $\phi_X$  the azimuth of  $g_x$  relatively to  $t_x$ , i.e.  $\phi_X := \angle(t_x, g_x)$ , and  $sg$  their sign function. The GS vector  $G^X$  is then simply deduced from  $\alpha$ :

$$G_X = \begin{pmatrix} \cos(\alpha) \cdot g_x \\ -\sin(\alpha) \end{pmatrix}. \quad (2.9)$$

If  $X$  is a toggle point, we cannot define SPS to fill the adjacent space of the iso- $\alpha$  regions. Instead, we use the LC tangent (denoted  $L^X$  on  $X$ ). As  $G_X \propto T_X$  and  $L^X \perp G_X$  (see Appendix II, Section 2.1), thus we can construct  $L^X$  from  $T_X$ .

**GS and LC vector propagation.** In the case  $X$  is not a toggle point, we can use SPS properties: GS and GSP are straight line portions within the iso- $\alpha$  regions  $S^\alpha$  and the iso- $\alpha$  domains  $s^\alpha$ , respectively. For a given point  $x \in a_\alpha$ , we can use the vector  $g_x$  to build the GS line  $g^x$  and deduce  $x' := a_{\alpha'} \cap g^x$  (Figure 4-2). The point  $X' \in A_{\alpha'}$  is constructed with the following formula:

$$X' = X + \frac{\Delta d}{\cos(\alpha)} \cdot G_X, \quad (2.10)$$

with  $\Delta d$  the distance between  $x$  and  $x'$ .

In the case  $X$  is a toggle point, we use a similar formula to propagate  $L_X$ , that drives the LC line  $L^X$ :

$$X' = X + \Delta d \cdot L_X, \quad (2.11)$$

**Propagation line crossing.** In the propagation, the two following cases can occur:

- Because ICP concavity,  $g^x$  or  $l^x$  crosses  $a_\alpha$  between  $x$  and  $x'$ , i.e.  $[x, x'] \cap a_\alpha \neq \emptyset$
- $g^x$  or  $l^x$  crosses another GSP or LCP line between  $x$  and  $x'$  i.e.  $\exists y \in a_\alpha$  and  $y' \in a_{\alpha'}$  such that  $[y, y']$  is a reconstructed surface segment and  $[x, x'] \cap [y, y'] \neq \emptyset$ .

To address these issues, we designed a simple correction strategy. This consists of storing the last point  $X'_b$  of OC correctly reconstructed. Then for the current point  $x$  of ICP, if either one of the above condition holds, then the theoretical value  $X'$  of OC as defined by equation 2.11 is discarded and replaced by value  $X'_b$ , i.e.,  $X' := X'_b$ .

**Surface construction.** In this chapter, we used SPS GS linear property to build a SFS method to propagate surface reconstruction. We will now interpolate the iso- $\alpha$  regions with SPS portion. Two consecutive lines propagation can lead us to miss a curve portion of  $A_{\alpha'}$  and the area defined by those two lines are not defined. If  $X$  is not a toggle point, we fit the surface portion defined by  $A_\alpha$ ,  $A_{\alpha'}$ ,  $G^{X_\alpha}$  and  $G^{Y_\alpha}$  with a SPS surface. This surface can be either (see Appendix II, Section 6):

- a plane, in the case where  $G^X$  and  $G^Y$  are collinear;
- a cone in the case where  $G^X$  and  $G^Y$  cross on a point (the apex of the cone);
- or a circular SPS in the case  $g^x$  and  $g^y$  cross but  $G^X$  and  $G^Y$  do not cross.

Choosing plane interpolation is a reasonable strategy as GS lines stay close enough to make local interpolation with plane. At the current stage of our PROP-SFS algorithm development, SPS are considered planar.

In the case  $X$  is a toggle point, the uncovered region is interpolated with a plane portion defined by the surface normal on  $X$ . Such as for the computation of  $L^X$ , we compute the normal from  $T_X$ .

**OC tangents updating.** Once the point  $X'$  is determined, it is necessary to update the associated tangents  $T_{X'}$  in order to propagate the GS reconstruction along the next iso- $\alpha$  regions, i.e. to use the Formulas 2.7, 2.8, 2.9 and 2.10. A naive reconstruction of  $T_{X'}$  is to use a neighboring point  $Y' \in A_{\alpha'}$  of  $X'$  and to deduce  $T_{X'}$  by combining  $t_{X'}$  together with the height of  $X'$  and  $Y'$ . As  $Y'$  is projected on  $y'$  which is estimated from  $G_Y$ , that makes the computation of  $T_{X'}$  dependent on  $G_X$ ,  $t_{X'}$  and  $G_Y$ . Because the discrete nature of the points, this solution is not optimal.

If we consider the generalized cylinder defined by  $a_{\alpha'}$  which contains  $A_{\alpha'}$ , then its normal on  $X'$  is equal to  $k_{x'}$ , the principal normal of  $a_{\alpha'}$  on  $x'$  because the cylinder property of developed surface. With this normal computation, we can use the proposition introduced in Appendix II Section 2.3 to make a finest estimation of  $T_{X'}$ :

$$T_{X'} = sg_n(x') \cdot (k_{x'} \times N_{X'}), \quad (2.12)$$

where  $N_{X'}$  is the SPS normal on  $X'$  directly deduced from  $G_X$ , and:

$$sg_n(x) = \begin{cases} +1 & \text{if } \angle(t_x, k_x) > 0, \\ -1 & \text{else.} \end{cases} \quad (2.13)$$

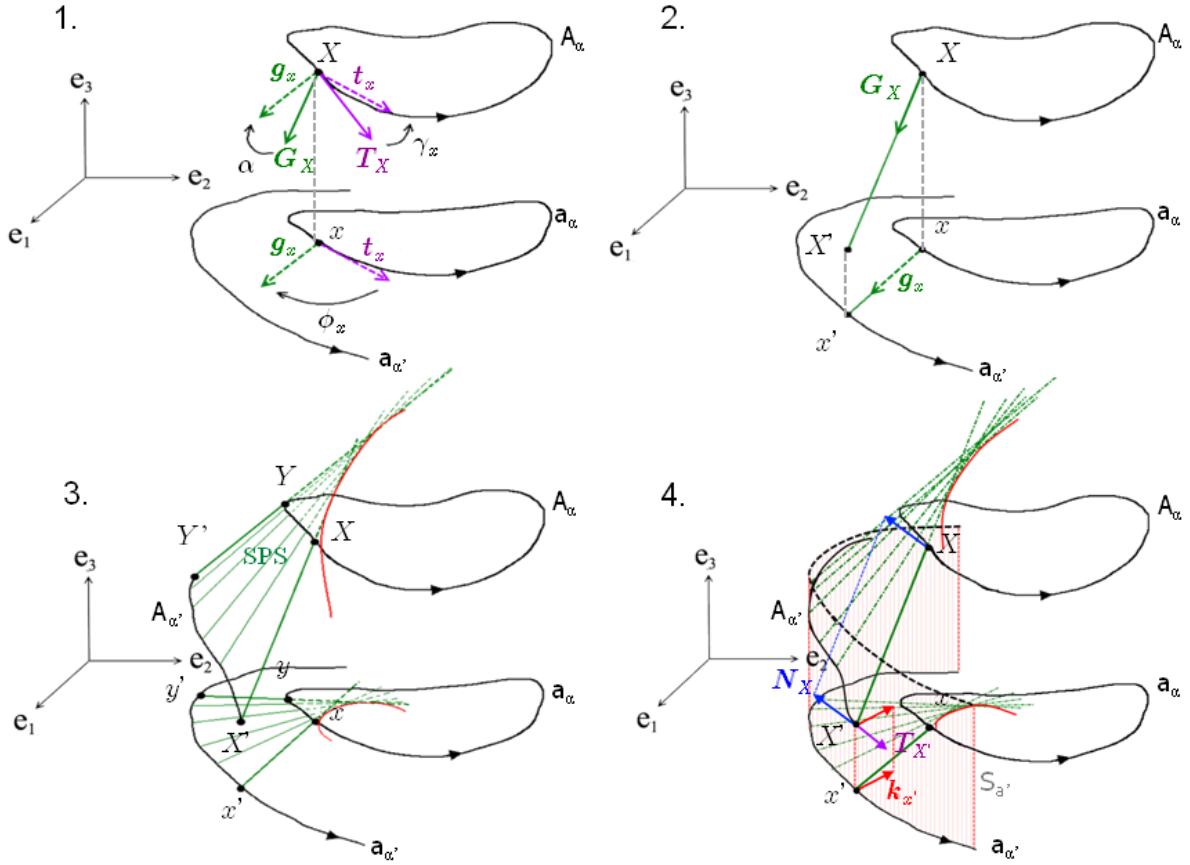
Because the normals of a SPS are constant along the GS,  $N_{X'}$  is directly deduced from  $G_X$ . The principal normal  $k_{x'}$  is directly deduced from the estimation of  $t_{x'}$ . With this property, the computation of  $T_{X'}$  depends on  $G_X$  and  $t_{x'}$  (see Figure 4-4). Similarly, the tangent can be updated with Formula 2.12 on the plane associated with toggle points.

**GS sign function updating.** Because the propagation of  $L_X$  from a toggle point does not necessarily build another toggle point on  $A_{\alpha'}$ , the new toggle points of  $A_{\alpha'}$  are updated once all the points of OC have been reconstructed. To do so, the algorithm seeks for a local maximum of  $\gamma_{X'}$  (i.e., the elevation of  $T_{X'}$ ) or points for which  $\gamma_{X'} > \alpha'$  in the neighborhood of the point  $X'$  that have been constructed from a toggle point of  $A_{\alpha}$ . Then, on each side of a toggle point, the last orientation is sought to update completely the GS sign function  $sg(\phi)$ .

## 2.5 Algorithmic set up

Our PROP-SFS pipeline can be summarized as follows (see Figure 5). First, we produce the iso- $\alpha$  chain of iso- $\alpha$  domains with associated boundary curves (see Figure 5-1): (i) the  $\alpha$ -matrix  $M^\alpha$  is quantized to construct iso- $\alpha$  domains, (ii) it is then segmented as a set of sub-domains  $\Sigma = \{\sigma_1, \dots, \sigma_K\}$ , and (iii) the boundary of the iso- $\alpha$  domains are extracted. Then, we proceed to the seed-based initialization: (i) the seeds height, and (ii) the GS sign function of their OC are initialized with the height matrix  $M^h$  (see Figure 5-2). Finally, we apply the PROP-SFS algorithm for every seed  $\sigma_k \in \Sigma$  and associated chain  $G^\sigma$  (see Figure 5-3).

To iterate our iso- $\alpha$  region reconstruction, we consider the iso- $\alpha$  domain  $s^i$  along decreasing  $i \in \{0, \dots, n\}$  the index associated with  $V_\alpha = \{\alpha_0, \dots, \alpha_i, \dots, \alpha_n\}$ . Those iso- $\alpha$  domains have associated



**Figure 4:** (1)  $G_X$  and  $g_x$  are built from  $A_\alpha$ . (2) Propagation of  $g_x$  and construction of  $X'$ . (3) A SPS is generated between two consecutive points  $X$  and  $Y$  of  $A_\alpha$ . (4) Construction of  $T_{X'}$  with the cylinder  $S_{\alpha'}$  and the SPS.

ICP and OCP respectively denoted  $a^i$  and  $a^{i+1}$ . The IC, denoted  $A^i$ , height values are known and we want to construct the OC denoted by  $A^{i+1}$ . We travel  $a^i$  and  $A^i$  counterclockwise, and consider consecutive  $x_j^i$  and  $X_j^i$  point, with increasing  $j$ . As it has been described in Section 2.4, the point  $X_j^{i+1} \in A^{i+1}$  is reconstructed with the linear propagation of  $G_j^i$ , i.e. the GS that passes by  $X_j^i$  (or  $L_j^i$  in the case of toggle points). Algorithm 5.1 gives details on the algorithmic procedure.

Three versions of our PROP-SFS method are available:

1. SFS-Simple with a GS propagation without area completion with SPS. This version only takes into account the stages 2, 3 and 6 of the Algorithm 5.1 (Figure 5-3, in white);
2. SFS-SPS that uses the SPS (in our case, planes) properties to complete OC and iso- $\alpha$  region area reconstruction. Compared to the SFS-Simple, this version takes into account stage 5 (Figure 5-3, in green); and
3. SFS-Buffer that manages curves and GS crossing. Compared to the two previous version, stages 1 and 4 are included (Figure 5-3, in blue).

---

**Algorithm 5.1**

---

**First point:** If  $j = 0$ , then the algorithm is run until a first point  $X_j^{i+1}$  of  $A^{i+1}$  is constructed, i.e.  $X_b^{i+1} = X_0^{i+1}$ , and  $j = j + 1$ .

**1. Curve crossing inspection:** If  $x_j^i \in a^i \cap a^{i+1}$  then  $X_j^{i+1} = X_j^i$  and we go to step 5. If not, then we go to the next step.

**2. GS and LC vector computation:**

**If  $X_j^i$  is a toggle point:**

We build  $L_j^i$ .

**Else:**

We construct  $G_j^i$  with the method previously described.

**3. GS and LC vector propagation:** The candidates  $X_j^{i+1}$  and corresponding projection  $x_j^{i+1}$  are constructed with the linear propagation of  $G_j^i$  or  $L_j^i$ .

**4. Propagation line crossing**

**a) Propagation line crosses the ICP:** If  $[x_j^i, x_j^{i+1}] \cap a^i \neq \emptyset$ , then  $X_j^{i+1} = X_j^i$ .

**b) Consecutive propagation lines cross:** If  $[x_{j-1}^i, x_{j-1}^{i+1}] \cap [x_j^i, x_j^{i+1}] \neq \emptyset$ , then  $T_j^{i+1} = -T_j^{i+1}$ .

**5. Surface construction :**

**if  $X_j^i$  is a toggle point:**

The surface portion between IC, OC,  $[X_{j-1}^i, X_{j-1}^{i+1}]$  and  $[X_j^i, X_j^{i+1}]$  is fit with a plane.

**else:**

The SPS is constructed between IC, OC,  $[X_{j-1}^i, X_{j-1}^{i+1}]$  and  $[X_j^i, X_j^{i+1}]$ .

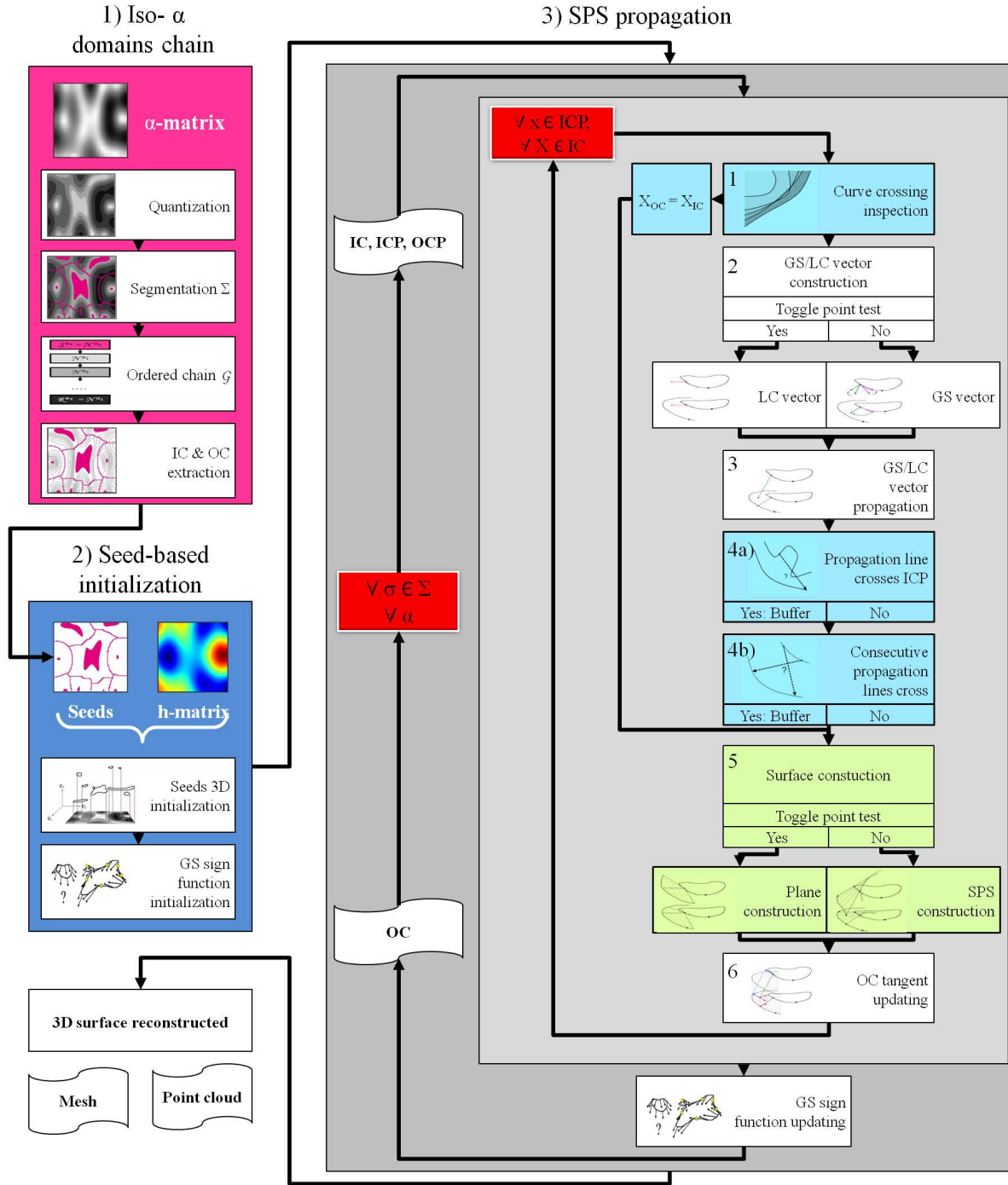
**6. OC tangent updating:** The tangent  $T_j^{i+1}$  is updated with  $G_j^{i+1}$  and  $t_{j+1}^{i+1}$ .

**Next point:** Increase  $j$ , i.e.,  $j = j + 1$ , and go back to 1.

**GS sign function updating:** Once every points  $X_j^{i+1}$  of  $A^{i+1}$  are constructed,  $sg(\phi)$  is updated.

**Next  $\alpha$ :**  $i$  is increased until the root of the chain is reached.

---



**Figure 5:** Algorithm pipeline.

### 3 Pipeline analysis

The algorithm has been implemented in Python with the following libraries: Numpy (matricial and algebrical operation); Scipy (image processing); Scikit-learn (linear regression); a watershed algorithm from VPlants' Asclepios library (segmentation); Matplotlib (2D plotting); and OpenAlea.PlantGL (mesh data structure and display). In the following, we will make: (i) a comparison between the three versions of our propagation algorithm, (ii) a short investigation on the segmentation module, (iii) a sensitivity analysis on the reconstruction, and (iv) an analysis of its complexity.

We define the average error  $\epsilon$  of the reconstruction as the error between the computed distance  $\hat{d}$  and the real distance  $d$  divided by the total height of the surface  $h_{tot} = h_{max} - h_{min}$ , i.e.:

$$\epsilon = \frac{\hat{d} - d}{h_{tot}}. \quad (3.1)$$

The absolute error  $|\epsilon|$  (in %) is the absolute error between the computed distance  $\hat{d}$  and the real distance  $d$  divided by the total height of the surface  $h_{tot}$ , i.e.:

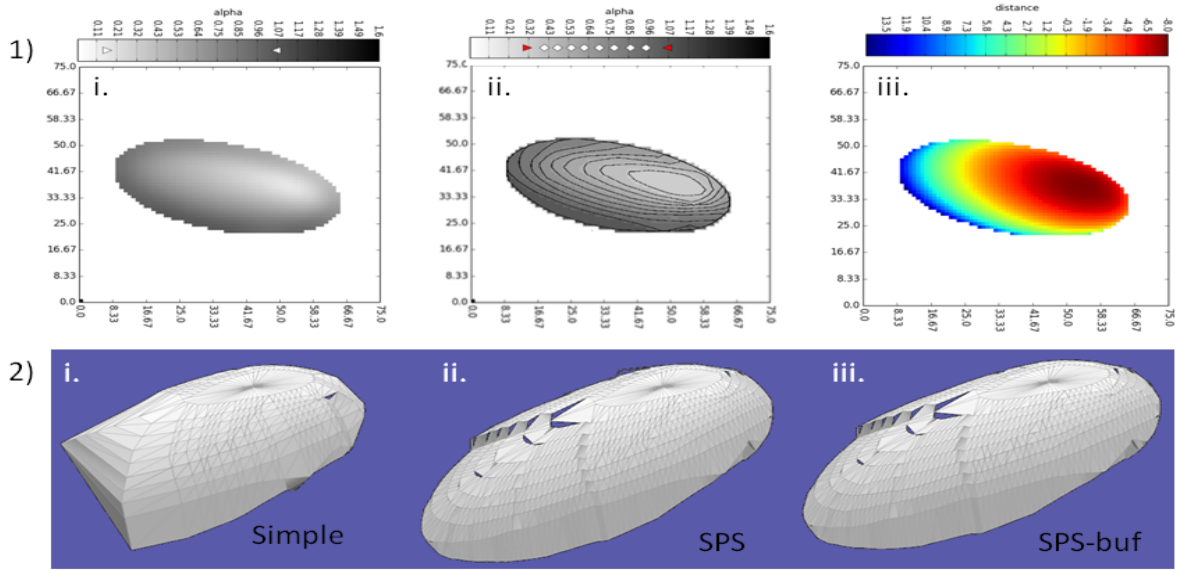
$$|\epsilon| = \frac{|\hat{d} - d|}{h_{tot}}. \quad (3.2)$$

The error matrix is the matrix representing the absolute error for each pixel, and the error distribution is their distribution.

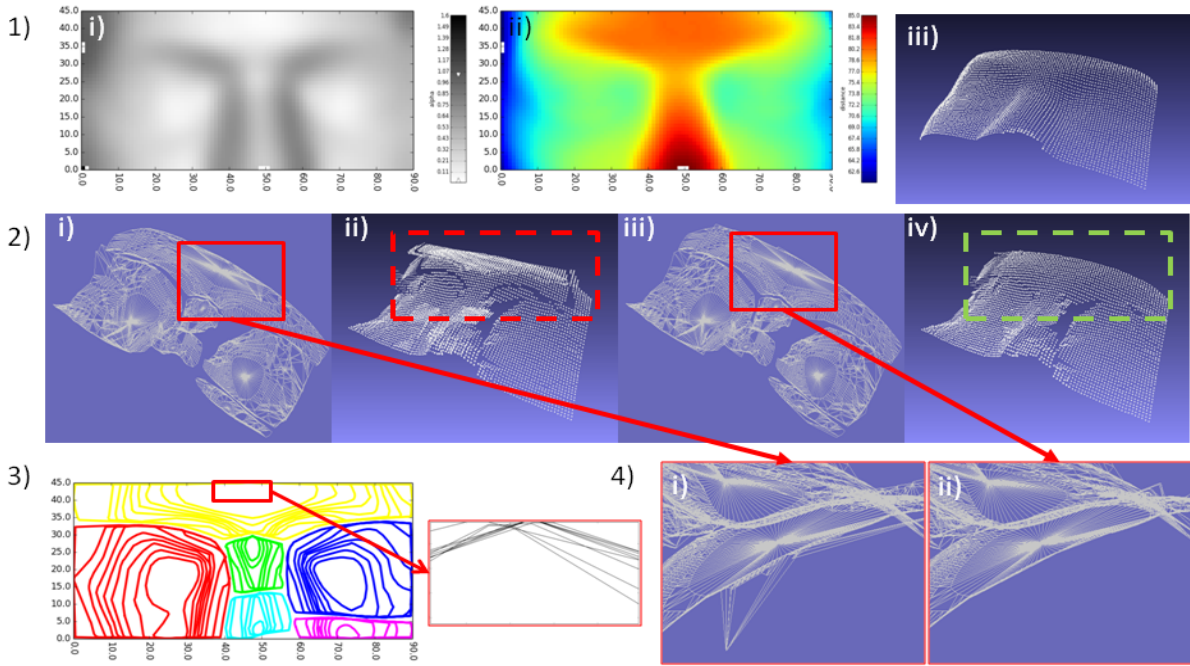
#### 3.1 Propagation algorithms comparison

**Ellipsoid.** An ellipsoid of principal diameters 30, 15 and 10 and with an elevation angle of  $\pi/8$ , and a roll angle of  $\pi/6$  (Figure 6-1.i and iii) is used to study the completion of the OC portion with the SPS. The  $\alpha$  values to quantify the  $\alpha$ -matrices are chosen such that they represent 10% of the domains (Figure 6-1.ii). Figure 6-2 shows the mesh of the ellipsoid reconstructed with the three versions of our PROP-SFS algorithm. Due to GS divergence, the propagation misses OC points that makes the reconstruction incomplete (Figure 6-2.i). The use of SPS surfaces in the SFS-SPS and SFS-Buffer algorithm is shown to be an important step to obtain complete surface reconstruction (Figure 6-2.ii and iii, respectively). In this particular example, no significant difference between those two last reconstructions is visible.

**Mozart's eyes.** Mozart's eyes (Figure 7-1, data extracted from [208]) are reconstructed with the SFS-SPS and SFS-Buffer algorithm (Figure 7-2.i and iii, respectively). The 2D curves extraction are shown in Figure 7-3. On the top of Mozart's forehead, curves are crossing (Figure 7-3 zoom). Those crossings are not taken into account with the SFS-SPS method: outlier triangles appear on those crossing points (Figure 7-4.i). Those triangles induce outlier points in the point cloud reconstruction (Figure 7-2.ii). The SFS-Buffer method avoids those triangles production and makes the point cloud reconstruction with less outlier points, and thus more realistic (Figure 7-2.iv).



**Figure 6:** (1) Inclined ellipsoid: (i)  $\alpha$ -matrix, (ii) iso- $\alpha$  domains, and (iii) distance matrix. (2) Reconstruction: (i) SFS-Simple, (ii) SFS-SPS, and (iii) SFS-Buffer.



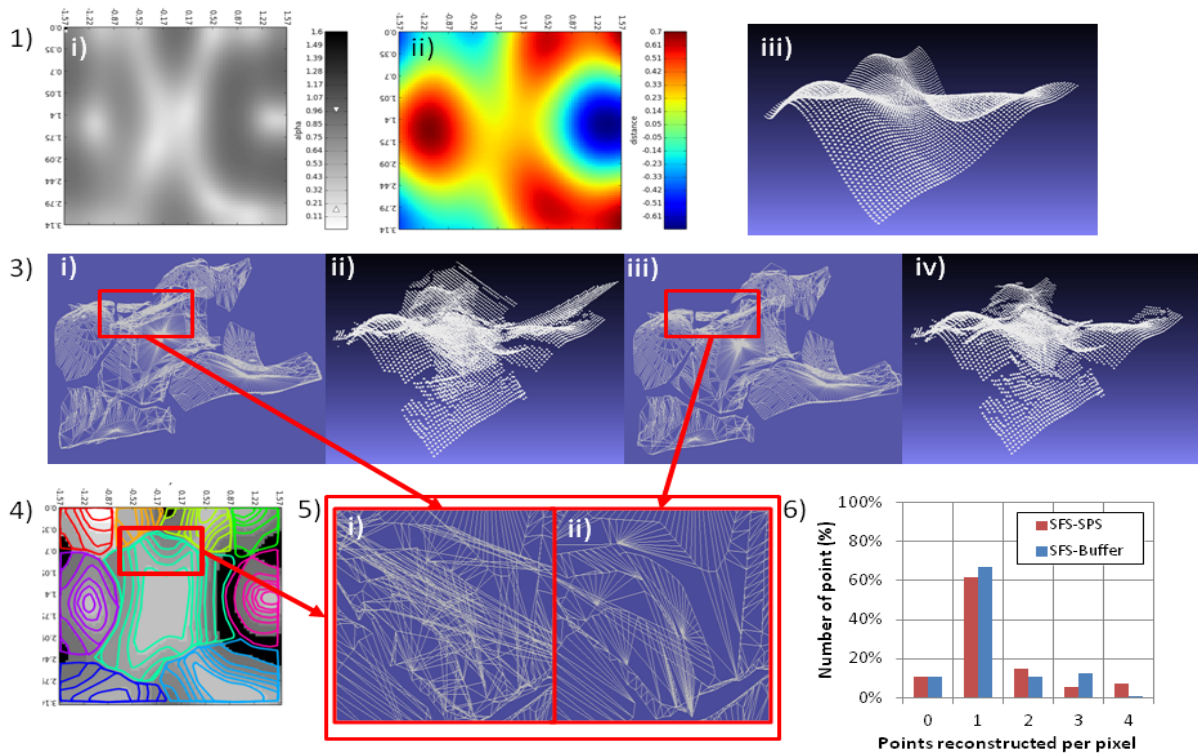
**Figure 7:** (1) Mozart's eyes: (i)  $\alpha$ -matrix, (ii) distance matrix, and (iii) original point. (2) Reconstruction: (i) SFS-SPS mesh, (ii) SFS-SPS point cloud, (iii) SFS-Buffer mesh, and (iv) SFS-Buffer point cloud. (3) Iso- $\alpha$  domains and zoom on the crossing curves. (4) Zoom on the mesh: (i) issues brought by the crossing curves (SFS-SPS), (ii) the issue is solved (SFS-Buffer).



**Complex surface.** Finally a complex surface is built to test completely the SFS-Buffer method. This surface has the following equation (Figure 8-1):

$$z = \frac{1}{10} \cdot (4 \cdot \sin(x) \cdot \cos(y) + 3 \cdot \cos(2x + \frac{\pi}{8}) \cdot \sin(\frac{y}{2} + \frac{\pi}{5}) + 2 \cdot \cos(\frac{x}{3}) \cdot \sin(4y) + 4 \cdot \cos(2x) \cdot \sin(y)) \quad (3.3)$$

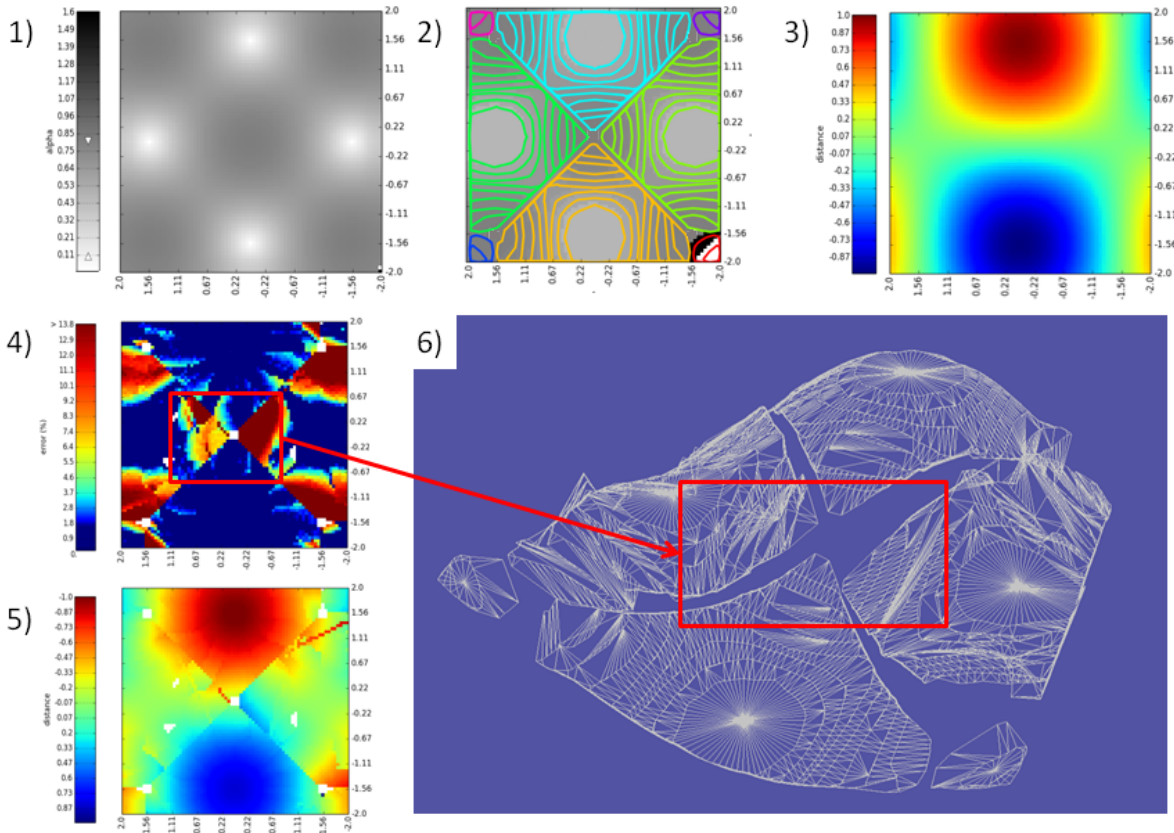
The reconstructions of this surface with the SFS-SPS and SFS-Buffer methods are shown in Figure 8-3. Issues brought by curves concavities (Figure 8-4) are not taken into account with the SFS-SPS method. The mesh reconstruction generates several crossing triangles (Figure 8-5.i). Consequently, a large amount of outlier points are generated with this method (Figure 8-3.ii). The SFS-Buffer method reduces those triangles crossings, especially on ICP concavity (Figure 8-5.ii) and the generated point cloud has less outliers (Figure 8-3.iv). The number of point generated per pixel (Figure 8-6) shows that the SFS-Buffer method is more efficient than the SFS-SPS method. Yet multiple points reconstruction per pixel is still an issue as crossing curves is not entirely managed. For instance, mesh triangles can cross OC (Figure 8-5.ii). This type of crossing is not taken into account in the SFS-Buffer method. In the following, only the SFS-Buffer version of our PROP-SFS pipeline will be used.



**Figure 8:** (1) Complex surface: (i)  $\alpha$ -matrix, (ii) distance matrix and (iii) original point cloud. (3) Reconstruction: (i) SFS-SPS mesh, (ii) SFS-SPS point cloud, (iii) SFS-Buffer mesh and (iv) SFS-Buffer point cloud. (4) Iso- $\alpha$  domains. (5) Zoom on the mesh: (i) SFS-SPS and (ii) SFS-Buffer. (6) Number of reconstructed points per pixel.

### 3.2 Segmentation

When there are several seeds, our PROP-SFS algorithm segments the  $\alpha$ -matrix. Because propagated errors [163], the further the propagation from the seed, the larger the reconstruction bias. This makes the joint between the segmented surface regions not necessarily consistent. In Figure 9-1 and 3, a surface with several sinks, summits and saddles points has been constructed. The segmentation generates height matrix domains (Figure 9-2). The reconstructed distance matrix shows the shift between the different region reconstructions (Figure 9-5). The mesh (Figure 9-6) and the error matrix also shows this shift, especially on the points joining the four largest surface regions (Figure 9-4, red frame).



**Figure 9:** Surface with several seeds: (1)  $\alpha$ -matrix, (2) segmented domains and their iso- $\alpha$  domains, (3) distance matrix, (4) error matrix, (5) matrix of the reconstructed distance, and (6) reconstructed mesh.

### 3.3 Sensitivity analysis

Several parameters should be taken into account to reconstruct surfaces with our PROP-SFS algorithm: matrix size, number of  $\alpha$  values taken into account in the quantification,  $\alpha$  and distance values quality. In the following, we will test the impact of those parameters using simple examples.

### 3.3.1 Quality of the $\alpha$ values and smoothing

Three synthetic hemispheres with noise of amplitude  $\pm 1.4^\circ$ ,  $\pm 2.8^\circ$  and  $\pm 5.7^\circ$  are generated to study noise impact on the reconstruction (Figure 10-1). Each of the associated  $\alpha$ -matrices are smoothed with a neighboring averaging of kernel 1. This smoothing process is applied 1, 2, 3, 4, 5, 10, 20, 30, 40, 50, 60, 70, 80 and 90 times. The  $\alpha$  values to quantify the  $\alpha$ -matrices are chosen such that their area represent 20% of the total domain area. They are called the quantification percentile and are denoted by  $\epsilon_\alpha$ .

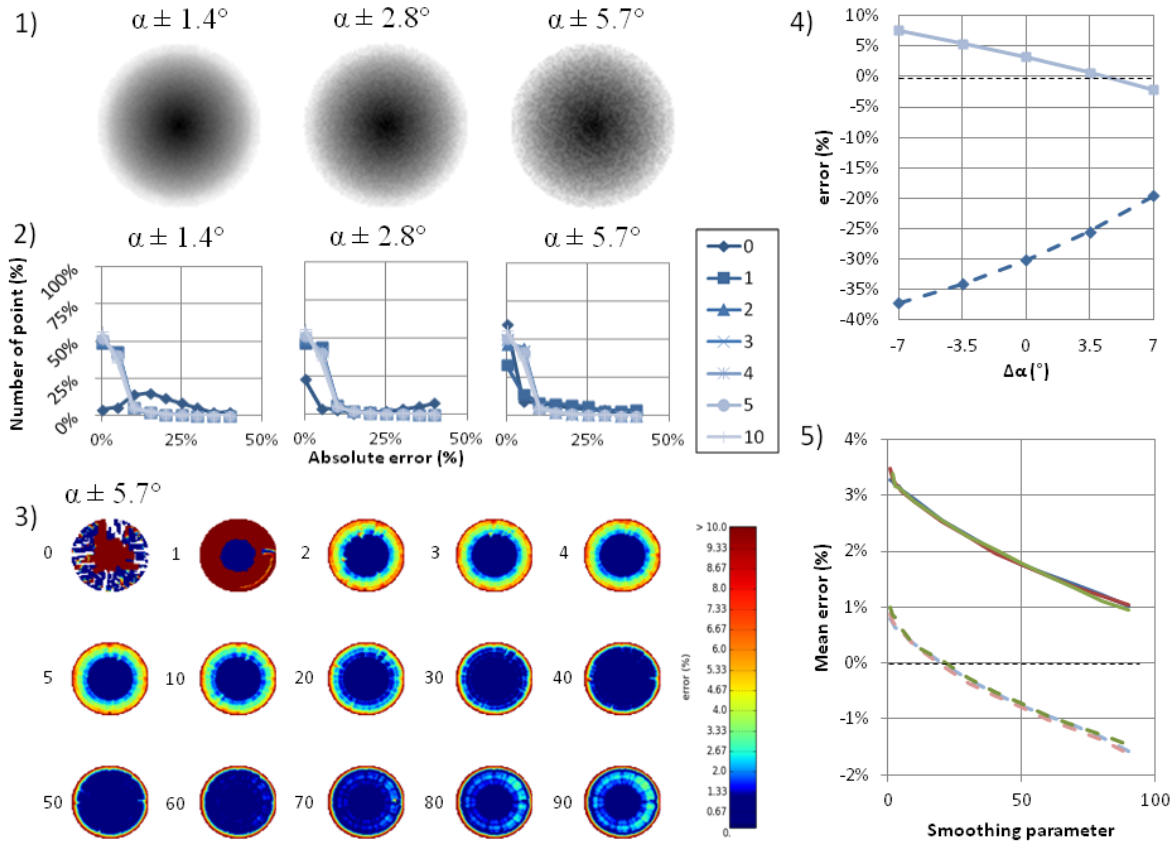
Error distribution (Figure 10-2) shows that if the smoothing method is applied between 1 and 10 times on the  $\alpha$ -matrices with noise amplitude of  $\pm 1.4^\circ$  and  $\pm 2.8^\circ$ , or between 2 and 10 times for the  $\alpha$ -matrices with noise amplitude of  $\pm 5.7^\circ$ , then the majority of the reconstructed point ( $> 95\%$ ) have an absolute error lower than 5% of the hemisphere radius and this error does not vary much. Figure 10-3 shows the error matrices of the  $\alpha$ -matrix with noise amplitude of  $\pm 5.7^\circ$  and with the different smoothing value. This figure confirms that the application of the smoothing method between 2 and 10 times does not change the global distribution of the error. Yet if the method is applied 20 to 70 times, the reconstruction becomes more accurate. It loses accuracy with a larger number of application though ( $\geq 80$ ). In addition, the local distribution shows a non-symmetrical pattern for an application of 2, 3 and 4 times. This is the consequence of an incorrect extraction of the iso- $\alpha$  curves. After a fifth smoothing application, the local distribution becomes symmetrical. In the case the smoothing procedure is not applied, the hemisphere is not reconstructed entirely (Figure 10-3, first matrix), and error distribution is not good (Figure 10-2).

Bias of  $-7^\circ$ ,  $-3.5^\circ$ ,  $0^\circ$ ,  $3.5^\circ$  and  $7^\circ$  on the  $\alpha$  values of an hemisphere  $\alpha$ -matrix without noise have also been tested. Figure 10-4 shows the average error for each of the reconstruction (plain curve) in addition to the error between the real hemisphere area and the reconstructed surface area (dashed curve). Results show that an increase of the  $\alpha$  values decreases the average error that makes, consequently, the reconstructed surface area closer to the real area.

Finally, hemisphere  $\alpha$ -matrices with and without a bias of  $7^\circ$  and with noise amplitude of  $\pm 2.8^\circ$  are generated. As it has been previously shown, the average error decreases with the application of the smoothing method for both with (dashed curves) and without (plain curves) the bias on the  $\alpha$  values (Figure 10-5). In the case of matrices without bias, this error is positive and the application of the smoothing method improves globally the reconstruction. In the case of a bias, this error becomes negative after 20 applications of the smoothing method. The two curves represented here are similar to a constant value which suggests that an  $\alpha$  value bias translates the average error in the case of the hemisphere reconstruction.

### 3.3.2 Size of the $\alpha$ -photograph and quantification

Synthetic hemispheres of radius 20 represented in  $\alpha$ -matrices of size 25, 34, 41, 47, 53 and 58 pixels are generated to study the impact of matrix size and  $\alpha$  quantification. The  $\alpha$  values of those matrix are either biased ( $\Delta\alpha = +3.5^\circ$ ) or non biased. Quantification percentile are chosen such



**Figure 10:** (1) Hemisphere  $\alpha$ -matrix with noise of  $\pm 1.4^\circ$ ,  $\pm 2.8^\circ$  and  $\pm 5.7^\circ$ . (2) Error distribution for the reconstruction of the hemispheres with different number neighboring averaging. (3) Error matrices for each step of the smoothing method. (4) Average error (plain) and area error (dashed) of the reconstruction of the hemisphere with biased  $\alpha$ . (5) Average error of the reconstruction for different value of smoothing application and with non-biased (plain) and biased (dashed)  $\alpha$ -matrix.

that they represent 5%, 10%, and 20% of the domains, and the seeds are chosen such they have a constant quantification percentile of 20%. Figure 11 shows the iso- $\alpha$  curves extraction (in red) with error matrices for the reconstruction carried out on the  $\alpha$ -matrices with and without bias. This figure shows that the reconstruction quality depends on the matrix resolution but also on the  $\alpha$  values chosen for the quantification.

Iso- $\alpha$  curves reconstruction depends on the  $\alpha$ -matrix resolution. This reconstruction is of lesser quality when the resolution is low. For instance, those curves are not perfectly circular for the matrices of size 25, 34 and 41 pixels. They rather have a polygonal shape. Conversely, the matrices of size 47, 53 and 58 pixels provide a better curves estimation: their polygonal shape is smoother. Consequently, the pattern of the absolute relative error matrices shows irregularity on the vertex of those polygon. For instance, the matrix of size 41 with a quantification percentile of 20% looks like a star with height spikes. The error matrices of size 47, 53 and 58 pixels have also spike like shapes, but those spike are more distant from the seed. This pattern is also induced by the use of planar SPS instead of conical or circular SPS. Polygonal shape of the iso- $\alpha$  curves makes GS divergence larger and consequently, the region that should be filled by those planar SPS become

larger. That amplifies the error made by planar SPS interpolation.

The accuracy of the iso- $\alpha$  curve extraction affect IC and OC estimation and initialization. If those curves are incorrectly approximated, GS estimation is of low quality and an error is propagated. In addition, the more  $\alpha$  values are taken into account in the quantification, the more this error is amplified. For instance, the reconstruction of the hemisphere from the  $\alpha$ -matrix of size 25 pixels is better with a quantification percentile of 20% than with a quantification percentile of 5%. However, the distance between two consecutive iso- $\alpha$  curves prevails over their accuracy if well extracted as it is the case with higher resolution  $\alpha$ -matrices. For instance, a quantification percentile of 20% provide a lesser quality reconstruction with the matrix of size 58 than a percentile of 10%. If this percentile is too low (e.g., 5%), the amplification of the error due to the number of curves met during the propagation is visible at the rim of the hemisphere silhouette.

Bias of the  $\alpha$  values can help to compensate the propagation error. For every resolution used in this study, error matrices have the same pattern when the hemisphere is reconstructed from both a quantification percentile of 10% without bias and a quantification percentile of 20% with a bias of  $3.5^\circ$ .

In conclusion, both the size of the  $\alpha$ -matrix and the quantification percentile affect the hemisphere reconstruction. If the matrix is small, the percentile should be large to avoid error propagation due to the low accuracy of the iso- $\alpha$  curve extraction. Conversely, if the matrix is large, this percentile can be small. In the case of a high resolution together with a large percentile, a bias in the  $\alpha$  values can be used to compensate the propagation of the error due to the distance between consecutive iso- $\alpha$  curves.

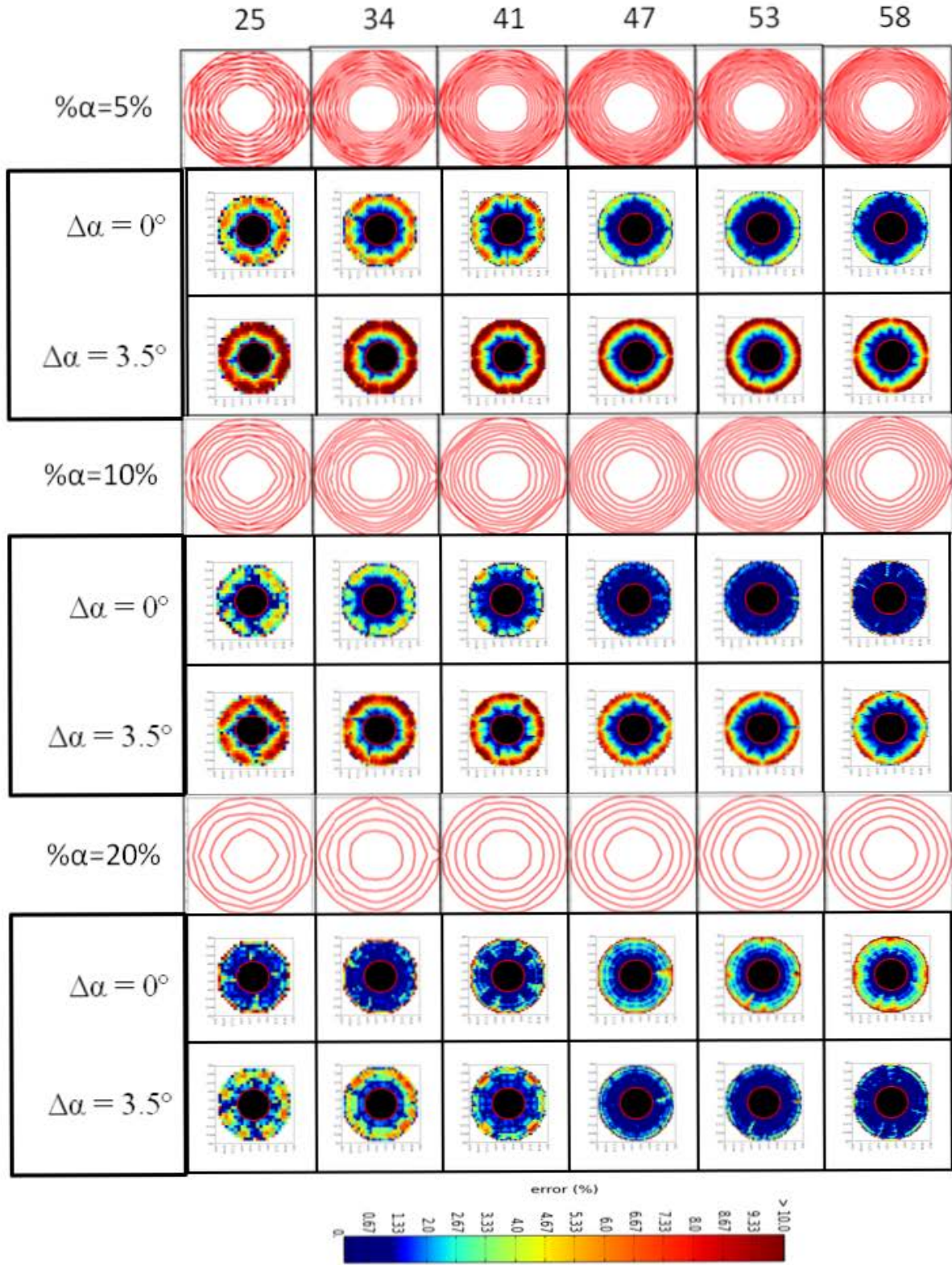
### 3.3.3 Low-pass filter parameter

The seeds OC can have noise and it is necessary to use method in order to extract correct 3D representation of their boundary curve. Noise is generally represented with high-frequency values whereas the curve signal, i.e., its shape, is rather represented with low-frequency values. In our pipeline, we have implemented a low-pass filter [207]. This filter consists of expressing the curve in the Fourier domain and to only keep the frequencies that are lower than a given bound, the cutoff value. Low-pass filter consists on keeping only those low-frequency signal. For instance, if a curve have a sinusoidal shape of frequency  $1/2$  and noise of frequency 1, a low-pass filter with a cutoff value of  $1/2$  can be used to extract the sinusoidal shape of the curve. If the noise has a frequency of  $1/2$  or less, then this filter is not adapted. In this way, assumptions on curve shape should be made to extract it correctly. For instance, if a curve is encircling a saddle point, then this curve has also a saddle shape, i.e., the shape of a sinusoidal with two peaks. If this curve has a length of  $l$ , then it has a sinusoidal period of  $l/2$ . A low-pass filter with a minimal cutoff value of

$$f_{min} = 2/l \quad (3.4)$$

can be used to extract this curve. Similarly, if this curve is encircling a monkey saddle, i.e., it has a shape of a sinusoidal with three peaks, then a cutoff value of  $f_{min} = 3/l$  can be used.

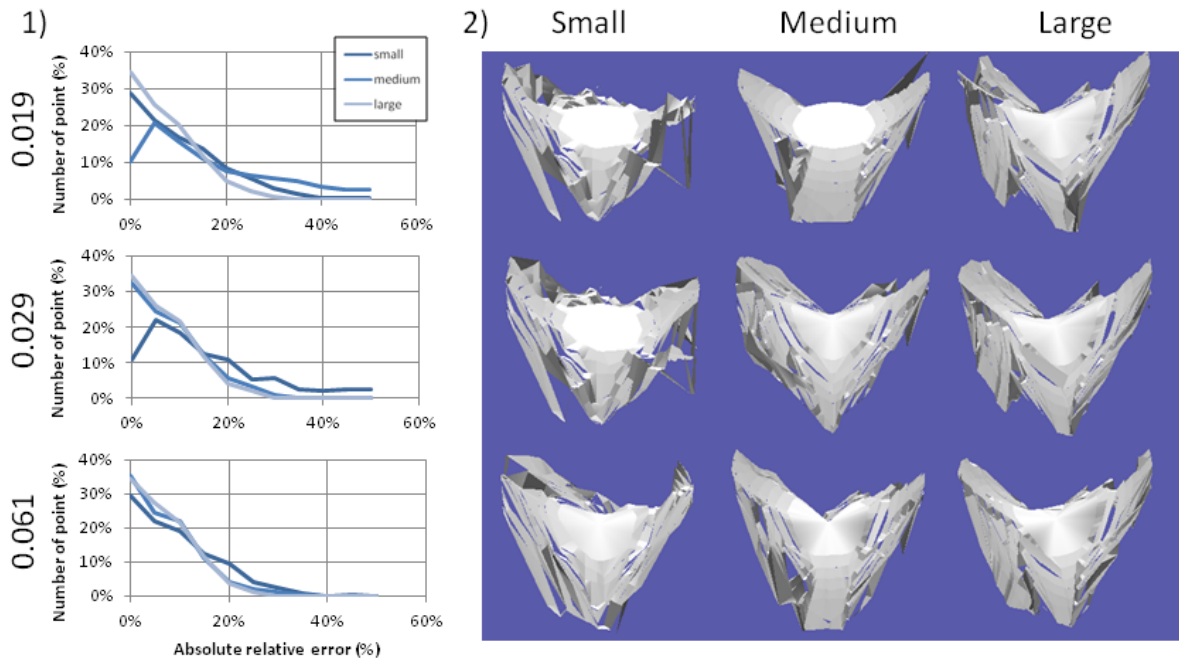




**Figure 11:** Iso- $\alpha$  curves of the hemisphere (in red) represented in a  $\alpha$ -matrix with a size of 25, 34, 41, 47, 53 and 58 pixels and with a quantification percentile of 5%, 10% and 20%. The seeds have the same size (black area). Error matrix of the reconstructed hemisphere with  $\alpha$ -matrix without and with biased  $\alpha$  ( $\Delta \alpha = 3.5^\circ$ ).

Three saddle surface are generated with noise amplitude on the distance 10% the total surface height. When their seed curves are extracted, the noise is of larger frequency than the curve frequency. Those three saddle surfaces are represented as matrices of size 25, 50 and 75 pixels (small, medium and large). The seed 2D curves are supposed to be circular, and they have an area of 88, 376 and 857 pixels and a perimeter length  $l$  of 33, 68 and 103, respectively. We use the Equation 3.4 to define the low-pass filter cutoff value. Those have a value of 0.061, 0.029 and 0.019, respectively.

Figure 12 shows the reconstruction of the three saddle surfaces together with the distribution of their absolute relative error for the three low-pass filter cutoff values. If the filter bound is too large, the noise is kept in the 3D representation of the seed OC (e.g., the value 0.061 for the large saddle surface). If this value is too small, the seed OC is flat and the reconstruction is affected (e.g., the value 0.019 for the small saddle surface). That shows that the choice of a good parameter is necessary to have a correct reconstruction. For instance, the bound value 0.061 is more adapted for the small saddle reconstruction than the value 0.019. This improvement is visible both in the error distribution and in the visual representation of the surface. In term of absolute error, a larger filter boundary make less perturbation in the accuracy of the reconstruction.



**Figure 12:** (1) Error distribution of the saddle surface reconstruction low-pass filter of cutoff value 0.019, 0.029 and 0.061 from a small, medium and large  $\alpha$ -matrix. (2) Mesh of the reconstruction.

### 3.3.4 Quantification and saddle point

In Section 3.3.2, we tested several values of quantification to reconstruct a hemisphere (case of a summit point type). In Section 3.3.3, we tested several low-pass filter cutoff values to reconstruct

saddle surfaces. We will now apply our algorithm with several values of quantification percentile on a saddle surface with a lesser symmetrical shape than in the previous section.

The saddle surface that is reconstructed is extracted from the synthetic vase example given by Durou et al. [169]. This vase is defined by the equations:

$$f(x) = \frac{1}{12.8} \cdot (-138.24 \cdot x^6 + 92.16 \cdot x^5 + 84.48 \cdot x^4 - 48.64 \cdot x^3 - 17.60 \cdot x^2 + 6.4 \cdot x + 3.2) \quad (3.5)$$

$$z = \begin{cases} (f(x)^2 - y^2)^{\frac{1}{2}} & \text{if } f(x)^2 \geq y^2 \\ 0 & \text{else} \end{cases} \quad (3.6)$$

To extract the vase col, i.e., its saddle area, we consider  $x \in [-5.54, -1.27]$  and  $y \in [-2.2, 2.2]$  (Figure 13-1).

The quantification percentile used are 20%, 10% and 5% with seeds of percentile 20%. The reconstruction of this saddle surface shows that the use of a small percentile decreases the local absolute error (Figure 13-3) and improves the reconstructed shape (Figure 13-2). In the error matrices, the corner of the surface are better reconstructed if the percentile is lower (Figure 13-3.iii) and the shape is more realistic. Yet on this corner the shape has the tendency to diverge from the real shape. This might be due to a bad management of the toggle point in this case: those ones are points that indicates a change in the GS propagation, yet in this vase col case, those GS keep the same orientation.

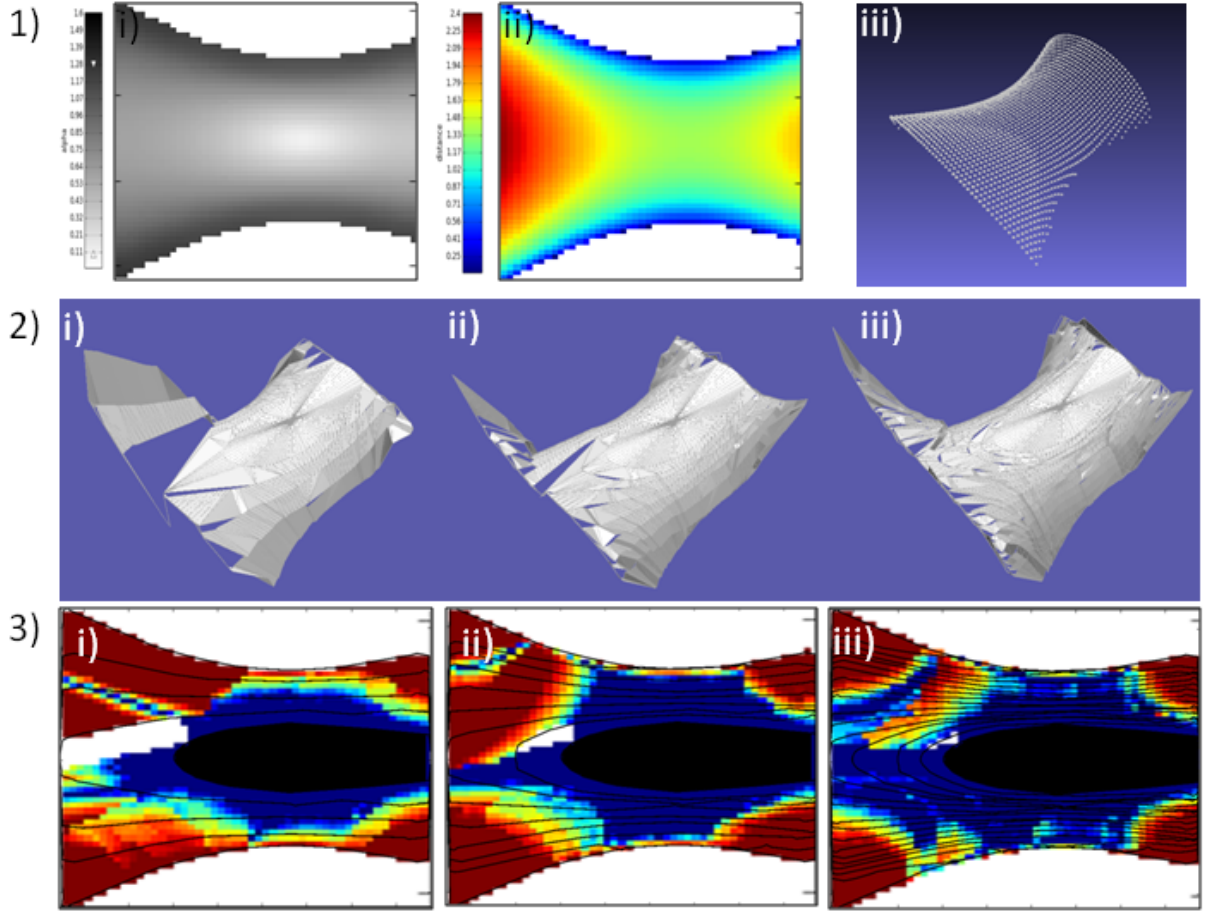
### 3.4 Complexity

The developed PROP-SFS method requires several pre-processing before the running of the propagation of the reconstruction. Surface domains segmentation, construction of the iso- $\alpha$  domains chain and seeds OC initialization are important steps. The smoothing of the  $\alpha$ -matrix could be necessary in case of noise and requires variable computing time. Finally, 2D curves extraction is a process for which computing time is difficult to estimate. The chosen curve extraction algorithm does not depend on the number of point, but rather on the local curvature of surface. Its computing time decreases with curvature increase [195]. Those pre-processing makes it difficult to estimate theoretically the complexity of our algorithm. We will rather make an empirical estimation of its computing time.

The produced data (iso- $\alpha$  chain, curves, 3D points, etc.) depends only on the number of pixel of the matrices and the quantification values used to extract the iso- $\alpha$  domains but neither on the  $\alpha$ -matrix smoothing nor the curve extraction process. Number of pixels (denoted  $a_{tot}$ ) and the chosen  $\alpha$  values to quantify the  $\alpha$ -matrix also affect the computing time. We assume that the size of the data (denoted  $s$ , in Mo) is linearly correlated to the computing time (denoted  $t$ ).

The relationship between the number of points of the  $\alpha$ -matrix, the  $\alpha$  values chosen to extract the iso- $\alpha$  domain and the computation time is studied on a synthetic hemisphere. A data set of hemispheres of radius 20 and represented in  $\alpha$ -matrices of size 25, 34, 41, 47, 53 and 58 pixels





**Figure 13:** (1) Vase col: (i)  $\alpha$ -matrix, (ii) distance matrix and (iii) initial point cloud. (2) Reconstruction with quantification percentile of: (i) 20%, (ii) 10%, and (iii) 5%. (3) Difference matrix with iso- $\alpha$  curves and the seed (in black) with quantification percentile of: (i) 20%, (ii) 10%, and (iii) 5%.

are generated. The quantification percentile (denoted  $\epsilon_\alpha$ ) are chosen such that they represent 5%, 10%, 15% and 20% of the domains.

In Figure 14-1, the file size  $s$  is related to the quantification percentile for each of the reconstructed hemisphere. An interpolation of this relationship provides the following equation:

$$s = \tau \cdot \epsilon_\alpha^{-1.12}, \quad (3.7)$$

with  $\tau$  a coefficient varying with  $a_{tot}$ . If related to  $a_{tot}$  (Figure 14-2), we obtain:

$$\tau = 0.025 \cdot a_{tot}^{1.37}. \quad (3.8)$$

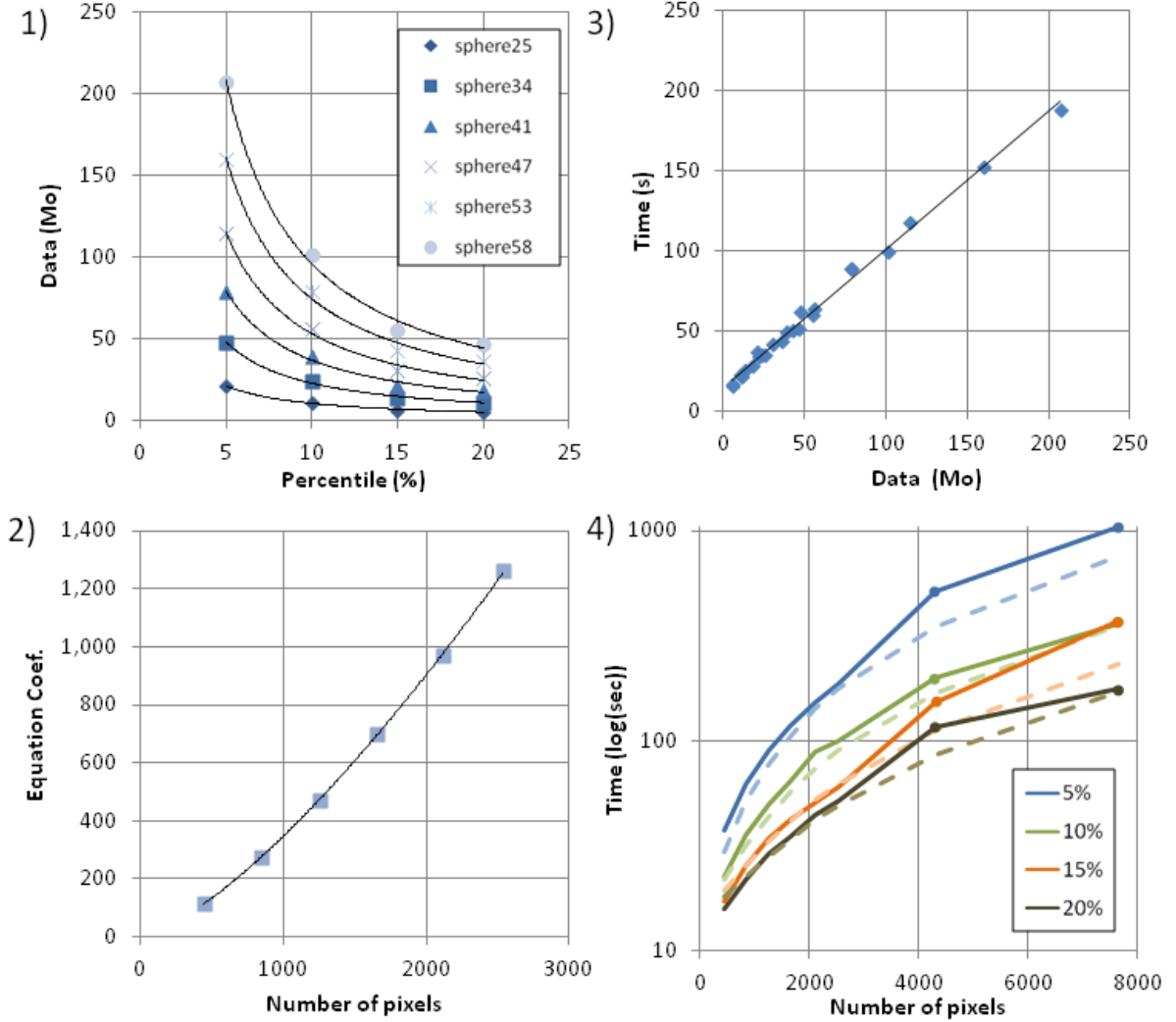
Combination of Equations 3.7 and 3.8 gives:

$$s = 0.025 \cdot \frac{a_{tot}^{1.37}}{\epsilon_\alpha^{1.12}}. \quad (3.9)$$

Each of the hemisphere are reconstructed four times and the shortest computing time are kept. The linear relationship between the files size  $s$  and computing time  $t$  is (Figure14-3):

$$t = 0.022 \cdot \frac{a_{tot}^{1.37}}{\epsilon_\alpha^{1.12}} + 14. \quad (3.10)$$

Additional  $\alpha$ -matrix of size 75 and 100 with the same quantification percentile are used to validate this equation (Figure 14-4, dots). Those extra data show that the equation 3.10 is reliable for the hemisphere reconstruction and for intermediate quantification percentile and  $\alpha$ -matrix size. This estimation is done for a simple case and cannot directly be extrapolated to other objects. Yet it gives an idea of computing time for object of such sizes.



**Figure 14:** (1) Size of the output data versus the quantification percentile for different image size. (2) Relationship between equation 3.7 coefficients and the number of pixels. (3) Correlation graph between the size of the output data and the computation time. (4) Comparison between modeled (dashed curves) and effective (plain curves) computation time. Dot: additional matrix to validate the model.

## 4 Conclusion

In Chapter 4 we proved that  $\alpha$ -photograph with constant  $\alpha$ -values is corresponding to SPS. In this chapter, we set up a PROP-SFS pipeline that uses SPS GS property to propagate surface iso- $\alpha$  regions reconstruction. We developed three main components: (i)  $\alpha$ -photograph matrix iso- $\alpha$  domain extraction and ordering, (ii) initialization of the 3D seed from distance data, and (iii)

propagation of the SPS starting from the seed and along consecutive surface iso- $\alpha$  region. To set up the last component, we used basic geometric and SPS properties to construct and propagate SPS greatest slope lines from a surface iso- $\alpha$  region boundary.

Our PROP-SFS method has been shown to be sensitive to: (i) picture size  $a_{tot}$  and quantification percentile  $\epsilon_\alpha$ , (ii) noise and bias on  $\alpha$ -values, and (iii) distance noise.

- (i) Reconstruction error are propagated [163]. This error depends on the distance of the reconstruction from the seed, but also, in our case, on the quality of the iso- $\alpha$  domain boundary extraction. Boundary estimation error is added to the propagation error throughout the propagation. In the case of small matrices, the quality of boundary extraction is low, whereas large matrices lead us to better boundary extraction. In the first case, it is thus necessary to extract a low amount of iso- $\alpha$  domains to limit error propagation caused by boundary estimation error.
- (ii) On a synthetic hemisphere  $\alpha$ -matrix with  $\alpha$ -noise of maximum  $\pm 5.7^\circ$ , we showed that local averaging smoothing method should be applied at least five times to obtain correct reconstruction. Yet this value cannot be used for every object  $\alpha$ -matrix as we did not take into account seed numbers and iso- $\alpha$  domain boundary complexity (e.g., curvature and concavities).
- (iii) SPS greatest slope computation depends on 3D curve shape. In particular, it depends on the 3D seed boundary shape. If this latest curve has been incorrectly extracted due to noise, the greatest slope computation is incorrect. Thus noise should be avoided on this curve as much as possible. A low-pass filter has been implemented to extract curve information from noisy distance data. A cutoff value can be chosen with assumption on curve shape (e.g., number of peaks).

Results of our PROP-SFS method were satisfactory. In addition, we managed to complete strategies proposed by Peternell, and Dragnea and Angelopoulou [196, 185], that are: (i) the generalization of the method to any isophote region, and (ii) the construction of GS lines from isophote region boundary.



## **Part III**

**Application: Conference pear tree leaf area  
and inclination estimation from TLS FARO  
LS880 data**



# Chapter 6

## Intensity properties of a TLS FARO LS880 to measure Conference pear tree leaves geometry

To recover leaves area from 3D scan of tree canopy, TLS distance data cannot be directly used because of the significant amount of outlier points around leaves edge. Nowadays, TLS system provides TLS beam intensity return data. As this intensity is related to the incidence angle  $\alpha$  between the surfaces and the laser beam, this intensity can be used as a geometrical indicator to correct outlier points and thus, to reconstruct realistic surfaces. To do so, we developed a PROPSFS method based on incidence angle  $\alpha$  information (Chapter 5). Yet TLS does not directly provide those incidence angle data. It rather provides intensity  $I$  and to get incidence angle  $\alpha$ , we have to set up relationship between  $I$  and  $\alpha$ . As it has been mentioned in Chapter 1, intensity depends on object distance due to light extinction. Yet the design TLS emitter/sensor system makes the recording of intensity different than the one described with the classic light extinction law [40]. Thus, we need to study the distance effect on intensity to correct it.

This chapter is based on the article “The properties of terrestrial laser system intensity for measuring leaf geometries: A case study with Conference pear trees (*Pyrus Communis*)” published in Sensors in January 2011 [42]. It proposes a distance effect on intensity correction based on the work of Kaasalainen et al. [40, 39] and it studies the relationship between the incidence angle  $\alpha$  and the TLS intensity both with laboratory and field condition.

## 1 Material and methods

### 1.1 TLS FARO LS880

#### 1.1.1 System characteristics

The TLS FARO LS880 is used in this study. The rotation of a mirror placed at  $45^\circ$  to the laser beam aperture (horizontal rotation) and the rotation of its trunnion (vertical rotation) provide a panoramic

view of the scene that is surrounding the TLS as a 3D point cloud in a Cartesian or in a spherical basis. The scans are proceeded with an angular resolution of  $0.018^\circ$  for both azimuthal and elevation rotation. This device uses the AM-CW technology: the amplitude of the laser is modulated and an analysis of the frequencies of the backscattered signal provides the distance. Between the mirror and the photo-diode of the scanner, optical elements (e.g., filters) reduce the intensity for small distances to avoid overexposure of the sensor. Therefore, the relationship between the intensity and distance follows neither the inverse square power law nor any linear function. In addition, the electric-converted signal passes through a logarithmic amplifier that provides a logarithmic relationship between different reflectance [39]. Each point has an extra dimensionless value that is the intensity (ranging from 0 to 2047 in digital numbers) measured by the system. Details on the features of the TLS FARO LS 880 are given Table 1.

<b>LiDAR technology</b>	Phase shift
<b>FOV (zenith <math>\times</math> azimuth)</b>	$320^\circ \times 360^\circ$
<b>Wavelength</b>	785 nm (NIR)
<b>Diameter beam aperture</b>	3 mm
<b>Beam divergence</b>	$0.014^\circ$
<b>Sensor FOV</b>	3 mrad
<b>Angle resolution used</b>	$0.018^\circ$
<b>Distance range</b>	0.6 m–76 m
<b>Distance accuracy</b>	$\pm 3$ mm at 25 m
<b>Distance precision @ 10m (RMS for filtered / raw data )</b>	
<b>90 % reflectance</b>	0.7/2.6 mm
<b>10% reflectance</b>	1.3/5.2 mm

**Table 1:** TLS FARO LS 880 technical specification provided by the constructor.

### 1.1.2 TLS intensity and its dependencies

Theoretically, the photometric appearance of an object depends on surface geometry, material properties, illumination and viewing direction of the camera (i.e., the TLS sensor) [209]. As it has been mentioned in Chapter 1, the relationship between the received light power  $P_R$  and the transmitted light power  $P_T$  is highly dependent on angle of incidence, distance and material reflectance properties [37]:

$$P_R = \eta \cdot \frac{A_R \cdot P_T \cdot \rho(\alpha) \cdot \cos(\alpha)}{\pi \cdot d^2}, \quad (1.1)$$

with  $A_R$  the receiver aperture area and  $\eta$  the receiver's efficiency,  $\alpha$  the angle of incidence with the material,  $\rho(\alpha)$  the reflectance value in function the angle of incidence between the TLS beam and the material surface (constant in the case of Lambertian material) and  $d$  the distance between the TLS beam aperture and the scanned object. As the TLS FARO LS880 has an intensity filter and with the assumption that this filter has only an impact on the intensity variations due to distance, the inverse square law could be replaced by a device specific distance function  $f$ . Finally, the intensity



is modified by a logarithmic converter. The received power could be expressed as follows:

$$P_R = \log \left( \eta \cdot \frac{A_R \cdot P_T \cdot \rho(\alpha) \cdot \cos(\alpha)}{\pi} \cdot f(d) \right) \quad (1.2)$$

$$= \underbrace{\log \left( \frac{A_R \cdot P_T}{\pi \cdot d^2} \right)}_{(a)} + \underbrace{\log(\rho(\alpha))}_{(b)} + \underbrace{\log(\cos(\alpha))}_{(c)} + \underbrace{\log(f(d))}_{(d)}, \quad (1.3)$$

where (a) is a constant term of the formula while (b), (c) and (d) are its variable terms. Expressed through a logarithmic function, the nature of the intensity, distance and angular dependencies changes:

- There is a vertical translation of the graphs representing the received power and distance relationship at a fixed angle of incidence appears and this, for two different material reflectances (b and d). This is due to the logarithmic product-to-sum reduction.
- With the same reasoning, the received power and angle of incidence relationship has the same shape through distance (c and d).

In [39, 43, 61, 210], the authors experiment with the influence of distance, material and angle of incidence on the intensity on a Spectralon® and retrieve those two properties. In this publication, we will consider the received power as the intensity recorded by the TLS. As the objects of our study are leaves, the diameter of the TLS beam footprint is an important parameter. A flat surface with an angle of incidence of  $\alpha$ , which has its center at a distance  $d$  from the TLS beam aperture and with a TLS beam radius of  $r$  and a divergence of  $\delta$ , one gets the footprint major axis  $\Delta d_{max}$ :

$$\Delta d_{max} = \frac{2 \cdot r}{\cos(\alpha)} + \left( \frac{d + r \cdot \tan(\alpha)}{\cos(\alpha - \delta)} + \frac{d - r \cdot \tan(\alpha)}{\cos(\alpha + \delta)} \right) \cdot \sin(\delta). \quad (1.4)$$

In the case that the TLS footprint size is too large compared to the scanned object dimensions, a crosstalk effect and a mixing of the intensity and distance in the point cloud occur [104].

According to the manufacturer, ambient light (e.g., sun) has little impact on the intensity. It does not fade out the signal and the intensity data are similar for scanned scene with different ambient light. However, there is more noise in the point cloud with increasing distance and sometimes even no data at all, especially for low intensity. The FARO LS880 has been designed to be insensitive to solar irradiance, at least for ranges smaller than 10 m and/or for surfaces with medium to high reflectance.

## 1.2 Measurement setup

### 1.2.1 Study of distance effect on TLS intensity

As discussed in Section 1.1.2, the relationship graph between the intensity as the received power and the distance follows the property of a vertical translation for different material reflectances (term (b) in Equation 1.3). In [39], Kaasalainen et al. showed that this relationship is more variable

for close distance ( $<3$  m) due to the filter in the front of the TLS sensor whereas they resemble the inverse square law of light intensity for greater distances. Thus, to avoid the distance effect as it has been done by Kaasalainen et al. in [40], materials with different reflectances are scanned at varying distances. Its aim is to retrieve this vertical translation of the relationship graph. For this publication, materials are scanned on a board perpendicular to the laser beam at 0.35, 0.45, 0.6, 0.75, 0.8, 1, 1.5, 1.85, 2.15, 2.6, 3.6, 5, 7.5 and 10 m. Materials reflectance properties are measured at 785 nm with a Spectra-Vista HR1024 spectroradiometer (spectral resolution of 3.5 nm between 350 and 1,000 nm). Measured materials are a 99% reflectance Spectralon® white panel, five mate Canson® drawing papers (with 3%, 68%, 48%, 80%, 83% reflectance), a 22% reflectance Kodak® Grey Card and a matte 3% reflectance painted board. All these materials are either Lambertian or matte to be able to neglect the intensity variation due to the geometry of the measurement (combination of a hemispherical scan with flat materials), especially for short distances. Each material has a size of at least 8 x 8 cm to avoid intensity mixing due to the TLS beam footprint size at the point representing the scanned surface at 10 m. Finally, a piecewise interpolation of the intensity in function of the distance is calculated to retrieve intensity values at intermediate distances. This measurement setup allows a distance correction of the intensity.

### **1.2.2 Setting the relationship between corrected intensity and beam incidence angle with leaf surfaces**

In [61, 210], Voegtle and Wakaluk, and Pfeifer et al. showed the relationship between the angle of incidence and the intensity for a 99%-Spectralon®. To study the influence of the angle of incidence on the intensity with materials such as leaves, a goniometric platform has been built (Figure 2). Goniometric platform allows complete rotations around its vertical (azimuth) and horizontal axes (elevation). Protractors were fixed onto the structure of the goniometric platform to show the azimuth/elevation and rolling angle. The rolling angle variation was not used in this study. The platform was painted with a 3% reflectance black paint for an easier segmentation of the point cloud.

Ten leaves were randomly picked from 30 2-year old Conference pear trees on June 16th 2010 (Figure 1). Those trees are planted in two rows of 15 trees in an East-West direction with a distance of 30 cm between the trees and 360 cm between the rows. They were located in Heverlee, Belgium  $50^{\circ}51'33.89''\text{N}$ ,  $4^{\circ}40'48.45''\text{E}$ . Since pear tree leaves are curled [211], the picked leaves were cut in two parts along their central vein to be flattened as much as possible before the scanning procedure. They were fixed (abaxial and adaxial side) on the goniometric platform with black painted strings (Figure 2) and were scanned within the hour after collection. The average length of those leaves was 6.47 cm (0.5 cm standard deviation) and their average (half)-width was 2.19 cm (0.38 cm standard deviation). The goniometric platform was placed at 2.16 m from the TLS beam aperture. An increment of  $20^{\circ}$  on the vertical axis and subsequently on the horizontal axis was applied for each scan to get an angle of incidence ranging from  $0^{\circ}$  (perpendicular to the laser beam) to  $80^{\circ}$  (almost parallel to the laser beam). For each leaf, one to three sub-selections were

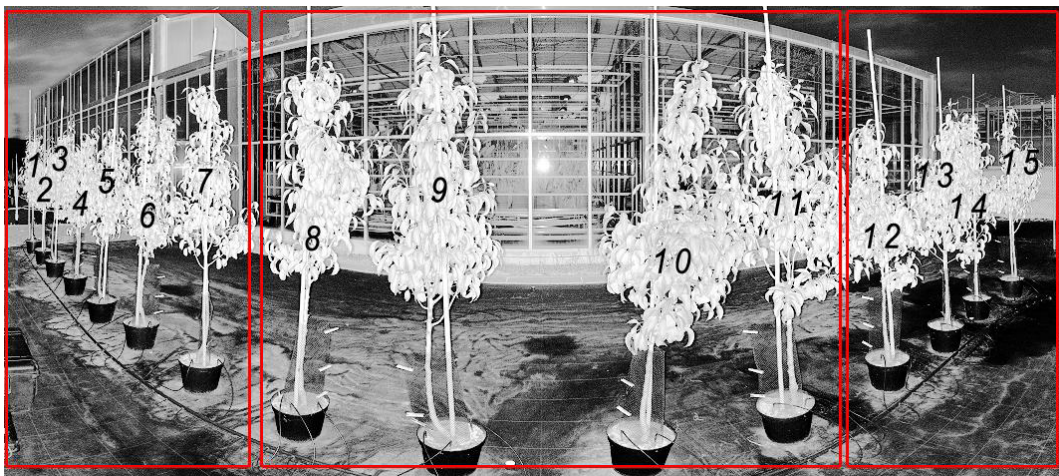
extracted from the point cloud depending on the angle of incidence and the size of the leaf. The angle of incidence with the leaf surface was then compared to the averaged corrected intensity on those sub-selections. The relationship between the intensity and the angle of incidence with pear tree leaves was so deducted.

In a second experiment, from each of the 15 pear trees of the first row, a second scan was made on June 24th 2010. A sub-selection of a flat part of each scanned leaf was made. The average corrected intensity of this sub-selection was then related to the angle of incidence provided by a Least Square Regression (LSR). This relationship was compared to the previously established intensity and angle of incidence relationship. Compared to the latter experiment, leaves were not at a constant distance and were not flat. Finally, the LSR was made on seven entire leaves for tree n°9 to gain a more thorough understanding of the leaves geometry impact on the TLS point cloud and intensity data.

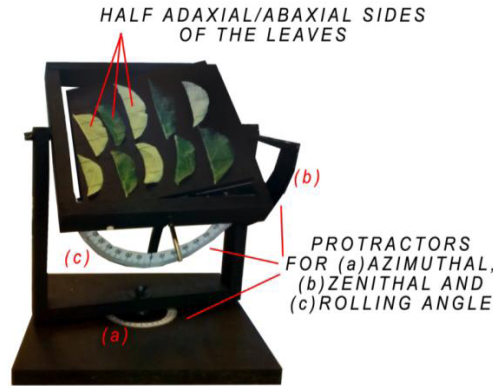
In this case, outlier points as wrinkles and curvatures are also selected. Then, the differences ( $\Delta\alpha$ ) between the angle of incidence found by this LSR and the angle of incidence provided by the intensity for each hit of the TLS beam are mapped for each of those seven leaves:

$$\Delta\alpha(x) = \alpha_1(x) - \alpha_{LSR} \quad (1.5)$$

with  $\alpha_1(x)$ , the angle of incidence computed with the intensity and angle of incidence relationship at a point  $x$  on the scanned leaf and  $\alpha_{LSR}$  the angle of incidence provided by the LSR on the entire leaf. The distributions (with normalized quantities) of those  $\Delta\alpha$  values are shown. The difference between the angle of incidence provided by the LSR and the one deduced by the average of the corrected intensity on the leaf is calculated.



**Figure 1:** Part of a hemispherical projection of a TLS scan of 15 two years old pear trees (first row). The corrected intensity and angle of incidence relationship is tested on leaves of those trees. Trees are grouped by their distance to the beam aperture (red frames).



**Figure 2:** The goniometric platform with its: (a) azimuth; (b) elevation and (c) rolling angle protractors. To be flattened, half adaxial and abaxial leaf faces were fixed with black strings.

### 1.3 TLS data pre-processing and analysis

First, a manual sub-selection of the point cloud and their corresponding intensity is made. A second sub-selection is made based on an intensity and distance threshold (Figure 3-i). To do so, a reference point is selected and neighboring points are considered hit points if their intensity and distance from the selected point are within the thresholds values. This approach limits the selection of edge effects of leaves as well as the distance and intensity crosstalk effect, mixing of multiple objects within the beam footprint [47, 24]. It also limits the selection of curvature and wrinkles of leaves. After data extraction, the analysis gives distance values, angle of incidence provided by the LSR, the average and standard deviation on the selected point's intensity and finally, the number of selected points.

#### 1.3.1 Correction of distance effect on intensity

A first study is made to establish the relationship between the intensity and the distance with the set up described in Section 1.2.1. In [39], Kaasalainen et al. showed that the relationship graph between intensity and distance for the FARO LS880 presents a vertical translation for the different reflectance. In this case, the relationship between intensity and distance can be interpolated by the same polynomial. In addition to the method suggested by Kaasalainen in [40], where the intensity is normalized by a 99%-Spectralon® intensity, an interpolation of the data is calculated to get intermediate values of intensity in function of the distance. As the relationship does not follow any analytical function because of the intensity filter (Equation 1.3), piecewise polynomial interpolations of order one or two are calculated and as those interpolations are equal, but vertically translated (Equations 1.3 and 1.4), only one piecewise polynomial interpolation should be calculated, namely, the one of the 99%-Spectralon® (denoted as  $f_{99\%}$ ).

Once done, a constant value  $c$  for a target material at a given incidence angle  $\alpha$  is determined by the difference between its intensity value and the intensity value of the 99%-Spectralon® at a fixed reference distance  $d_{ref}$ . One has  $c_{ref} = f_{99\%}(d_{ref}) - I(d_{ref})$  with  $I(d_{ref})$  the recorder intensity at an arbitrary reference distance. For each intensity  $I(d)$  for this same target at distance  $d$ , the

calibrated intensity,  $I_c$  (which is now independent of distance) is calculated as:

$$I_c = \frac{I(d)}{f_{99\%}(d) + c_{ref}} \cdot I(d_{ref}). \quad (1.6)$$

To know the quality of the distance correction, a Root Mean Square Error (RMSE) between the value of the piecewise polynomial interpolation  $f_{99\%}$  and the corrected intensity is calculated for each distance. Finally, as the value  $f(d_{ref})$  is unknown, the distance effect on the intensity is corrected with the following formula (Figure 3-ii):

$$I_c = f_{99\%}(d_{ref}) + c \quad (1.7)$$

with  $c = f_{99\%}(d) - I(d)$ .

Further investigation on the intensity correction, reflectance relationship and radiometric calibration could be done. In [41], Wagner defined a back-scattering coefficient related to the intensity in the case that the angle of incidence with the scanned surface is unknown. In [39], Kaasalainen et al. defined a logarithmic correction to estimate the reflectance value of a scanned object placed perpendicular to the TLS beam. They aimed to be able to compare different TLS intensity. Unlike this paper, the logarithmic correction is not made because of the reliability of the materials used in this study. Therefore, we assume that the sensor of TLS does not change over time. Thus, a full radiometric calibrated intensity will be needed for future research.

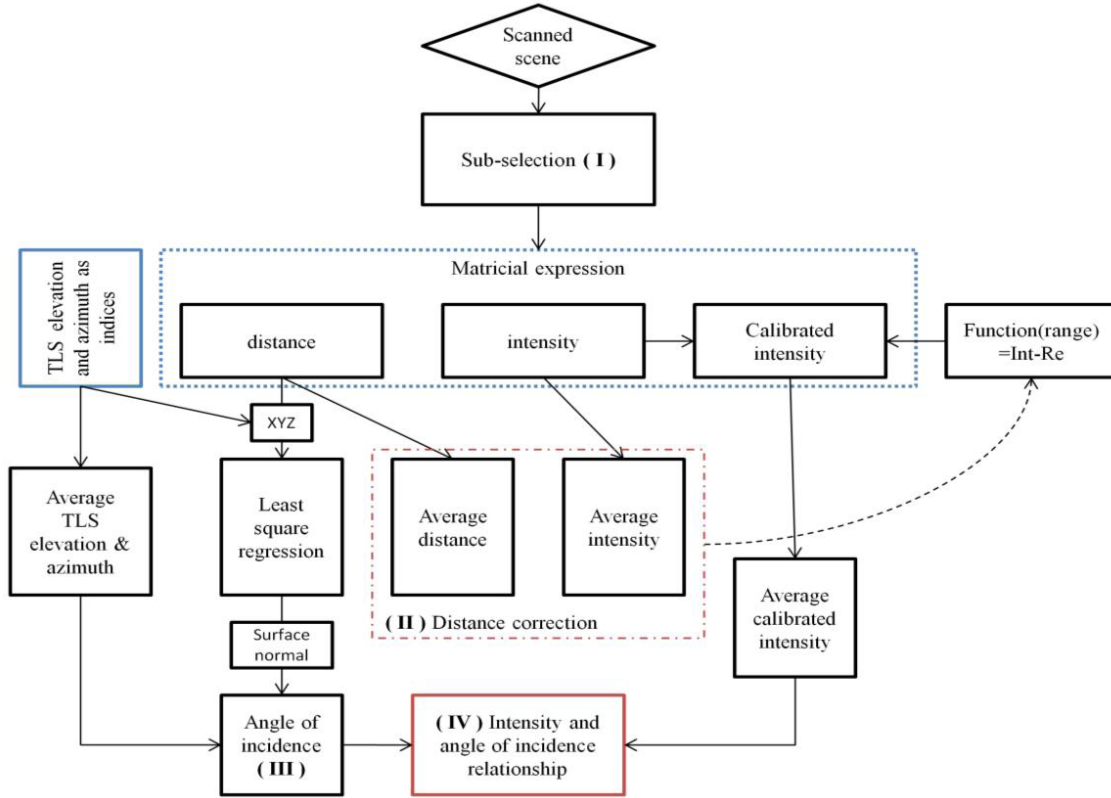
### 1.3.2 Determination of incidence angle with a Least Square Regression (LSR)

To obtain the angle of incidence with a surface (flat by assumption) represented by a selection from the point cloud, a Least Square Regression (LSR) is proceed on the sub-selection (Figure 3-iii). As there are three different LSRs related to each vector of the XYZ-basis, the LSR is selected that minimizes the RMSE and allows at most 5% of the point cloud outside a pre-defined orthogonal distance  $d_i$  to the fitted plane. Finally, the normal angle to the plane is given by the coefficient of the plane equation. The angle of incidence  $\alpha$  with the surface equals:

$$\alpha = |\cos\left(\frac{\mathbf{n} \cdot \mathbf{x}_s}{\|\mathbf{n}\| \cdot \|\mathbf{x}_s\|}\right) - \pi| \quad (1.8)$$

with  $\mathbf{x}_s$  the vector representing a reference point in the sub-selection and  $\mathbf{n}$  the normal to the surface calculated by the LSR.

The accuracy and precision of this method is tested with the goniometric platform with increments of  $10^\circ$  of its azimuthal and elevation angles. As statistical indicators, the  $r^2$ , slope and intercept of a linear regression of the angle determined by the LSR and the goniometric platform angle are given. The targeted platform is placed at approximately 2.05 m from the TLS beam aperture. Knowing the angle of incidence provided by the LSR, it can finally be related to the intensity averaged over the cloud of points selected (Figure 3-iv).



**Figure 3:** Analysis flowchart: (i) A semi-automatic and manual selection in the point cloud is proceeded. It takes into account a distance and an intensity threshold to limit unwanted point as outlier point or leaf curvature. (ii) The average distance and average intensity are calculated from the selected point cloud. Their relationship is used to correct the distance effect by replacing the intensity value by a reference value (correction of the distance effect on the intensity). (iii) The angle of incidence with the selected surface is calculated thanks to a LSR. (iv) The corrected intensities values of the selected points are averaged. The angle of incidence is then related to this averaged corrected intensity.

## 2 Results

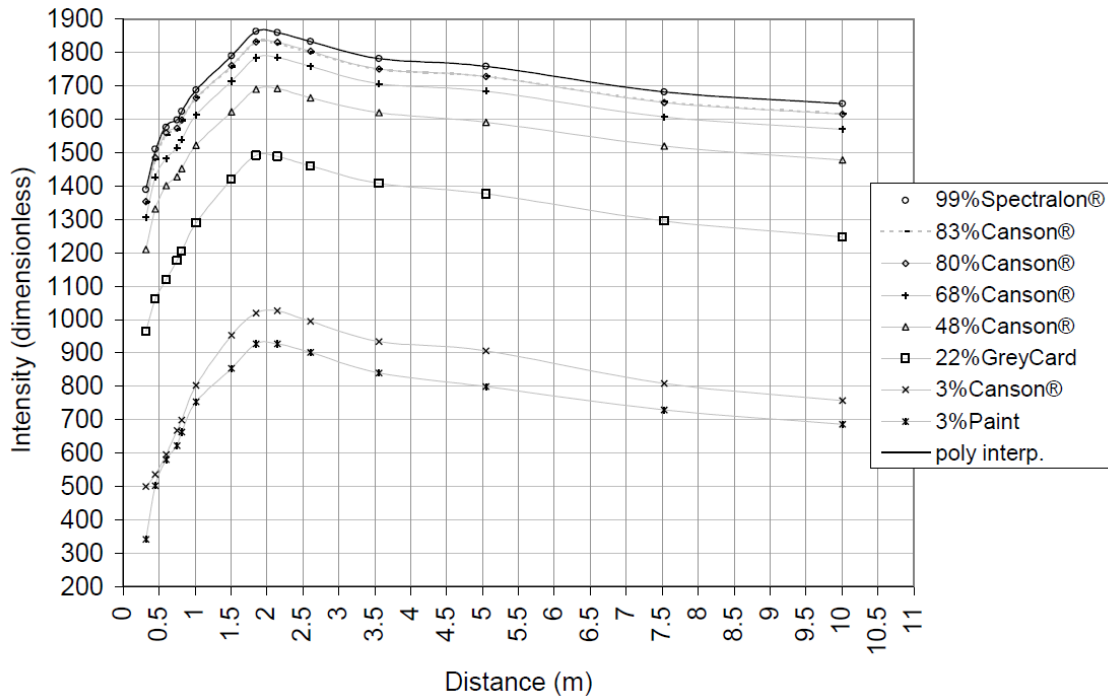
### 2.1 Correction of the distance effect on TLS intensity

As in [39], a vertical translation between the different intensity and distance relationships is revealed (Figure 4). Those translations have a very low standard deviation for materials with a reflectance value larger than 48% as presented in Table 2. This enables the generation of a reference piecewise polynomial interpolation on the 99%-Spectralon® graph and to correct the distance effect on the intensity as discussed in point 1.3.1.

Figure 5 shows the intensity correction given by the Equation 1.6. With the equation notation, the reference distance used ( $d_{ref}$ ) is 3.56 m and  $f_{99\%}$  intensity units. The LS880 logarithm filter effect is clear as can show relationships between the various reflectances measurements. The distance effect correction with the piecewise polynomial is valuable for a distance larger than 1 m, especially for materials with a reflectance larger than 48%, while the 22% reflectance Canson® paper yields results of inferior quality. This result is analogous to the FARO LS HE80 used by Kaasalainen

in [39]. The distance effect corrections of intensity value from materials with a reflectance of 3% (Canson® and paint) have the worst quality and the graph shows unexpected differences in terms of reflectance that have not been detected by the spectroradiometer. Similarly, the difference between the 80% and the 83% Canson® papers is not clear. The logarithmic correction suggested by Kaasalainen [40] is not performed because of those two last reasons.

The RMSE between the translated 99%-spectralon piecewise polynomial interpolation used as reference at a distance of 3.56 m (Equation 1.6) and the corrected intensity is lower than 4 units (corrected intensity) for materials with a reflectance larger than 48%, whereas it is larger than 10 units (corrected intensity) for reflectance values smaller than 22% (Table 2).

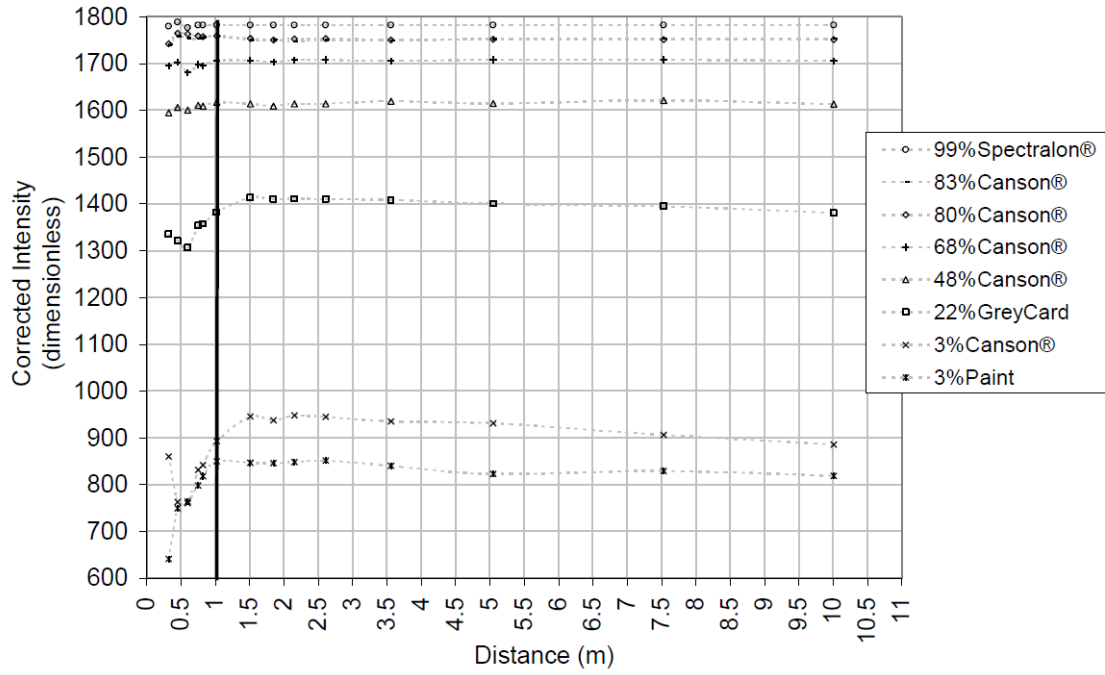


**Figure 4:** *Intensity and distance relationship for the FARO LS880 for different materials placed perpendicularly to the laser beam.*

## 2.2 Validation of the incidence angle provided by a LSR

The angle of incidence provided by the LSR provides acceptable results with the goniometric platform. The regression of the correlation graph between the angle of incidence calculated manually and the one given by the LSR provides an  $R^2$  of 1, a slope of 1 for both horizontal and vertical rotation and an intercept of  $1^\circ$  for vertical and  $2.8^\circ$  for horizontal rotation.





**Figure 5:** Correction of the distance effect on the intensity. The correction is valuable for distance greater than 1 m. The reference distance is 3.56 m.

	(i) Shift average (Raw value)	(ii) Standard deviation (Raw value)	(iii) Raw value at 3.56m	(iv) RMSE (corrected intensity)
<b>83% Canson®</b>	30.24	3.90	1749	2.98
<b>80% Canson®</b>	27.84	4.88	1750	2.50
<b>68% Canson®</b>	79.07	5.76	1705	1.60
<b>48% Canson®</b>	169.55	5.36	1619	3.66
<b>22% GreyCard</b>	399.30	29.87	1408	11.49
<b>3% Canson®</b>	884.93	49.66	839	21.52
<b>3% Paint</b>	961.55	34.09	935	11.49

**Table 2:** (i) Vertical translation (average on the distance) between the intensity value of the 99%-Spectralon® and the intensity value of other materials, (iii) Raw value at the reference distance (3.56 m), (iv) RMSE between the interpolation function  $f_{99\%}$  of the 99%-Spectralon® intensity (minus a constant, at the reference distance) and the measured intensity for distance larger than 1 m. Raw values range between 0 and 2047.



## **2.3 Relationship between intensity and incidence angle for Conference pear tree leaves**

### **2.3.1 Establishing relationship between intensity and incidence angle with leaves placed on a goniometric platform**

The angles of incidence provided by the LSR approximate the ones given by the protractors of the goniometric platform. Figure 6 shows that the angles of incidence vary with a maximum amplitude of  $\pm 10^\circ$  around the angle of incidence measured manually. At  $50^\circ$ , there is a shift of  $+10^\circ$  in the angle of incidence provided by the LSR. Indeed, despite the strings that are flattening the leaves, it is difficult to avoid wrinkling leaves when attached to the goniometric platform. In this way, the angles of incidence provided by the LSR are more realistic than the manually measured ones. Thus, those one are substituted by the angle of incidence provided by the LSR. Figure 6 shows that the intensity values increases with the decrease of the angle of incidence. In a first step, it increases quickly ( $+150$  units for  $10^\circ$ ) for angle of incidence decreasing from  $85^\circ$  to  $55^\circ$  and it starts to level off ( $+30$  units for  $10^\circ$ ) for angle of incidence decreasing from  $55^\circ$  to  $0^\circ$ . In addition, the variations of the intensity values are larger for angle of incidence larger than  $55^\circ$  ( $\pm 100$  units) whereas they are smaller for angle of incidence smaller than  $55^\circ$  ( $\pm 30$  units).

No clear difference appears between the azimuthal rotation of the goniometric platform and the elevation rotation. Given with a resolution of  $5^\circ$ , the curve of relationship between the corrected intensity and angle of incidence for the two different rotations are similar and the maximal absolute difference for the intensity is 20 units (corrected intensity) for an angle of incidence of  $10^\circ$ . This is negligible compared to the intensity variation as a function of angle of incidence. We get similar results in the comparison of the abaxial and adaxial sides of the leaves where the maximal absolute intensity difference 38 units (corrected intensity) for an angle of incidence of  $10^\circ$ , which is also negligible. Because of those two results, both cases are not taken into account in this study (graphs not shown).

Because of the size of the beam diameter and divergence, its footprint diameter could become larger than the leaf itself. It ranges from 0.046 m for an angle of incidence of  $85^\circ$  to 0.004 m for an angle of incidence of  $0^\circ$ . Figure 7 shows the variation of the footprint diameter as a function of angle and for the distance of 1, 2.16, 5 and 10 m. The diameter is calculated using Equation 1.4. Those footprint diameters are compared to the average widths and lengths of half pear tree leaves that were picked for the experiment. So, depending on the angle of incidence, the leaf size and the distance, the intensity values for the leaf material could be more sensitive to surrounding material. In Figure 6, the impact of the goniometric platform appears clearly for large angle of incidence. At this range (2.16 m) the intensity values decrease could be explained by the mixing of the goniometric platform and the leaves intensities.

At this distance, the TLS beam footprint diameter is 20% of the leaf width for an angle of incidence smaller than  $20^\circ$ , it is 45% of the leaf width for an angle of incidence greater than  $65^\circ$  and it exceeds the leaf width for an angle of incidence greater than  $80^\circ$ . Though the type of the laser

sensor is unknown, the weight of the goniometric platform intensity could be lower than suggested in Figure 7 and the previous discussion, especially if it is Gaussian as discussed by Lindenbergh et al. [212]. In addition, the LSR may present some issues to accurately represent a surface with a large angle of incidence because the point cloud quality is worse at those angle of incidence compared to the one of a surface that is perpendicular to the beam [212].

In conclusion, retrieving the angle of incidence with the intensity would have a precision of  $\pm 5^\circ$  and because of the diameter of the TLS beam footprint, it is not possible to measure the angle of incidence with the intensity for angle larger than  $55\text{--}60^\circ$ .

At a first sight, a logarithmic or cosine fitting could be made as it is insinuated in Equation 1.3-(b) and (c). The intensity and angle of incidence relationship can be expressed as:

$$\log(\rho(\alpha) \cdot \cos(\alpha)) \quad (2.1)$$

As one can see, three functions appear:

- the logarithmic function that has not been corrected,
- a cosine function, and
- the reflectance value  $\rho$  as a function of angle of incidence  $\alpha$  with the leaf surface.

As the optical properties of the leaves are unknown (they are not Lambertian [213]) and the logarithmic correction [39] cannot be made because their value of the TLS intensity for different reflectances are not consistent, as for example for low reflectance material (see Section 2.1), a fourth order polynomial fitting is finally made on the relationship between intensity and angle of incidence.

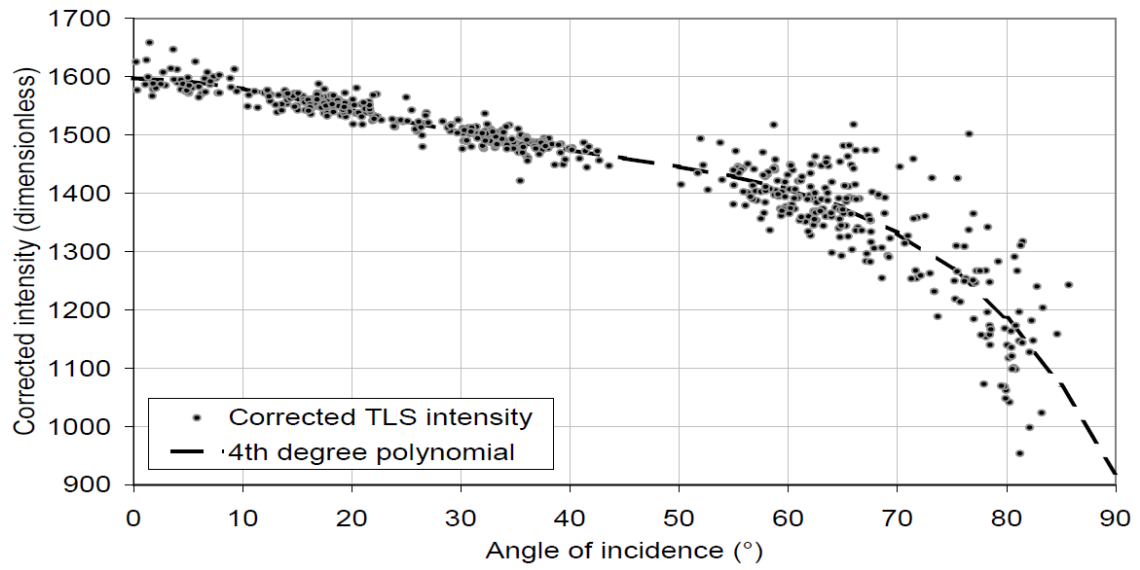
### 2.3.2 Testing relationship between corrected intensity and incidence angle on in-situ leaves

The test shows a vertical and positive translation in the intensity values for angles smaller than  $60^\circ$  (Figure 8) compared to the previously established relationship. It presents more variability. There is no clear difference between the different distances intensities, which means that the distance correction is valid.

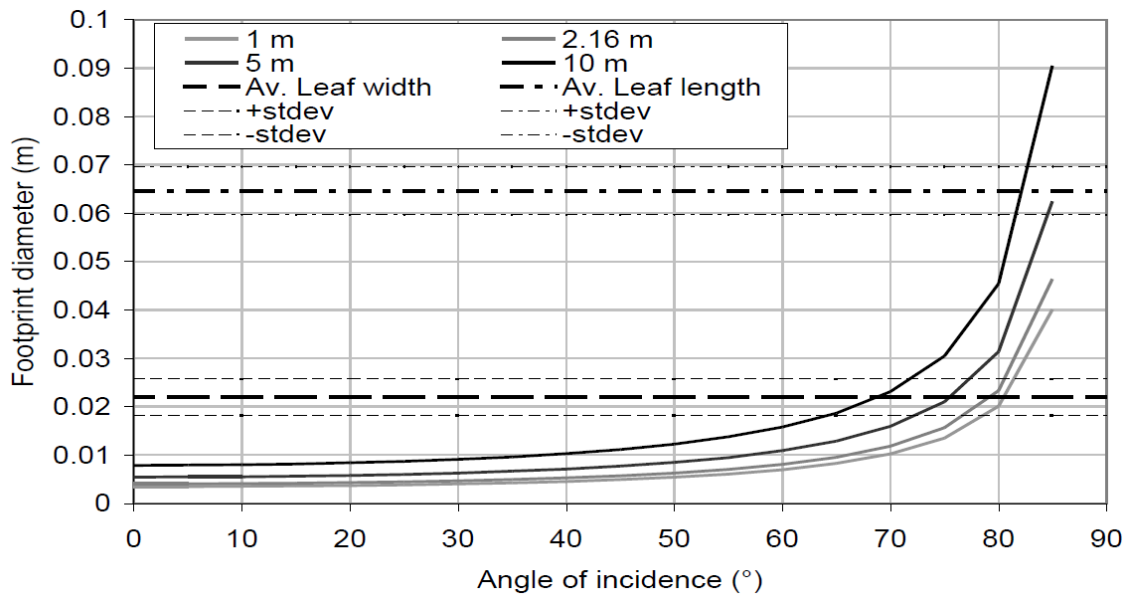
As in the previous experiment, the intensity increases with an angle of incidence decrease, but the measured intensity values are higher. It could be interpreted in two ways: (i) it is higher in terms of intensity and is vertically translated to +50 units (corrected intensity) or (ii) it is larger in terms of angle of incidence and is horizontally translated to  $+10^\circ$ .

In addition, the precision to find an angle of incidence from the corrected intensity for angles of incidence smaller than  $60^\circ$  is larger than in the previous experiment: (i)  $\pm 10^\circ$  for angles of incidence smaller than  $30^\circ$  and (ii)  $\pm 15^\circ$  for angles of incidence ranging from  $60^\circ$  to  $30^\circ$ .

Many reasons could occur to explain those two facts:



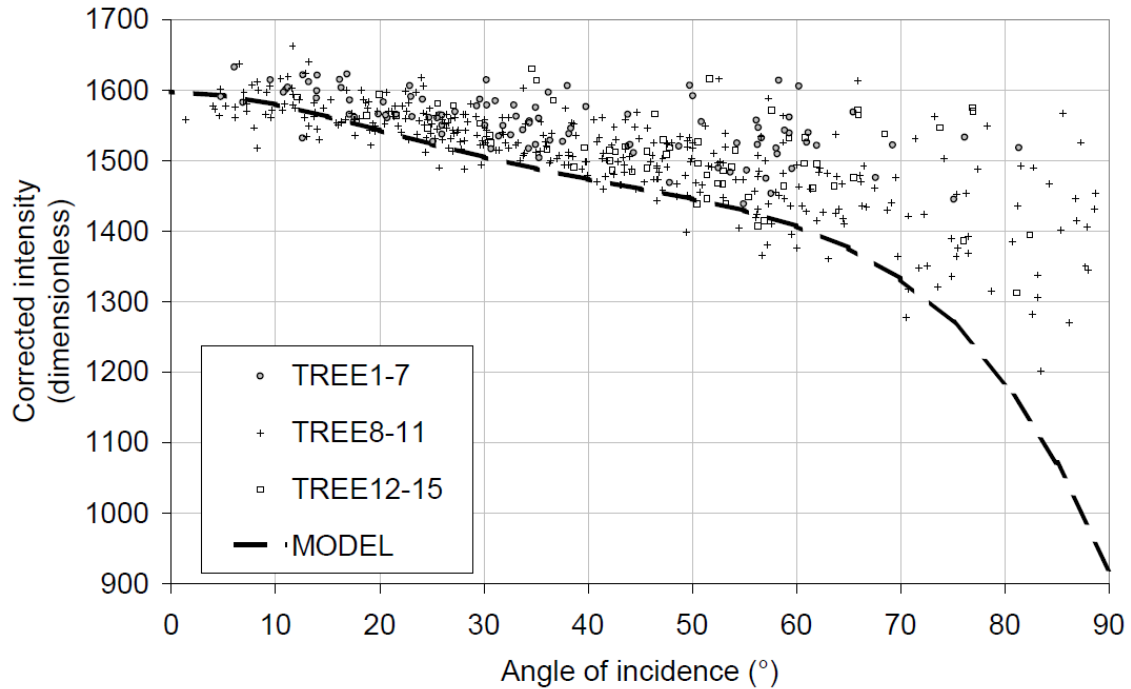
**Figure 6:** Corrected intensity and angle of incidence relationship for pear tree leaves placed on the goniometric platform. (•) is the average intensity of the selected point cloud representing the leaf. A fourth degree polynomial fitting is made to model this relationship (bold line). The angles of incidence is found by the LSR on the selected point cloud.



**Figure 7:** TLS beam footprint diameter as a function of angle of incidence and distance. This beam footprint diameter is compared to the average leaf widths and lengths.

- (i) **Curvatures:** It is possible that in the selection, undesirable parts of the point cloud are selected. Their intensity have a varying impact in the average intensity depending on the quantity of these undesirable points, whereas those points can easily have an impact in the LSR and thus on the angle of incidence. For instance:
- a. if a leaf that is perpendicular to the beam is selected and if this selection includes a sub-selection which forms a plane which is almost parallel to the beam, then, the LSR on this selection will provide an angle of incidence larger than expected and with a higher intensity (depending on the quantity of undesired points that are selected). That would be the reason why Figure 8 presents only a few selections with an angle of incidence smaller than  $5^\circ$ .
  - b. With a similar reasoning, the selection of a leaf including a zone which has a large angle of incidence with the TLS beam and a curved zone could present a smaller angle of incidence than expected.
- (ii) **Wrinkles:** In the case where a leaf that has many wrinkling is selected, then the impact of these on the intensity is significant whereas the LSR will not consider them.
- (iii) **Footprint and point cloud quality:** As the leaves are not placed onto on a larger flat surface such as the goniometric platform, the quality of the point cloud representing those leaves is lower especially for large angle of incidence and for increasing distances. This is the reason why there is a lack of data for the two groups of trees 1-7 and 12-15, especially for angle of incidences ranging from  $90^\circ$  to  $60^\circ$  (Figure 8 and Table 9). As it has been showed by Soudarissanane et al. [63], an increase of the angle of incidence implies a decrease in the point cloud precision.
- (iv) **Footprint and intensity mixing:** As in point 2.3.1, the footprint has a great impact on the intensity, especially for angles of incidence larger than  $60^\circ$  (Figure 7). This may be the reason why the data are different for those angles as the surrounding scene is different. However, the intensity values should be more accurate than the ones provided by the measurement on the goniometric platform, especially for angles of incidence smaller than  $60^\circ$  and despite the decrease in precision.
- Physiology:** The scans did not proceed at the same time. There is an 8 days difference between the scans with the leaves placed on the goniometric platform and the scans of the trees.
- Multiple scattering:** The scans proceeded under different conditions than in the case of leaves placed on the goniometric platform. Because of the complexity of the canopy, it is possible that a multiple scattering effect occurs which results in a higher than expected intensity.
- TLS radiometric calibration:** Due to the fact that the TLS has not been entirely calibrated, it is possible that the intensity of low reflectance objects changed through time.

Nevertheless, the scans having 8 days difference, one might expect that the sensitivity of the sensor has not moved as in [39].



**Figure 8:** Test of relationship between intensity and angle of incidence for leaves of in-situ pear trees. The bold line represents the reference curve established with the leaves on the goniometric platform.

Tree n°	Min. dist. (m)	Max. dist. (m)	# data
1-5	2.92	4.30	26
6	2.43	3.22	21
7	1.83	2.52	50
8	1.55	1.99	100
9	1.44	1.83	100
10	1.32	1.94	70
11	1.36	1.96	70
12	1.68	2.55	30
13	2.15	3.06	24
14	3.02	3.15	4
15	X	X	X

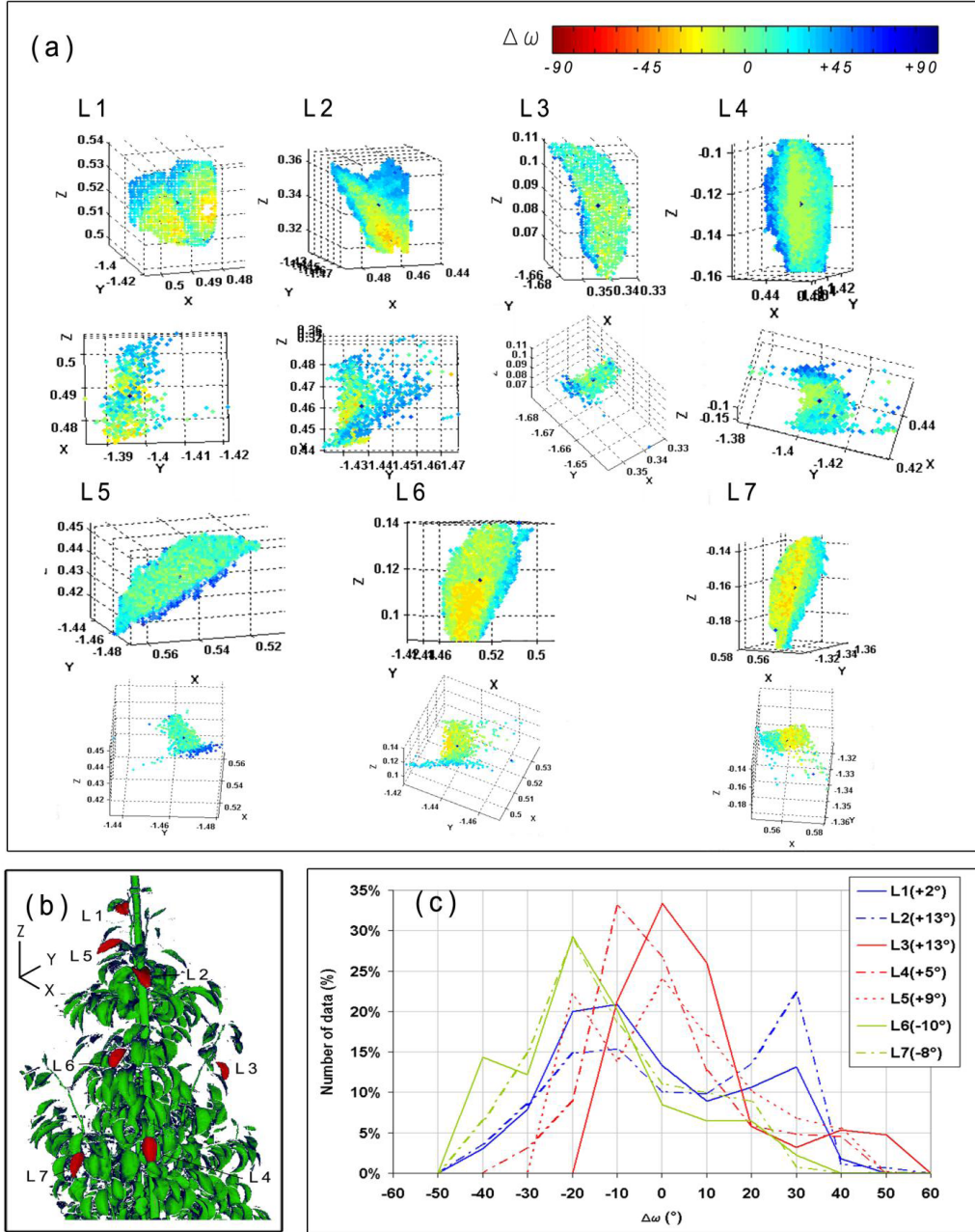
**Figure 9:** Distances of the point cloud sub-selections for each of the 15 trees and their number of sub-selections that have been made for the LSR plane fitting. The increase of the distance increases the difficulty to make a correct LSR (no extraction is possible for tree n°15). Trees are grouped by their distances to the beam aperture (>1 m).

### 2.3.3 Testing relationship between corrected intensity and incidence angle on an entire leaf

Figure 10-b shows a selection of seven entire leaves on tree n°9 (see also Figure 1). For those selections, outlier points are mostly retained. A LSR is made on those entire leaves and provides a reference angle of incidence that is subsequently compared to the angle of incidence provided by the average intensity for each point of the selected leaves (see Figure 6). The differences  $\Delta\alpha$  (Equation 1.5) are plotted for each point (Figure 10-a) the fitted plane lies on the points that have a  $\Delta\alpha$  equal to zero (green) If  $\Delta\alpha$  tends to be yellow or red, then it means that the leaf tends to face the beam compared to the LSR angle of incidence, whereas if it is blue or purple, the leaf tends to be on the side. The distributions (quantity normalized of the  $\Delta\alpha$  are shown (Figure 10-c) In addition, the difference between the LSR angle of incidence and the one provided by the average intensity is given (Figure 10-c, inset). Those differences could have an uncertainty of  $+10$  to  $+15^\circ$  because of the presence of a vertical translation in the intensity and angle of incidence graph as it has been previously discussed.

Some of the assumptions of the previous section are confirmed by these measurements:

- (i) **Curvatures:** It appears that leaves with a simple curvature (similar to a cylinder) as leaves n° 3 to 7, have a skewed normal distribution for their  $\Delta\alpha$ . For leaves n° 3 to 5, this distribution is translated to respectively  $+13^\circ$ ,  $+5^\circ$  and  $+9^\circ$ . It means that their average intensity represents well the angle of incidence provided by the LSR as it has been previously seen.  
At the opposite, the average intensity for leaves n° 6 and 7 is translated to respectively  $-10^\circ$  and  $-8^\circ$ . For leaf n° 6 it could be explained by the case (i.a) of the Section 2.3.2 as the side of the leaf forms a large angle of incidence with the beam. This provides a larger angle of incidence (Figure 10-a) which is not balanced by the low intensity of this set of point in the average intensity (Figure 10-c).
- (ii) **Wrinkles:** Leaves n° 1 and n° 2 illustrate well the impact of wrinkles on the intensity. Both show a multimodal distribution.
- (iii) **Footprint and point cloud quality:** In general, outlier points are presents for surface with large angle of incidence as it is also shown by the other leaves. Thus, one can consider that a point with a low intensity has a higher probability to be a outlier point. Leaf n° 2 shows a large surface that has a large angle of incidence with the beam but those points does not look like outlier points. In fact, this leaf seems to be lengthened. In this case, it would be more efficient not to delete those point, but to correct them, depending on their positions on the leaf.
- (iv) **Footprint and intensity mixing, physiology, multiple scattering and TLS radiometric calibration:** those factors are not tested since the scan used in this last study is the same than in the previous one.



**Figure 10:** (a) The figures shows the leaves as they appear to the TLS (up) and their side view (down).  $\Delta\alpha$  is plotted (Colors). X, Y and Z are the points coordinates in the scan (m). (b) Selection of seven leaves on tree n°9. (c) Distribution (normalized) of  $\Delta\alpha$  and difference between the angle of incidence provided by the LSR on the entire leaf and the intensity VS angle of incidence relationship (caption). Three groups are emphasized depending on the shape of the distribution: (blue) two peaks, (red) centered but stopped at  $\sim +20^\circ$ , (green) positive shift.

### 3 Discussion

In this study, Conference pear tree leaves are scanned and the intensity data provided by the TLS is analyzed with a particular focus on its properties for describing geometry of leaves. Prior to that, the intensity is corrected for the distance effect and the angle of incidence provided by the LSR is tested on the goniometric platform. Then the relationship between the corrected intensity and the angle of incidence is determined with flattened leaves placed on a goniometric platform. Next, this relationship is tested on flat part of the leaves that are still attached to the pear trees. Finally, the angle of incidence is determined using a LSR on an entire leaf, and this notwithstanding leaf curvatures and wrinkles. The  $\Delta\alpha$  (see Equation 1.5) is mapped on the selection to understand the impact of those curvatures and of those wrinkles on the data. To summarize, the three set-ups of measurement are resulting in a LSR for four different conditions:

- for the goniometric platform only,
- for flattened leaves placed on the goniometric platform,
- for some parts of the leaves that are fixed on the tree,
- for entire leaves that are fixed on the tree.

It appears that the flattened leaves on goniometric platform provide a good precision ( $\pm 5^\circ$ ) but maybe a poor accuracy in terms of finding the angle of incidence with the intensity and because of the incomplete radiometric calibration of the TLS intensity. In the case where this radiometric calibration is sufficient, the test made on the partial selection of leaves on the tree would provide a more accurate result (+50 units of corrected intensity). Still, this last test brings a lower precision in the definition of the relationship (from  $\pm 10^\circ$  to  $\pm 15^\circ$  depending on the angle of incidence). This shift in the accuracy could be explained either by:

- the LSR conditions (a low RMSE with a limited number of points that are away of the LSR plane) and the leaf curvatures and its wrinkles,
- the impact of the footprint diameter of the TLS beam,
- the physiological state of the plant, the radiometric calibration of the TLS or even a multiple scattering occurring in the canopy.

In the last test, it is clear that wrinkles and undulations are playing a large role in the precision. It is also shown that angles of incidence larger than  $60^\circ$  with pear tree leaves will provide bad results in term of accuracy and precision. Even the measurement on the goniometric platform could not provide better information because of the 3%-reflectance painting surrounding the leaves and so in the mixing of their intensity in the point cloud. As previously seen, scanning larger leaves could reduce this angle of incidence limit. In addition, if the second experiment shows a consistency



in the distance correction, it appears that distance plays a great role in the capacity to extract a good point cloud and this to make a LSR with enough points. That probably depends on leaf size, and one might expect that the measurements should be extended to a wider range and with larger leaves. In general, distance, angle of incidence and leaves dimensions should be taken into account for the set-ups of scanning that aim at extracting leaf geometry. The measurement set-ups suggested in [30] could be improved in this way.

In addition, it would be also recommended to test the relationship between intensity and angle of incidence for trees with flat leaves to study the multi-scattering effect and/or to change the conditions of selection for the LSR set in Section 1.3.2. In the future, a complete radiometric calibration should be set to guaranty the consistency of accuracy of the relationship.

Notwithstanding the aforementioned issues, different potential uses for the intensity can be envisaged. First, the third experiment emphasized the fact that intensity could help in determining the points having a higher probability to be a outlier point:

- The points with a low intensity have a higher probability to be outlier points because they are on the part of the leaves having a large angle of incidence. Those points could be directly deleted or corrected.
- In the case where points with a low intensity constitute a large zone on the leaf, it is more difficult to determine whether they are outlier points or not. This zone appears larger than in the reality. In conclusion, closer is the point to the leaf border, higher is the probability that this one is a outlier point. In those cases, the points should be only corrected as their deletion would diminish the size of the leaf.

Those two points could be used to eliminate outlier points and view as an improvement of the pre-processing methods for point cloud (as e.g., [214]). In addition, the intensity could help to extract the angle of incidence to the leaf and thus, the normal of the leaf surface as shown in the Equation 1.8.

Alternatively, using the difference between the angle of incidence provided by the LSR and comparing it to the incidence angle provided by the intensity for each point of the selected leaves ( $\Delta\alpha$ ) would give an estimation of the curving and the wrinkling of the leaves and this thanks to the  $\Delta\alpha$  distribution. This could be used as a wrinkle indicator as the amplitude of those ones might be not large enough compared to the distance precision of the TLS. Finally, a promising future in the use of the intensity is given by its use as representing the normal of the surface of leaves.

## 4 Conclusion

We have investigated the properties of intensity in relation to distance and angle of incidence with leaf surfaces. The distance effect on intensity has been corrected to set a constituent relationship between the intensity and the angle of incidence. The variation of the intensity through angle of

incidence seems to be a good indicator to help in the extraction of leaves geometries from TLS point cloud.

Results show that one can expect a precision of  $\pm 5^\circ$  to derive the angle of incidence from intensity data in the case of flat leaves. The results with curved leaves have clearly shown that the curvatures and the wrinkles are the reason for the degradation of the precision in the relation between the intensity and the angle of incidence. Therefore, we could expect to use the intensity to determine angle of incidence with a precision of  $\pm 5^\circ$ .

# Chapter 7

## PROP-SFS method for Conference pear tree leaf area and inclination estimation from TLS FARO LS880 data

Terrestrial LiDAR scanner (TLS) provides a novel tool for generating, at a high measurement rate, an accurate and comprehensive 3D geometrical description of canopy. Despite the good accuracy of the measurement (a few millimeters for most TLS in the measured range), only general indicators such as leaf area index, vertical plant profile and vegetative volume have been extracted (e.g. [16]). Several techniques based on surface fitting have been developed to digitize isolated leaves [131, 138, 18], however they rely on user intervention that remains tedious for entire canopy reconstruction. In addition, they do not deal with outlier points present along leaves edges [24]. Because large amount of outlier points in TLS scan of fruit tree, we showed in Chapter 2 that automatic organ reconstruction is difficult.

In Chapter 5, a PROP-SFS algorithm based on  $\alpha$ -photograph has been developed to tackle outliers impact on surface reconstruction. In Chapter 6, we corrected distance effect on TLS FARO LS880 intensities and transformed them into incidence angle values. In this Chapter, we seek to validate our PROP-SFS algorithm with manual measurement of leaf area, elevation and azimuth carried out on *Conference* pear tree leaves.

### 1 Material and Method

#### 1.1 Orchard

Measurements were performed on August 20th 2010 in a Conference pear tree orchards situated in Bierbeek, Belgium (Figure 1). Trees were trained in a V-Shape with an aperture of  $40^\circ$  and they were planted in rows distanced by 3.4 m from each others. Trees approximate height averaged 2.43 m without the new woody shoots, and 2.95 m with the new shoots. Distance between two

neighboring trees averaged 1.05 m and distance between two neighboring branches was 0.55 m. Orchard rows were oriented at a 130° of magnetic North (North-East direction).

- a = 40°
- b = 3.40 m
- c = 1.05 m
- d = 0.55 m
- e = 2.43 m
- f = 2.95 m
- g = 130°NE



**Figure 1:** *Conference pear tree orchards. (a) V-system. (b) Distance between rows, (c) between trees, and (d) between two neighboring branches. (e) Height of the trees without new branching shoot and (f) with new branching shoot. (g) Row orientation.*

## 1.2 TLS FARO LS880 data

The pear trees were scanned with a hemispherical TLS FARO LS880 (see technical specification in Chapter 6, Table 1). The expected accuracy of the distance measured for this TLS ranges from  $\pm 2.6$  mm to  $\pm 5.2$  mm with object placed at 10 m from the TLS aperture and with 90% to 10% reflectance, respectively. TLS angle resolution was set up at  $0.018^\circ$  that made the scan time duration of 15 minutes. In addition to the distance, the FARO LS880 provides the intensity return of the reflected laser beam for a given angular coordinate  $(\theta, \phi)$  of the TLS rotating platform. This intensity is dimensionless and its value ranges from 0 to 2044. In Chapter 6, we proposed a method to correct distance effect on intensity in addition to an intensity-to-incidence angle transformation map. In this chapter, the correction method was applied on TLS data and the intensity was transformed into incidence angle  $\alpha$  values with a precision of  $\pm 5^\circ$  and for values ranging between 0 and  $90^\circ$ .

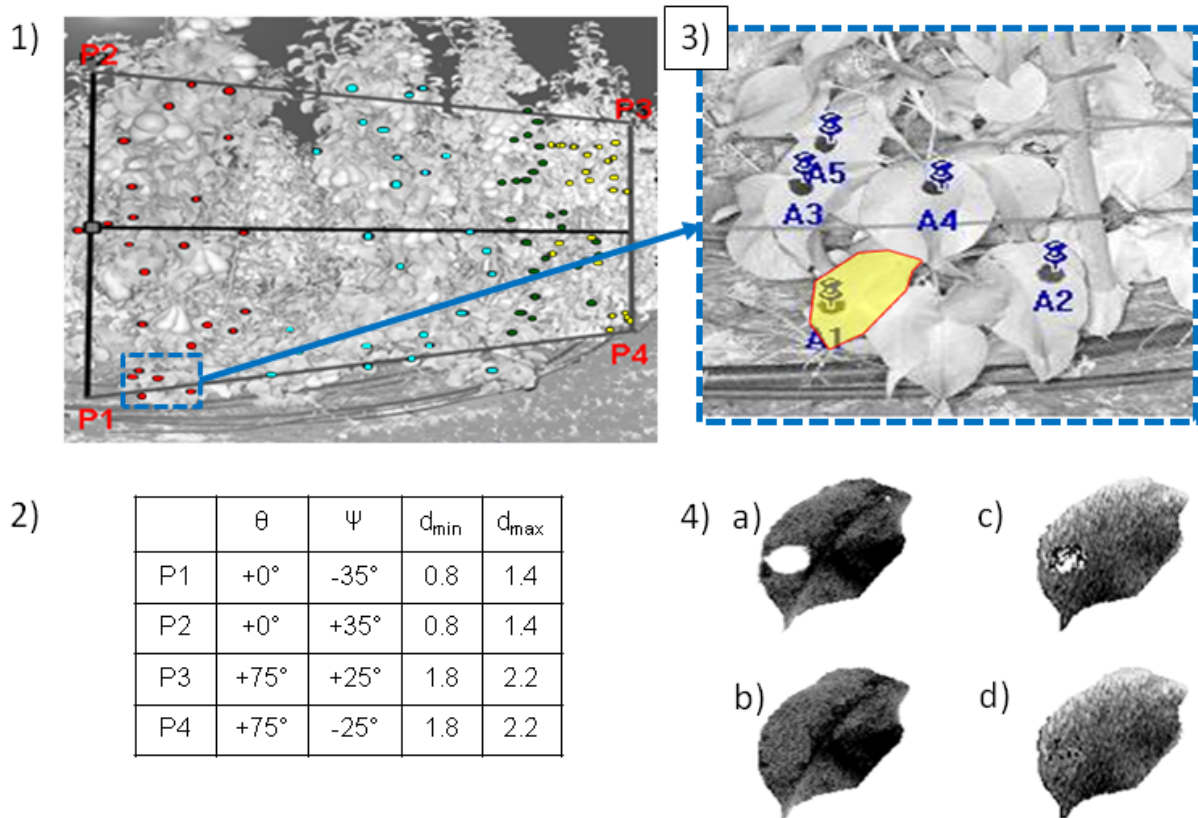
A cardboard arrow was placed in the scan to indicate the North-direction. Azimuth was obtained by computing the orientation with the arrow direction, i.e., angle between  $x$  axis and North, which is  $109^\circ$ .

## 1.3 Leaf measurement

One hundred leaves were randomly selected on four neighboring branches such that those leaves were placed in the TLS field of view. They were marked with black round stickers of diameter 1 cm

to be visible in the scan (Figure 2). Leaves distance ranged from 0.8 to 2 m from the TLS aperture. Before the LiDAR scan, leaf principal vein elevation and azimuth direction were measured with a protractor and a compass. Because limited accessibility, azimuth of the leaves placed at the top of the canopy were not measured. Azimuth measurements ranged from 0°N to 120°NE, with a resolution of 10°, and elevation from 0° to -120°, with a resolution of 5°. After LiDAR scan, leaves were pruned and scanned with a flatbed scanner to extract their area. Because pear tree leaves are not flat [211], they were cut along their principal vein. Obtained area were ranging between 12 and 65 cm<sup>2</sup>, for average area of 35 cm<sup>2</sup>.

In TLS scan, only 58 leaves of the 100 were entirely visible. Those leaves were selected manually in the point cloud with FARO Scene® software. Their point density ranged from 29 to 272 points/cm<sup>2</sup>. Black stickers had a different intensity than leaves and their point cloud was of lower quality (missing data, lower precision, etc.). Their intensity and distance values were corrected manually to makes it possible to apply our PROP-SFS algorithm. This correction consisted of making them visually coherent by copying surrounding texture and pasting this texture on the sticker area (Figure 2).



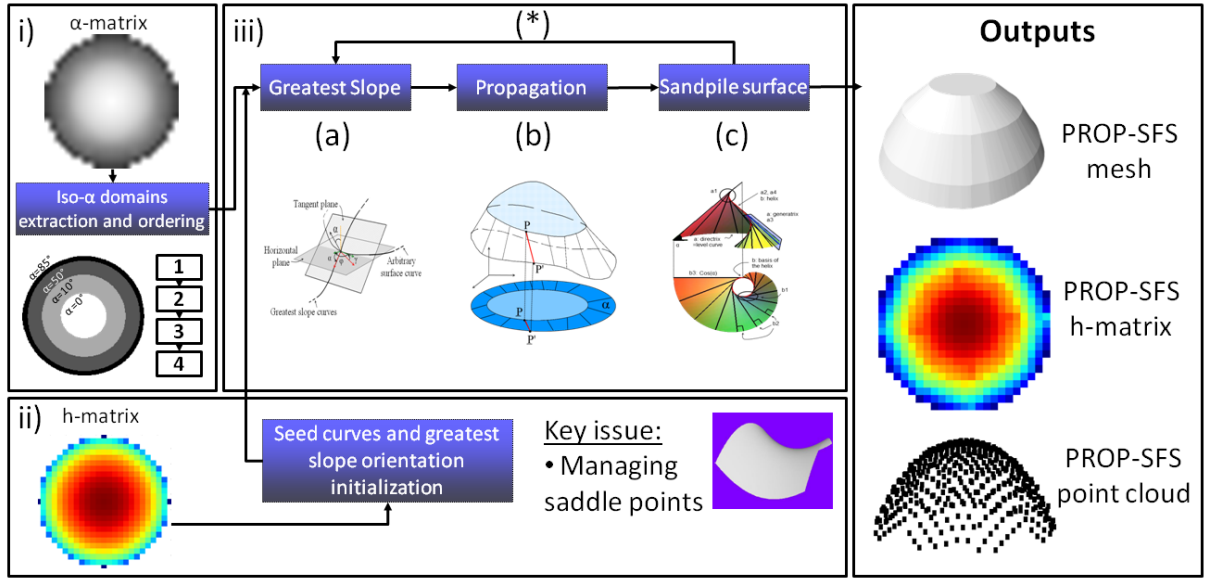
**Figure 2:** (1) LiDAR intensity map representing Conference pear tree canopy. One hundred leaves were selected (dots). Red: branch n°1, leaf 1-25. Light blue: branch n°2, leaf 26-50. Green: branch n°3, leaf 51-75. Yellow: branch n°4, leaf 76-100. Gray square represent TLS coordinates  $(\theta, \phi) = (0, 0)$ . (2) Coordinates of points P1, P2, P3 and P4. (3) Zoom on leaves 1-5 and selection of leaf #1 in the LiDAR intensity map. (3) Correction of the stickers: (a) intensity map with sticker (hole); (b) intensity map corrected; (c) distance map with sticker; (d) distance map corrected.

## 1.4 PROP-SFS pipeline description

In Chapter 5, we developed a PROP-SFS pipeline that reconstruct surface from  $\alpha$ -photograph. This pipeline carries out sand-pile surface propagation from a seed of minimal  $\alpha$  value and along consecutive iso- $\alpha$  domains. This pipeline requires as inputs: (i) an  $\alpha$ -matrix, (ii) an original distance matrix ( $h$ -matrix) and (iii) a map to pass from matrix index coordinates to original coordinates. Those input should be in Cartesian coordinates, i.e., orthonormal, but as scanned leaves are small compared to their distance to TLS aperture, our PROP-SFS assumption on orthographic camera holds. In other words, the coordinates system used to apply the propagation are the TLS spherical coordinates  $(\theta, \phi, h)$  that were assumed locally orthonormal. The output of our PROP-SFS pipeline is a mesh representation of the surface, called PROP-SFS mesh, and a point cloud generated with sand-pile surface equations, called PROP-SFS point cloud. Our PROP-SFS pipeline gathers several components (Figure 3): (i) iso- $\alpha$  domains extraction and ordering, (ii) seed distance initialization, and (iii) sand-pile surface propagation algorithm. Those components can be described as follows (Figure 3):

- (i) Iso- $\alpha$  domains are extracted and ordered. The  $\alpha$ -matrix is quantized with a given set of  $\alpha$ -values to obtain iso- $\alpha$  domains. It is segmented such that each of the produced part contains one and only one propagation seed. Finally, iso- $\alpha$  domains are ordered by inclusion.
- (ii) 3D initialization from the original  $h$ -matrix is applied to construct the seed 3D boundary curves. Local least square regression applied on a neighboring point set of size  $s$  is used to estimate greatest slope orientation at each point of the initial 3D seed curves. This initializes the propagation orientation, i.e., that defines the summit, sink and saddle cases.
- (iii) Finally, the sand-pile surface propagation is iterated to each iso- $\alpha$  domains, starting from the seed to the last iso- $\alpha$  domains of the chain. This component is composed of three main steps:
  - (a) Sand-pile surface greatest slope directions are estimated from 3D inner curves of a current iso- $\alpha$  domain and with associated  $\alpha$  value,
  - (b) They are linearly propagated outwards to reach the current iso- $\alpha$  domain outer boundary curve, and
  - (c) Sand-pile surfaces are used to fill empty space between propagation lines.
  - (\*) Consecutive iso- $\alpha$  regions of the surface are reconstructed with those three steps until the last iso- $\alpha$  region is reconstructed.

As an output, a mesh is generated with the propagation lines and the 3D iso- $\alpha$  regions boundary curves. New  $h$ -matrix and 3D point cloud are constructed with the sand-pile surface equations.



**Figure 3:** *PROP-SFS pipeline. (i) iso- $\alpha$  domains extraction and ordering, (ii) seed distance initialization, and (iii) sand-pile surface propagation algorithm with three main steps: (a) greatest slope direction estimation, (b) greatest slope propagation, and (c) sand-pile surface fitting.*

## 1.5 PROP-SFS extension

Four parameters drive components (i) and (ii) of our pipeline: (1)  $\alpha$ -value quantification, (2) low-pass filter cutoff frequency to smooth out initial curves from  $h$ -matrix, (3) number of times the  $\alpha$ -matrix is smoothed with local averaging, and (4) point set size  $s$  for the propagation orientation initialization with the local least-square regression applied on the  $h$ -matrix. Additional components for  $\alpha$ -value quantification and optimal low-pass filter cutoff frequency are included in our PROP-SFS pipeline. Those ones together with guideline to choose parameters (3) and (4) are discussed below.

- (1) In Chapter 5, we saw that  $\alpha$ -value quantification should be carried out such that there is enough distance between two consecutive iso- $\alpha$  domain curve boundaries. This is especially true for the last iso- $\alpha$  domain encircling all the other iso- $\alpha$  domain. We call this last iso- $\alpha$  domain the  $\alpha$ -matrix shell, and its width is called the shell number  $\mu$  (in pixel). If the shell is forming a square of size  $\Theta$  of shell number  $\mu = 1$  (Figure 4-1), then its area  $a_{s,\mu=1}$  equals the perimeter of the square, i.e.:

$$a_{s,\mu=1} = 4.(\Theta - 1). \quad (1.1)$$

If the shell number  $\mu = 2$ , then  $a_{s,\mu=2} < 2.a_{s,\mu=1}$ , and in general:

$$a_{s,\mu} < \mu.a_{s,\mu=1} \quad (1.2)$$

In other words, we can use Equation 1.2 to bound the shell area and to make it large enough for the PROP-SFS propagation. We define the quantification percentile  $\varepsilon_\alpha$



with this boundary:

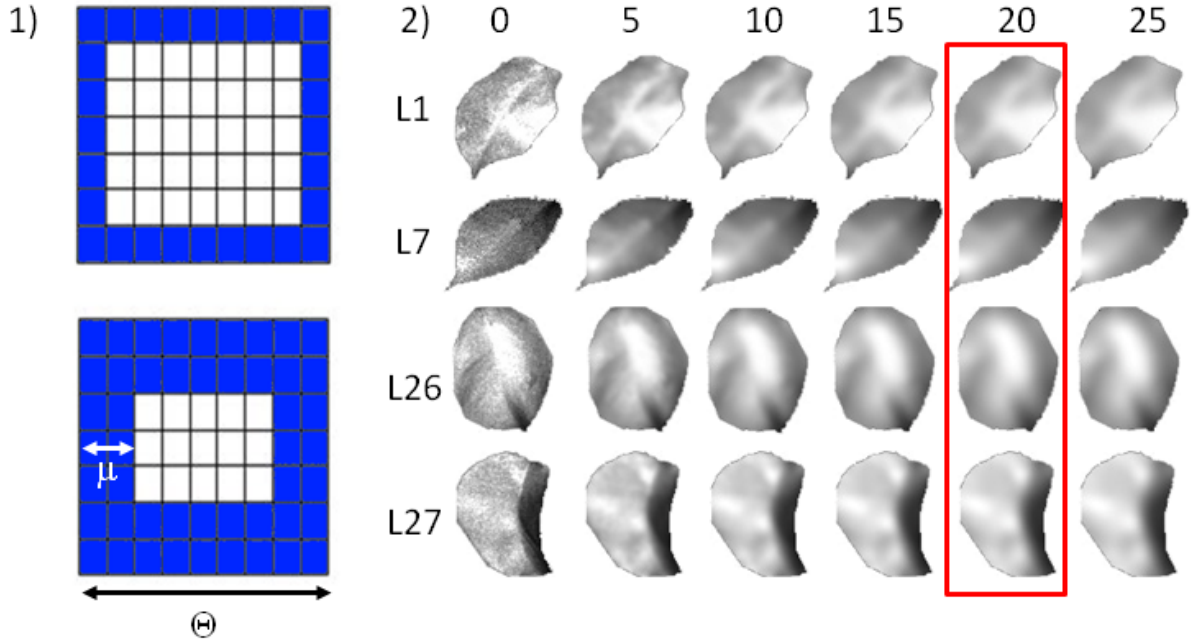
$$\epsilon_{\alpha} := \frac{\mu \cdot a_{s, \mu=1}}{a_{tot}}, \quad (1.3)$$

where  $a_{tot}$  is the total pixel area of the  $\alpha$ -matrix. In the component managing  $\alpha$ -value quantification, user can provide an additional parameter defining seed size as a multiple of the quantification percentile, i.e.,  $\epsilon_{\alpha}^{seed} := v \cdot \epsilon_{\alpha}$ .

- (2) Original  $h$ -matrix has noise and our PROP-SFS algorithm requires a smooth initial curve to construct propagation lines. A component to estimate low-pass filter cutoff frequency adapted to both curve shape (number of curve peak) and length is implemented. To set this cutoff frequency, the seed area of pixel area  $a_{seed}$  is assumed to form a round of perimeter length  $l$ . As majority of pear tree leaves have saddle shape, we suppose that the seed 3D boundary curve has two peaks and we define the low-pass filter bound at  $l/2$ , such as it is advised in Chapter 5.
- (3) In Chapter 5, the number of times the  $\alpha$ -matrix is smoothed with local averaging showed satisfactory results when the method was carried out at least five times on a hemisphere  $\alpha$ -matrix with  $\pm 5.7^{\circ}$  of  $\alpha$ -noise, i.e., the actual  $\alpha$ -noise of our data. This particular value cannot be directly reused for leaf reconstruction as they have more complicated shape. Carrying consecutive smoothing process on a few leaf  $\alpha$ -matrices makes it possible to visually choose the best smoothing parameter such that number of seeds and iso- $\alpha$  domain concavities are reduced (Figure 4-2). In this figure, smoothing parameter of 10 to 25 times shows to be adequate. We arbitrary chose to set this parameter at 20 times.
- (4) To set up propagation orientation, initial greatest slope orientation is estimated along the seed boundary curve with a local least square regression of neighboring size  $s$  on the  $h$ -matrix. This neighboring size should be set large enough to make the selected points forming a visible slope. In Chapter 5, a neighboring radius of five pixels has shown to provide a good propagation estimation. We kept this neighboring radius value of five pixels to reconstruct the 58 leaves.

Once the PROP-SFS algorithm was run on our data, extraction of geometrical variables such as leaf area and inclination (elevation and azimuth) was achieved to validate our reconstruction with manual measurements. The PROP-SFS mesh was used to estimate those variables. Leaf area was computed as the total area of the mesh's triangles representing a leaf. Leaf principal vein azimuth and elevation were made equal, respectively, to the azimuth and zenith angle of the mesh normal computed as the sum of triangle normals weighted by triangle area. Leaf principal vein azimuth estimation was corrected with TLS azimuth. This angle estimation supposes symmetrical leaf shape and orientation to correspond to the leaf principal vein inclination measurement.





**Figure 4:** (1) Pixel area of an  $\alpha$ -matrix represented in a square of size  $\Theta$ . In blue: last iso- $\alpha$  domain with shell value 1, and shell value 2. (2) Smoothing with local averaging is carried out 0 to 25 times on  $\alpha$ -matrix representing leaves number 1, 7, 26 and 27.

## 1.6 Analysis

Results of Chapter 5 made it possible to set up automatically low-pass filter cutoff frequency and to fix both the  $\alpha$ -matrix smoothing parameter and propagation estimation neighboring size value. In this same chapter, we tested the quantification percentile and seed size impacts on hemisphere reconstruction. In this chapter, we want to reconstruct leaf shapes from TLS scan. Those leaves have more complicated shape than hemisphere. Thus we need to test again quantification percentile and seed size impact for their reconstruction. To do so, we tested four parameter sets T1, T2, T3 and T3\* with our PROP-SFS pipeline. Those parameter sets were defined as follows:

- T1, T2 and T3 had, respectively, shell number value of  $\mu=2, 3$ , and 4, and seed percentile  $\epsilon_{\alpha}^{seed} = 2.\epsilon_{\alpha}$ ; and
- T3\* with  $\mu = 4$  and  $\epsilon_{\alpha}^{seed} = 1.\epsilon_{\alpha}$ .

In the next section, we assess if our PROP-SFS algorithm met one of our major goal, that was to correct TLS outlier points. Leaf area, elevation and azimuth values were estimated from the PROP-SFS mesh that was compared with the manual measurements to validate our PROP-SFS algorithm application to traditional plant geometry extraction. Linear regression slope, intercept and  $R^2$  coefficients were computed from their correlation graph.

Then, few of the leaf reconstructions were examined to give a short insight of various configuration and results (good reconstruction versus wrong reconstruction). PROP-SFS mesh and point cloud were compared to the original point cloud. A second mesh was reconstructed from the PROP-SFS

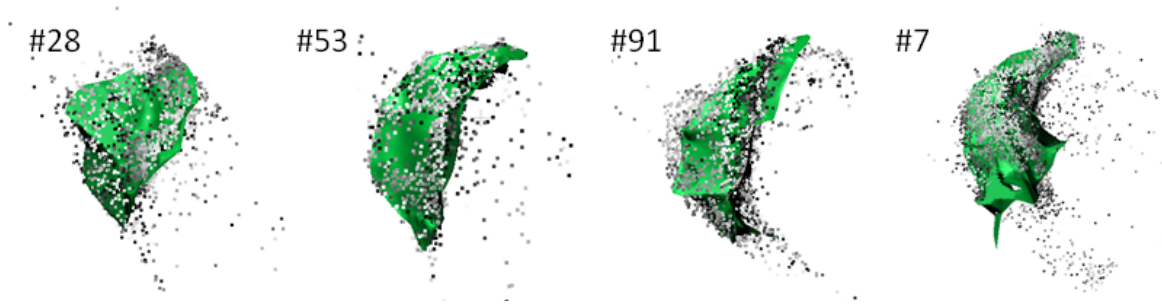
point cloud with a 3D Delaunay triangulation method found in Cloud-Compare software. This second mesh was compared with the original point cloud.

At the moment of this thesis writing, our PROP-SFS reconstruction was not take into account all the cases of complex iso- $\alpha$  domains configuration shapes. As we will see below, several distance point per pixel of the PROP-SFS  $h$ -matrix can be computed. For each reconstructed leaves, we counted the number of  $h$ -matrix pixels having  $n$  reconstructed distance relatively to the total  $h$ -matrix point ( $rppp_n$ ). For instance,  $rppp_1$  is the ratio of number of points having one and only one reconstructed distance value to the total  $h$ -matrix number of points. This  $rppp_1$  can be used as a quality factor to assess non-redundancy in the reconstruction. For each parameter set, we built the  $rppp_1$  distribution as a function of the number of reconstructed leaves to indicate which parameter set provides globally the best result in term of non-redundancy.

## 2 Results and discussion

### 2.1 Primary results

To illustrate good results of our PROP-SFS algorithm, we selected four 3D leaf reconstruction for which the 3D Delaunay triangulation method applied on PROP-SFS point cloud provided satisfactory reconstruction. Those leaves are illustrated in Figure 5. Those reconstructed leaves show realistic shapes and are not affected by outlier points. That fulfills qualitatively one major aim of our study.



**Figure 5:** 3D Delaunay mesh built from PROP-SFS point cloud of well reconstructed leaves 28, 53, 91 and 7. Parameter set used is T3.

### 2.2 Geometrical variable extraction from PROP-SFS mesh

The four parameter sets T1, T2, T3 and T3\* were tested. Validation results for PROP-SFS area, elevation and azimuth estimation, are presented in Table 1. Correlation graphs for area (with BIAS correction), elevation and azimuth estimation are shown in Figures 6, 7, and 8, respectively.

Compared to real area  $a$ , estimated area  $\hat{a}$  is satisfactory: we obtained  $R^2$  values of 0.7 for T1 and T2, 0.7 for T3 and 0.77 for T3\*. Yet our PROP-SFS area estimation had a *BIAS*, that is the value defined such that the mean relative error (MRE) computed on our reconstruction set equals to zero,

i.e.:

$$MRE := \frac{1}{n_{leaf}} \cdot \sum \frac{(\hat{a}_{leaf} + BIAS) - a_{leaf}}{a_{leaf}} = 0, \quad (2.1)$$

where  $\hat{a}_{leaf}$ ,  $a_{leaf}$  and  $n_{leaf}$  are respectively, estimated leaf area, real leaf area and number of reconstructed leaves. Those  $BIAS$  range from -1.5 to -5 cm<sup>2</sup>. That shows a global under-estimation of leaf area. With a closer look at the correlation graph that compared  $a$  with  $(\hat{a} + BIAS)$  (Figures 6), results with T3 are shown to be more aligned with the 1:1 line than the three other tests. In addition, its linear regression has the best slope and the sampling (#leaves) was larger. In this way, the  $BIAS$  value of T3 (-4.5 cm<sup>2</sup>) was the most representative

Results on inclination angle estimation were less convincing, especially for azimuth. In the case of elevation estimation, T2, T3 and T3\* provide correlation graphs with a clear tendency (Figure 7). This tendency was even more enhanced if the few outliers were deleted: we obtained a  $R^2$  equals to 0.65 with parameter set T3\* if the single point with wrong estimation was deleted. Elevation precision obtained was equal to  $\pm 20^\circ$ . Azimuth validation provides less satisfactory results probably because the measurement range was too short (Figure 8), i.e., between  $0^\circ$  and  $120^\circ$ . Yet if measurements are extrapolated to the entire azimuth range, i.e., the represented point cloud in the correlation graphs of Figure 8 were repeated between  $-180^\circ$  to  $+180^\circ$ , azimuth precision obtained would be at least equal to  $\pm 40^\circ$ .

	$\mu$	$\varepsilon_{\alpha}^{seed}$	#leaves(%)	<u>Leaf Area</u>				<u>Elevation</u>			<u>Azimuth</u>		
				BIAS	Slope	Intercept	R <sup>2</sup>	Slope	Intercept	R <sup>2</sup>	Slope	Intercept	R <sup>2</sup>
T1	2	2. % $\alpha$	74%	-3	0.86	0.73	0.7	0.5	-45	0.36	0.27	-51	0.17
T2	3	2. % $\alpha$	69%	-5	0.78	1.16	0.7	0.51	-43	0.56	0.30	-50	0.20
T3	4	2. % $\alpha$	97%	-4.5	0.95	-3.06	0.74	0.52	-43	0.44	0.25	-48	0.12
T4	4	1. % $\alpha$	74%	-1.5	0.78	0.77	0.77	0.54	-40.5	0.59	0.30	-49	0.19

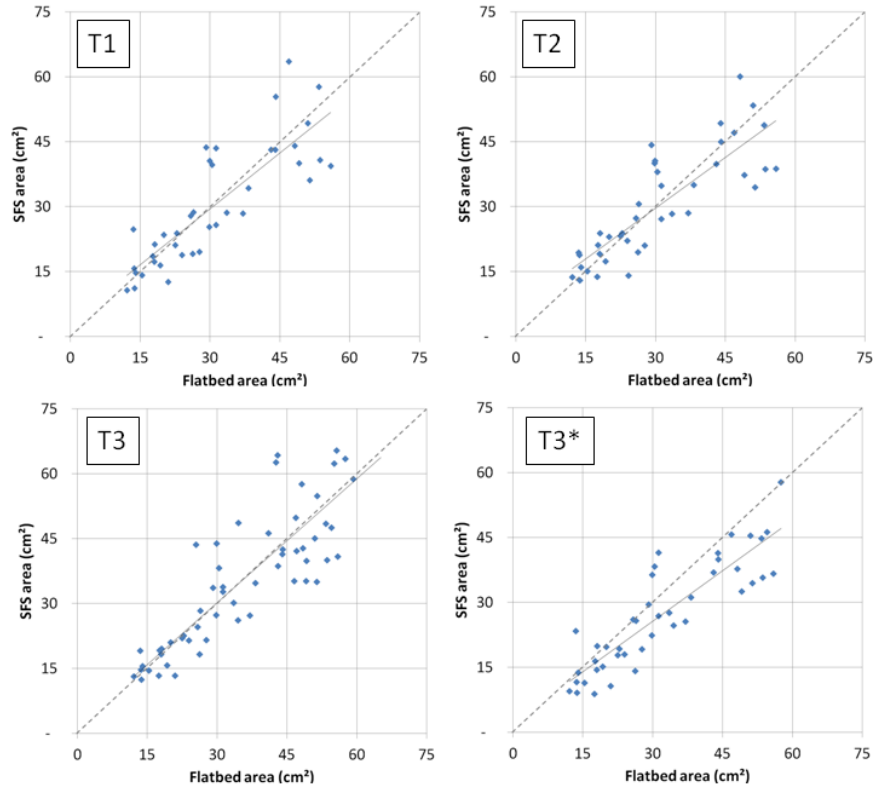
**Table 1:** PROP-SFS estimation comparison with measurement for T1, T2, T3 and T3\*. Leaf area intercept is without BIAS correction.

## 2.3 Mesh reconstruction from PROP-SFS point cloud

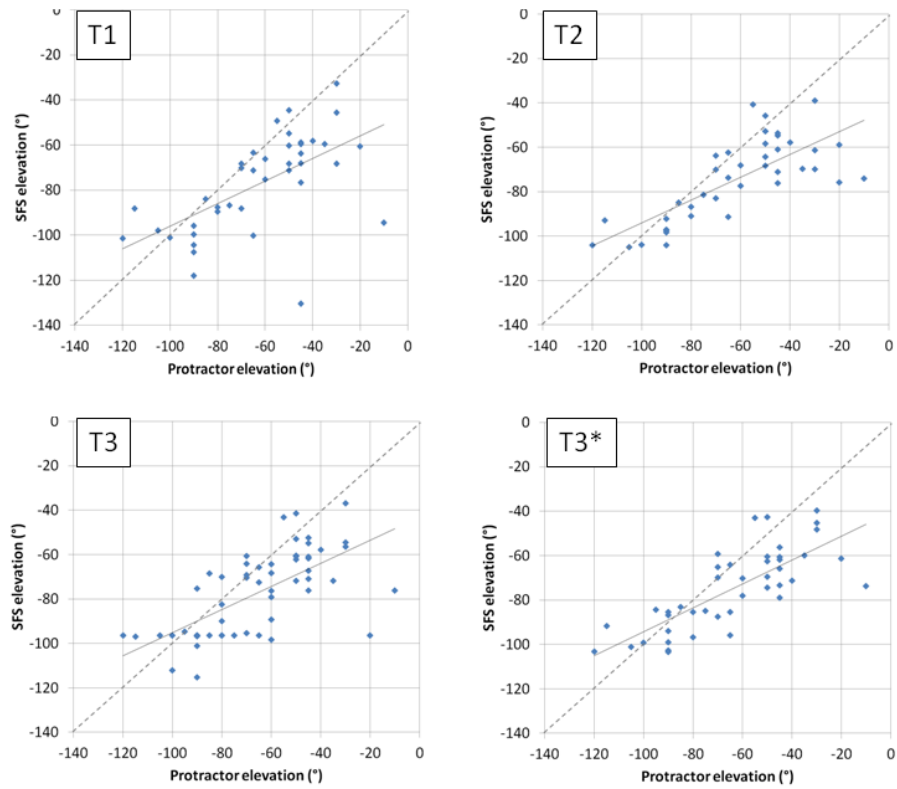
### 2.3.1 Parameter set comparison

To illustrate the source of reconstruction issue, we selected three leaves (leaves 37, 49 and 56) reconstructed with parameter sets T3, T3\* and T1 (leaf 56). Figure 9 shows those leaves  $\alpha$ -matrix, iso- $\alpha$  domain selection, original point cloud (with black sticker) and reconstruction. Table 2 shows manual measurements and PROP-SFS estimation of area, elevation and azimuth estimation for those three leaves and parameter sets.

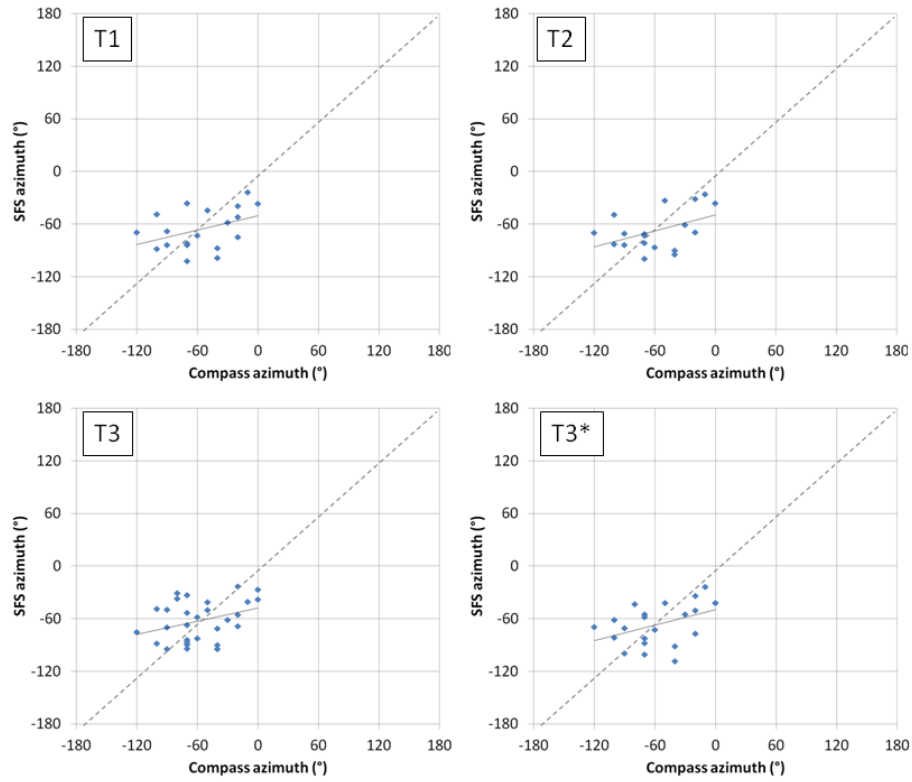
A close view to the reconstructions of leaves 37 and 49 in Figure 9 shows that a large seed selection can be necessary to initialize the propagation orientation properly: the shape of the PROP-SFS point cloud is more similar to the original point cloud when computed with T3 than with T3\* (in particular, see leaf 37, Figure 9-2, 5i and 5ii). Despite global curvature shape changes (concave



**Figure 6:** Correlation graph for leaf area between flatbed and PROP-SFS measurements (BIAS corrected) for T1, T2, T3 and T3\*.



**Figure 7:** Correlation graph for leaf elevation between flatbed and PROP-SFS measurements for T1, T2, T3 and T3\*.



**Figure 8:** Correlation graph for leaf azimuth between compass and PROP-SFS measurements for T1, T2, T3 and T3\*.

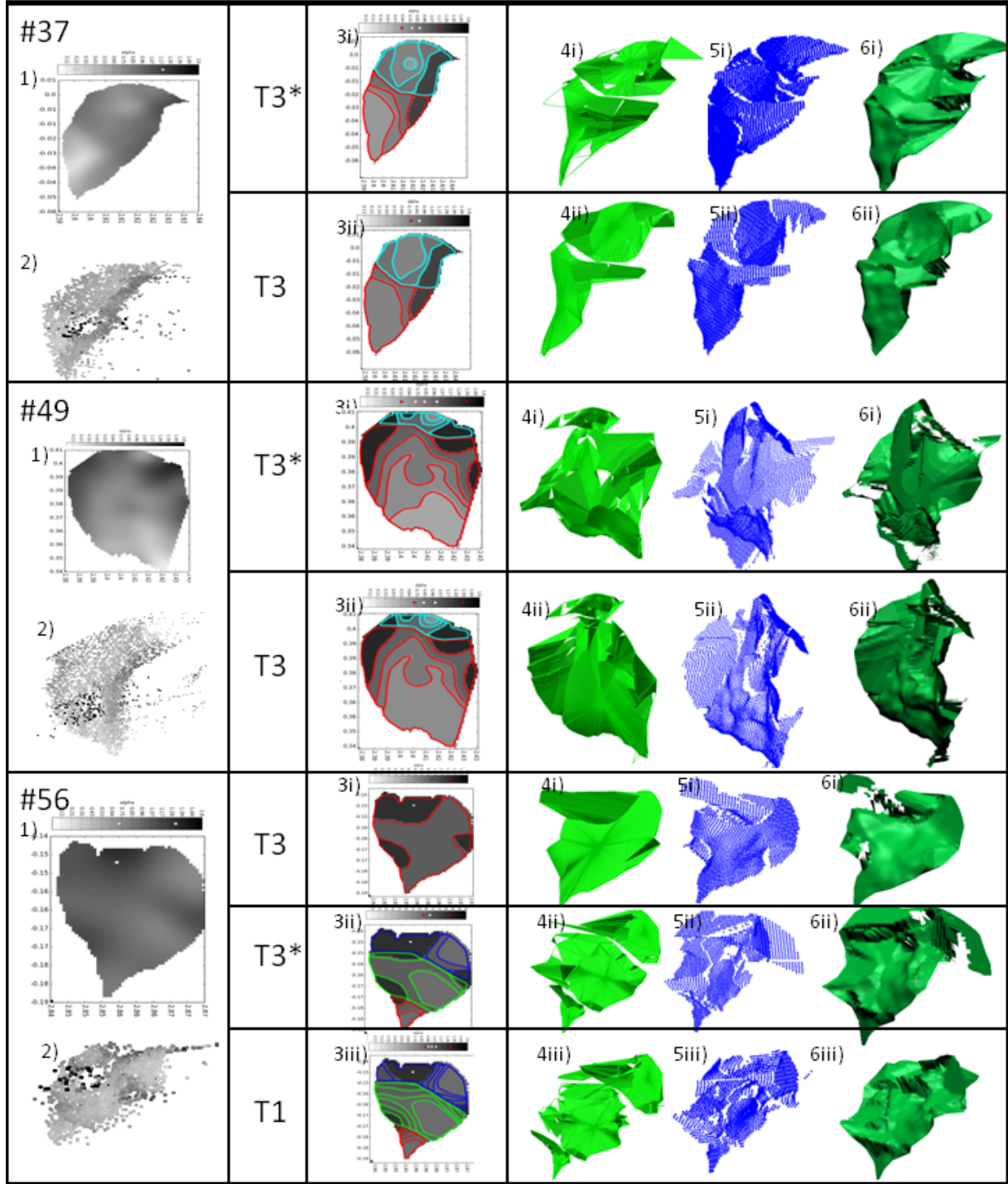
versus convex), leaf 37 area computed with T3\* is closer to the real area than when it is computed with T3 though (see Table 2).

Leaf 56 reconstruction illustrates the impact of seed number and  $\alpha$ -value selection on PROP-SFS reconstruction. If several seeds are used, gaps between segmented regions in the PROP-SFS mesh were visible (Figure 9-3ii and 3iii, leaf 56). In addition, leaf 56 reconstruction showed the impact of larger amount of  $\alpha$ -values caused by the choice of a smaller shell number  $\mu$ . Iso- $\alpha$  domains constructed with the parameter set T1 made the propagation reaching some areas (e.g., Figure 9-3iii, leaf 56, in blue) that were under-represented with T3\* (e.g., Figure 9-3ii, leaf 56, in blue). That made the PROP-SFS point cloud and second mesh more realistic (Figure 9-6iii versus 6ii, leaf 56).

Despite PROP-SFS mesh shape varies with the different parameter sets, there was no great change in the associated area, elevation and azimuth estimation (Table 2). In general, Figure 9 and Table 2 show the difficulty to choose an adequate parameter set to reconstruct realistic leaf shape and extract correct area and inclination.

## 2.4 PROP-SFS algorithm analysis

Figure 10 shows  $\alpha$ -matrix, iso- $\alpha$  domain selection, original point cloud (with black sticker) and reconstruction of leaves 1, 34, 93 and 27: (i) leaf 1 was a rather flat leaf with small  $\alpha$ -values, (ii) leaf 34 had more pronounced curved shape than leaf 1 and consequently had larger  $\alpha$ -values, and



**Figure 9:** Leaves number 37, 49 and 56: (1)  $\alpha$ -matrix, (2) original point cloud (with black sticker), (3) iso- $\alpha$  domain selection, (4) PROP-SFS mesh, (5) PROP-SFS point cloud, (6) mesh reconstructed with the PROP-SFS point cloud.

		Area (1 cm <sup>2</sup> )		Elevation (5°)		Azimuth (10°)	
		Mes.	SPS	Mes.	SPS	Mes.	SPS
L37	T3*		25		-60		-80
	T3	26	20	-45	-70	-100	-90
L49	T3*	53	43	-70	-90	nan	-70
	T3		44		-95		-70
L56	T3		23		-70		-70
	T3*	30	21	-35	-60	-90	-70
	T1		22		-60		-70

**Table 2:** Manual versus PROP-SFS measurement of area, elevation (rounded at 5°) and azimuth (rounded at 10°) for leaves number 37, 49 and 56, for parameter sets T3, T3\* and T1 (leaf 56).

(iii) leaves 93 and 27 had typical pear tree leaf shape with vertical inclination, and were viewed from the side, i.e., their half limbs were oriented within the TLS beam direction.

Figure 10 shows our PROP-SFS reconstruction errors:

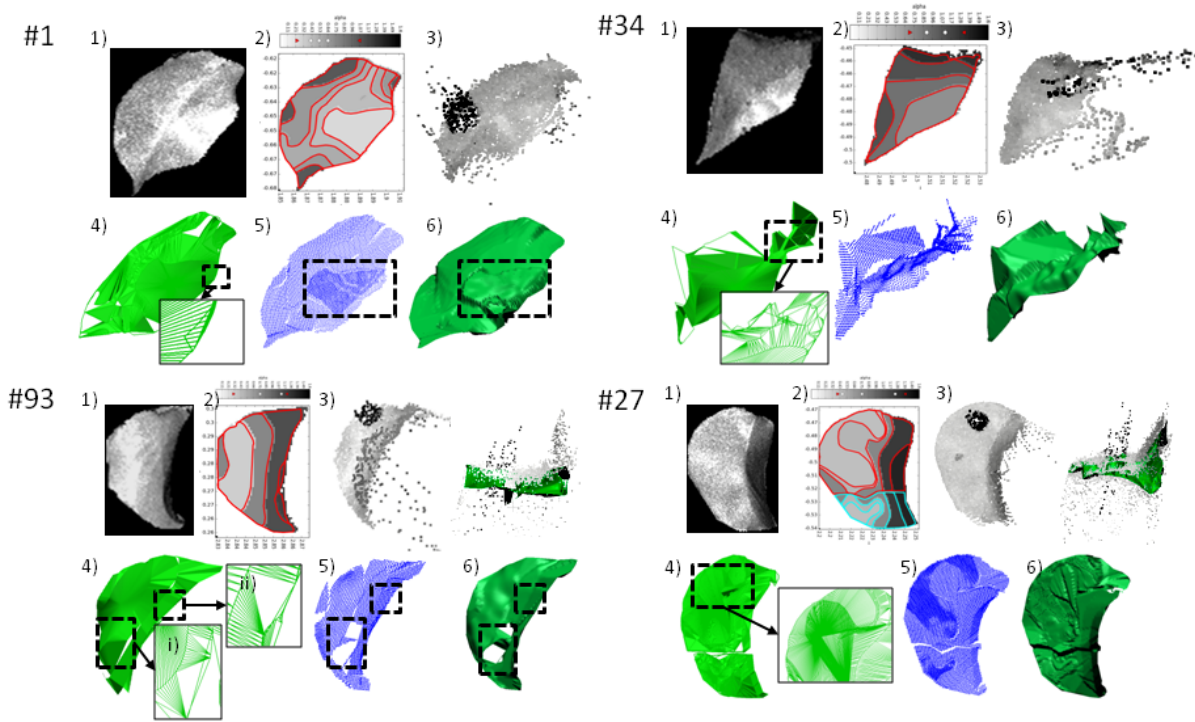
- Some of the PROP-SFS meshes had visible mesh holes along outer iso- $\alpha$  domain boundary curves (see leaf 1 in Figure 10-4) as no strategy to fill PROP-SFS mesh in reverse propagation (such as for the  $h$ -matrix construction) was set up. Those holes are inherent in our PROP-SFS algorithm.
- There were still PROP-SFS mesh outlier triangles (see leaf 1 in Figure 10-4, zoom), and crossing curves (see leaf 27 in Figure 10-4, zoom) that created redundancy in the PROP-SFS point cloud.
- PROP-SFS mesh triangles were not necessarily handling well PROP-SFS point cloud reconstruction for sans-pile surface filling. For instance, leaf 93 PROP-SFS mesh showed two cases of large triangle set with same vertex (see leaf 93, in Figure 10-4, zoom), i.e., using the same buffer point. Sans-pile surface filling was well handled in the first case whereas it was not in the second case that made point cloud holes visible in the PROP-SFS point cloud (see leaf 93, in Figure 10-5, frame).
- Propagation orientation can be wrongly initialized. If too many toggle points are computed, the reconstructed surface has wrinkles (see leaf 34 in Figure 10-4, zoom).

Table 3 shows manual versus PROP-SFS estimation of leaf area, elevation and azimuth. Leaves 1 and 34 area and elevation were well estimated, whereas leaves 93 and 27 were respectively under and over estimated. Leaf 1 PROP-SFS mesh was visually correct despite few mesh holes that explain small under-estimation (1 cm<sup>2</sup>) of its area. Leaf 34 area estimation was correct despite its PROP-SFS mesh has an approximated leaf shape. This mesh had large mesh holes but also wrinkle shapes. The combination of both compensates area computation. Leaf 27 iso- $\alpha$  domain concavities created a large amount of crossing PROP-SFS mesh triangles. This explains over-estimation of leaf 27 area. Finally, leaf 93 PROP-SFS mesh had no noticeable issue except its half



limb was not reconstructed. This half limb had a too steep incidence angle. Consequently, it was not well represented in the iso- $\alpha$  domain set and it was not taken into account in the reconstruction.

Leaves 1 and 93 elevation was well estimated. Leaf 1 had no particular issue impacting on elevation estimation. Leaf 93 was vertical that made its elevation estimation good even if its half limb was missing in the reconstruction. Wrong estimation for leaf 27 elevation might have been caused by redundant PROP-SFS mesh triangles. Finally, leaf 34 PROP-SFS mesh wrinkles and general shape caused severe bias in elevation and azimuth estimation. PROP-SFS azimuth estimation for leaves 1 and 27 were within the expected ranges of precision established in Section 2.2,



**Figure 10:** Leaves 1, 34, 93 and 27: (1)  $\alpha$ -matrix, (2) iso- $\alpha$  domain selection, (3) original point cloud (with black sticker) (Leaves 93 and 27: side view with mesh), (4) PROP-SFS mesh, (5) PROP-SFS point cloud, (6) mesh reconstructed with the PROP-SFS point cloud.

		Area (1cm <sup>2</sup> )		Elevation (5°)		Azimuth(10°)	
		Mes.	SPS	Mes.	SPS	Mes.	SPS
L1	T3*	29	28	-50	-45	-50	-40
L34	T3*	18	18	-30	-50	-100	-60
L93	T3*	51	33	-90	-85	nan	-90
L27	T3	65	75	-85	-70	-70	-80

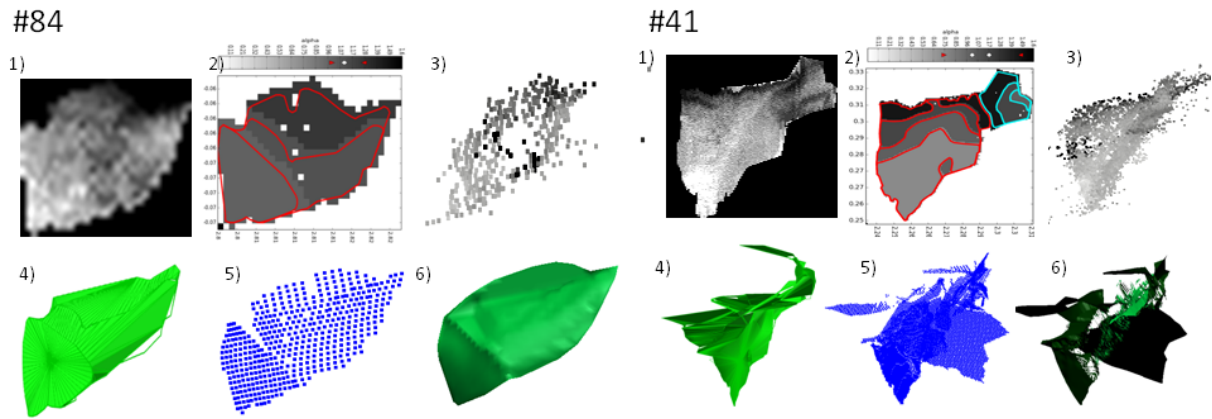
**Table 3:** Manual versus PROP-SFS measurement of area, elevation (rounded at 5°) and azimuth (rounded at 10°) for leaves number 1, 34, 93 and 27.



## 2.5 Extreme cases

Figure 11 shows leaf 84 reconstruction with parameter set T3\*. Leaf 84 was one of the furthest (1m90 from TLS aperture) and smallest leaf (17 cm<sup>2</sup>) of our leaf set. Thus it had the point cloud with the lowest points density (29 points/cm<sup>2</sup>). Even if its area, elevation and azimuth were incorrectly estimated (estimated minus real values equaling -10 cm<sup>2</sup>, -40° and 50°, respectively), our PROP-SFS method was shown to tackle outlier points and to provide realistic leaf shape with object with such size and distance.

Figure 11 shows leaf 41 reconstruction with T3. Leaf 41 was one of the largest leaf (55 cm<sup>2</sup>), it was at a medium distance from TLS aperture (1.15 m) and a medium points density (112 points/cm<sup>2</sup>). The particularity of this leaf was its strong inclination and its complex silhouette shape. Its PROP-SFS mesh had several triangle outliers. Compared to leaf 27 in Figure 10, leaf 41 PROP-SFS mesh outlier triangles made the PROP-SFS point cloud and 3D Delaunay triangulation incorrect. Those ones created redundant points in the PROP-SFS point cloud: rppp<sub>1</sub> was at 47%. Without the point redundancy, the general aspect of this PROP-SFS point cloud was realistic though.



**Figure 11:** Leaves 84 and 41: (1) original  $\alpha$ -matrix, (2) iso- $\alpha$  domains, (3) original point cloud (with black sticker), (4) PROP-SFS mesh, (5) PROP-SFS point cloud, (6) mesh reconstructed with the PROP-SFS point cloud.

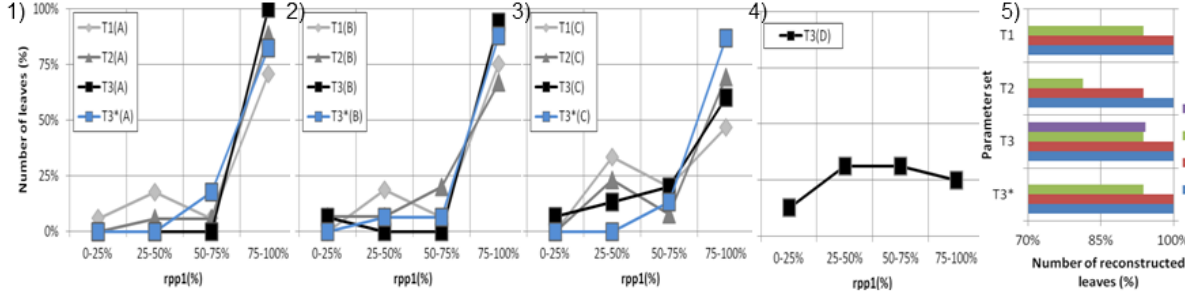
## 2.6 rppp<sub>1</sub> distribution

To classify redundancy, four groups of 14-16 leaves with  $\alpha$ -matrix size <2ko, 3ko, 4-5ko, and >6ko were built and denoted A, B, C and D, respectively.

Figure 5 shows the total number of leaves (in %) reconstructed for each leaves and parameter set. Each of the parameter sets managed to reconstruct every leaves of leaf set A. Parameter sets T1, T2 and T3\* did not worked on leaf set D whereas T3 did. In general, T3\* functioned on 97% of the leaves, whereas less than 75% were reconstructed with the other parameter sets (see Table 1).

Figure 12-1 to 3 shows rppp<sub>1</sub> distribution for leaf sets A-C with parameter set T1, T2, T3 and T3\*, in addition to rppp<sub>1</sub> distribution for leaves set D with T3 (Figure 12-4). In term of non-redundancy, the larger the number of leaves with high rppp<sub>1</sub> is, the better the parameter set is. In this way, T3

gave the best results with leaf sets A and B whereas it was T3\* that gave the best result with leaf set C. T3 is the only parameter set that worked on D. Yet T3 rppp<sub>1</sub> distribution was of lower quality with  $\alpha$ -matrix set D (Figure 12-4): half of the leaves had a rppp<sub>1</sub> lower than 50% that indicates heavy memory use because redundancy. We guess this memory use was too large for T1, T2 and T3\* that made the PROP-SFS reconstruction failing.



**Figure 12:** Distribution of rppp<sub>1</sub> for: (1) leaf set A, (2) leaf set B, (3) leaf set C and (4) leaf set D, with parameter set T1, T2, T3 and T3\*. (5) Number of reconstructed leaves per parameter set.

### 3 Discussion

Our PROP-SFS algorithm fulfilled our objectives to correct outlier points. Leaf reconstructions fit original point cloud and avoid outlier points impact in the final reconstructed shape. We estimated leaf area, elevation and azimuth from leaf PROP-SFS mesh and those estimations were assessed with different shell number and seed size. Leaf area estimation showed in general satisfactory results ( $R^2 = 0.77$  for the best set), but with a general underestimation represented by a BIAS of 4.5 cm<sup>2</sup>. Elevation estimation precision was equal to  $\pm 20^\circ$  and azimuth precision was shown to be at least equal to  $\pm 40^\circ$ .

Quality of the PROP-SFS mesh reconstruction can be related to the results of the leaf area, elevation and azimuth estimation. Holes in the PROP-SFS mesh make area under-estimated whereas wrinkles make it over-estimated. Still, under-estimation caused by mesh holes can compensate over-estimation caused by wrinkles. Holes and wrinkles also affect elevation and azimuth estimation. In general, good PROP-SFS reconstructions were providing correct area and inclination estimations, even if the method to extract inclination from PROP-SFS reconstruction should be improved to general leaves configuration (e.g., asymmetrical shape and not vertical principal vein).

The quality of area and inclination estimation is not necessarily correlated to the quality of the PROP-SFS point cloud reconstruction: for instance, a large amount of PROP-SFS mesh outlier triangles can lead to wrong area estimation whereas it can have either small or large impact on the PROP-SFS point cloud shape. Conversely, the estimated shape can be of opposite convexity and provides a good area estimation.

Results of our validation lead us to consider two possible improvements for our PROP-SFS area and inclination estimation: (1) to add an additional PROP-SFS pipeline component to correct

mesh outlier triangles and holes (that have been discussed in Section 2.4), and (2) to optimize the parameter set choice. Parameter optimization can be done with: (i) better quantification percentile, (ii) seed size choice, and (iii) redundant point analysis:

- (i) We showed that it was better to start with a large seed to avoid false toggle point detection.
- (ii) In Chapter 5, reconstruction quality showed that the quantification percentile depends on matrix size. In the case of large matrix, small  $\epsilon_\alpha$  can be used. In the case of small matrices,  $\epsilon_\alpha$  should be chosen large enough to avoid error propagation from iso- $\alpha$  curves estimation. In this chapter, no clear tendency appears between different  $\epsilon_\alpha$  values. Yet, we showed that this value should also be adapted to leaf shape complexity.
- (iii) Redundant point is also a quality factors that can be used to adapt parameter choice. First, the amount of rppp<sub>1</sub> at the end of the computing process can be taken into account to decide a change in the parameter set. Secondly, redundant point construction makes computing time longer. Conversely, long computing time can indicate the chance of large amount of redundant point reconstruction. A computing clock can be implemented to change our PROP-SFS parameters in case of too long computing time.

## 4 Conclusion

Measuring plant geometry at organs scale is an important step to study plant physiology with model such as functional-structural-plant-modeling (FSPM). 3D scanner have been showed to be adequate to extract plant geometry at this scale (e.g., [71, 18, 136]), yet a very few were used to extract *in situ* plant geometry at organ scale. Method for voxel representation at organ scale derived from TLS data were set up (e.g., [113]) but single organ shape, area and inclination were not extracted because the large amount of outlier points [215].

In Chapter 5, we developed a PROP-SFS method based on propagation along iso- $\alpha$  domain. In this chapter, we tested this method for Conference pear tree leaves geometry extraction from TLS data with several PROP-SFS parameter set (shell number and seed size). 100 leaf area and inclination were manually measured. 58 leaves that were entirely visible in the scan were manually selected in the TLS point cloud to be reconstructed with our algorithm. The reconstruction were shown to fit original point cloud and to correct outlier points. Area estimation provided satisfactory results: the best correlation coefficient obtained was  $R^2 = 0.77$ . A BIAS of 4.5 cm<sup>2</sup> was observed for those area estimation though. Elevation estimation precision was equal to  $\pm 20^\circ$  and azimuth precision was shown to be at least equal to  $\pm 40^\circ$ , yet elevation estimation from PROP-SFS mesh could be improved if adapted to non-symmetrical and non vertical leaves. New azimuth measurement, with larger sample, should be carried out to make it possible to proceed to a better validation.

This chapter also allowed us to point out improvement for our algorithm. Those improvement concerned outlier triangle, holes processing, optimization of shell number and choice of the seed size.

As a first validation of our PROP-SFS algorithm, area and inclination estimations were satisfactory. Compared to other leaf area, inclination and shape extraction method (e.g., [136, 18]), our PROP-SFS reconstruction provided less accurate area and inclination estimation. Yet those studies extract geometrical variables only on picked leaves or from single stems placed close to the 3D scanner aperture and such that the leaves were perpendicular to their 3D scanner viewing direction. In other words, they used high resolution and high quality data with the best measuring conditions. Compared to those previous studies, we gave the first leaf area, inclination and shape estimation for complex canopy leaves shape scanned under *in situ* conditions and from a phase-shift TLS device and we validated our reconstruction for leaf point cloud density ranging from 29 to 272 points/cm<sup>2</sup>. In addition, if our PROP-SFS propagation is improved to avoid mesh outlier triangles and holes, and if optimal quantification percentile values and seed sizes are automatically selected, our PROP-SFS algorithm can be expected to provide better results.

# **Part IV**

## **Conclusion**



Horticulturists and agronomists seek to improve and optimize their orchards management to decrease their expenses and increase their orchard yield quality. Orchard management mainly depends on plant growth and reaction to biotic and abiotic stresses, and the understanding of the plant functioning can lead horticulturists and agronomist to improve their yields. Plant physiology study can be carried out with computer models and plant geometry description at organ scale is an important information for this purpose. Scanner 3D can be used to extract such information.

Because their portability and their high measurement rates, TLS became a common metrology tool for plant geometry measurements. Despite they have been broadly used for global (e.g., LAI) and distributive (e.g., VLAD, voxelized 3D space of LAD, etc.) descriptors extraction, they were not used to extract complex canopy geometry at organ scale and under *in situ* condition. Outlier points presence along organs edge was the major limiting factor to segment and reconstruct organs from TLS scanner as they represent a large amount of points in plant TLS point cloud. For instance, we observed that pear tree leaves of 9 cm length have a ratio outlier/point (see Chapter 2, Section 2.5) representing from 8% to 33% of their point cloud when placed at 1.5 to 5 meter from the TLS aperture, respectively. Consequently, we showed that outliers deletion was not an adequate method to process TLS scan when used to extract geometrical information of plant organs, such as leaf area, inclination and shape. This was the reason why we rather proposed to develop an outlier point correction.

In canopy scan configuration, the detection of outlier points was a difficult task: organ shape complexity and their large amount within tree canopy made it difficult to detect whether a point is an inlier or an outlier point. As intensity return of TLS laser beam became a common data provided by actual TLS devices, it was possible to consider it a new source of information to detect those outlier points. Intensity data is related to scanned object reflectance property and geometry, i.e., inclination and distance to TLS aperture. The analysis of different geometrical configuration cases showed that intensity has a different behavior than distance to surface configuration (inclination and edge, Chapter 2, Section 2.3). Intensity and distance data are coherent when TLS measures the inner part of a surface. They can be incoherent at object edge measurement points though. In this way, intensity and distance inconsistency can be used to indicate the presence of outlier points. In this thesis, we decided to use TLS intensity information to correct those outlier points. To do so, we proposed a SFS method to reconstruct scanned object surface.

## **PROP-SFS design**

SFS consists of using intensity data of object photograph to reconstruct their shape in 3D dimension. As we have seen, the point cloud of a scanned object usually have outlier points along the edge of the object. Yet they also have local parts that are of higher quality. Those ones are the surface portions that are perpendicular to the TLS laser beam and which have consequently the maximal intensity value. In this thesis, our idea was to design a computational method to reconstruct surfaces from the high quality point cloud area and to propagate the reconstruction outwards

the surface to correct the outlier points. In other words, those two types of point (outlier and maximal intensity points) in TLS point cloud made our choice to develop a PROP-SFS method to reconstruct surfaces from TLS scans.

Under certain assumptions on object material, surface isophote regions (i.e., constant incident angle  $\alpha$  between a surface and a light ray) correspond to iso-intensity domains of photographs. In 1850, Monge [197] stated that SPS are isophote surfaces. In this thesis, we considered the photograph iso-intensity domains as domains with constant  $\alpha$ -value. We proved that  $\alpha$ -photographs with constant  $\alpha$ -values are necessarily corresponding to SPS. Those surfaces have a convenient computational property: their greatest slope curves are straight line portions. We used this last property to set up a PROP-SFS algorithm by SPS propagation for surface iso- $\alpha$  regions reconstruction.

This PROP-SFS consists of three principal components: (i) the  $\alpha$ -photograph matrix segmentation and iso- $\alpha$  domain ordering, (ii) the initialization of the 3D seed from distance data, and (iii) the propagation of the SPS starting from the seed for each segmented domains and along consecutive surface iso- $\alpha$  region. To set up the last component, we used basic geometric properties to construct and propagate SPS greatest slope lines from a surface iso- $\alpha$  region boundary. Yet this propagation raises the issue that points were not reconstructed between propagation lines. To complete the propagation, we used SPS equation to fill in missing points. Once our PROP-SFS pipeline was set up, we tested this algorithm on synthetic surfaces and validated its application for the extraction of Conference pear tree leaf geometry from TLS scan.

## PROP-SFS result

Our PROP-SFS method can reconstruct simple but also complex shapes. We made an empirical computing time  $t$  estimation on hemisphere  $\alpha$ -photograph and obtained  $t \sim a_{tot}^{1.37} / \epsilon_{\alpha}^{1.12}$ , with  $a_{tot}$  the total pixel area of the object and  $\epsilon_{\alpha}$  the quantification percentile representing the  $\alpha$ -values chosen for iso- $\alpha$  domain extraction. Yet redundant points of PROP-SFS point cloud are still generated with the construction of wrong PROP-SFS triangle. Those redundant points can lead us to incorrect PROP-SFS reconstructions and make computing time way longer. To limit that, TLS data should be pre-processed and optimal parameters chosen.

Our PROP-SFS method has been shown to be sensitive to: (i) picture size  $a_{tot}$  and quantification percentile  $\epsilon_{\alpha}$ , (ii) noise and bias on  $\alpha$ -values, and (iii) distance noise. With this knowledge, we set up methods and strategies to make optimal PROP-SFS reconstructions in terms of accuracy and redundancy.

- (i) It is widely known that PROP-SFS reconstruction makes a reconstruction error propagation [163]. This error depends on the distance of the reconstruction from the seed, but also, in our case, on the quality of the iso- $\alpha$  domain boundary extraction. Boundary estimation error is added to the propagation error throughout the propagation. In the case of small matrices, the quality of boundary extraction is low, whereas large



matrices lead us to better boundary extraction. In the first case, it is thus necessary to extract a low amount of iso- $\alpha$  domains to limit error propagation caused by boundary estimation error. A strategy of extracting iso- $\alpha$  domains with fixed size (in pixel) can be used to control the iso- $\alpha$  domain number as a function of  $\alpha$ -photograph size. Upstream of our PROP-SFS pipeline, we added a method to select a quantification percentile value as a function of the size of the picture shell (in pixel), i.e., the outer iso- $\alpha$  domain that is encircling the other iso- $\alpha$  domains.

- (ii) Analysis of PROP-SFS reconstruction carried out on noised  $\alpha$ -matrices showed that it is necessary to avoid  $\alpha$  noise. We set up a  $\alpha$ -matrix smoothing method by local averaging. On a synthetic hemisphere  $\alpha$ -matrix with  $\alpha$ -noise of maximum  $\pm 5.7^\circ$ , we showed that this method should be applied at least five times to obtain correct reconstruction. In the case of more complex shapes, the number of consecutive  $\alpha$ -matrix smoothing can be selected with visual inspection of the smoothed  $\alpha$ -matrices. This choice should take into account the number of visible seeds and iso- $\alpha$  domain boundary complexity (e.g., curvature and concavity) to limit complex propagation scheme and thus redundancy. Bias of the  $\alpha$ -values has also been shown to drive the reconstruction quality and can make it more accurate. Yet we did not make any suggestion about the use of artificial  $\alpha$ -values bias.
- (iii) SPS greatest slope computation depends on 3D curve shape. In particular, it depends on the 3D seed boundary shape. If this latest curve has been incorrectly extracted due to noise, the greatest slope computation is incorrect. Thus noise should be avoided on this curve as much as possible. A low-pass filter has been implemented to extract curve information from noisy distance data. A cutoff value is chosen with assumption on curve shape (e.g., number of peaks).

After proper TLS intensity calibration, Conference pear tree leaves geometry (area, inclination and shape) were extracted from PROP-SFS reconstruction ran on TLS data. We tested several parameter sets with various quantification percentile values and 2D seed sizes. Our major goal to correct outlier points was met and the reconstructed shapes were realistic. Leaf area estimation showed an underestimation of 4.5 cm<sup>2</sup> for average leaf area of 35 cm<sup>2</sup> and best correlation coefficient obtained was 0.77. Leaf elevation were extracted with a precision of  $\pm 20^\circ$  and azimuth with a precision of  $\pm 40^\circ$ . We observed that quantification percentile values and seed sizes should be adapted to leaf complexity and to matrix size to obtain better results. As a first strategy, we proposed to use computing time and point redundancy to change parameter if needed. Finally, missing steps of our PROP-SFS propagation were shown to impact in our results: SFS-PROP mesh outlier triangles were still constructed and create a bias in the area and inclination estimation.

Compared to other leaf area, inclination and shape extraction method (e.g., [136, 18]), our PROP-SFS reconstruction provided less accurate area and inclination estimation. However, those studies extract those geometric variables only on picked leaves or from single stems placed close to the

3D scanner aperture and such that the leaves were perpendicular to their 3D scanner viewing direction. In other words, they used high resolution and high quality data with best measuring conditions. Compared to those previous studies, we gave the first leaf area, inclination and shape estimation for complex canopy leaves shape under *in situ* conditions and from a phase-shift TLS device and we validated our reconstruction for leaf point cloud density ranging from 29 to 272 points/cm<sup>2</sup>. In addition, if our PROP-SFS propagation is improved to avoid mesh outlier triangles and holes, and if optimal quantification percentile values and seed sizes are automatically selected, our PROP-SFS algorithm can be expected to provide better results.

## Perspective

As a first trial, we managed to extract leaf shape, area and inclination from TLS scan of pear trees under *in situ* conditions. In the framework of plant geometry extraction for extensive study of plant physiology, results of our thesis makes it possible to reach new goals.

**PROP-SFS improvement.** In addition to the improvements aforementioned, two other points can be investigated to makes our PROP-SFS method more optimal. The first point concerns the investigation of the saddle toggle points. Those points define area where propagation cannot be carried out normally with SPS. We used plane portion to fill those areas. Yet we did not make the mathematical analysis of those toggle points. With comparable analysis than done in Chapter 4, we can seek for specific surface to use with such points and improve our PROP-SFS algorithm. The second point concerns the integration of distance data in the PROP-SFS reconstruction. TLS principal data is distance and in our PROP-SFS, only a few distance points are used. Our PROP-SFS pipeline can be augmented with a method that integrates and merges distance information to the reconstruction during the propagation. This method can be for instance a Kalman filter [216].

**Scan segmentation.** Two types of segmentation of TLS scan of plants are required: (i) woody versus leaf material, and (ii) leaf segmentation. Béland et al. [17] used intensity to classify and segment woody part versus foliage in their scans. Yet they observed that their method always likely involves a level of misclassification between wood and leaf components. The analysis we did on the intensity relation with surface inclination makes it possible to complete their classification. For instance, the comparison of distance and intensity information can be done: local inclination can be computed in the point cloud and thus transformed into  $\alpha$ -values. Comparison with actual  $\alpha$ -values represented by the TLS intensities can be used to detect the boundary of potential segmented area.

**Plant representation.** Traditional global and distributive geometric variables (LAI, VLAD, voxelized 3D space of LAD, etc.) have been already estimated quite accurately from TLS data. Yet it would be interesting to assess our PROP-SFS reconstruction quality on those variable estimations. First results obtained from pear tree leaf reconstructions showed that we can expect satisfactory results for those global and distributive variables estimation. For instance, our results

showed that our PROP-SFS reconstruction method can be used to detect leaf movements such it has been done by Thanisawanyangkura et al.[105].

With our method, we managed to extract leaf shape of complex canopy scanned with TLS under *in situ* conditions. Combined with tree architecture extraction method such as the one proposed by Preuksakarn [122], it would be possible to reconstruct virtual plants from real observation using TLS scans. Yet techniques to attach reconstructed leaves to virtual tree branches should be developed. Signal occlusion caused by leaves avoid us to get complete plant scan. Specific measurement protocols, such as plant scan through growth, should be set up.

**Plant physiology.** The general framework of this thesis was the use of TLS scans for extensive physiological studies of plants to improve orchard management. Two main issues were discussed: (i) tree architecture manipulation, and (ii) disease and stress detection.

Tree architecture manipulation depends on fruit quality and quantity objectives. Willaume et al. [2] showed that the quantity and position in the canopy of spur leaves versus shoot leaves were affecting fruit quality. Our PROP-SFS method could be used to detect fruit and reconstruct leaves. Yet architecture information is highly required to make useful canopy models and additional studies, as above mentioned, should be carried out. Ideally, spur leaves versus shoot leaves detection tools should be developed.

Diseases and stresses induce plant morphology changes. Our PROP-SFS algorithm has shown to provide realistic representations of leaves. Consequently, it can be used to detect and study biotic and abiotic stresses.

In conclusion, my thesis objective to correct TLS outlier points with PROP-SFS algorithm has been fulfilled. My PROP-SFS algorithm can provide realistic object reconstruction from a TLS scan, even for objects with low points density. We showed that the correction of outliers was a mandatory step for the reconstruction of foliage when scanned with *in situ* conditions. We also showed that the obtained reconstructions were satisfactory as first results. As it can be expected in any computer method development, other components should be added upstream or downstream to our PROP-SFS method to improve the quality of the reconstructions. A complete pipeline for organs reconstruction would produce closer results to those obtained in laboratory conditions. In general, this method should be integrated in a larger set of computing methods such as organs segmentation, labeling, and architecture extraction, in order to produce virtual plants that would be optimal for physiological studies.



# **Part V**

## **Appendices**



# Appendix I

## Traditional point cloud process

After a scene is scanned by a 3D scanner device, e.g., a TLS, it is in general necessary to process the generated point cloud in order to extract the scene geometries such as objects area, position and orientation. It could be interesting to reconstruct the object surface, that is, to generate a mesh, i.e., a points set together with its connection segments.

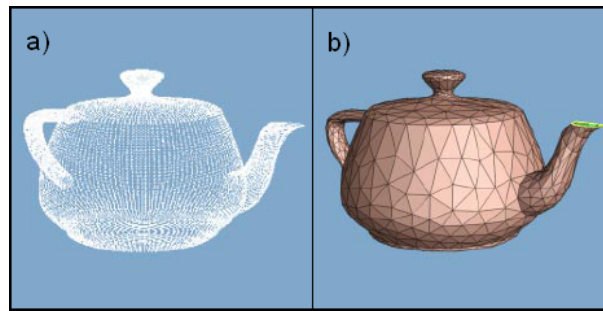
As it has been discussed in Chapter 1, TLS scanner provide 3D point cloud that has several features and dependencies. For instance, precision and density depends on the distance and material reflectance, holes are present because occlusion, and there are outliers along the edge of the scanned objects. In addition, geometrical (object, scan setup) and topological (genus and smoothness) configuration of the scanned surfaces may differ among scans. In other words, every scene has its own features and it is very difficult, if not impossible, to set up a general point cloud processing to reconstruct the scene surfaces. Still, there is commonality and three main steps for surface reconstruction can be defined: (i) the point cloud pre-processing; (ii) the reconstruction of the object; and (iii) the post-processing of the reconstruction. The framework of this thesis is the numerical reconstruction of *in situ* plant canopy. Because most of the plant canopies are complex and dense, manual and semi-automatic process are irrelevant.

In this appendix, we give a (non-exhaustive) summary on the main classifications made on automatic point cloud processes. A basic description of surfaces reconstruction is made in Section 1. We can notice that pre-processing on point cloud are the same than post-processing on mesh vertices (e.g., [217]). Pre- and post-process description are described in Section 2.

### 1 Generation of the virtual surface

Surface reconstruction is a very broad domain and it is very complicated to classify the methods. Fabio [218] proposed to report them according to some classifications which we summarize below. First, he made a classification based on the type of the surface representation:

- **Parametric representation:** the surface is considered as a set of parametric surface patches, described by parametric equations (e.g. B-spline, Bezier curves, etc.).



**Figure 1:** From [29]: (a) Point cloud representing a tea-pot. (b) Surface reconstruction from the tea-pot's point cloud.

- **Interpolated surface:** the surface is defined with a parametric representation and each point of the point clouds is contained in the reconstructed surface.
- **Implicit representation:** those methods try to find a smooth function that passes through all positions where the implicit function is evaluated to some specified value.
- **Simplicial representation:** the surface is a collection of simple entities including points, edges and triangles. To build the edges and triangles, this reconstruction can be carried out from a simple point cloud, e.g. a Delaunay triangulation [219].
- **Approximated surfaces:** those representations do not contain all the original points, but points as near as possible to them. For instance, the warping-based surface reconstruction (deformation of an initial surface) is of this kind.

Then, his classification is done according to the quality (or type) of the input data:

- **Unorganized point clouds:** the algorithms only work on the spatial position of the points.
- **Structured point cloud:** the algorithms can take into account additional information (e.g. break lines, local orientation).

Then, he categorized the algorithms by their spatial subdivision:

- **The surface oriented algorithm:** the output of the reconstruction is a surface.
- **The volume oriented algorithm:** the output of the reconstruction is a volume

Finally, he classified the reconstruction method according to the different assumption on the algorithm:

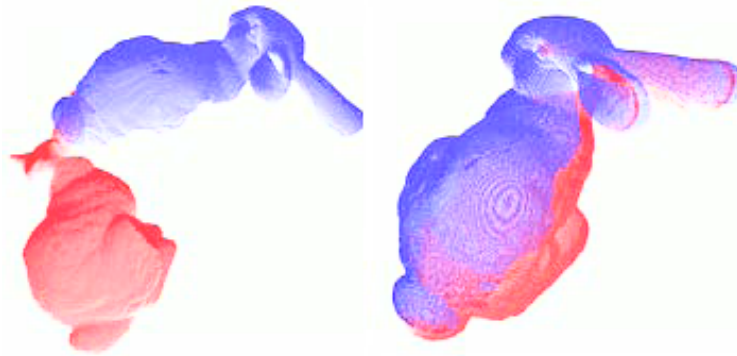
- **Fixed topology:** The algorithm assumes fixed topological type (e.g. genus, continuity).
- **Variable topology:** The algorithm exploits structure or orientation information such as adjacency relationship of data for multiple scan, or local surface orientation when surface gradients are provided.



## 2 Pre- and post-processing

### 2.1 Scan registration

In general, TLS scan is a partial representation of a scene. Only surfaces within the TLS field-of-view are visible. However several scans make it possible to obtain, in the best cases, a full representation of the scene. Registration method is a mandatory step to get coherent scans though (see Figure 2): each scan are expressed in the local Cartesian coordinate system, for which the TLS is the center, and a common coordinate system should be built. To do so, registration ball [174, 220] or target [221] are placed in the TLS field-of-view and are automatically detected to define a common coordinate system. Then an optimization of the registration can be carried out, e.g. an iterative closest point algorithm [222].



**Figure 2:** *Point cloud registration of the Stanford's rabbit. From[223].*

### 2.2 Objects segmentation, recognition and classification

In general, a scene composed of several objects. One of the first operation that a computer vision system must perform is the separation of objects, e.g. the background [224]. This is called the segmentation of the scene.

According to Hoover et al. [225], producing an image segmentation consist of: (i) make a set of scene subsets, i.e., the segments, such that their union is equal to the scene; (ii) each segment is connected [226]; (iii) the intersection of two segments is empty; iv) repeating the segmentation make the same set of scene segments. Wang and Shan [227] categorized traditional segmentation algorithms into five groups of method, that we have summarized below:

- **Edge-detection:** the TLS data are converted into range image to make it suitable to traditional image edge-detection methods (see Figure 3).
- **Surface-growing:** the points are grouped around surface patches, i.e. the seed of the process. The grouping is based on similarity measures, such as proximity, slope, curvature or surface normal.

- **Scan-line:** the range image is split into scan lines along a given direction. Then segments of lines are merged together based on some similarity measures in a region growing fashion.
- **Clustering:** each point is associated with a feature vector and the TLS data is segmented using a clustering technique, such as k-means or maximum likelihood.
- **Graph partitioning:** each TLS point or group of TLS points in a small neighborhood is a node of a graph and the connection between those nodes consists of the connections/edge between a pair of point. Each edge has a weight to measure the similarity of the pair of points. The segmentation is achieved with finding the optimized graph cuts.

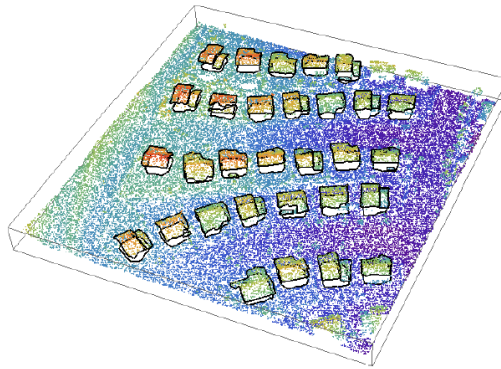
As previously mentioned, a TLS device also provides an intensity, i.e. a photograph of the scene. Similar techniques than for the point cloud can be applied to this photograph to segment the scene [224].

Sometimes, it is not possible to segment objects with the only point cloud (e.g. to segment grass from roads [228]). In this case, both of the TLS distance and intensity can be used to segment the image: the distance is used to segment objects with different shape and orientation, and intensity is used to segment objects with different gray level. Still, there could be an uncertainty if the material share close gray level [23].

Once the scene is segmented, an identification, location and description of the object can be carried out, i.e. it is the recognition process. According to Jain and Kasturi [224], 3D object recognition implies awareness of something already known, i.e. a model is necessary. The recognition process involves an algorithm to perform matching between models and data description and might include data- and model-driven sub-processes, e.g. a learning process. They classified the 3D recognition methods in three different type [224]:

- **The object representation schemes:** for instance, a wire-frame, i.e. a set of characteristic vertex points together with a list of edges corresponding to vertices pairs, can be used to recognize a specific object. A smooth deformation of the wire-frame is carry out until the object shape is matched.
- **The aspect graphs and characteristic views:** an object is represented in characteristic viewpoints, which gives the same qualitative view (number and type of features) of the projected object, called the “aspect” of the object. Connection in the aspect graph is defined when a changes in the aspect take place between two characteristic viewpoints.
- **The object recognition system:** for instance, the model-based system ACRONYM [229] for 3D interpretation of 3D images. ACRONYM is a modular system which uses view-independent volumetric object model and it is based on the prediction-hypothesis-verification paradigm.

Another kind of scene partitioning is the scene classification. Scene sections are annotated by high-level or low-level semantic information [230]. Compared to the recognition process, this operation output is an annotated segmentation of the image, e.g. vegetation versus building (low-level semantic); or a label for the image itself, e.g., forest versus city (high-level semantic). Similarly to segmentation, both of TLS distance and intensity could be used to classified complex scene, e.g., the land covers which are forming a landscape.

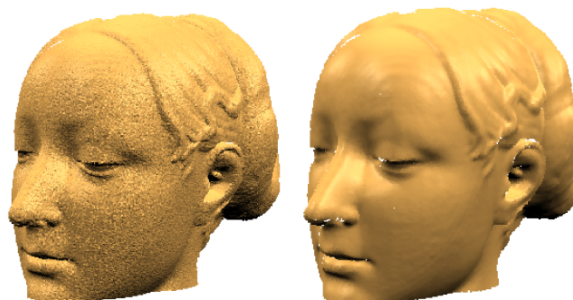


**Figure 3:** *Example of point cloud segmentation made with an edge detection algorithm: house roofs versus ground. From [227]*

## 2.3 Noise reduction

Some surface reconstruction methods can be very sensitive to noise. Noise removal could be an important step in the pre-processing of noisy TLS data. The reduction of TLS distance noise can be inspired by noise reduction methods for intensity photograph [231] such as median or averaging filter. As well as for photograph, those type of noise reduction algorithm can also smooth shape information. Noise reduction methods which consider a kernel with a curvature-dependent geometry, e.g., anisotropic approach [232], or with adaptive kernel size [233], are methods which remove noise together with keeping the shape information (Figure 4).

Another traditional noise removal method is to estimate local orientation with a moving least square algorithm applied on the point cloud [214]. This local orientation is used to define a piece of plane which would fit locally the point cloud and neighboring points are projected onto this piece of plane.

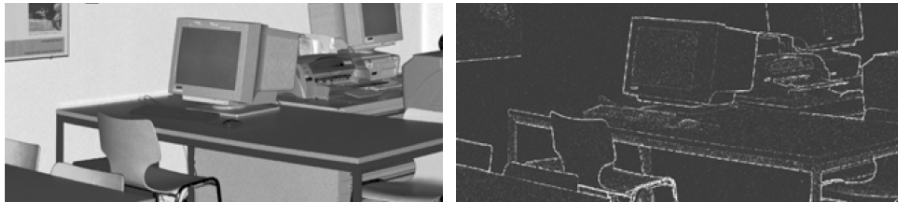


**Figure 4:** *Example of noise reduction with Gaussian filter with adaptive kernel. From [233].*

## 2.4 Outliers correction

It is possible to delete the outliers manually, however this task can be time-consuming. Algorithms for outliers detection can be classified in two kinds [50]:

- **Distance based algorithm:** a point is considered as an outlier if a defined portion of the scanned surface is at least at a minimal distance.
- **Density based algorithm:** a point is considered as an outlier if it has not enough neighbors in its surrounding. This last algorithm needs the knowledge of local density, which is not always easy to estimate (Figure 5).



**Figure 5:** Distance based outlier detection of a TLS scan of an office. From [50].

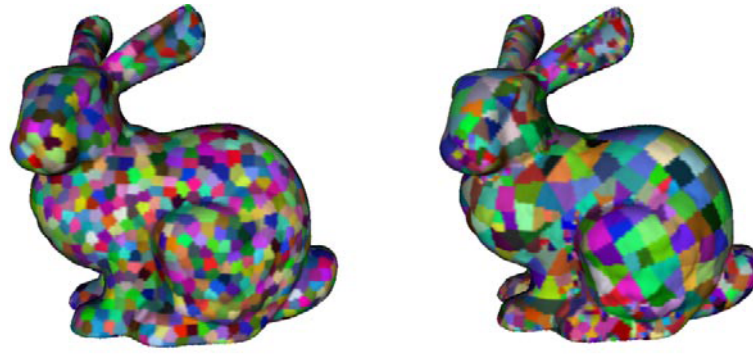
## 2.5 Simplification

The scan of a scene can be redundant in terms of distance sampling. Depending on the object shape, it is neither necessary to keep every point of the TLS point cloud nor of the produced mesh vertices. Pauly et al. [234] proposed to classify the points set simplification methods in three kinds:

- **Clustering:** the points set is divided into grid cells. All sample points that fall into the same cell are represented by a common representative. This method fails in the correct representation of complex shape. Still, a region-growing clustering has been developed to be curvature adaptive.
- **Iterative simplification:** the number of points is reduced by using a down-sampling operator. For instance, specific points can be removed from the original point cloud to keep the representative points. In general, an error-metric is used to quantify the error caused by the down-sampling.
- **Particle simulation:** particles are randomly spread across the surface and their position is equalized using a point repulsion algorithm.

## 2.6 Surface completion

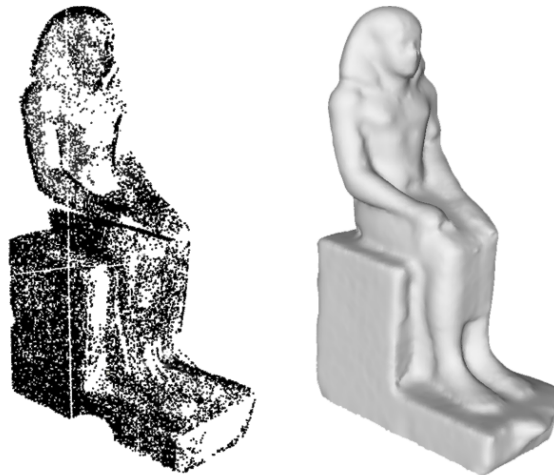
Holes and under-sampling in the point cloud (Figure 7) can be generated because of occlusions, critical reflectance properties, constraints in the scanning path, or limited sensor resolution [235].



**Figure 6:** *Clustering simplification on the Stanford's rabbit mesh. From [234].*

To get a correct surface reconstruction, it is necessary to complete the points set. Schnabel et al. [236] gave a short review of the different approaches:

- **Surface completion based on level-set PDE and energy minimization:** a smooth geometry is inferred in missing area.
- **Example-based approach:** those methods discover similarity in (or between) model in order to infer the missing information from other fully captured surface part.
- **Mesh-repair:** to fill small gaps in the mesh.
- **Range image completion:** this approach consists in continuing primitive shapes that reach a hole boundary.



**Figure 7:** *Example of holes filling. From [235].*

### 3 Discussion

In this appendix, we have seen that several concepts can be used to classify surfaces reconstruction, and pre- and post- processes. Those classifications have been summarized in Table 1-1 and 2, respectively. There are several ways to reconstruct surfaces and to carry out a correct representation

of the surface reconstruction, and each of them assumes a certain quality of the point cloud. Intuitively, we can guess that it is necessary to perform point cloud processes to get a correct surface representation (Table 1-3):

- We can easily imagine that point cloud segmentation is a necessary step before starting the surface reconstruction;
- Noise reduction might be an important step if the correctness of the points position is needed, as it is the case for the parametric, implicit, simplicial and interpolated representation. However, the reconstruction which is using an approximated representation might not need a noise reduction.
- Outliers correction is an important step in a point cloud processing as they might create a large bias in the surface reconstruction.
- Simplification seems to be an optional step as it reduces redundancies of the point cloud and does not improve correctness of the surface representation.
- Surface completion depends on the knowledge of the surface topology (e.g., genus) and/or on the feature of the surface reconstruction. In addition, reconstructions can intrinsically get rid of small holes. In conclusion, this type of process depends on the surface that should be reconstructed and on the method of reconstruction.
- Registration is rather a process that depends on the availability of extra 3D point cloud and it should not be a necessary step for surface reconstruction.
- Recognition and classification are semantic processes. They can help in the choice of a surface reconstruction method, but are not mandatory.

In addition, in Table 1-2 , we see that some process have been developed to take into account both of the intensity and distance image.

1)

Surface reconstruction	Quality of the input data	Spatial subdivision	Type of representation	Assumption
Classification	Unorganized point cloud	Surface oriented	Parametric	Topology
	Structured point cloud	Volume oriented	Implicit	Structure/Orientation
			Simplicial	
			Approximated	
			Interpolated	

2)

Process	Registration	Segmentation	Recognition	Classification	Noise reduction	Outliers correction	Simplification	Surface completion
Type	Geometric	Edge-detection	Object-representation scheme	Segmentation	Filter	Distance-based algorithm	Clustering	Energy minimization
	Optimization	Surface-growing	Aspect graph and characteristic view	Recognition	Surface projection	Density-based algorithm	Iterative simplification	Example-based approach
		Scan-line	Object recognition system				Particle simulation	Mesh-repair
		Clustering						Range image completion
		Graph-partitioning						
Intensity + Range		X		X				

3)

	Registration	Segmentation	Recognition	Classification	Noise reduction	Outliers correction	Simplification	Surface completion
Parametric		X			X	X	?	?
Implicit		X			X	X	?	?
Simplicial		X			X	X	?	?
Approximated		X			?	X	?	?
Interpolated		X			X	X	?	?

**Table 1:** (1) Summary of the surface reconstruction classification. (2) Summary of the processes. (3) X: the process is necessary for a correct surface reconstruction. ?: the process might be necessary.





# Appendix II

## Geometry

### 1 Curve

#### 1.1 Frenet trihedron

Let  $\mathcal{C}$  a 3D curves that is at least  $C^{m'}$ -continuous with  $m' \geq 2$ . Let  $c : I \subset \mathbb{R} \rightarrow \mathbb{R}^3$  a parametric representation  $C^{m'}$ -continuous of  $\mathcal{C}$ . Its tangent  $t$  is defined by:

$$t(s) = \frac{\frac{d}{ds}c(s)}{|\frac{d}{ds}c(s)|}. \quad (1.1)$$

The curvature vector  $k$  of  $\mathcal{C}$  is defined by:

$$k(s) = \frac{d}{ds}t(s) = \dot{t}(s). \quad (1.2)$$

Let  $|k(s)| = \kappa(s)$  be the curve curvature. We define the principal normal unit vector  $n$  as:

$$n(s) = \frac{k(s)}{\kappa(s)}. \quad (1.3)$$

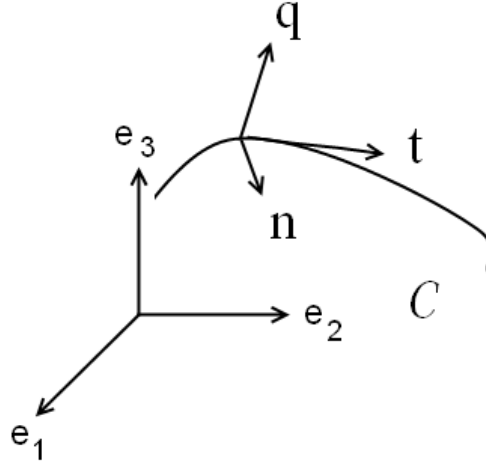
Finally, the binormal vector of the curve is defined as:

$$q(s) = t(s) \times n(s). \quad (1.4)$$

We call  $(t, n, q)$  the Frenet trihedron of the curve  $\mathcal{C}$  (see Figure ). The Frenet-Serret equations relating  $t$ ,  $n$  and  $q$  are (See Chapter 5 of [198]):

$$\begin{cases} \dot{t}(s) = \kappa(s).n(s) \\ \dot{n}(s) = -\kappa(s).t(s) + \tau(s).b(s) \\ \dot{q}(s) = -\tau(s).n(s) \end{cases} \quad (1.5)$$

with  $\tau$  the torsion of the curve. In the case of a planar curve, the torsion is null, i.e.,  $\tau(s) = 0$ .



**Figure 1:** *Frenet trihedron of the curve  $C$ .*

## 1.2 Inflexion point of a curve

An inflexion point is a point of a curve  $C$  such that the direction of the curvature vector changes relatively to the tangent of  $C$ , i.e.,  $c(s)$  is an inflexion point of the curve  $C$  if and only if  $k(s) = 0$  and if there exists  $\epsilon > 0$ , small enough, such that  $\kappa(s + \epsilon)$  and  $\kappa(s - \epsilon)$  are of opposite sign.

## 1.3 Involute and evolute

An involute is a curve  $\xi^*$  obtained from another given curve  $\xi$  by attaching an imaginary taut string on  $\xi$  and tracing the traveling of a given string point of this taut string while it is wound onto that given curve:

$$\xi^*(s) = \xi(s) + r(s) \cdot t_\xi(s), \quad (1.6)$$

where  $t_\xi(s)$  generates the line that represents the taut string.

Involute curve has the following properties of curve length conservation (Figure 2):

$$|\xi^*(s') - \xi(s')| = \ell(\xi(s') - \xi(s)) + |\xi^*(s) - \xi(s)|, \quad (1.7)$$

and:

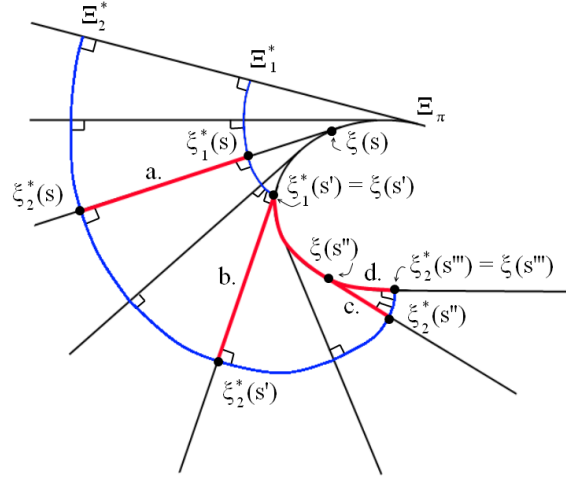
$$|\xi_2^*(s') - \xi_1^*(s')| = |\xi_2^*(s) - \xi_1^*(s)|, \quad (1.8)$$

where  $\xi_1^*$  and  $\xi_2^*$  are two involute curves.

## 1.4 Helix

A generalized 3D helix curve  $C$  is a curve which tangent  $T$  forms constant angle  $\alpha$  with a given direction  $V$ , i.e.:

$$T \cdot V = \cos(\alpha). \quad (1.9)$$



**Figure 2:** Involute properties.

If  $V$  is the vertical direction, the a helix can be viewed as the lift of a 2D curve  $c$ , with:

$$\begin{cases} C_1(s) = c_1(s), \\ C_2(s) = c_2(s), \\ C_3(s) = \tan(\alpha) \cdot \int \left| \frac{dc(s')}{ds'} \right| \cdot ds'. \end{cases} \quad (1.10)$$

A circular helix is the lift of a circle.

## 1.5 Chapter 4: Lemma 15 on curves.

**Lemma.** Let  $C^0$  and  $C^1$  be two planar curves with their parametric representation  $c^0$  and  $c^1$  and their Frenet trihedron  $(t^0, n^0, q^0)$  and  $(t^1, n^1, q^1)$ , respectively. Let us suppose that both  $c^0$  and  $c^1$  has no inflexion point and  $c^0$  is a natural representation of  $C^0$ . If there exists  $a : \mathbb{R}^+ \rightarrow \mathbb{R}^+$  strictly increasing and such that (see Figure 3):

$$\begin{cases} (1) \ c^1(s) = c^0(s) + a(s) \cdot n^0(s), \\ (2) \ c^1(0) = c^0(0), \\ (3) \ t^1(0) = t^0(0), \end{cases} \quad (1.11)$$

then  $\angle(n^0(s), n^1(s))$  and  $\angle(t^0(s), n^0(s))$  are of same sign.

*Proof.* Deriving Equation 1.11-1, we obtain:

$$\frac{dc^1}{ds}(s) = \frac{dc^0}{ds}(s) + a(s) \cdot \frac{dn^0}{ds}(s) + \frac{da}{ds}(s) \cdot n^0(s). \quad (1.12)$$

Because  $c^0$  is a natural representation of a curve, then  $\frac{dc^0}{ds}(s) = t^0(s)$ . With the Frenet-Serret equations (see Section 1.1), and because the two curves are planar, we obtain:

$$\frac{dc^1}{ds}(s) = (1 - a(s) \cdot \kappa^0(s)) \cdot t^0(s) + \frac{da}{ds}(s) \cdot n^0(s), \quad (1.13)$$

on which we can apply the dot product with  $t^0$ :

$$t^0(s) \times \frac{dc^1}{ds}(s) = \frac{da}{ds}(s) \cdot (t^0(s) \times n^0(s)), \quad (1.14)$$

$$t^0(s) \times t^1(s) = \frac{\frac{da}{ds}(s)}{|\frac{dc^1}{ds}(s)|} \cdot (t^0(s) \times n^0(s)). \quad (1.15)$$

As we have:

$$c^1(0) = c^0(0), \quad (1.16)$$

$$t^1(0) = t^0(0), \quad (1.17)$$

and as  $a$  is strictly increasing, the two curves have the same curvature sign in the neighboring of 0, i.e., we have:

$$t^1(\epsilon) \times n^1(\epsilon) = t^0(\epsilon) \times n^0(\epsilon), \quad (1.18)$$

with  $\epsilon \geq 0$  and small. As  $c^0$  and  $c^1$  have no inflexion point, then the last assertion is always true, i.e.:

$$t^1 \times n^1 = t^0 \times n^0. \quad (1.19)$$

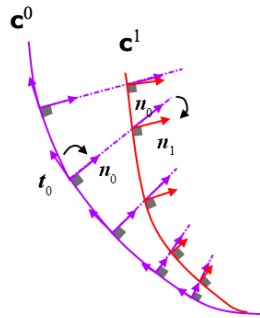
With proper application of the dot product of  $t^0$  and  $n^1$ , this last equation is equivalent to:

$$t^0 \times t^1 = n^0 \times n^1. \quad (1.20)$$

Combined with Equation 1.15, we obtain:

$$n^0(s) \times n^1(s) = \frac{\frac{da}{ds}(s)}{|\frac{dc^1}{ds}(s)|} \cdot (t^0(s) \times n^0(s)). \quad (1.21)$$

Because  $a$  is strictly increasing, then  $\frac{da}{ds}(s) > 0$ . Thus  $\angle(n^0(s), n^1(s))$  and  $\angle(t^0(s), n^0(s))$  are of same sign.  $\square$



**Figure 3:** *Curves property.*

## 2 Surface

Let  $\Omega$  an open and connected subset of  $\mathbb{R}^2$  and  $\mathcal{S}$  a surface of  $\mathbb{R}^3$  defined by its height function  $h$ :

$$\begin{aligned} h : \Omega &\rightarrow \mathbb{R} \\ (x_1, x_2) &\mapsto h(x_1, x_2). \end{aligned} \quad (2.1)$$

We suppose that  $\mathcal{S}$  is at least  $C^m$ -continuous ( $m > 3$ ). We denote by  $(e_1, e_2, e_3)$  the Cartesian coordinates system of  $\mathbb{R}^3$ .

### Notation:

- $w$  is a point of  $\mathcal{S}$  and  $x$  its projection on  $\Omega$ .
- $\underline{g}_w$  and  $\underline{g}_w$ : greatest slope vector on  $w \in \mathcal{S}$  and its projection.
- $\underline{o}_w$  and  $\underline{o}_w$ : level curve tangent on  $w \in \mathcal{S}$  and its projection.
- $N_w$ : normal to the surface on  $w$ .
- $T_w\mathcal{S}$ : the tangent plane of  $\mathcal{S}$  on  $w$ .
- $c$ : curve representation of the 2D curve  $\mathcal{C} \in \Omega$ . We have:

$$c = c_1.e_1 + c_2.e_2. \quad (2.2)$$

- $c^*$ : curve representation of the 3D curve  $\mathcal{C}^* \in \mathcal{S}$ . We have:

$$c^* = c_1.e_1 + c_2.e_2 + h(c).e_3. \quad (2.3)$$

- $t_w^c$  and  $\underline{t}_w^c$ : tangent of  $c$  on point  $w$  and its projection

### 2.1 Greatest slope, level curve and gradient property

**Proposition.** Let  $x \in \Omega$  such that  $\nabla h(x) \neq 0$  and  $w$  its corresponding point on  $\mathcal{S}$  a surface that is at least  $C^m$ -continuous ( $m > 3$ ).

We have:

1. The projection of the greatest slope vector  $\underline{g}_w$  is collinear to the height function gradient on  $x$ , i.e.,  $\underline{g}_w \propto \nabla h(x)$ .
2.  $\underline{g}_w$  and  $\underline{g}_w$  are orthogonal to  $\underline{o}_w$  and  $\underline{o}_w$ , respectively.
3.  $\angle(\underline{g}_w, \underline{g}_w) = \alpha(w)$ , where  $\alpha(w) = \angle(N_w, e_3)$ .

*Proof.* (1) Let consider a curve  $C$  on  $\Omega$  and its  $C^{m'}$ -continuous natural representation  $c$  (with  $m' \geq 2$ ). We have:

$$\frac{d}{ds}h(c(s)) = \frac{\partial}{\partial c_1}h(c(s)) \cdot \frac{d}{ds}c_1(s) + \frac{\partial}{\partial c_2}h(c(s)) \cdot \frac{d}{ds}c_2(s), \quad (2.4)$$

$$= \nabla h(c(s)) \cdot \frac{d}{ds}c(s), \quad (2.5)$$

with  $\cdot$  the scalar product of two vectors. As we can see on Figure 4, the quantity  $\frac{d}{ds}h(c(s))$  can be positive or negative depending on the traveling direction of  $c(s)$ . We choose it positive. Because the Cauchy-Schwarz inequality theorem, we have the two following assertions:

$$0 \leq \nabla h(c(s)) \cdot \frac{d}{ds}c(s) \leq |\nabla h(c(s))| \cdot \left| \frac{d}{ds}c(s) \right| = |\nabla h(c(s))|, \quad (2.6)$$

and:

$$\nabla h(c(s)) \cdot \frac{d}{ds}c(s) = |\nabla h(c(s))| \iff \nabla h(c(s)) \propto \frac{d}{ds}c(s). \quad (2.7)$$

Let us consider  $c'(s) := \operatorname{argmax}_{c: \mathbb{R} \rightarrow \mathbb{R}^2} \left\{ \frac{d}{ds}(h \circ c(s)) \right\}$ , i.e.,  $c'(s) = \nabla h(c(s)) \cdot \frac{d}{ds}c(s) = |\nabla h(c(s))|$ . From assertion 2.7, it has its tangents collinear to  $\nabla h(c'(s))$  for every  $s \in \mathbb{R}$ . Let us now consider  $c'^*$  be the 3D curve parametrization of  $C'^* \in \mathcal{S}$  and  $w := c'^*(s_w) \in C^*$ . We have  $t_w^{c'^*} \in T_w S$ . By definition of  $c'$ ,  $t_w^{c'^*}$  is the vector of  $T_w S$  which has the largest projection on  $e_3$ . Lets now the steepest descent curve  $G^* \subset \mathcal{S}$  of natural representation  $g^*$  that passes by  $w$ .  $g_w$  is the vector of  $T_w S$  which forms the greatest elevation angle, i.e., it is the vector of  $T_w S$  with the largest projection on  $e_3$ . It is equal to  $t_w^{c'^*}$ . That means:

$$g_w = t_w^{c'^*} \implies \underline{g_w} = \underline{t_w^{c'^*}}. \quad (2.8)$$

As,  $\underline{t_w^{c'^*}} \propto \underline{t_x^c}$ , then from assertion 2.7:

$$\underline{g_w} \propto \underline{t_x^c} \propto \nabla h(x). \quad (2.9)$$

(2) For the level curve representation, it is obvious that we have for every  $\sigma \in \mathbb{R}$ ,  $\frac{dh}{ds}(\underline{o}(\sigma)) = 0$  and thus from equation 2.4:

$$\nabla h(\underline{o}(\sigma)) \cdot \frac{d}{d\sigma}\underline{o}(\sigma) = 0. \quad (2.10)$$

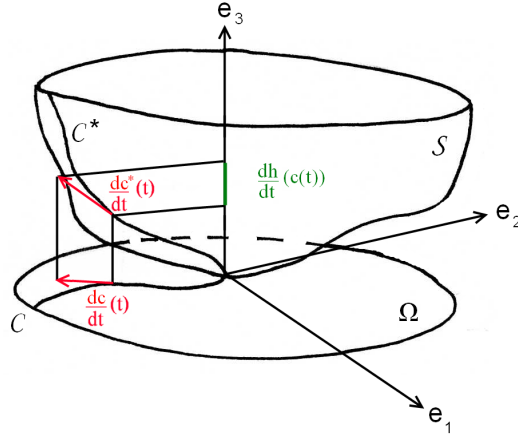
For a given  $x := \underline{o}(\sigma)$  we have by hypothesis  $\nabla h(x) \neq 0$ . As  $\frac{d}{d\sigma}\underline{o}(\sigma) \propto \underline{t_x^o}$  is non-zero, it is thus necessarily orthogonal to  $\nabla h(x)$ . As we have previously seen, we have  $\nabla h(x) \propto \underline{g_w}$ . Thus:

$$\underline{g_w} \perp \underline{t_x^o}. \quad (2.11)$$

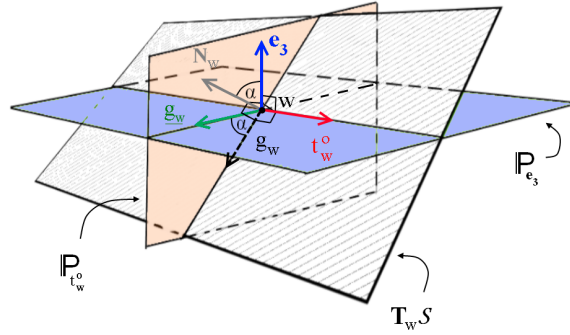
Similarly:

$$g_w \perp t_w^o. \quad (2.12)$$

(3) The vector  $\underline{g_w}$ ,  $g_w$  and  $e_3$  are on the same plane  $\mathbb{P}$ . Because  $\underline{t_w^o} \perp e_3$  and  $\underline{t_w^o} \perp \underline{g_w}$ ,  $\mathbb{P}$  is actually  $\mathbb{P}_{\underline{t_w^o}}$  and thus we also have  $g_w \perp \underline{t_w^o}$ . We have  $\underline{t_w^o} \in T_w S$  and thus  $\underline{t_w^o} \perp N_x$  meaning that  $N_w$  is also on  $\mathbb{P}_{\underline{t_w^o}}$ . Finally, we have  $g_w \in T_w S$  that means  $g_w \perp N_w$ . In conclusion, as  $\angle(e_3, N_w) = \alpha(x)$  and  $\angle(N_w, g_w) = \pi/2$ , then  $\angle(e_3, g_w) = \alpha(x) + \pi/2$ . In other words,  $\angle(\underline{g_w}, g_w) = \alpha(x)$  (Figure 5).  $\square$



**Figure 4:** Instant height variation (in green) along a curve  $C$  when lifted up on  $S$ .



**Figure 5:** Greatest slope elevation.

## 2.2 Chapter 5: Equation 2.7

**Proposition.** Let  $w$  be a point on a  $C^m$ -continuous surface  $S$  ( $m \geq 3$ ) and let  $r$  be a vector of the tangent plane  $T_w S$ . We denote by  $\alpha := \angle(\underline{g}_w, g_w)$ ,  $\gamma := \angle(\underline{r}, r)$  and  $\phi = \angle(\underline{r}, \underline{g}_w)$ . Lets us define:

$$\varepsilon = \begin{cases} +1 & \text{if } \phi \geq 0, \\ -1 & \text{else.} \end{cases} \quad \text{and} \quad \vartheta = \begin{cases} 1 & \text{if } \gamma \geq 0, \\ 0 & \text{else.} \end{cases} \quad (2.13)$$

Then:

$$\phi = \varepsilon \cdot \left( |\vartheta \cdot \pi - \arccos\left(\frac{\tan(|\gamma|)}{\tan(|\alpha|)}\right)| \right). \quad (2.14)$$

*Proof.* We construct the following points (see Figure 6):

- $W := w$ .
- Let  $A$  be the head of  $\underline{g}_w$  (with  $|\underline{g}_w| = 1$ ).
- Let  $B$  be the intersection point between the two lines which are directed by  $r$  and  $\underline{r}_w^o$  and passing by  $W$  and  $A$ , respectively.

- Let  $W'$  be the intersection point between the two lines directed by  $t_w^o$  and  $g_w$  and passing by  $W$  and  $B$ , respectively.
- Lets us consider the points  $\underline{A}$  and  $\underline{B}$  the projected points of  $A$  and  $B$ , respectively, on the horizontal plane  $\mathbb{P}_{e_3}$ . We remark that  $[W, \underline{B}]$  is directed by  $\underline{r}$ .

We have the following assertions:

- As it is recalled by proposition presented in Section 2.1 of this appendix,  $t_w^o \perp g_w$ . Thus,  $[W, A] \perp [W, W']$ . As  $[W, W'] \parallel [A, B]$  and  $[W, A] \parallel [W', B]$ , thus  $WABW'$  is a rectangle.
- As  $[A, B] \parallel [W, W']$  and  $[W, W']$  is horizontal, then  $[A, B]$  is also horizontal. As  $[A, \underline{A}]$  and  $[B, \underline{B}]$  are vertical, then  $[A, \underline{A}] \perp [A, B]$  and  $[B, \underline{B}] \perp [A, B]$ , respectively. In addition,  $[A, \underline{A}]$  and  $[B, \underline{B}]$  are orthogonal to any lines within  $\mathbb{P}_{e_3}$  and in particular to  $[A, B]$ . Thus  $ABBA$  is a rectangle.
- Finally, as  $WABW'$  and  $ABBA$  are rectangle, then  $[A, B] \parallel [A, \underline{B}]$  and  $[A, B] \parallel [W, W']$ . Thus  $[A, \underline{B}] \parallel [W, W']$ . As we also have  $t_w^o \perp g_w$  from the proposition of Section 2.1, then  $[A, W] \perp [A, \underline{B}]$ . Because rectangle property, we have  $\ell([W, W']) = \ell([A, B]) = \ell([A, \underline{B}])$ , with  $\ell$  the length of the segment. Then  $WABW'$  is a rectangle.

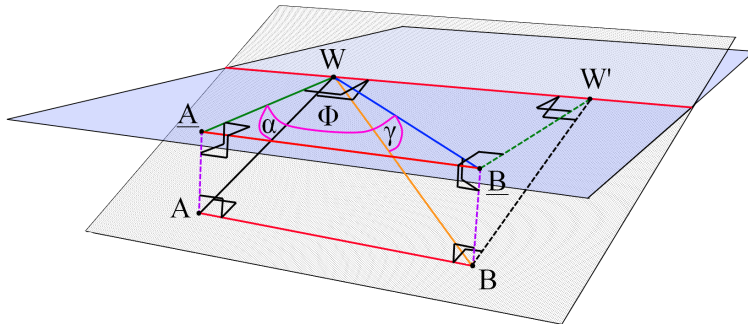
From basic trigonometric formulas, we know that  $\ell([A, A]) = \sin(\alpha)$ . As  $ABBA$  is a rectangle, then  $\ell([B, B]) = \sin(\alpha)$ . Because  $\underline{B}$  is the projection of  $B$  on  $\mathbb{P}_{e_3}$ , then  $WBB$  is a right triangle with its right angle on  $\underline{B}$ . As  $\gamma := \angle(\underline{r}, r)$ , then  $\ell([W, \underline{B}]) = \frac{-\sin(\alpha)}{-\tan(\gamma)}$ . Finally, as  $\ell([W, A]) = \cos(\alpha)$ , and as  $WAB$  is a right triangle with its right angle on  $\underline{A}$ , then:

$$\phi = \arccos\left(\frac{\tan(\gamma)}{\tan(\alpha)}\right) \quad (2.15)$$

In this discussion, vectors inclination and orientation were absolute. If we take into account their relative inclination and orientation (Figure 7), we can improve the Equation 2.15. As the greatest slope is always pointing down, we make the analysis on the vector  $r$  situation relatively to  $g_w$  and we obtain:

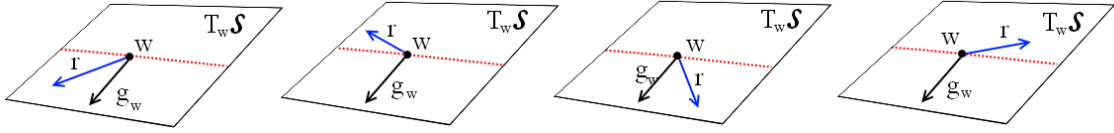
$$\phi = \varepsilon \cdot \left( |\vartheta \cdot \pi - \arccos\left(\frac{\tan(|\gamma|)}{\tan(|\alpha|)}\right)| \right). \quad (2.16)$$

□



**Figure 6:** Geometrical construction for the proof.





**Figure 7:** Different cases of vectors  $r \in T_w S$  orientation and inclination relatively to  $g_w$  and the horizontal (red).

## 2.3 Chapter 5: Equation 2.12

**Proposition.** Let  $S$  be a smooth surface,  $w$  a point of  $S$ ,  $\mathcal{A} \subset S$  a curve on this surface that passes by  $w$  and parameterized by  $a$ , and  $\underline{\mathcal{A}} \subset \Omega$  its projection of parametrization  $\underline{a}$  that passes through a point  $x := \underline{w}$ . We have:

$$t_w^a = \rho \cdot (n_x^a \times N_w) \quad (2.17)$$

with  $t_w^a$  the tangent of  $a$  on  $w$ ,  $n_x^a$  principal normal to the curve  $\underline{a}$  on  $x$ ,  $N_w$  the normal to the surface  $S$  on  $w$  and:

$$\rho = \begin{cases} +1 & \text{if } \angle(t_x^a, n_x^a) \geq 0, \\ -1 & \text{else,} \end{cases} \quad (2.18)$$

with  $t_x^a$  the tangent of  $\underline{a}$  on  $x$ . If  $\kappa_x^a$ , the curvature of  $\underline{\mathcal{A}}$ , equals zero, then we consider  $n_x^a$  as being the vector in  $\mathbb{P}_{e_3}$  (plane orthogonal to  $e_3$ , i.e., horizontal plane) such that  $\angle(t_x^a, n_x^a) > 0$  and  $t_x^a \perp n_x^a$ .

*Proof.* As  $\underline{\mathcal{A}}$  is the projection of  $\mathcal{A}$ , they are on the same generalized vertical cylinder  $Q$ . Thus at a point  $x \in Q$ , the normal  $N_x^Q$  lies within  $\mathbb{P}_{e_3}$ , the plane orthogonal to  $e_3$ . As  $Q$  is a developed surface (see Section 2.4), its tangent plane (and thus its normal) is invariant along its generatrices generated by  $e_3$ . As  $\underline{\mathcal{A}}$  is a level curve of  $Q$ , then  $t_x^a$  lies within  $T_x Q$  and is orthogonal to  $N_x^Q$  by definition of the tangent plane. The vector which is orthogonal to  $t_x^a$  and which is in  $\mathbb{P}_{e_3}$  is necessarily collinear to  $n_x^a$ . Thus  $N_x^Q = \pm n_x^a$  depending on the curvature sign of  $\underline{\mathcal{A}}$ . Actually,  $N_x^Q = \rho \cdot n_x^a$ .

We have:

$$\mathcal{A} = Q \cap S \quad (2.19)$$

A basic property of differential geometry states that at a given point, the tangent of the curve formed by the intersection of two smooth surfaces equals the dot product of the two surfaces normal at this point. In other words, we have:

$$t_w^a = \rho \cdot n_x^a \times N_w \quad (2.20)$$

that concludes the proof.  $\square$

## 2.4 Ruled and developed surfaces

A ruled surface is generated by the sweeping of a line along a curve. It is a developed surface if the lines are the tangents of the curve. Lelong-Ferrand and Arnaudès [201] gave the following definitions:

**Definition (Ruled Surface).** A  $C^k$ -continuous ruled surface  $S$  is a surface defined by the parametrization:

$$\begin{aligned}\mathbb{R}^2 &\rightarrow \mathbb{R}^3 \\ (u, v) &\mapsto X(u, v) = F^0(u) + v \cdot F^1(u),\end{aligned}\tag{2.21}$$

where  $F^0 : \mathbb{R} \rightarrow \mathbb{R}^3$  is a  $C^k$ -continuous function and  $F^1 : \mathbb{R} \rightarrow \mathbb{R}^3$  a  $C^k$ -continuous function that maps a real to a vector and such that  $F^1(u) \neq 0$ . The curve defined by  $F^0$  is called the directrix and the line defined by  $F^1$  are the generatrices.

**Definition (developed surface).** Let  $S$  be a  $C^k$ -continuous ruled surface. It is said to be a developed surface if for every  $u \in \mathbb{R}$ :  $\frac{dF^0}{du}$ ,  $\frac{dF^1}{du}$  and  $F^1$  are coplanar.

We can identify three kinds of developed surfaces depending on the relationship between  $\frac{dF^0}{du}$ ,  $\frac{dF^1}{du}$  and  $F^1$  [201]:

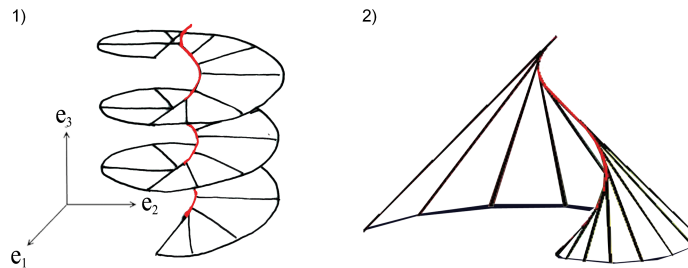
- the conical for which  $F^0$  is a constant function of  $\mathbb{R}^3$ ;
- the cylindrical for which  $F^1$  is constant; and
- the development of the tangent of a curve. In this latest case, the parametrization of the surface can be written as:

$$\begin{aligned}\mathbb{R}^2 &\rightarrow \mathbb{R}^3 \\ (u, v) &\mapsto X(u, v) = F(u) + v \cdot \frac{dF}{du}(u),\end{aligned}\tag{2.22}$$

with  $F : \mathbb{R} \rightarrow \mathbb{R}^3$  a  $C^k$ -continuous function. The curve represented by  $F$  is called the regression edge of the developed surface.

And we have the following property:

**Proposition.** *The tangent plane is identical along any generatrix of a developed surface.*



**Figure 8:** *Helicoid (ruled surface based on a helix) and circular SPS (developed surface of a helix)*

## 2.5 Sand-pile surface

Sand-pile surfaces (SPS), or constant-slope surface, are developed surfaces which have been introduced by Monge in the 19th century [197]. Basically, SPS can be viewed as the envelope of a vertical cone swept along a given planar curve, i.e.:

**Definition** (Sand-pile surface).  $S$  is called a sand-pile surface (or constant slope surface, denoted SPS) of angle  $\alpha$  if it is either a plane of inclination angle  $\alpha$ ; a circular cone of angle  $\alpha$  or a developed surface with a generalized helix of angle  $\alpha$  as regression edge.

Inflexion points of helix makes discontinuous definition of SPS. We generally consider sand-pile surfaces on helix portion without inflexion points.

We notice that the regression edge projection split the horizontal plane in two part: (i) where the SPS is defined, (ii) where it is not. As SPS is a developed surface of a helix, it is defined on the other side of the principal normal direction of its helix projection.



## Appendix III

# Tangent-driven reconstruction of discrete contour

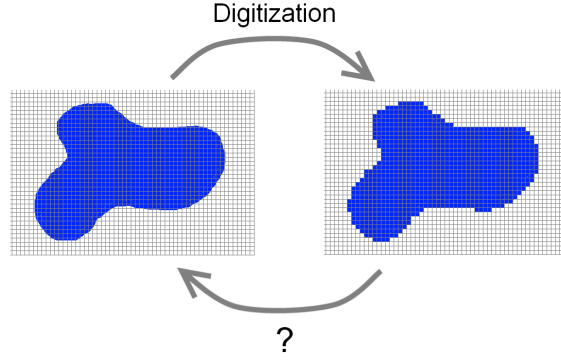
Dealing with a 2D digitized picture raises the problem of the quantification of the objects contour due to the discrete nature of data storage (pixel, see Figure 1). One way to make a picture look more real is to increase the density of pixels per area (centimeter<sup>2</sup>, inch<sup>2</sup>, etc.) to create the illusion of a smooth contour. However, this is not always possible, especially when: (i) the object has a complex shape that is at the scale of the pixel density; (ii) only rough camera are available; or (iii) we want to reduce the size of the pictures, i.e., the density of pixel.

With digitized images, the knowledge of the precise geometry (e.g. contour tangential) remains complex. Several techniques have been developed to approximate digitized contours, e.g., rewriting methods, spline approximation, discrete convolution (smoothing aliasing effect), among others.

These methods do not guarantee two primordial constraints in the approximation of such contour:

1. The real representation of the discrete boundary should not modify the initial digital information, i.e. once the recovered boundary is computed, one can retrieve the original discrete boundary if re-digitized.
2. The recovered contour does not depend on the starting point and orientation that would be taken by the method. In this way, we guarantee that a region and its complement share exactly the same boundary.

In [195], Braquelaire & Vialard presents a simple way to approximate the real boundary underlying the discrete boundary of a digitized 2D region that satisfied those two constraints. In the following paragraphs, we make a description of their algorithm and theory adapted from their witting [195] with some of our commentary remarks.



**Figure 1:** *Digitization of a scene consists of discretizing point position: instead of having continuous contour, digitized object have a discrete contour.*

## 1 Prerequisite

A digital image is a rectangular grid of pixels. A pixel could be represented either by a unit square or by an intersection point in a grid.

We consider an infinite digital image in bijection with the plane  $\mathbb{Z}^2$ , also called the discrete plane. A discrete point  $P$  is a point of the discrete plane. In the following, we generally consider pixels represented by unit squares centered on an integer point. As such, the pixel of center  $(X_P, Y_P)$  is identified with the discrete point  $P$ .

### 1.1 Freeman code

Two discrete points  $P$  and  $Q$  are said to be 4-adjacent if  $|X_P - X_Q| + |Y_P - Y_Q| = 1$ . They are said to be 8-adjacent if  $\max(|X_P - X_Q|, |Y_P - Y_Q|) = 1$ . A 4-connected discrete path is a sequence of discrete points  $(P_0, \dots, P_n)$  such that  $\forall i, 1 \leq i \leq n, P_{i-1}$  and  $P_i$  are 4-adjacent. Similarly a (resp. 8-connected discrete path is a sequence of 8-adjacent discrete points.

A 4-connected discrete path composed of  $n + 1$  points  $(P_0, \dots, P_n)$  can be represented by its first point  $P_0$  and its Freeman code, i.e., the sequence  $(m_0, \dots, m_{n-1})$ , where  $m_i$  encodes the elementary move from  $P_i$  to  $P_{i+1}$ . The four elementary vectors between a discrete point and its neighbors are numbered from 0 to 3. In the case of 8-connected discrete path, the height elementary vectors between a discrete point and its neighbors are numbered from 0 to 7. The elementary moves are numbered counterclockwise, the “east” move being numbered 0.

According to the 4-connectivity, two consecutive Freeman directions define a quadrant. Similarly, two consecutive Freeman directions define an octant when we talk about 8-connectivity. For instance, the first quadrant is the part of the plane bounded by the two half-lines starting from the origin of the coordinates system and of Freeman directions 0 and 1. Both quadrants and octants are numbered counterclockwise.

In the same way, we say that a discrete path belong to a quadrant or an octant (e.g., first quadrant)

if all of its Freeman code direction step belong to this quadrant or octant, respectively (e.g., the steps are uniquely composed of 0 and 1).

## 1.2 Euclidean path

Let  $P = (X, Y)$  be a discrete point. The cell of  $P$  is the set of points  $(x, y) \in \mathbb{R}^2$  verifying:

$$|X - x| < \frac{1}{2}, |Y - y| < \frac{1}{2}. \quad (1.1)$$

In other words, the cell of a point  $P$  is the unit square centered on  $P$ .

Let  $P$  be a discrete point. We say that the real point  $p$  is a Euclidean point associated with  $P$  if and only if  $p$  belongs to the cell of  $P$ .

Let  $\Pi$  be the discrete path  $(P_0, \dots, P_N)$ . By associating an Euclidean point  $p_i$  with each discrete point  $P_i$ , we obtain a sequence of real points  $\bar{\Pi} = (p_0, \dots, p_n)$  that we call a Euclidean path associated with  $\Pi$ .

## 1.3 Remarks

The definition of the Euclidean point associated with a discrete point ensures the reversibility of the transformation of the discrete point into an Euclidean point, i.e. if we round the coordinates of an Euclidean point  $p$  belonging to the cell of  $P$ , we retrieve  $P$ . This is also true for the Euclidean path associated to a discrete path. Thus, if we want to retrieve the real contour from a digitized contour, considering the Euclidean path ensures us to satisfy the first constraint seen previously.

However, there is an infinite Euclidean path associated to a discrete path and thus, an infinite methods to set an Euclidean path associated to a discrete contour. In [195], Braquelaire & Vialard develop a method that computes the discrete tangent at a boundary point, i.e. depending only on the point and on its neighborhood. Their method allows to reconstruct the Euclidean path of a discrete contour that does not depend on the choice of the starting point of the contour: that meets the second constraints.

## 1.4 Discrete line

A discrete line  $L$  is the set of points  $(x, y) \in \mathbb{Z}^2$  which satisfy the double inequality  $\mu \leq ax - by < \mu + \omega$  with  $a, b, \mu \in \mathbb{Z}^2$  and  $\omega \in \mathbb{N}$ .

The four coefficients  $(a, b, \mu, \omega)$  are called the characteristics of the discrete line  $L$ . The fraction  $a/b$  is the slope of  $L$ . The integer  $\mu$  describes its position in the discrete plane and  $\omega$  its thickness. If  $\omega$  is equal to  $\max(|X_P - X_Q|, |Y_P - Y_Q|) = 1$ ,  $L$  is an 8-connected discrete line; if it is equal to  $|X_P - X_Q| + |Y_P - Y_Q| = 1$ ,  $L$  is a 4-connected one.

The upper and lower leaning lines of a discrete line  $L$  are the two real lines of respective equations:

$$ax - by = \mu, \quad (1.2)$$

$$ax - by = \mu + \omega - 1. \quad (1.3)$$

It is clear that we can also define the points of the discrete line as the integer points that are inside the strip bounded by the two leaning lines and including these two lines. An upper leaning point is a discrete point belonging to the upper leaning line. Similarly, a lower leaning point is a discrete point belonging to the lower leaning line. Notice that the leaning points are points of the discrete line. If we consider only a segment of a discrete line, we can define the upper and lower leaning points of minimum abscissa and denote them respectively by  $U_m$  and  $L_m$ . In the same way, we denote by  $U_M$  and  $L_M$  the upper and lower leaning points of maximum abscissa.

The centered line of a discrete line  $L$  is the real line located in the middle of the two leaning lines of  $L$ . Its equation is:

$$ax - by = \mu + \frac{\omega - 1}{2}. \quad (1.4)$$

Because one can retrieve the thickness from  $\mu$  and the lower/upper leaning points ( $L_m, L_M$  and  $U_m, U_M$ ), this scalar will be omitted.

It is clear from equations 1.2 and 1.3 that the two leaning lines are parallels. This property will be used to detect the line that will fit a discrete path portion.

## 1.5 8-connected discrete line segment recognition algorithm

In [195], Braquelaire & Vialard propose a modified version of Debled's algorithm of 8-connected discrete line segment recognition. This algorithm looks for the longest segment line of characteristics  $(a, b, \mu)$  that will "fit" a discrete segment line. It considers an 8-connected discrete segment that is on the first octant, i.e. its Freeman code is only composed with 0 and 1. The initial values of the characteristics are provided by the first Freeman code, i.e. the direction between the first point and its follower. Then points of the considered segment line are added one by one to an original segment  $S$  to form a larger one  $S'$ , while its characteristics are updated from  $(a, b, \mu)$  to  $(a', b', \mu')$ . In some cases, it is not possible to build an upper and lower leaning lines that are parallel. In this case the algorithm stops and the greatest segment line that can be fit from the starting point is returned with its characteristic.

**Initialization.**  $S_0 = (P_0)$  with  $P_0$  the first point of the 8-connected path with Freeman code composed with only 0 ("east" direction) and 1 ("north-east"). Two cases are possible when considering the first Freeman step  $m_0$ :

$$m_0 = 0 \implies (a, b, \mu) = (0, 1, 0), U_m = L_m = (0, 0), U_M = L_M = (1, 0), \quad (1.5)$$

$$m_0 = 1 \implies (a, b, \mu) = (1, 1, 0), U_m = L_m = (0, 0), U_M = L_M = (1, 1). \quad (1.6)$$

**Construction of the segment line.** We want to build the segment line  $S_i = (P_0, \dots, P_{i-1}) \cup P_i$  by adding the point  $P_i$  to the temporal segment  $S_{i-1} = (P_0, \dots, P_{i-1})$ . Let  $(x_P, y_P)$  being the coordinates of  $P_i$  and  $r = ax_P - by_P$ . Several cases showed in Table 1 and 2 appear.



As we can see, the previous algorithm returns the characteristics of the segment line that fit the best a part of a discrete path from a starting point. In the case the discrete path is too “curved”, the algorithm stops and the range of the segment line is not the entire path but a neighbor of the starting point. By “curved” we mean that if one adds a point to the temporal segment in regards with the Freeman code and if the updating of the leaning lines brings two lines that are not parallels, one gets a case that is not consistent with respect to the discrete line definition that has been seen previously.

$r = ax_P - by_P$	$(a', b', \mu'),$ $r' = a'x_P - b'y_P$	$U'_m$	$U'_M$	$L'_m$	$L'_M$	Discussion
$\mu < r < \mu + b - 1$	$(a, b, \mu)$	$U_m$	$U_M$	$L_m$	$L_M$	$S$ and $S'$ have the same characteristics
$r = \mu + b - 1$	$(a, b, \mu)$	$U_m$	$U_M$	$L_m$	$P$	$S$ and $S'$ have the same characteristics
$r = \mu$	$(a, b, \mu)$	$U_m$	$P$	$L_m$	$L_M$	$S$ and $S'$ have the same characteristics
$r = \mu - 1$	$(y_P - y_{U_m}, x_P - x_{U_m}, r')$	$U_m$	$P$	$L_M$	$L_M$	$S'$ has a higher slope than $S$
$r = \mu + b$	$(y_P - y_{L_m}, x_P - x_{L_m}, r' - b' + 1)$	$U_M$	$U_M$	$L_m$	$P$	$S'$ has a lower slope than $S$
Else: break	-	-	-	-	-	$S'$ is not a segment line

**Table 1:** Positive cases

$r = ax_P - by_P$	$(a', b', \mu'),$ $r' = a'x_P - b'y_P$	$U'_m$	$U'_M$	$L'_m$	$L'_M$	Discussion
$\mu < r < \mu + b - 1$	$(a, b, \mu)$	$U_m$	$U_M$	$L_m$	$L_M$	$S$ and $S'$ have the same characteristics
$r = \mu + b - 1$	$(a, b, \mu)$	$U_m$	$U_M$	$P$	$L_M$	$S$ and $S'$ have the same characteristics
$r = \mu$	$(a, b, \mu)$	$P$	$U_M$	$L_m$	$L_M$	$S$ and $S'$ have the same characteristics
$r = \mu - 1$	$(y_{U_M} - y_P, x_{U_M} - x_{U_M}, r')$	$P$	$U_M$	$L_m$	$L_m$	$S'$ has a lower slope than $S$
$r = \mu + b$	$(y_{L_M} - y_P, x_{L_M} - x_P, r' - b' + 1)$	$U_m$	$U_m$	$P$	$L_M$	$S'$ has a higher slope than $S$
Else: break	-	-	-	-	-	$S'$ is not a segment line

**Table 2:** Negative cases

**Discrete tangential of a contour.** The idea of Braquelaire & Vialard is to use this algorithm to deduce discrete tangent of a 4-connected contour [195]. For each point of the contour, they extract the greatest Freeman code of same quadrant that encloses this point. With the fact that we have a complementarity between 4-connected and 8-connected line segment, they use the modified version of Debled’s algorithm (with in addition the “negative” case) to find the slope of the segment line that fit the best the neighbor of the considered point.

**Euclidean points from a discrete point and its discrete tangential.** To retrieve the Euclidean point associated to a discrete point of the 4-connected discrete path, one uses the parametrization of the path course:

$$t = x + y, \quad (1.7)$$

where  $t$  is the numbering of the discrete point (i.e. the time) that equals the abscissa plus the ordinates of the considered point. In other word:

$$P_t = P_{(x_P+y_P)}. \quad (1.8)$$

Combined with the formula 1.4, one obtains the parametric equation of the centered line associated to the 4-connected discrete path of characteristic:

$$\begin{cases} x = \frac{b-a}{b}t + \alpha \\ y = \frac{a}{b}t + \alpha \end{cases} \quad \text{with } \alpha = \frac{-1+b+2\mu}{2b}, \quad (1.9)$$

the real point  $p = (x(t_P), y(t_P))$  is called the canonical projection of  $P$  on the real tangent. As  $P$  is the origin of the coordinate system,  $t_P = x_P + y_P = 0$  and thus the canonical projection on its tangent is  $p = (\alpha, -\alpha)$  that is chosen as the Euclidean point associated to the discrete point. Braquelaire and Vialard ensure with a Lemma that  $|\alpha| < 1/2$  and thus that this point verifies the desired constraint of the Euclidean point definition.

## 2 Algorithm

The idea of this algorithm is to smooth a domain contour and for each points, to get a tangential. With the prerequisite presented bellow, we will be able to define a methodology to construct such contour.

### 2.1 Path extraction

Once a connected domain  $\mathcal{D} = \{(x, y) \in \mathbb{Z}^2 \mid \text{value}(x, y) = 1\}$  of gender 0, is extracted, we want to create its 4-connected contour path. To do so, we will use the mathematical binary morphology operation on this domain. With the notation of [205], we proceed the following operation. First we consider the squared structuring element:

$$\mathcal{E} = \begin{pmatrix} 1 & 1 & 1 \\ 1 & 1 & 1 \\ 1 & 1 & 1 \end{pmatrix}, \quad (2.1)$$

or  $\mathcal{E} = \{(0, 0), (0, 1), (0, 2), (1, 0), (1, 1), (1, 2), (2, 0), (2, 1), (2, 2)\}$ . We apply a first erosion to  $\mathcal{D}$  with this structuring element:

$$\mathcal{D}_e = \mathcal{D} \ominus \mathcal{E}, \quad (2.2)$$

then a dilation to retrieve  $\mathcal{D}'$  without single and double pixel on its border:

$$\mathcal{D}' = \mathcal{D}_e \oplus \mathcal{E}, \quad (2.3)$$

and then again an erosion of this latest. The difference between  $\mathcal{D}'$  and the last domain eroded  $\mathcal{D}'_e = \mathcal{D}' \ominus \mathcal{E}$  provides the 4-connected discrete path  $\mathcal{P}$ .

$$\mathcal{P} = \mathcal{D}' \cap \mathcal{D}'_e. \quad (2.4)$$

Once this contour is built, it is necessary to order its point in the counterclockwise direction and to build its Freeman code. To do so, we have used the matrix representation of the contour and travel along in the counterclockwise direction.

The case of non connected domain and/or of gender  $> 0$  are special cases that need to be brought to this specific case.

## 2.2 Discrete tangent and Euclidean point calculation

Once the freeman code of a 4-connected contour path is computed, one applies the previously seen properties for each point  $P_i = (x_{p_i}, y_{p_i})$  of the discrete path  $\mathcal{P}$  with its Freeman code associated  $m_{p_i} = \mathcal{F}_4(P_{i+1} - P_i)$  where  $\mathcal{F}_4$  is the function that code a 4-connected elementary move into its Freeman code for 4-connected discrete path.

1. First, we extract the quadrant associated to  $P_i$ : we look in the Freeman code, at the considered point, the first code change, in the forward and backward direction.
2. Then, a rough 4-connected segment is built: we retrieve all the steps that are associated to this quadrant, around the considered point.
3. We consider the expression of this segment in the first quadrant: its Freeman code is expressed in modulo 2. The considered point is then considered as the origin  $(0,0)$  in this frame.
4. Points per points, we apply the algorithm seen previously to compute the discrete tangent: once the segment characteristics  $(a, b, \mu)$  and the leaning points  $L_m, L_M, U_m$  and  $U_M$  are computed for the first step  $m_{P_i}$ , we update those latest when a positive and negative point is added. The algorithm stops when there are no more points to add. In the case where we cannot add positive or negative point, the algorithm continues for the negative or positive addition, respectively.
5. The Euclidean point associated to the discrete point has the coordinate  $(\alpha, -\alpha)$ , with:

$$\alpha = \frac{-1 + b + 2\mu}{2b}. \quad (2.5)$$

6. Finally, we recall the computed value in the corresponding quadrant and for an 4-connected quadrant. We apply the transformation indicated in Table 3.

quadrant n°	characteristics	Euclidean point
1	$(a, b - a, \mu)$	$(x_P + \alpha, y_P - \alpha)$
2	$(a, a - b, -\mu - b + 1)$	$(x_P - \alpha, y_P - \alpha)$
3	$(-a, a - b, \mu)$	$(x_P - \alpha, y_P + \alpha)$
4	$(-a, b - a, -\mu - b + 1)$	$(x_P + \alpha, y_P + \alpha)$

**Table 3:** *Quadrant to Euclidean point transformation.*

### 3 Time complexity

The time complexity of the tangent-driven Euclidean path computation is the same as the complexity of the tangent recognition algorithm. As a matter of fact the Euclidean point associated with a discrete point is directly deduced from the characteristics of the discrete tangent at this point ( $\alpha$  computation). The time complexity of the construction algorithm is  $O(l \times n)$ , where  $l$  is the average length of the discrete line segments contained in the discrete contour and  $n$  is the number of points of the discrete contour. The computation time depends thus on the shape of the contour. The more a discrete curve is rectilinear the more the computation of the associated Euclidean path is costly. However, for a given image size the shape of the discrete curve to be processed becomes more irregular when its length increases. In other words, the value of  $l$  tends to decrease when the value of  $n$  increases.

# List of publications

Some of the ideas, results and figures contained in this document have previously appeared in the following publications and/or oral presentations:

## Publication

- (in progress) Balduzzi, M.A.F. & Godin C. “A sand-pile surface approach to shape-from-shading”, *Journal of Mathematical Imaging and Vision*.
- M.A.F. Balduzzi, D. Van der Zande, J. Stuckens, W.W. Verstraeten, P. Coppin. “The Properties of Terrestrial Laser System Intensity for Measuring Leaf Geometries: A Case Study with Conference Pear Trees (*Pyrus Communis*)”. *Sensors* 2011, 11, pp. 1657-1681.

## Conferences

- M.A.F. Balduzzi, F. Boudon & C. Godin, “Optimal 3D reconstruction of plants canopy from terrestrial laser scanner data by fusion of the 3D point information and the intensity value”, *FSPM 2013 Conferences*, Saariselkä, Finland, 9-14 Juin 2013. (Extended abstract)
- M.A.F. Balduzzi, D. van der Zande & P. Coppin, «3D features extraction of tree foliage with a ground-based LiDAR» *3D-Documentation Conferences*, Essen, Allemagne, 17-18 Mai 2011.
- M.A.F. Balduzzi, D. Van der Zande & P. Coppin, “3D scanning with TLS for vegetative system analysis”. *FARO conferences*, Amsterdam, Pays-Bas, 9th Décembre 2010.
- M.A.F. Balduzzi, D. Van der Zande, W.W. Verstraeten, B. Somers & P. Coppin; “The intensity return behavior of a high resolution terrestrial 3D laser scanner for foliage structure measurements in citrus orchards.” *Silvilaser*, Freiburg, Allemagne, 14-17 Septembre 2010. (Proceeding, pp 555-565)

## Workshops

- M.A.F. Balduzzi & C. Godin, «Utilisation de la donnée d'intensité fournie par un TLS pour la correction des points aberrants dans les scans de feuillage d'arbre.», 5ème atelier TLiDAR, Nancy, France, 18-19 Novembre, 2014. (Abstract, p2-3)
- M.A.F. Balduzzi & C. Godin, «Modélisation géométrique de la canopée à partir d'images scanner 3D: utilisation d'information 3D et de l'intensité réfléchie et création d'algorithme de maillage mixte», 3ème atelier TLiDAR, Montpellier, France, 28-29 Novembre, 2012

## Seminaries

- M.A.F. Balduzzi, D. Van der Zande & P. Coppin «Numérisation 3d du feuillage d'un poirier Conférence: de l'analyse du nuage de point à sa triangulation – utilisation de l'intensité fournie par un lidar terrestre.» Séminaire de Mathématiques, UHA, Mulhouse, France, January 20th 2011.

## Posters

- M.A.F. Balduzzi, F. Boudon<sup>2</sup>, C. Godin, “Reconstruction Optimale de la Géométrie des Canopées de Vergers : Fusion des Données d'Intensité et de Distance d'un Scanner LiDAR pour la Correction des Points Aberrants”. 2ème journée scientifique du Labex NUMEV, 2013 July.
- M.A.F. Balduzzi, F. Boudon, D. Van der Zande, P. Coppin, C. Godin, “Modélisation Géométrique de la Canopée à partir d'Image Scanner 3D : Utilisation de l'Information 3D et de l'Intensité Réfléchie et Création d'un Algorithme de Maillage Mixte”. 1ère journée scientifique du Labex NUMEV, 2011 November.

# Bibliography

- [1] T.L. Robinson, A.N. Lakso, and Z. Ren. Modifying apple tree canopies for improved production efficiency. *HortScience*, 26(8):1005–1012, 1991.
- [2] M. Willaume, P.-E. Lauri, and H. Sinoquet. Light interception in apple trees influenced by canopy architecture manipulation. *Trees*, 18(6):705–713, 2004.
- [3] X. Xu, P. Wu, P. Thorbek, and K. Hyder. Variability in initial spray deposit in apple trees in space and time. *Pest management science*, 62(10):947–956, 2006.
- [4] J. Palacín, T. Pallejà, M. Tresanchez, R. Sanz, J. Llorens, M. Ribes-Dasi, J. Masip, J. Arno, A. Escola, and J.R. Rosell. Real-time tree-foliage surface estimation using a ground laser scanner. *Instrumentation and Measurement, IEEE Transactions on*, 56(4):1377–1383, 2007.
- [5] P. Room, J. Hanan, and P. Prusinkiewicz. Virtual plants: new perspectives for ecologists, pathologists and agricultural scientists. *Trends in Plant Science*, 1(1):33–38, 1996.
- [6] Y. Guo, T. Fourcaud, M. Jaeger, X. Zhang, and B. Li. Plant growth and architectural modelling and its applications. *Annals of botany*, 107(5):723–727, 2011.
- [7] R. Fernandez, P. Das, V. Mirabet, E. Moscardi, J. Traas, J.-L. Verdeil, G. Malandain, and C. Godin. Imaging plant growth in 4d: robust tissue reconstruction and lineaging at cell resolution. *Nature Methods*, 7(7):547–553, 2010.
- [8] F. Boudon, C. Pradal, T. Cokelaer, P. Prusinkiewicz, and C. Godin. L-Py: an L-system simulation framework for modeling plant architecture development based on a dynamic language. *Frontiers in plant science*, 3, 2012.
- [9] M. Cieslak, A.N. Seleznyova, P. Prusinkiewicz, and J. Hanan. Towards aspect-oriented functional-structural plant modelling. *Annals of botany*, 108(6):1025–1041, 2011.
- [10] P.H. de Visser, G.H. Buck-Sorlin, and G.W. van der Heijden. Optimizing illumination in the greenhouse using a 3D model of tomato and a ray tracer. *Frontiers in plant science*, 5, 2014.
- [11] C. Godin and H. Sinoquet. Functional–structural plant modelling. *New Phytologist*, 166(3):705–708, 2005.

- [12] R.A. Haugerud, D.J. Harding, S.Y. Johnson, J.L. Harless, C.S. Weaver, and B.L. Sherrod. High-resolution LiDAR topography of the puget lowland, washington. *GSA Today*, 13(6):4–10, 2003.
- [13] F.C.J. Cornuet. Contribution du modèle LiDAR pour la caractérisation de surfaces urbaines et le paramétrage de modèles de simulation des flux atmosphériques en pollution de l’air. *Projet de Master, Ecole Polytechnique Fédérale de Lausanne, Suisse*, 2011.
- [14] D.D. Benito. Automatic 3D modelling of train rails in a LiDAR point cloud. *Master Thesis, University of Twente, the Netherlands*, 2012.
- [15] I. Moorthy, J.R. Miller, B. Hu, J. Chen, and Q. Li. Retrieving crown leaf area index from an individual tree using ground-based LiDAR data. *Canadian Journal of Remote Sensing*, 34(3):320–332, 2008.
- [16] J.R. Rosell, R. Sanz, J. Llorens, J. Arno, A. Escola, M. Ribes-Dasi, J. Masip, F. Camp, F. Gracia, F. Solanelles, T. Palleja, L. Val, S. Planas, E. Gil, and J. Palacin. A tractor-mounted scanning LiDAR for the non-destructive measurement of vegetative volume and surface area of tree-row plantations: A comparison with conventional destructive measurements. *Biosyst. Eng*, 102:128–134, 2009.
- [17] M. Béland, D. Baldocchi, J.-L. Widlowski, R.A. Fournier, and M.M. Verstraete. On seeing the wood from the leaves and the role of voxel size in determining leaf area distribution of forests with terrestrial LiDAR. *Agricultural and Forest Meteorology*, 184:82–97, 2014.
- [18] J.-C. Chambelland, M. Dassot, B. Adam, N. Donès, P. Balandier, A. Marquier, M. Saudreau, G. Sonohat, and H. Sinoquet. A double-digitising method for building 3D virtual trees with non-planar leaves: application to the morphology and light-capture properties of young beech trees (*fagus sylvatica*). *Functional Plant Biology*, 35(10):1059–1069, 2008.
- [19] C. Stocker, F. Uhrmann, O. Scholz, C. Hugel, T. Rademacher, M. Siebers, and U. Schmid. A machine learning approach to drought stress level classification of tobacco plants. 2013.
- [20] F. Hosoi, K. Nakabayashi, and K. Omasa. 3D modeling of tomato canopies using a high-resolution portable scanning LiDAR for extracting structural information. *Sensors*, 11(2):2166–2174, 2011.
- [21] C. Hopkinson, L. Chasmer, C. Young-Pow, and P. Treitz. Assessing forest metrics with a ground-based scanning LiDAR. *Can. J. Forest Res.*, (34):573–583, 2004.
- [22] J.F. Côté, J.L. Widlowski, R.A. Fournier, and M.M. Verstraete. The structural and radiative consistency of three-dimensional tree reconstructions from terrestrial LiDAR. *Remote Sens. Environ.*, (113):1067–1081, 2009.



- [23] M. Béland, J.-L. Widlowski, R.A. Fournier, J.-F. Côté, and M.M. Verstraete. Estimating leaf area distribution in savanna trees from terrestrial LiDAR measurements. *Agricultural and Forest Meteorology*, 151(9):1252–1266, 2011.
- [24] M. Hebert and E. Krotkov. 3D measurements from imaging laser radars: How good are they? *Image and Vision Computing*, 10:170–178, 1992.
- [25] D.D. Lichti. Error modelling, calibration and analysis of an am–cw terrestrial laser scanner system. *ISPRS Journal of Photogrammetry and Remote Sensing*, 61(5):307–324, 2007.
- [26] J.-H. Song, S.-H. Han, K.Y. Yu, and Y.-I. Kim. Assessing the possibility of land-cover classification using LiDAR intensity data. *International Archives of Photogrammetry Remote Sensing and Spatial Information Sciences*, 34(3/B):259–262, 2002.
- [27] T. Varady, R.R. Martin, and J. Cox. Reverse engineering of geometric models-an introduction. *Computer-Aided Design*, 29(4):255–268, 1997.
- [28] J.-F. Côté, R.A. Fournier, and R. Egli. An architectural model of trees to estimate forest structural attributes using terrestrial LiDAR. *Environmental Modelling & Software*, 26(6):761–777, 2011.
- [29] H. Hoppe, T. DeRose, T. Duchamp, M. Halstead, H. Jin, J. McDonald, J. Schweitzer, and W. Stuetzle. Piecewise smooth surface reconstruction. In *Proceedings of the 21st annual conference on Computer graphics and interactive techniques*, pages 295–302, 1994.
- [30] D. Van der Zande, W. Hoet, I. Jonckheere, J. van Aardt, and P. Coppin. Influence of measurement set-up of ground-based LiDAR for derivation of tree structure. *Agricultural and Forest Meteorology*, 141(2):147–160, 2006.
- [31] FARO. FARO LS 840-880 specification sheet. url: <http://www2.faro.com/FaroIP/Files/File/Techsheets>
- [32] J.R. Rosell, J. Llorens, R. Sanz, J. Arno, M. Ribes-Dasi, J. Masip, A. Escola, F. Camp, F. Solanelles, F. Gracia, E. Gil, and other. Obtaining the three-dimensional structure of tree orchards from remote 2d terrestrial LiDAR scanning. *Agr. Forest Meteorol*, (149):1505–1515, 2009.
- [33] D. Van der Zande, S. Mereu, N. Nadezhdina, J. Cermak, B. Muys, P. Coppin, and F. Manes. 3D upscaling of transpiration from leaf to tree using ground-based LiDAR: Application on a mediterranean Holm Oak (*Quercus ilex* L.) tree. *Agr. Forest Meteorol*, 149:1573–1583, 2009.
- [34] F. Hosoi, Y. Nakai, and K. Omasa. Estimating the leaf inclination angle distribution of the wheat canopy using a portable scanning LiDAR. *Journal of Agricultural Meteorology*, 65(3):297–302, 2009.

- [35] J. Shan and C.K. Toth. *Topographic laser ranging and scanning: principles and processing*. CRC Press, 2008.
- [36] T. Whester. The reality: time-of-flight versus phased based scanners. url: <http://www.lidarnews.com>.
- [37] M.D. Adams. LiDAR design, use and calibration concepts for correct environmental detection. *IEEE Trans. Robot. Autom. Soc.*, 16:753–761, 2000.
- [38] Inverse square law. *Wikipedia*.
- [39] S. Kaasalainen, A. Kukko, T. Lindroos, P. Litkey, H. Kaartinen, J. Hyypä, and E. Ahokas. Brightness measurements and calibration with airborne and terrestrial laser scanners. *IEEE Geoscience in Remote Sensing Letter*, 46:528–534, 2008.
- [40] S. Kaasalainen, A. Krooks, A. Kukko, and H. Kaartinen. Radiometric calibration of terrestrial laser scanners with external reference targets. *Remote Sensing*, 1:144–158, 2009.
- [41] W. Wagner. Radiometric calibration of small-footprint full-waveform airborne laser scanner measurements: Basic physical concepts. *ISPRS Journal of Photogrammetry and Remote Sensing*, 65(6):505–513, 2010.
- [42] M.A.F. Balduzzi, D. Van der Zande, J. Stuckens, W.W.Verstraeten, and P. Coppin. The properties of terrestrial laser system intensity for measuring leaf geometries: a case study with Conference pear trees (*pyrus communis*). *Sensors*, 11:1657–1681, 2011.
- [43] T. Voegtli, I. Schwab, and T. Landes. Influences of different materials on the measurements of a terrestrial laser scanner (TLS). In *Proceedings of the XXI congress, the international society for photogrammetry and remote sensing, ISPRS2008*, volume 37, pages 1061–1066, 2008.
- [44] S. Kaasalainen, H. Niittymäki, A. Krooks, K. Koch, H. Kaartinen, A. Vain, and H. Hyypä. Effect of target moisture on laser scanner intensity. *IEEE Transactions on Geoscience and Remote Sensing*, 48(4):2128–2136, 2010.
- [45] N. Pfeifer and C. Briese. Geometrical aspects of airborne laser scanning and terrestrial laser scanning. *International Archives of Photogrammetry, Remote Sensing and Spatial Information Sciences*, 36(3/W52):311–319, 2007.
- [46] J.L. Lovell, D.L.B Jupp, G.J. Newnham, and D.S. Culvenor. Measuring tree stem diameters using intensity profiles from ground-based scanning LiDAR from a fixed viewpoint. *ISPRS Journal of Photogrammetry and Remote Sensing*, 66(1):46–55, 2011.
- [47] J.U.H. Eitel, L.E. Vierling, and D.S. Long. Simultaneous measurements of plant structure and chlorophyll content in broadleaf saplings with a terrestrial laser scanner. *Remote sensing of environment*, 114(10):2229–2237, 2010.

- [48] R.N. Swift, W.B. Krabill, and F.E. Hoge. Applications of the airborne oceanographic LiDAR to shoreline mapping. *00 DEPARTMENT OF DEFENCE*, page 151, 1981.
- [49] E.P. Baltsavias. Airborne laser scanning: basic relations and formulas. *ISPRS Journal of Photogrammetry and Remote Sensing*, 54(2):199–214, 1999.
- [50] S. Sotoodeh. Outlier detection in laser scanner point clouds. *International Archives of Photogrammetry, Remote Sensing and Spatial Information Sciences XXXVI-5*, 297e302, 2006.
- [51] R.A. Hodge. Using simulated terrestrial laser scanning to analyse errors in high resolution scan data of irregular surfaces. *ISPRS Journal of photogrammetry and remote sensing*, 65:227–240, 2010.
- [52] S. Magnussen and P. Boudewyn. Derivations of stand heights from airborne laser scanner data with canopy-based quantile estimators. *Canadian Journal of Forest Research*, 28(7):1016–1031, 1998.
- [53] Spherical coordinate system. *Wikipedia*.
- [54] Cylindrical coordinate system. *Wikipedia*.
- [55] J. Alda. Laser and gaussian beam propagation and transformation. *Encyclopedia of Optical Engineering*, pages 999–1013, 2003.
- [56] D.D. Lichti and S. Jantcho. Angular resolution of terrestrial laser scanners. *The Photogrammetric Record*, 21(114):141–160, 2006.
- [57] P. Rieger, N. Studnicka, M. Pfennigbauer, and G. Zach. Boresight alignment method for mobile laser scanning systems. *Journal of Applied Geodesy*, 4(1):13–21, 2010.
- [58] A. Pesci and G. Teza. Effects of surface irregularities on intensity data from laser scanning: an experimental approach. *Annals of Geophysics*, 51(5-6):839–848, 2008.
- [59] N. Pfeifer, P. Dorninger, A. Haring, and H. Fan. Investigating terrestrial laser scanning intensity data: quality and functional relations. In *Proc. of VIII conference on Optical 3D measurement tech*, 2007.
- [60] B. Hofle, M. Rutzinger, and N. Pfeifer. Terrestrial laser scanner Optech ILRIS 3D, experiment on the angle of incidence and recorded intensity. *Technical Report, Institute of Geography, University Innsbruck*, May 2006.
- [61] T. Voegtle and S. Wakaluk. Effects on the measurements of the terrestrial laser scanner HDS 6000 (Leica) caused by different object materials. *Proceedings of ISPRS Work*, 38:68–74, 2009.

- [62] D. van der Zande, I. Jonckheere, J. Stuckens, W.W. Verstraeten, and P. Coppin. Impact of the sampling design on the quality of ground-based LiDAR datasets. In *Proceedings of SilviLaser 2008, Edinburgh, UK, 17-19 September, 2008.*, pages 305–314, 2008.
- [63] S. Soudarissanane, R. Lindenbergh, M. Menenti, and P. Teunissen. Incidence angle influence on the quality of terrestrial laser scanning points. In *ISPRS Workshop Laserscanning*, 2009.
- [64] T.P. Kersten, H. Sternberg, and K. Mechelke. Investigations into the accuracy behaviour of the terrestrial laser scanning system Mensi GS100. *Proc. in the Optical 3D Measurement Techniques*, 1:122–131, 2005.
- [65] M. Dassot, T. Constant, and M. Fournier. The use of terrestrial LiDAR technology in forest science: application fields, benefits and challenges. *Annals of forest science*, 68(5):959–974, 2011.
- [66] R.C. Ebel, E.L. Proebsting, and R.G. Evans. Deficit irrigation to control vegetative growth in apple and monitoring fruit growth to schedule irrigation. *HortScience*, 30(6):1229–1232, 1995.
- [67] G.D. Farquhar and T.D. Sharkey. Stomatal conductance and photosynthesis. *Annual review of plant physiology*, 33(1):317–345, 1982.
- [68] R. Bradbury, R. Hill, D. Manson, S. Hinsley, J. Wilson, H. Balzter, G. Anderson, M. Whittingham, I. Davenport, and P. Bellamy. Modeling relationships between birds and vegetation structure using airborne LiDAR data: A review with case studies from agricultural and woodland environments. *IBIS*, 147:443–452, 2005.
- [69] F. Hosoi and K. Omasa. Voxel-based 3D modeling of individual trees for estimating leaf area density using high-resolution portable scanning LiDAR. *Geoscience and Remote Sensing, IEEE Transactions on*, 44(12):3610–3618, 2006.
- [70] B. Hofle. Radiometric correction of terrestrial LiDAR point cloud data for individual maize plant detection. *IEEE Geoscience and Remote Sensing Letters*, 2013.
- [71] J. Hanan, B. Loch, and T. McAleer. Processing laser scanner plant data to extract structural information. In *Proceedings of the 4th International Workshop on Functional-Structural Plant Models (FSPM 2004)*, pages 9–12. UMR AMAP, 2004.
- [72] T. Dornbusch, S. Lorrain, D. Kuznetsov, A. Fortier, R. Liechti, I. Xenarios, and C. Fankhauser. Measuring the diurnal pattern of leaf hyponasty and growth in arabidopsis—a novel phenotyping approach using laser scanning. *Functional Plant Biology*, 39(11):860–869, 2012.
- [73] O.H. Gordon. *Life: The science of biology*. Sinauer Associates and W. H. Freeman. 8th edition, 2007.

- [74] J.N. Wünsche, A.N. Lakso, T.L. Robinson, F. Lenz, and S.S. Denning. The bases of productivity in apple production systems: the role of light interception by different shoot types. *Journal of the American Society for Horticultural Science*, 121(5):886–893, 1996.
- [75] S. Simon, B. Sauphanor, and P.-E. Lauri. Control of fruit tree pests through manipulation of tree architecture. *Pest Techn*, 1:33–37, 2007.
- [76] J. de La Quintinie. *Instruction pour les jardins fruitiers et potagers avec un Traité des orangers et des réflexions sur l’agriculture*. Bordelet, 1739.
- [77] P.E. Lauri and J.M. Lespinasse. The vertical axis and solaxe systems in france. *Acta Horticulturae*, pages 287–296, 2000.
- [78] A. Mahhou, A. Aziz, and M. Ayello. Formes de conduite du nectarinier [*Prunus Persica* (L.) Batsch]. *Revue Marocaine des Sciences Agronomiques et Vétérinaires*, 18(2):109–116, 2010.
- [79] S. Hieke, C.M. Menzel, and P. Lüdders. Effects of leaf, shoot and fruit development on photosynthesis of lychee trees (*litchi chinensis*). *Tree physiology*, 22(13):955–961, 2002.
- [80] J.N. Wünsche, A.N. Lakso, S.S. Denning, and J. Barnard. Estimating the contribution of canopy components to direct light interception of apple trees using a laser-assisted scanning device. *Environmental and experimental botany*, 37(1):63–72, 1997.
- [81] P.-E. Lauri and F. Laurens. *Architectural types in apple (*Malus x domestica* borkh.)*. Helsinki, FIN : WFL Publisher, 2005.
- [82] J.M. Lespinasse and J.F. Delort. Apple tree management in vertical axis: appraisal after ten years of experiments. In *III International Symposium on Research and Development on Orchard and Plantation Systems 160*, pages 139–156, 1984.
- [83] Hortanswers. Apple tree. url: <http://urbanext.illinois.edu/hortanswers>.
- [84] J. Carroll. Pear rust mites: Fixing pear rust mite damage in pear trees. url: <http://www.gardeningknowhow.com/edible/fruits/pear/pear-rust-mite-damage.htm>.
- [85] G. Garin, C. Pradal, B. Andrieu, V. Houlès, C. Robert, and C. Fournier. A generic model of interactions between fspm, foliar pathogens and microclimate. In *7th International Conference on Functional-Structural Plant Models*, pages 339–341, 2013.
- [86] C. Gigot, C. de Vallavieille-Pope, M. Leconte, C. Maumené, L. Huber, and S. Saint-Jean. Using 3D virtual plants to evaluate the canopy role in the progression of a splash-dispersed crop disease: a case study based on wheat cultivar mixtures. *FSPM2013 Proceedings (ISBN 978-951-651-408-9)*, 2013.

- [87] K. Omasa, F. Hosoi, and A. Konishi. 3D LiDAR imaging for detecting and understanding plant responses and canopy structure. *Journal of Experimental Botany*, 58(4):881–898, 2007.
- [88] C. Pradal, S. Dufour-Kowalski, F. Boudon, C. Fournier, and C. Godin. OpenAlea: a visual programming and component-based software platform for plant modelling. *Functional plant biology*, 35(10):751–760, 2008.
- [89] P.J. Zarco-Tejada and S.L. Ustin. Modeling canopy water content for carbon estimates from MODIS data at Land EOS validation sites. In *Geoscience and Remote Sensing Symposium, 2001. IGARSS'01. IEEE 2001 International*, volume 1, pages 342–344. IEEE, 2001.
- [90] J. Peñuelas, I. Filella, C. Biel, L. Serrano, and R. Save. The reflectance at the 950–970 nm region as an indicator of plant water status. *International journal of remote sensing*, 14(10):1887–1905, 1993.
- [91] M. Monsi and T. Saeki. On the factor light in plant communities and its importance for matter production. *Annals of Botany*, 95(3):549–567, 2005.
- [92] Beer-lambert law. *Wikipedia*.
- [93] I. Jonckheere, S. Fleck, K. Nackaerts, B. Muys, P. Coppin, M. Weiss, and F. Baret. Review of methods for in situ leaf area index determination: Part I. Theories, sensors and hemispherical photography. *Agricultural and forest meteorology*, 121(1):19–35, 2004.
- [94] N.J.J. Bréda. Ground-based measurements of leaf area index: a review of methods, instruments and current controversies. *Journal of experimental botany*, 54(392):2403–2417, 2003.
- [95] J.S. Broadhead, A.R. Muxworthy, C.K. Ong, and C.R. Black. Comparison of methods for determining leaf area in tree rows. *Agricultural and forest meteorology*, 115(3):151–161, 2003.
- [96] J.M. Chen and T.A. Black. Defining leaf area index for non-flat leaves. *Plant, Cell & Environment*, 15(4):421–429, 1992.
- [97] G. Zheng and L.M. Moskal. Retrieving leaf area index (LAI) using remote sensing: theories, methods and sensors. *Sensors*, (9):2719–2745, 2009.
- [98] S.G. Leblanc, J.M. Chen, R. Fernandes, D.W. Deering, and A. Conley. Methodology comparison for canopy structure parameters extraction from digital hemispherical photography in boreal forests. *Agricultural and Forest Meteorology*, 129(3):187–207, 2005.
- [99] F.M. Danson, D. Hetherington, F. Morsdorf, B. Koetz, and B. Allgöwer. Forest canopy gap fraction from terrestrial laser scanning. *IEEE Geosc. Rem. Sens. Lett.*, (4):157–160, 2007.

- [100] R.O. Chávez, J.G.P. Clevers, M. Herold, M. Ortiz, and E. Acevedo. Modelling the spectral response of the desert tree *Prosopis Tamarugo* to water stress. *International Journal of Applied Earth Observation and Geoinformation*, 21:53–65, 2013.
- [101] G. Biswas. Some new leaf normal-angle distribution models and their influence on geometry functions and area scattering phase functions related to radiative transfer problems in vegetative canopies. *J. Quant. Spectrosc. Radiat.*, (108):197–219, 2007.
- [102] W.-M. Wang, Z.-L. Li, and Su H.-B. Comparison of leaf angle distribution functions: Effects on extinction coefficient and fraction of sunlight foliage. *Agr. Forest Metrol.*, 143:106–122, 2007.
- [103] J.M. Vose, B.D. Clinton, N.H. Sullivan, and P.V. Bolstad. Vertical leaf area distribution, light transmittance, and application of the beer-lambert law in four mature hardwood stands in the southern appalachians. *Canadian Journal of Forest Research*, 25(6):1036–1043, 1995.
- [104] A. Takenaka, Y. Inui, and A. Osawa. Measurement of three-dimensional structure of plants with a simple device and estimation of light capture of individual leaves. *Functional Ecology*, 12(1):159–165, 1998.
- [105] S. Thanisawanyangkura, H. Sinoquet, P. Rivet, M. Cretenet, and E. Jallas. Leaf orientation and sunlit leaf area distribution in cotton. *Agricultural and Forest Meteorology*, 86(1):1–15, 1997.
- [106] F. Hosoi and K. Omasa. Factors contributing to accuracy in the estimation of the woody canopy leaf area density profile using 3D portable LiDAR imaging. *Journal of Experimental Botany*, 58(12):3463–3473, 2007.
- [107] A. Cescatti. Modelling the radiative transfer in discontinuous canopies of asymmetric crowns. I. Model structure and algorithms. *Ecological Modelling*, 101(2):263–274, 1997.
- [108] M. Chelle and B. Andrieu. The nested radiosity model for the distribution of light within plant canopies. *Ecological Modelling*, 111(1):75–91, 1998.
- [109] A. Iio, Y. Kakubari, and H. Mizunaga. A three-dimensional light transfer model based on the vertical point-quadrant method and monte-carlo simulation in a *fagus crenata* forest canopy on mount naeba in japan. *Agricultural and Forest Meteorology*, 151(4):461–479, 2011.
- [110] D. Van der Zande. Mathematical modeling of 3D canopy structure in forest stands using ground-based LiDAR. *Ph.D. thesis in bio-engineering, Katholieke Universiteit Leuven, Belgium*, 2008.
- [111] J.-F. Côté, R.A. Fournier, G.W. Frazer, and N.K. Olaf. A fine-scale architectural model of trees to enhance LiDAR-derived measurements of forest canopy structure. *Agricultural and Forest Meteorology*, 166:72–85, 2012.

- [112] F. Hosoi, Y. Nakai, and K. Omasa. 3D voxel-based solid modeling of a broad-leaved tree for accurate volume estimation using portable scanning LiDAR. *ISPRS Journal of Photogrammetry and Remote Sensing*, 82:41–48, 2013.
- [113] M. Béland, J.-L. Widlowski, and R.A. Fournier. A model for deriving voxel-level tree leaf area density estimates from ground-based LiDAR. *Environmental Modelling & Software*, 51:184–189, 2014.
- [114] C. Godin. Representing and encoding plant architecture: a review. *Annals of forest science*, 57(5):413–438, 2000.
- [115] P. Prusinkiewicz. Art and science of life: Designing and growing virtual plants with L-systems. In *XXVI International Horticultural Congress: Nursery Crops; Development, Evaluation, Production and Use 630*, pages 15–28, 2002.
- [116] J.B. Evers, A.R. van der Krol, J. Vos, and P.C. Struik. Understanding shoot branching by modelling form and function. *Trends in plant science*, 16(9):464–467, 2011.
- [117] J.M. Norman and J.M. Welles. Radiative transfer in an array of canopies. *Agronomy Journal*, 75(3):481–488, 1983.
- [118] C. Cluzeau, J.L. Dupouey, and B. Courbaud. Polyhedral representation of crown shape. a geometric tool for growth modelling. In *Annales des Sciences forestières*, volume 52, pages 297–306. EDP Sciences, 1995.
- [119] T. Palleja, M. Tresanchez, M. Teixido, R. Sanz, J.R. Rosell, and J. Palacin. Sensitivity of tree volume measurement to trajectory errors from a terrestrial LiDAR scanner. *Agricultural and forest meteorology*, 150(11):1420–1427, 2010.
- [120] C. Godin, E. Costes, and Y. Caraglio. Exploring plant topological structure with the AMAP-mod software: an outline. *The Finnish Society of Forest Science and The Finnish Forest Research Institute*, 1997.
- [121] S.N. Martens, S.L. Ustin, and J.M. Norman. Measurement of tree canopy architecture. *International Journal of Remote Sensing*, 12(7), 1991.
- [122] C. Preuksakarn. *Reconstructing plant architecture from 3D laser scanner data*. PhD thesis, Montpellier 2, 2012.
- [123] A. Bucksch, R. Lindenbergh, and M. Menenti. Skeltre. *The Visual Computer*, 26(10):1283–1300, 2010.
- [124] H. Xu, N. Gossett, and B. Chen. Knowledge and heuristic-based modeling of laser-scanned trees. *ACM Transactions on Graphics (TOG)*, 26(4):19, 2007.



- [125] N. Pfeifer, B. Gorte, and D. Winterhalder. Automatic reconstruction of single trees from terrestrial laser scanner data. In *Proceedings of 20th ISPRS Congress*, pages 114–119, 2004.
- [126] P. Prusinkiewicz and A. Lindenmayer. *The Algorithmic Beauty of Plants*. Springer-Verlag, 2004.
- [127] P.-H. Cournède, M.-Z. Kang, A. Mathieu, J.-F. Barczy, H.-P. Yan, B.-G. Hu, and P. De Reffye. Structural factorization of plants to compute their functional and architectural growth. *Simulation*, 82(7):427–438, 2006.
- [128] P. Ferraro and C. Godin. A distance measure between plant architectures. *Annals of Forest Science*, 57(5):445–461, 2000.
- [129] H. Sinoquet, G. Sonohat, J. Phattaralerphong, and C. Godin. Foliage randomness and light interception in 3D digitized trees: an analysis from multiscale discretization of the canopy. *Plant, Cell & Environment*, 28(9):1158–1170, 2005.
- [130] S. Delagrange and P. Rochon. Reconstruction and analysis of a deciduous sapling using digital photographs or terrestrial-LiDAR technology. *Annals of botany*, 108(6):991–1000, 2011.
- [131] B. Loch, J. Belward, and J. Hanan. Application of surface fitting techniques for the representation of leaf surfaces. In *MODSIM 2005 International Congress on Modelling and Simulation*, pages 12–15, 2005.
- [132] M.N. Oqielat, J.A. Belward, I.W. Turner, and B.I. Loch. A hybrid clough-tocher radial basis function method for modelling leaf surfaces. In *MODSIM 2007 International Congress on Modelling and Simulation*, pages 400–406, 2007.
- [133] T. Santos and J. Ueda. Automatic 3D plant reconstruction from photographs, segmentation and classification of leaves and internodes using clustering. In *7th International Conference on Functional-Structural Plant Models*, 2013.
- [134] T.T. Santos and A.A. de Oliveira. Image-based 3D digitizing for plant architecture analysis and phenotyping. In *Workshop on Industry Applications (WGARI) in SIBGRAPI 2012 (XXV Conference on Graphics, Patterns and Images)*, Ouro Preto, MG, Brazil, 2012.
- [135] X. Sirault, J. Fripp, A. Paproki, P. Kuffner, C. Nguyen, R. Li, H. Daily, J. Guo, and R. Furbank. Plantscan, a three-dimensional phenotyping platform for capturing the structural dynamic of plant development and growth. In *7th International Conference on Functional-Structural Plant Models*, 2013.
- [136] A. Paproki, X. Sirault, S. Berry, R. Furbank, and J. Fripp. A novel mesh processing based technique for 3D plant analysis. *BMC plant biology*, 12(1):63, 2012.

- [137] D. Bradley, D. Nowrouzezahrai, and P. Beardsley. Image-based reconstruction and synthesis of dense foliage. *ACM Trans. Graphics (Proceedings of SIGGRAPH)*, 32(4):74:1–74:10, 2013.
- [138] L. Quan, P. Tan, G. Zeng, L. Yuan, J. Wang, and S.B. Kang. Image-based plant modeling. *ACM Trans. Graph.*, 25(3), 2006.
- [139] T. Dornbusch and B. Andrieu. Lamina2shape: An image processing tool for an explicit description of lamina shape tested on winter wheat (*Triticum Aestivum* L.). *Computers and electronics in agriculture*, 70(1):217–224, 2010.
- [140] M. Bylesjö, V. Segura, R.Y. Soolanayakanahally, A.M. Rae, J. Trygg, P. Gustafsson, S. Jansson, and N.R. Street. Lamina: a tool for rapid quantification of leaf size and shape parameters. *BMC Plant Biology*, 8(1):82, 2008.
- [141] G. Lobet, X. Draye, and C. Périlleux. An online database for plant image analysis software tools. url: <http://www.plant-image-analysis.org>, 2013.
- [142] D. Boltcheva, E. Casella, R. Cumont, and F. Hétry. A spectral clustering approach of vegetation components for describing plant topology and geometry from terrestrial waveform LiDAR data. In *FSPM2013-7th International Conference on Functional-Structural Plant Models*, 2013.
- [143] G. Guennebaud, M. Germann, and M. Gross. Dynamic sampling and rendering of algebraic point set surfaces. In *Computer Graphics Forum*, volume 27, pages 653–662. Wiley Online Library, 2008.
- [144] E. Mingolla and J.T. Todd. Perception of solid shape from shading. *Biological Cybernetics*, 53:137–151, 1986.
- [145] J. Van Diggelen. A photometric investigation of the slopes and the heights of the ranges of hills in the maria of the moon. *Bulletin of the astronomical institutes of the Netherlands*, (XI.423), 1951.
- [146] T. Rindfleisch. A photometric method for deriving lunar topographic information. *Technical report - Jet Propulsion Laboratory*, (32-786), 1965.
- [147] B.K.P. Horn. Shape from shading: a method for obtaining the shape of a smooth opaque object from one view. *Technical report 232, MIT Artificial Intelligence Laboratory*, 1970.
- [148] K. Ikeuchi and B.K.P. Horn. Numerical shape from shading and occluding boundary. *Artificial Intelligence*, 17:141–184, 1981.
- [149] T. Morvan, P. Lamata, M. Reimers, E. Samset, and J. Declerck. Exploiting shading information for endoscopic augmentation. In *IGTSI’08 MICCAI workshop on Image guidance and computer assistance for soft-tissue interventions*, New-York, September 2008.

- [150] C. Wu. 3D reconstruction of anatomical structures from endoscopic images. *Ph.D. thesis, the Robotics Institute Carnegie Mellon University, Pittsburgh*, January 2010.
- [151] T. Okatani and K. Deguchi. Shape reconstruction from an endoscope image by shape from shading technique for a point light source at the projection center. *CVIU*, 66(2):119–131, 1997.
- [152] M.H. Mostafa, S.M. Yamany, and A.A. Farag. Integrating shape from shading and range data using neural networks. In *Conference on Computer Vision and Pattern Recognition (CVPR 99), Ft. Collins, CO, USA*, pages 2015–2020. IEEE Computer Society, 23-25 June 1999.
- [153] J.-F. Methot, D. Poussart, and R. Bergevin. Fusion of registered 2d intensity and 3D range data on an simd machine. *Proc. SPIE Sensor Fusion and Aerospace Applications*, 1956:236–247, 1993.
- [154] S. Kumar and M. Kumar. Application of neural network in integration of shape from shading and stereo. *Journal of King Saud University-Computer and Information Sciences*, 24(2):129–136, 2012.
- [155] E. Coleman and R. Jain. Obtaining 3-dimensional shape of textured and specular surfaces using four-source photometry. *Computer Graphics and Image Processing*, 18(4):309–328, 1982.
- [156] Y. Wang and D. Samaras. Estimation of multiple directional light sources for synthesis of augmented reality image. *Graphical Models*, 65:185–205, 2003.
- [157] M.A. Kreslavsky and R.V. Vdovichenko. Subresolution clinometry with magellan radar images-height of lava flow edges on venus. In *Lunar and Planetary Institute Science Conference Abstracts*, volume 28, page 759, 1997.
- [158] M.J. Brooks. Two results concerning ambiguity in shape from shading. *Proceedings of the National Conference for Artificial Intelligence, American Association for Artificial Intelligence, Washington DC*, pages 26–39, 1983.
- [159] A.R. Bruss. The eikonale equation: some results applicable to computer vision. *Journal of mathematical physics*, 23(5):890–896, 1982.
- [160] R. Kozera. Uniqueness in shape from shading revisited. *Journal of Mathematical Imaging and Vision*, 7:123–138, 1987.
- [161] J. Oliensis. Uniqueness in shape from shading. *International Journal of Computer Vision*, 6(2):75–104, 1991.
- [162] E. Prados and O. Faugeras. Shape from shading. *Handbook of mathematical models in computer vision*, pages 375–388, 2006.

- [163] B.K.P. Horn and M.J. Brooks, editors. *Shape from shading*. The MIT Press, 1989.
- [164] E. Prados, O. Faugeras, and E. Rouy. Shape-from-shading and viscosity solution. *Rapport de recherche INRIA*, 4638, Novembre 2002.
- [165] F.R. Nicodemus, J.C. Richmond, J.J. Hsia, I.W. Ginsberg, and T. Limperis. Geometrical consideration and nomenclature for reflectance. *National Bureau of Standard, Washington D.C.*, 1977.
- [166] G. Schaepman-Strub, M.E. Schaepman, T.H. Painter, S. Dangel, and J.V. Martonchik. Reflectance quantities in optical remote sensing - definitions and case studies. *Remote sensing of Environment*, 103:27–42, 2006.
- [167] B.K.P. Horn and R.W. Sjöberg. Calculating the reflectance map. *Appl. Opt.*, 18(11):1770–1779, Jun 1979.
- [168] R. Jain, R. Kasturi, and B.G. Schunck. *Machine Vision, Chapter 9*. McGraw-Hill, 1995.
- [169] J.-D. Durou, M. Falcone, and M. Sagona. Numerical methods for shape-from-shading: A new survey with benchmarks. *Computer Vision and Image Understanding*, 109(1):22–43, 2008.
- [170] R.J. Woodham. Photometric method for determining surface orientation from multiple images. *Optical Engineering*, 19(1), 1980.
- [171] E. Prados and O. Faugeras. Shape from shading: some new theoretical results and new algorithms for orthographic and pinhole cameras. *Actes du 14ème Congrès de Reconnaissance des Formes et Intelligence Artificielle*, 2004.
- [172] E. Prados and O. Faugeras. Shape from shading: a well-posed problem? *IEEE Conference on Computer Vision and Pattern Recognition*, pages 870–877, 2005.
- [173] Eikonal equation. *Wikipedia*.
- [174] J.-D. Durou, M. Falcone, and M. Sagona. A survey of numerical methods for shape from shading. *Rapport de recherche IRT*, (N°2004-2-R), 2004.
- [175] M. Falcone and M. Sagona. An algorithm for the global solution of the shape-from-shading model. *Proceedings of the 9th international conference on image analysis and processing*, 1:596–603, 1997.
- [176] P. Daniel and J.-D. Durou. From deterministic to stochastic methods for shape from shading. *Proceeding of the 4th Asian Conference on Computer Vision, Taipei, Taiwan*, pages 187–192, 2000.
- [177] P.-S. Tsai and M. Shah. Shape from shading using linear approximation. *Image and Vision Computing*, 12:487–498, 1994.

- [178] R. Zhang, P.-S. Tsai, J.E. Cryer, and M. Shah. Shape from shading: A survey. *IEEE transaction on pattern analysis and machine intelligence*, 21(8):690–706, 1999.
- [179] H. Theisel. Are isophotes and reflection lines the same? *Computed aided geometric design*, 18:711–722, 2001.
- [180] O. Vogel, M. Breuß, T. Leichtweis, and J. Weickert. Fast shape from shading for phong-type surfaces. In *Proceedings of the Second International Conference on Scale Space and Variational Methods in Computer Vision*, SSVM '09, pages 733–744, Berlin, Heidelberg, 2009. Springer-Verlag.
- [181] G. Healey and T.O. Binford. Local shape from specularity. *Technical report, Stanford University*, 1986.
- [182] T. Collins, J.-D. Durou, P. Gurdjos, and A. Bartoli. Single-view perspective shape-from-texture with focal length estimation: A piecewise affine approach. In *Proc. 3D Data Processing, Visualization and Transmission*, 2010.
- [183] Phong reflection model. *Wikipedia*.
- [184] K.J. Voss, A. Chapin, M. Monti, and H. Zhang. Instrument to measure the bidirectional reflectance distribution function of surfaces. *Applied optics*, 39, 2000.
- [185] V. Dragnea and E. Angelopoulou. Direct shape from isophotes. *Ben-COS05*, pages 45–50, 2005.
- [186] D. Carter. The structure of the isophotes of elliptical galaxies. *Monthly Notices of the Royal Astronomical Society*, 182, 1978.
- [187] H. Hagen, Th. Schreiber, and E. Gschwind. Methods for surface interrogation. *Proceeding Visualization, IEEE Computer society Press - Los Alamitos, California*, pages 187–193, 1990.
- [188] T. Poeschl. Detecting surface irregularities using isophotes. *Computer Aided Geometric Design*, 1:163–168, 1984.
- [189] B.K.P. Horn, R.S. Szeliski, and A.L. Yuille. Impossible shaded images. *IEEE Transactions on Pattern Analysis and Machine Intelligence*, 15(2):166–170, 1993.
- [190] A. Crouzil, X. Descombes, and J.-D. Durou. A multiresolution approach for shape from shading coupling deterministic and stochastic optimization. *INRIA Rapport de Recherche*, 2003.
- [191] E. Prados and O. Faugeras. A rigorous and realistic shape from shading method and some of its applications. *Technical Report, INRIA*, 5133, 2004.

- [192] A.M. Bruckstein. On shape from shading. *Computer vision, graphics, and image processing*, 44:139–154, 1988.
- [193] R. Kimmel and A.M. Bruckstein. Global shape from shading. *Computer vision and image understanding*, 62(3):360–369, 1995.
- [194] A. Braquelaire and B. Kerautret. Reconstruction of lambertian surfaces by discrete equal height contours and regions propagation. *Image and Vision Computing*, 23(2):177–189, 2005.
- [195] J.P. Braquelaire and A. Vialard. Euclidean paths: a new representation of boundary of discrete regions. *Graphical Models and Image Processing*, 61(1):16–43, 1999.
- [196] M. Peternell and T. Steiner. A geometric idea to solve the eikonal equation. In *Spring Conference on Computer Graphics 2005*, pages 43–48, 2005.
- [197] G. Monge. *Application de l’analyse à la géométrie*. 5ème édition, revue, corrigée et annotée par M.Liouville, Paris. Bachelier Imprimeur, 1850.
- [198] S. Lipschutz. *Differential Geometry*. Schaum’s Outlines, 1969.
- [199] S. Hahmann, A. Belyaev, L. Busé, G. Elber, B. Mourrain, and C. Rössl. Shape interrogation. In *Shape Analysis and Structuring*, pages 1–51. Springer, 2008.
- [200] R. Bricard. *Géométrie descriptive*. Octave Doin & Fils, Paris, 1911.
- [201] J. Lelong-Ferrand and J.-M. Arnaudiès. *Cours de mathématiques, tome 3: Géométrie et cinématique*. Dunod, 2001.
- [202] R.K. Mishra and Y. Zhang. A review of optical imagery and airborne LiDAR data registration methods. *The Open Remote Sensing Journal*, 5:54–63, 2012.
- [203] H. Maître. *Le traitement des images*. IC2: Serie Traitement du signal et de l’image. Hermes Science Publications, 2005.
- [204] M. Gondran and M. Minoux. *Graphes et algorithmes*, volume 6. Eyrolles Paris, 1985.
- [205] R.M. Haralick, S.R. Sternberg, and X.Zhuang. Image analysis using mathematical morphology. *IEEE Transactions on Pattern Analysis and Machine Intelligence*, 9(4):532–550, 1987.
- [206] H. Freeman. On the encoding of arbitrary geometric configurations. *IRE Transactions on Electronic Computers*, (2):260–268, 1961.
- [207] Low-pass filter. *Wikipedia*.
- [208] E. Prados. Real and synthetic images for the shape from shading problem. url: <http://steep.inrialpes.fr/people/Prados/demos/SFS/imagesDataBase>.

- [209] T.P. Wu and C.K. Tang. Separating specular, diffuse, and subsurface scattering reflectances from photometric images. In *Computer Vision-ECCV 2004*, pages 419–433. Springer, 2004.
- [210] N. Pfeifer, B. Höfle, C. Briese, M. Rutzinger, and A. Haring. Analysis of the backscattered energy in terrestrial laser scanning data. *Int. Arch. Photogramm. Remote Sens. Spat. Inf. Sci.*, 37:1045–1052, 2008.
- [211] T.A. Baugher. *Anatomy and taxonomy, in Concise Encyclopedia of Template Tree Fruit*. The Haworth Press: New York, NY, USA, 2004.
- [212] R. Lindenbergh, N. Pfeifer, and T. Rabbani. Accuracy analysis of the leica hds3000 and feasibility of tunnel deformation monitoring. In *Proceedings of the ISPRS Workshop, Laser scanning*, volume 36, page 3, 2005.
- [213] L. Bousquet, S. Lachérade, S. Jacquemoud, and I. Moya. Leaf BRDF measurements and model for specular and diffuse components differentiation. *Remote Sensing of Environment*, 98(2):201–211, 2005.
- [214] B. Mederos, L. Velho, and L.H. de Figueiredo. Robust smoothing of noisy point clouds. 2004(1):2, 2003.
- [215] R. Cifuentes, D. Van der Zande, C. Salas, J. Farifteh, and P. Coppin. Correction of erroneous LiDAR measurements in artificial forest canopy experimental setups. *Forests*, 5(7):1565–1583, 2014.
- [216] R.E. Kalman. A new approach to linear filtering and prediction problems. *Journal of basic Engineering*, 82(1):35–45, 1960.
- [217] R.B. Rusu and S. Cousins. 3D is here: Point cloud library (pcl). In *Robotics and Automation (ICRA), 2011 IEEE International Conference on*, pages 1–4. IEEE, 2011.
- [218] R. Fabio. From point cloud to surface: the modeling and visualization problem. *International Archives of Photogrammetry, Remote Sensing and Spatial Information Sciences*, 34(5):W10, 2003.
- [219] Delaunay triangulation. *Wikipedia*.
- [220] M. Franaszek, G.S. Cheok, and C. Witzgall. Fast automatic registration of range images from 3D imaging systems using sphere targets. *Automation in Construction*, 18(3):265–274, 2009.
- [221] Leica Geosystem. Targets for the Leica Scanstation C10 and HDS6200. url: <http://www.leica-geosystems.us>.
- [222] P.J. Besl and N.D. McKay. Method for registration of 3D shapes. In *Robotics-DL tentative*, pages 586–606. International Society for Optics and Photonics, 1992.

- [223] A. Makadia, A. Patterson, and K. Daniilidis. Fully automatic registration of 3d point clouds. In *Computer Vision and Pattern Recognition, 2006 IEEE Computer Society Conference on*, volume 1, pages 1297–1304. IEEE, 2006.
- [224] R. Jain and R. Kasturi. *Computer Vision*. IEEE Computer Society Press, 1991.
- [225] A. Hoover, G. Jean-Baptiste, X. Jiang, P.J. Flynn, H. Bunke D.B. Goldgof, K. Bowyer, D.W. Eggert, A. Fitzgibbon, and R.B. Fisher. An experimental comparison of range image segmentation algorithms. *Pattern Analysis and Machine Intelligence, IEEE Transactions on*, 18(7):673–689, 1996.
- [226] Connected space. *Wikipedia*.
- [227] J. Wang and J. Shan. Segmentation of LiDAR point clouds for building extraction. In *Proceedings of the 2009 ASPRS annual conference, ASPRS, Baltimore*.
- [228] X. Hu, C.V. Tao, and Y. Hu. Automatic road extraction from dense urban area by integrated processing of high resolution imagery and LiDAR data. *International Archives of Photogrammetry, Remote Sensing and Spatial Information Sciences. Istanbul, Turkey*, 35:B3, 2004.
- [229] R.A. Brooks, R. Creiner, and T.O. Binford. The ACRONYM model-based vision system. In *Proceedings of the 6th international joint conference on Artificial intelligence-Volume 1*, pages 105–113. Morgan Kaufmann Publishers Inc., 1979.
- [230] L.-J. Li, H. Su, Y. Lim, and L. Fei-Fei. Objects as attributes for scene classification. In *Trends and Topics in Computer Vision*, pages 57–69. Springer, 2012.
- [231] J.C. Russ. *The image processing handbook*. CRC press, 2011.
- [232] C. Lange and K. Polthier. Anisotropic smoothing of point sets. *Computer Aided Geometric Design*, 22(7):680–692, 2005.
- [233] O. Schall, A. Belyaev, and H.-P. Seidel. Robust filtering of noisy scattered point data. In *Proceedings of the Second Eurographics/IEEE VGTC conference on Point-Based Graphics*, pages 71–77. Eurographics Association, 2005.
- [234] M. Pauly, M. Gross, and L.P. Kobbelt. Efficient simplification of point-sampled surfaces. In *Proceedings of the conference on Visualization’02*, pages 163–170. IEEE Computer Society, 2002.
- [235] T. Weyrich, M. Pauly, R. Keiser, S. Heinzle, S. Scandella, and M. Gross. Post-processing of scanned 3D surface data. In *Proceedings of the First Eurographics conference on Point-Based Graphics*, pages 85–94. Eurographics Association, 2004.



- [236] R. Schnabel, P. Degener, and R. Klein. Completion and reconstruction with primitive shapes. In *Computer Graphics Forum*, volume 28, pages 503–512. Wiley Online Library, 2009.

